Towards fault tolerant quantum computation

Dissertation

ZUR ERLANGUNG DES DOKTORGRADES AN DER
FAKULTÄT FÜR MATHEMATIK, INFORMATIK UND PHYSIK
DER LEOPOLD-FRANZENS-UNIVERSITÄT INNSBRUCK

vorgelegt von

Mag. Daniel Nigg

durchgeführt am Institut für Experimentalphysik
unter der Leitung von

Univ.-Prof. Dr. Rainer Blatt

INNSBRUCK, DEZEMBER 2016

Für meine Familie Catherina und Felix

Abbreviations

AAPT	Ancilla assisted process tomography
AOM	Acousto-optic modulator
BSM	Bell state measurement
CSS	Calderbank, Shor, Steane
CCD	Charge-coupled device
COM	Centre-of-mass
DC	Direct current
DCQD	Direct characterization of quantum dynamics
DCRT	Direct characterization of relaxation times
EOD	Electro optical deflector
FTQC	Fault tolerant quantum computation
GHZ	Greenberger-Horne-Zeilinger
GM	Generalized method
ML	Maximum-likelihood
MS-gate	Mølmer and Sørensen gate
PDH	Pound-Drever-Hall
PID controller	Proportional-integral-derivative controller
PD	Photodiode
PBS	Polarizing beamsplitter
PMT	Photomultiplier tube
QEC	Quantum error correction
QND	Quantum non demolition
RF	Radio frequency
SB-cooling	Sideband cooling
SLM	Spatial light modulator
SQPT	Standard quantum process tomography
VCO	Voltage controlled oscillator

Kurzfassung

Seit einigen Jahrzehnten ist die Entwicklung eines zuverlässigen Quantenrechners eine der zentralen Forschungsschwerpunkte. Quantenrechner versprechen bestimmte Probleme zu lösen, welche für klassische Rechner nicht zu bewältigen sind. Ein Beispiel ist die Simulation von quantenmechanischen Systemen. Bei der experimentellen Umsetzung eines Quantenrechners ist das zugrundeliegende quantenmechanische System unvermeidlich von Störeinflüssen betroffen. Trotz dieser Störungen ermöglichen ausgefeilte Fehlerkorrekturverfahren die Realisierung eines Quantenrechners, indem die Information eines logischen Quantenbits auf mehrere physikalische Quantenbits verteilt wird. Diese Technik ermöglicht die Ausführung beliebig langer Quantenalgorithmen, obwohl die zugrundeliegenden physikalischen Komponenten fehlerhaft sind. Im Rahmen dieser Arbeit wird die Kodierung eines logischen Quantenbit in sieben physikalischen Quantenbits, bestehend aus $^{40}\mathrm{Ca}^{+}$ Ionen demonstriert. Das implementierte Protokoll entspricht einem funktionsfähigen, zweidimensionalen, topologischen Fehlerkorrekturcode und ebnet somit den Weg für einen fehlertoleranten Quantenrechner. Eine Grundvoraussetzung für die Realisierung eines fehlertoleranten Quantenrechners ist die Implementierung universeller Quantengatter, angewandt auf dem logischen Quantenbit. Die Rechenkapazität des Systems wird gezeigt, indem eine Reihe von Quantengattern, im Speziellen Clifford-Gatter, auf dem logischen Quantenbit angewandt werden. Die Leistungsfähigkeit eines Fehlerkorrekturcodes ist von den Eigenschaften der Störeinflüsse des jeweiligen Systems abhängig. Wichtige Merkmale eines Fehlerkorrekturcodes, wie zum Beispiel die maximal tolerierbare Fehlerrate werden durch theoretische Simulationen ermittelt. Diese Simulationen stützen sich hauptsächlich auf die Grundlage von einfachen Fehlermodellen ohne Berücksichtigung von räumlichen Korrelationen. Im Rahmen dieser Arbeit wird eine Methode zur Charakterisierung von räumlichen Korrelationen allgemeiner Quantenprozesse beschrieben und an einem realen Störprozess demonstriert.

Abstract

The development of a reliable quantum computer has been a central focus of research during the last decades. A quantum computer promises to solve certain problems, that are intractable for classical computers, such as simulating any quantum mechanical system. In experimental realizations of a quantum computer it is unavoidable that noise acts on the quantum system. Nevertheless, the construction of a quantum computer is possible using sophisticated error correction procedures that distribute the information of a single logical qubit over multiple physical qubits. This error correction enables arbitrarily long quantum computations to be performed on the encoded logical qubit even if the underlying physical components are faulty. In this work, the encoding of a logical qubit in seven physical qubits, consisting of trapped atomic $^{40}\mathrm{Ca}^{+}$ ions is demonstrated. The implemented code represents the minimal instance of a fully functional two-dimensional topological quantum error correction code, the color code, paving the way towards fault tolerant quantum computation. The realization of a fault tolerant quantum computer requires the implementation of a universal set of gates on the logical level. Here, we demonstrate the computational capabilities of the system by performing the entire set of Clifford operations on the encoded qubit. The performance of any quantum error correction code for fault tolerant quantum computation relies on the characteristics of the noise of the particular physical system. Theoretical simulations used to obtain important characteristic parameters, such as the maximum tolerable error probability of the faulty components, are typically based on simple models where spatial correlations are not considered. In the course of this work, a method is described that enables the quantification of spatial correlations of an arbitrary quantum process and is demonstrated on real noise processes.

Contents

Chapter 1

Introduction

The development of *quantum mechanics* at the beginning of the 20^{th} century was certainly one of the most revolutionary contributions to physics. The field of quantum mechanics not only changed our fundamental understanding of the microscopic world of atoms and their interaction with light but also paved the way towards novel applications in science and in our daily life, including superconductivity, magnetic resonance imaging, light-emitting diodes, lasers and electron microscopy, just to name a few examples. The foundation of quantum mechanics was laid around 1900 with the description of two physical phenomena that could not be explained by physicists at this time: first, the question of the black-body radiation and the resulting solution of the "ultraviolet catastrophe" by Max Planck [1] and second, the photoelectric effect, discovered in 1887 by Heinrich Hertz and explained by Albert Einstein in 1905 [2]. Subsequently, in the mid-twenties, a profound mathematical description of the state of a quantum mechanical system (e.g., molecules and atoms) was formulated in a groundbreaking work by Erwin Schrödinger [3].

At that time, discussions about the non-classical behaviour of single particles were of a theoretical nature, since experiments with single atoms or molecules did not seem to be achievable [4]. However, in the following years Wolfgang Paul and Hans Georg Dehmelt realized the first ion traps, enabling the storage and control of single particles [5]. Their pioneering work had far-reaching consequences, since quantum mechanical phenomenons, such as the discovery of quantum jumps [6–8] as well as techniques for the control of single particles, could now be investigated [9, 10].

At the same time, physicists investigated the question whether quantum systems could be useful for computational tasks. This question arises naturally from the rapid development of classical computers and especially the incredible increase of computer hardware power, first described by Moore's law in 1965. Continuing improvements in computer power boosted by shrinking electronic components will inevitably lead us to a situation where quantum effects starting to play a role. Motivated by this progression, the idea was born to make a fundamental change and to use quantum systems for computation following the rules of quantum mechanics instead of classical physics. Further motivation for the development of a quantum computing device was the pioneering work of Richard Feynman in 1982, in which he showed that any quantum mechanical system cannot be simulated efficiently with a classical computer but could be with a potential quantum computer [11]. Here, inefficient means that the computation time scales exponentially with the size of the simulated system. This important statement can be understood intuitively by the fact that the number of parameters required to describe the state of a quantum system scales exponentially with the number of particles in the system. In 1985, David Deutsch described the first concrete concept of a universal quantum computer, which is able to perform arbitrary computations and, even more important, has the potential to outperform a classical computer [12]. This exceptional result, that a quantum computer could solve computational problems more efficiently than classical computers, was proven by Peter Shor ten years later with the development of the *Shor algorithm*, enabling efficient prime factorization of any integer with a quantum computer [13]. The invention of the Shor algorithm had far-reaching impact, since and demonstrated the computational power of quantum computers, since no efficient algorithm has yet been found for prime factorization on a classical computer.

About one year later, Peter Zoller and Ignacio Cirac proposed a theoretical concept for the realization of a quantum computer with trapped atomic ions [14]. Following these ideas, the first realization of a two-qubit controlled-NOT quantum gate was demonstrated by the Innsbruck ion-trap group [15], enabling further achievements, such as for example deterministic quantum teleportation [16, 17] and large scale entanglement of up to 14 ions [18–20]. In the years since, prototypes of quantum computers have been implemented in various physical systems, including nuclear magnetic spins, single photons, superconducting electrodes and neutral atoms in optical lattices [21]. The requirements to realize a quantum computer are independent of the particular physical system and were formulated by DiVincenzo in 1996 [22]:

- a scalable system with well-characterized qubits,
- the ability to initialize the system in a given state,
- a universal set of quantum gates,
- coherence times much longer than the time required for the quantum gate operations,
- a qubit-specific measurement procedure.

In real world systems, the implementation of a quantum computer is challenging, as quantum systems cannot be shielded perfectly from the environment, which interacts with the systems, resulting in faulty quantum operations — referred to as *decoherence*. As a consequence, a quantum computer that is able to run extensive algorithms will not be achievable without correcting errors affecting the quantum system during the computation. Even the information encoded in a system acting as a quantum memory is prone to errors and cannot be successfully restored. The developers of early classical digital computers faced similar problems, as these machines were also affected by noise processes, leading to erroneous computation. It was proven that arbitrarily long computations are possible with classical digital computers in the presence of noise by using error correction procedures, thus enabling *fault-tolerant computation* [23].

Classical fault-tolerant computing is based on redundancy, which means that an intended operation is applied to several copies of the original information. After the computation, the copies are compared and a majority vote reveals the original information. Fault-tolerant computation was used as early as in the 1960s, e.g., for the Saturn V rocket guidance computer. Further applications of fault-tolerant computing have been to guarantee correct operation of critical computers, e.g., in nuclear power plants.

It was not clear at first whether the concept of redundancy could be applied to quantum computers, as the state of a qubit can not be copied, as proved by Wooters and Zurek in 1982 [24]. Peter Shor and Andrew Steane provided the first *quantum error correction codes* with their pioneering work in 1996 and revolutionized the development of quantum computers [25, 26]. The idea of any quantum error correction (QEC) code is to distribute the information of a quantum bit (qubit) over several qubits using entanglement. These QEC protocols provide an essential ingredient for fault-tolerant quantum computation (FTQC) [21].

FTQC is based on encoding the information using a quantum error correction code and executing all required operations on the encoded qubit while performing repetitive error correction. Dorit Aharonov and Michael Ben-Or showed that the successful realization of FTQC is possible if the error probability of the individual qubits is below a certain threshold — also known as the *quantum threshold theorem* [27, 28]. Fulfilling this threshold implies that the probability of an uncorrectable error on the encoded qubit during the computation is smaller than the error probability of the individual qubits, which enables the computation of arbitrarily long quantum algorithms.

The construction of "good" QEC codes for FTQC is not a trivial task, since codes differ in the number of physical qubits, the tolerable error rate and the overhead to implement quantum operations on the encoded qubit. As an example, consider the smallest QEC code distributing the information of one qubit over five qubits, developed by Raymond Laflamme in 1996 [29]. Laflamme's code requires only five qubits compared to seven qubits in the case of the Steane code, which seems to be advantageous. Nevertheless, the five-qubit code requires nontrivial entangling operations on the entire register to realize quantum operations on the encoded qubit. In contrast, performing the same quantum operation on qubits encoded in the Steane code requires only bit-wise operations on each physical qubit — a property known as *transversality*. Transversality of QEC codes is a powerful property, as any transversal code entails the implementation of quantum operations in a fault tolerant way.

A widely used method to realize FTQC is to combine elementary QEC codes (e.g. Steane code, Shor code, etc.) in multiple layers, which is known as *concatenation*. The concept of concatenation originates from classical computation theory and was developed by Dave Forney in 1966 [30]. Effectively, the error probability of the encoded qubit is reduced with the number of concatenated layers, leading to an enhancement of the robustness against noise but with the drawback of an exponential increase in the number of required qubits. Estimated error rate thresholds for concatenated codes are typically on the order of 10^{-5} [31].

A different and revolutionary course was set by Alexei Kitaev in 1997 with his studies on two-dimensional spin lattices [32]. Kitaev suggested that qubits arranged on a two-dimensional lattice with periodic boundary conditions (a torus) can be used as a quantum computer and proposed the first topological QEC code, the *Kitaev toric code*. The hallmark of topological codes is that information is encoded in global degrees of freedom, and therefore they are robust against perturbations that act locally on a subgroup of qubits [33]. The original toric code was adapted to open boundaries, which is a more realistic approach towards the experimental implementation [34]. In 2006, Hector Bombin and Miguel A. Martin-Delgado proposed a new class of topological codes, the *color codes*.

To date, topological codes represent the most promising approach towards the realization of a fault tolerant quantum computer, as they provide error thresholds on the order of 1%, which is orders of magnitude larger than in concatenated codes [35]. The behavior of a QEC code is estimated by theoretical simulations based on certain noise models. These simulations typically assume simple noise models, such as spatially uncorrelated noise. The influence of spatial correlations on a QEC code is of particular interest to current research. A method developed recently by Angel Rivas and Markus Müller enables the characterization of the amount of spatial correlations of an arbitrary quantum process [36]. The method is based on full tomography of the corresponding process, which scales unfavorably — in fact exponentially — with the system size [21]. Tomographic methods using additional qubits (ancilla qubits) and entangled states enable the tomography of processes with a reduced number of experimental settings [37].

The experiments described within this work were carried out on an ion-trap based quantum computer [38]. Here, the quantum information is encoded in electronic states of single $^{40}\mathrm{Ca}^{+}$ions, trapped in a string in a linear Paul trap [39]. In particular, this work is focused on the first experimental implementation of the minimal instance of the color code in a string consisting of seven ions. The capability of detecting arbitrary single-qubit errors as well as the implementation of multiple operations on the encoded qubit are demonstrated. The thesis is structured in the following way:

- **Chapter** 2 presents a theoretical introduction to the basics of quantum computation.
- **Chapter** 3 gives a detailed description of our ion-trap based quantum computer and the experimental realization of coherent and incoherent operations.
- The implementation of ancilla-assisted process tomography of unitary and non-unitary operations on a single qubit is discussed in **Chapter** 4.
- **Chapter** 5 describes the method used to quantify the amount of spatial correlations of arbitrary processes. In particular, in Sec. 5.1 the theoretical model is introduced, whereas in Sec. 5.2 the measured spatial correlations of real noise processes in our system are shown.
- In **Chapter** 6, the concept of QEC is introduced with the emphasis on FTQC and stabilizer codes. Furthermore, the basic principles of topological quantum codes is introduced with emphasis on the Kitaev toric code (Sec. 6.3.1) and the color code (Sec. 6.3.3).
- **Chapter** 7 presents the experimental results of the implementation of the topological color code in our system. In particular, Sec. 7.1 details the encoding of the logical qubit. Demonstration of the error detection capabilities is given in Sec. 7.4. The implementation of transversal Clifford operations on the encoded qubit as a major requirement for FTQC is described in Sec. 7.6.

Chapter 2

Quantum computation

2.1 Introduction to quantum computation

This chapter gives a basic introduction to quantum computation as well as a more detailed theoretical understanding for the characterization of coherent and incoherent quantum processes.
In classical computation, the smallest unit of information is called *bit* and can either be in the state 0 or 1. The quantum mechanical counterpart to the classical bit, the quantum bit (*qubit*), is theoretically described as a quantum mechanical two-level system. Independent of the physical platform encoding the qubit, it is treated as a mathematical object following the rules of quantum mechanics. The qubit is spanned by the two states $|0\rangle$ and $|1\rangle$, which are named computational basis states and correspond to the states 0 and 1 of the classical bit. The difference between the qubit and a classical bit is that the qubit can also be in a superposition of the two basis states

$$|\psi\rangle = a\,|0\rangle + b\,|1\rangle \,,$$

with the complex numbers a and b satisfying $|a|^2 + |b|^2 = 1$. Measuring the qubit will result in state $|0\rangle$ with probability $|a|^2$ and $|1\rangle$ with probability $|b|^2$, respectively. Therefore the qubit state $|\psi\rangle$ corresponds to an element of a two-dimensional vector space with the orthonormal basis $|0\rangle$ and $|1\rangle$ [21]. The quantum state $|\psi\rangle$ can also be expressed by the following equation:

$$|\psi\rangle = \cos(\theta/2)\,|0\rangle + e^{i\phi}\sin(\theta/2)\,|1\rangle \,, \tag{2.1}$$

with the rotation angle $0 \leq \theta \leq \pi$ and the phase $0 \leq \phi \leq 2\pi$. An intuitive and commonly used picture of the state $|\psi\rangle$ is the Bloch sphere representation, which is shown in Fig. 2.1. Each single qubit state $|\psi\rangle$ with the angles θ and ϕ define one point on the Bloch sphere. The states $|0\rangle$ and $|1\rangle$ define the north and south pole of the Bloch sphere, whereas the equatorial plane is spanned by the superposition states $1/\sqrt{2}(|0\rangle + e^{i\phi}\,|1\rangle)$. We will see later on that also single qubit operations can be visualized in the Bloch sphere representation.
In general, the state $|\psi\rangle_N$ of an N-qubit register can be expressed by the superposition of all possible basis states $|k\rangle_N$ [21]:

$$|\psi\rangle_N = \sum_{i=0}^{2^N-1} c_i\,|i\rangle_N \,, \tag{2.2}$$

where the pre-factors c_i fulfill the normalization condition $\sum_{i=0}^{2^N-1}|c_k|^2 = 1$ and the notation of the basis states is equivalent to the binary representation of the number i in an N-digit register.

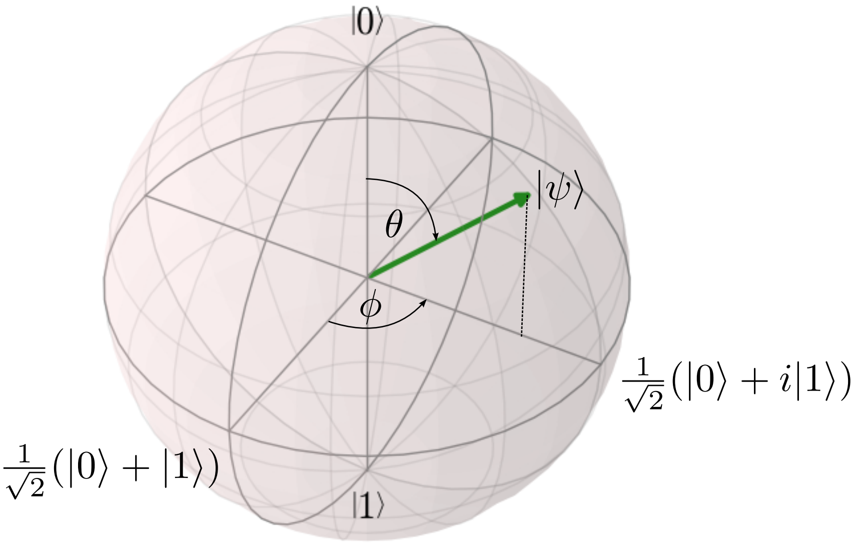

Figure 2.1: Bloch sphere representation: Bloch sphere representation of a single qubit where each state $|\psi\rangle$ is defined by one point on the Bloch sphere. The significant points are given by the states $|0\rangle$ and $|1\rangle$ on the north and south pole as well as the four superposition states $\frac{1}{\sqrt{2}}(|0\rangle \pm |1\rangle$ and $\frac{1}{\sqrt{2}}(|0\rangle \pm i\,|1\rangle$ arranged on the equatorial plane.

For example, the state $|5\rangle_3$ of a 3-qubit register corresponds to the state $|101\rangle$ $(101 = (1)2^2 + (0)2^1 + (1)2^0)$. An alternative formulation of quantum states is the density matrix (operator). The density matrix ρ of a quantum system is given by [21]:

$$\rho = \sum_{i=0}^{2^N-1} p_i \,|\psi_i\rangle \langle\psi_i| \,,$$

with the probability p_i of the system occupying the state $|\psi_i\rangle$. The density matrix formalism is used to describe ensembles of quantum states and effective decoherence [21]. The density matrix yields a complete description of a quantum system and has to fulfill the following conditions: (1) $tr(\rho) = \sum_n \rho_{nn} = 1$, which is equivalent to the normalization condition and (2) that ρ is a positive semidefinite operator satisfying $\langle i|\,\rho\,|i\rangle \geq 1$ for any state vector $|i\rangle$. Furthermore, if the system is prepared in a known state $|\psi\rangle$ the density operator is given by $\rho = |\psi\rangle\langle\psi|$, also referred to as a pure state. In contrast, if the state is not known exactly, the density operator describes a mixed state with relative probabilities p_i. The quantum system described by the density operator ρ is in a pure state only if $tr(\rho^2) = 1$ and otherwise $(tr(\rho^2) \leq 1)$ in a mixed state. A more detailed and extensive introduction is given in Ref. [21].

The term quantum computation describes the manipulation of quantum information by applying changes to the state of a quantum register. In the simplest case, the transformation of a single qubit state $|\psi\rangle = a\,|0\rangle + b\,|1\rangle$ to the output state $|\psi'\rangle = a'\,|0\rangle + b'\,|1\rangle$ can be expressed by

$$|\psi'\rangle = \begin{pmatrix} a' \\ b' \end{pmatrix} = \begin{pmatrix} U_{11} & U_{12} \\ U_{21} & U_{22} \end{pmatrix} \begin{pmatrix} a \\ b \end{pmatrix} , \tag{2.3}$$

with the 2x2-dimensional transformation matrix U. Because of the fact that the output state $|\psi'\rangle$ has to fulfill the normalization condition as well, there is the restriction of U being a unitary matrix, meaning that $UU^\dagger$ corresponds to the identity operation $\mathbb{1}$. An important set of single-qubit unitary gates are the Pauli matrices $\{X = \sigma_x, Y = \sigma_y, Z = \sigma_z\}$:

$$\sigma_x = \begin{pmatrix} 0 & 1 \\ 1 & 0 \end{pmatrix}, \sigma_y = \begin{pmatrix} 0 & -i \\ i & 0 \end{pmatrix}, \sigma_z = \begin{pmatrix} 1 & 0 \\ 0 & -1 \end{pmatrix}. \tag{2.4}$$

Further on, the Pauli matrices can be used to define arbitrary rotations around the (x, y, z) axis of the Bloch sphere by the following unitary rotation matrices [21]:

$$R_x(\theta) = e^{-i\frac{\theta}{2}X} = \begin{pmatrix} \cos(\theta/2) & -i\sin(\theta/2) \\ -i\sin(\theta/2) & \cos(\theta/2) \end{pmatrix} \tag{2.5}$$

$$R_y(\theta) = e^{-i\frac{\theta}{2}Y} = \begin{pmatrix} \cos(\theta/2) & -\sin(\theta/2) \\ \sin(\theta/2) & \cos(\theta/2) \end{pmatrix} \tag{2.6}$$

$$R_z(\theta) = e^{-i\frac{\theta}{2}Z} = \begin{pmatrix} e^{-i\theta/2} & 0 \\ 0 & e^{i\theta/2} \end{pmatrix}. \tag{2.7}$$

For example the unitary operation $R_x(\pi/2)$ corresponds to a $\pi/2$ rotation around the x-axis of the Bloch sphere. In classical computation a subset of logical operations (e.g. AND, NOT) are used to perform all kind of computational tasks. Similar to that, a set of quantum gates exists also for the quantum computer. A set of quantum gates, which has the capability to implement arbitrary unitary operations is referred to as *universal set of gates*. It can be proven that each unitary operation U can be decomposed into a product of single-qubit unitary gates and controlled NOT-gates (CNOT), which enables universal quantum computation [21]. The CNOT operation is an example of a conditional gate and acts on a system of two qubits. The operation of the CNOT gate is demonstrated in Table. 2.1. The target qubit is flipped if the state of the control qubit is $|1\rangle$ and otherwise left unchanged.

Control qubit	Target qubit	CNOT	Control qubit	Target qubit
$\|0\rangle$	$\|0\rangle$	→	$\|0\rangle$	$\|0\rangle$
$\|0\rangle$	$\|1\rangle$	→	$\|0\rangle$	$\|1\rangle$
$\|1\rangle$	$\|0\rangle$	→	$\|1\rangle$	$\|1\rangle$
$\|1\rangle$	$\|1\rangle$	→	$\|1\rangle$	$\|0\rangle$

Table 2.1: Controlled NOT-gate: The targer qubit is flipped dependent on the state of the control qubit. Is the control qubit is in the state $|1\rangle$, then the target qubit is flipped from $|0\rangle$ to $|1\rangle$ and vice versa.

One possible set of single-qubit operations included in the universal set of gates consists of the *Hadamard gate* H, the *Phase gate* S and the $\pi/8$ gate T:

$$H = 1/\sqrt{2}\begin{pmatrix} 1 & 1 \\ 1 & -1 \end{pmatrix}, S = \begin{pmatrix} 1 & 0 \\ 0 & i \end{pmatrix}, T = \begin{pmatrix} 1 & 0 \\ 0 & e^{i\pi/4} \end{pmatrix}.$$

Similar to the circuit diagrams in classical quantum information, the performance of a quantum algorithm is illustrated by quantum circuits, as shown in Fig. 2.2 for the given set of universal quantum gates. Each line represents one qubit and the timeline proceeds from left to right.

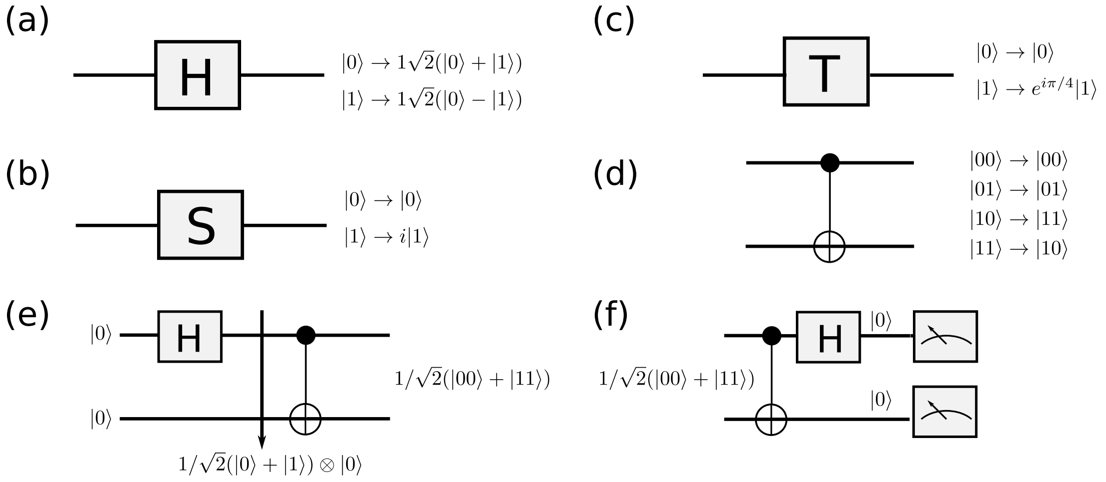

Figure 2.2: Universal set of quantum gates: Circuit representation of a universal set of quantum gates, consisting of the single-qubit (a) Hadamard gate H, (b) phase gate S, (c) T gate and (d) the two-qubit CNOT operation. In (e) the creation of a maximally entangled state is shown as a demonstration of a two-qubit algorithm.

A simple two qubit quantum algorithm is shown in Fig. 2.2(e), consisting of only one Hadamard operation and one CNOT gate. The resulting output state $|\psi\rangle = \frac{1}{\sqrt{2}} |00\rangle + |11\rangle$ belongs to a class of states, which exhibit strong non-classical correlations between the qubits and have the property that they can not be described by a product of two states $|\psi\rangle \neq |\psi_1\rangle |\psi_2\rangle$ - also known as *entanglement*. Entanglement is assumed to be the key element why quantum computers can outperform classical computers with algorithms like Shor's factorization, quantum simulations or quantum teleportation. The experimental implementation of the introduced universal set of quantum gates in a system of $^{40}\text{Ca}^{+}$ions is described in Sec. 3.

2.2 Characterization of a quantum system

2.2.1 Quantum operations and measurements

Within the following section a more detailed insight into the description of unitary and non-unitary quantum operations is provided as well as the concept of projective measurements in a certain basis will be given. Furthermore, the basics about state and process tomography with the focus on the Choi-Jamiolkowski isomorphism will be discussed. In the previous section, elementary quantum operations used to realize universal quantum computation were introduced. This section gives a more general picture of quantum operations, describing also non-unitary operations, which are fundamental for the understanding of noise processes in quantum information science.

Assume a system is initially prepared in the state ρ and a unitary process U acting on that system leads to an output state $\rho^{'} = \mathcal{E}(\rho) = U\rho U^{\dagger}$. The unitary process can be seen as a black box, which could for example stand for a certain quantum algorithm. Here, $\mathcal{E}$ represents the process mapping an input state ρ to an output state $\rho^{'}$. For closed quantum systems, the process can be described by the unitary transformation but in the case of open systems the situation is different. The evolution of an open quantum system can be described by the interaction of the system of interest ρ with the environment. In more detail, assume that the system and the environment initially form a product state $\rho \otimes \rho_{env}$. The system and the environment interact with each other, described by the transformation U and finally the environment is traced out to obtain the information of the system of interest [21, 40]:

$$\mathcal{E}(\rho) = tr_{env}[U(\rho \otimes \rho_{env})U^\dagger]. \tag{2.8}$$

In general, the output state $\mathcal{E}(\rho)$ can not be represented by a unitary transformation applied to the initial state. Within this representation of a quantum operation, knowledge about the state of the environment is required. Nevertheless, Equ. 2.8 can be formulated differently in terms of operators acting on the system of interest [21]

$$\epsilon(\rho) = \sum_k E_k \rho E_k^\dagger, \tag{2.9}$$

with the Kraus operators E_k. This formulation is known as *operator sum representation* and is a convenient method to describe the dynamics of a quantum system, since the information is given by the operators and no assumptions about the environment have to be made. Quantum systems can interact in a different way with the environment but lead to the same quantum process. For a trace preserving operation, the operators have to fulfill the relation $\sum_k E_k^\dagger E_k = \mathbb{1}$ [21]. This may also be interpreted as the fact that no population of the Hilbert space is being lost.

The operator sum representation will later be experimentally demonstrated by two non-unitary processes, namely amplitude- and phase damping (dephasing). Theses processes are essential elements for the description of different errors affecting a quantum system. The experimental quantification of these processes is discussed in Sec. 4. Amplitude damping leads to a loss of the population and coherence of a quantum system, whereas phase damping causes only a loss of the coherence without changing the population. The Kraus operators for amplitude and phase damping are given in Table 2.2.

Process	E_0	E_1
phase damping	$\sqrt{1-p}\begin{pmatrix}1 & 0\\0 & 1\end{pmatrix} = \sqrt{1-p}\,\mathbb{1}$	$\sqrt{p}\begin{pmatrix}1 & 0\\0 & -1\end{pmatrix} = \sqrt{p}\,Z$
amplitude damping	$\begin{pmatrix}1 & 0\\0 & \sqrt{1-\gamma}\end{pmatrix}$	$\sqrt{\gamma}\begin{pmatrix}0 & 1\\0 & 0\end{pmatrix}$

Table 2.2: Amplitude- and Phase damping: Kraus operators of phase- and amplitude damping operations as essential processes in the theory of quantum error correction.

The effect of the two processes on a quantum system initially prepared in the state ρ can be described using the operator sum representation $\mathcal{E}(\rho) = E_0\rho E_0^\dagger + E_1\rho E_1^\dagger$. The output state $\mathcal{E}_{phase}(\rho)$ for the phase damping process and the output state $\mathcal{E}_{ampl}(\rho)$ for the case of amplitude damping is given by:

$$\mathcal{E}_{phase}(\rho) = \begin{pmatrix} \rho_{11} & \rho_{12}(1-2p) \\ \rho_{21}(1-2p) & \rho_{22} \end{pmatrix} \tag{2.10}$$

$$\mathcal{E}_{ampl}(\rho) = \begin{pmatrix} 1-(1-\gamma)(1-\rho_{11}) & \rho_{12}\sqrt{1-\gamma} \\ \rho_{21}\sqrt{1-\gamma} & \rho_{22}(1-\gamma) \end{pmatrix}. \tag{2.11}$$

The error probabilities for the phase- and amplitude damping process are related to the parameters p and γ respectively. From the Kraus operators in Table 2.2 the phase damping process can be interpreted as phase flip operations occuring with the probability p. Complete dephasing occurs at a phase damping parameter $p = 0.5$. The probability of the population decay into the ground state is given by the parameter γ. In the case of full amplitude damping ($\gamma = 1$) the off-diagonal elements vanish, which is indicating dephasing and the whole population is in the ground state $|0\rangle$.

A convenient illustration of a quantum process is the Bloch sphere representation, which was introduced in the previous section. The idea is simply to apply the process of interest to each single qubit state lying on the surface of the Bloch sphere, which corresponds to a mapping of the initial Bloch sphere to the Bloch sphere of the output state. In Fig 2.3 the amplitude and phase damping processes are applied to the single qubit Bloch sphere.

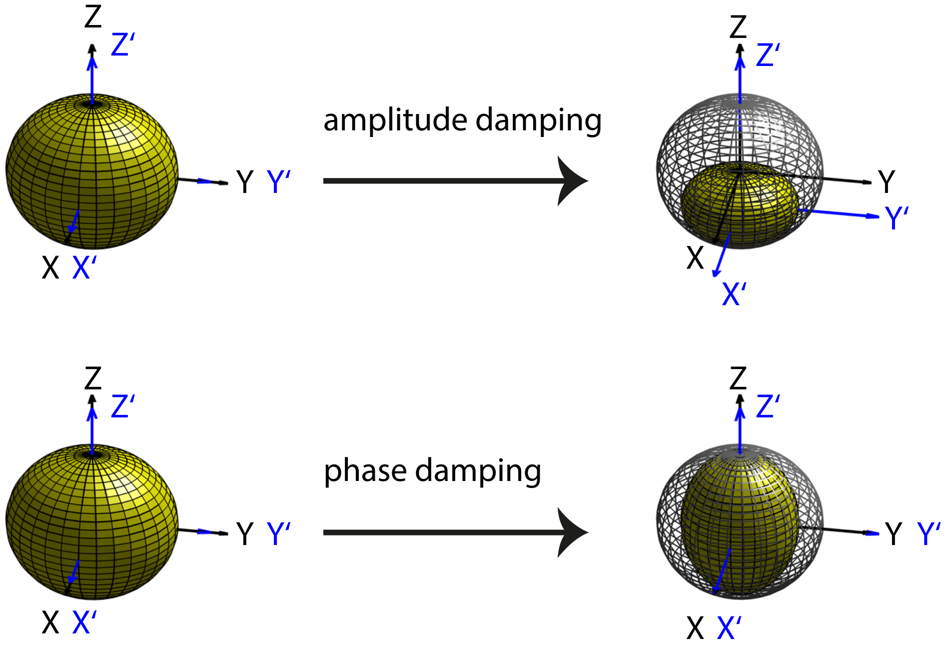

Figure 2.3: Amplitude- and phase damping: Illustration of the amplitude and phase damping process acting on the single qubit Bloch sphere. The particular process is applied to each state of the Boch sphere leading to a new deformed Bloch sphere.

The phase damping process is characterized by the fact that the whole Bloch sphere is shrinking along the X-Y plane, whereas in addition the amplitude damping process leads to a damping along the Z-axis towards the ground state. The black axes (X,Y,Z) in Fig 2.3 corresponds to the frame of the unperturbed Bloch sphere and the blue axes (X',Y',Z') belong to the mapped Bloch sphere. This allows the illustration of rotations around different axes.

The operator sum representation is a powerful tool to describe irreversible decoherence processes arising in every quantum system. Especially the theory of quantum error correction is based on this representation of incoherent processes, where the parameters p and γ are related to the probability at which an error occurs (see Sec. 6). Another more phenomenological interpretation of decoherence is based on the relaxation processes appearing in NMR systems. The spin-spin interactions and the thermalization of the spins to the temperature of the environment lead to an exponential damping of the density matrix elements. Note that the phase and amplitude damping processes also lead to a damping of the density matrix elements. The density matrix transformation can be described by the following relation [21]:

$$\rho = \begin{pmatrix} a & b \\ b^* & (1-a) \end{pmatrix} \rightarrow \begin{pmatrix} (a-1)e^{-t/T_1} + 1 & b\, e^{-t/T_2} \\ b^* e^{-t/T_2} & (1-a)e^{-t/T_1} \end{pmatrix}, \tag{2.12}$$

with the longitudinal relaxation time T_1 and the transverse relaxation time T_2. The parameters T_1 and T_2 are characteristic for any quantum system and allow the quantification of the coherence time T_2. In our system, T_1 corresponds to the natural lifetime of the qubit transition (see Sec.3). Please note that both descriptions of incoherent processes are identical but dependent on the purpose one or the other description is used. For example, in the framework of quantum error correction the operator sum representation is very advantageous, since processes can be related to error probabilities. This allows a comparison between different quantum systems, which is difficult when comparing the relaxation times. During the following chapters, both descriptions of incoherent processes will be used.

Measurements

So far, the described quantum algorithms included only coherent operations acting on the qubits. For qubit preparation, reset and measurements, incoherent operations are required. At the end of a quantum algorithm, the experimenter aims to obtain the information of the register or parts of it. In general, we are interested in measuring a certain *observable* M, which corresponds to an Hermitian operator acting on the state space of the system [21]. The observable M can be decomposed into the projectors P_m onto the eigenspace of the observable M with the eigenvalues m:

$$M = \sum_m m P_m. \tag{2.13}$$

The probability of obtaining the outcome m when measuring the observable M of the state $|\psi\rangle$ is given by $p(m) = \langle\psi| P_m |\psi\rangle$. The state $|\psi\rangle_{meas}$ after the measurement if the outcome m was observed is given by:

$$|\psi\rangle_{meas} = \frac{P_m |\psi\rangle}{\sqrt{p_m}}. \tag{2.14}$$

For example, let's assume the measurement of the observable $Z = \sigma_z$ with the eigenvalues $m = \{\pm 1\}$ and the corresponding eigenstates $\{|0\rangle, |1\rangle\}$. Preparing the coherent superposition state $|\psi\rangle = 1/\sqrt{2}(|0\rangle + |1\rangle)$ and measuring $Z = |0\rangle\langle 0| - |1\rangle\langle 1|$ would result in the outcome

± 1 with probability $1/2$. Measuring the outcome 1 projects the system to the state $|0\rangle$ and alternatively the outcome -1 leads to the output state $|1\rangle$. Therefore the measurement destroys the coherence of the system and leads to a collapse of the state, which is a main property of quantum mechanics.

Our experimental measurement procedure (see Sec. 3) corresponds to the described projective measurement in the computational basis $\{|0\rangle, |1\rangle\}$. In fact, dependent on the implemented algorithm, we aim to perform a measurement in a different basis than the experimentally feasible measurement in the computational basis. For example the realization of quantum teleportation requires the measurement in the *Bell basis* [16]. The measurement in the Bell basis is an important application in Sec. 4 and therefore will be discussed in more detail. The Bell states belong to the class of maximally entangled states. The quantum circuit creating the Bell states is shown in Fig. 2.2(e). Given the two qubit computational basis states $\{|00\rangle, |01\rangle, |10\rangle, |11\rangle\}$ as input states to this circuit (Fig. 2.2(e)), the resulting output states correspond to the Bell states $B = \{|\phi^+\rangle, |\phi^-\rangle, |\psi^+\rangle, |\psi^-\rangle\}$:

$$|00\rangle \xrightarrow{U_{bell}} \frac{1}{\sqrt{2}}(|00\rangle + |11\rangle) = |\phi^+\rangle \tag{2.15}$$

$$|11\rangle \xrightarrow{U_{bell}} \frac{1}{\sqrt{2}}(|00\rangle - |11\rangle) = |\phi^-\rangle \tag{2.16}$$

$$|10\rangle \xrightarrow{U_{bell}} \frac{1}{\sqrt{2}}(|10\rangle + |01\rangle) = |\psi^+\rangle \tag{2.17}$$

$$|01\rangle \xrightarrow{U_{bell}} \frac{1}{\sqrt{2}}(|01\rangle - |10\rangle) = |\psi^-\rangle \,. \tag{2.18}$$

The circuit diagram creating the four Bell states can also be expressed by a unitary operation U_{bell} acting on the computational basis states:

$$U_{bell} = (H \otimes \mathbb{1})\, CNOT = 1/\sqrt{2} \begin{pmatrix} 1 & 0 & 0 & 1 \\ 0 & 1 & 1 & 0 \\ 1 & 0 & 0 & -1 \\ 0 & -1 & -1 & 0 \end{pmatrix} . \tag{2.19}$$

Therefore, the unitary U_{bell} corresponds to the transformation of the computational basis states to the Bell basis, forming an orthonormal basis ($\langle B_i | B_j \rangle = \delta_{i,j}$). The measurement in the Bell basis can be performed by undoing the unitary U_{bell}, which transforms the Bell basis into the computational basis. This simply means that the circuit in Fig. 2.2(e) has to be inverted by applying first the CNOT operation on the entangled state followed by the Hadamard operation on the control qubit and measuring in the computational basis (see Fig. 2.2(f)). Analog to the projective measurement, the probabilities p_m of obtaining the Bell state B_m when measuring the state $|\psi\rangle$ in the Bell basis is given by the following equation:

$$p_m = \langle \psi | B_m \rangle \langle B_m | \psi \rangle = \langle \psi | \, U \, P_m \, U^{-1} \, | \psi \rangle \,, \tag{2.20}$$

with $P_m = \{|00\rangle\langle 00|, |01\rangle\langle 01|, |10\rangle\langle 10|, |11\rangle\langle 11|\}$ the projector onto the two qubit computational basis states. Note that this procedure can also be applied to any other basis of interest as long as the unitary transformation to the computational basis is known.

2.2.2 Quantum tomography of states and processes

The evolution of open- and closed quantum systems is theoretically described by quantum operations, which were introduced in the previous section. The question arises if the measurement of quantum operations can be related to experimentally accessible parameters. This section provides an answer to this question and describes the experimental tomography of quantum states and most importantly of quantum operations.

Quantum state tomography:

The goal of quantum state tomography is to reveal experimentally all elements of a density matrix ρ. It is well known that it is not possible to identify with certainty a quantum state given only one copy [21]. Nevertheless, if there exist many copies of the same state ρ, it is possible to describe the quantum state by measuring a set of observables. Assume the description of the state ρ by a set of matrices forming an orthonormal basis. Here, the set of matrices corresponds to the Pauli matrices $\{\mathbb{1}, X, Y, Z\}$. Therefore the state ρ of a single qubit can be expressed by:

$$\rho = \frac{\mathbb{1} + \mathrm{tr}(X\rho)X + \mathrm{tr}(Y\rho)Y + \mathrm{tr}(Z\rho)Z}{2}, \tag{2.21}$$

with the observables $(\mathrm{tr}(X\rho), \mathrm{tr}(Y\rho), \mathrm{tr}(Z\rho))$ corresponding to the expectation values $(\langle X\rangle, \langle Y\rangle, \langle Z\rangle)$ respectively. The expectation value $\langle Z\rangle$ can be obtained by a projective measurement of the operator Z [21]:

$$\langle Z\rangle = \sum_m m\, p(m), \tag{2.22}$$

with the possible outcomes $m = \{+1, -1\}$ and the probability $p(m) = \mathrm{tr}(P_m P_m^\dagger \rho)$ of measuring the outcome m. The value $p(m)$ corresponds to the probability of measuring the two computational states $|0\rangle, |1\rangle$, which can be measured in our experimental setup (see Sec. 3). Therefore, simply performing a projective measurement of the state ρ with a certain number of repetitions results in the probability $p(m)$ and therefore the expectation value of the Z operator. With a number of repetitions N, the uncertainty of measuring the probability $p(m)$ is given by the projection noise $\Delta p(m) = \sqrt{\frac{p(m)(1-p(m))}{N}}$ [41].

The measurement of the two remaining operators X and Y can be performed by mapping the eigenstates $\{|+\rangle_X, |-\rangle_X\}$ and $\{|+\rangle_Y, |-\rangle_Y\}$ of the X and Y operators to the Z eigenstates via a unitary matrix U analog to the Bell state measurement. Therefore the measurement of $\langle X\rangle$ and $\langle Y\rangle$ can be performed by:

$$\langle\psi| U_y^\dagger\, Z\, U_y |\psi\rangle = \langle\psi| X |\psi\rangle \tag{2.23}$$

$$\langle\psi| U_x^\dagger\, Z\, U_x |\psi\rangle = \langle\psi| Y |\psi\rangle, \tag{2.24}$$

i.e. by applying unitary operations $U_y = R_y(\pi/2)^\dagger$ and $U_x = R_x(\pi/2)$ corresponding to $\pi/2$ rotations around the Y and X axis of the Bloch sphere respectively. This procedure can be extended to measure the density matrix of an N qubit register, which requires 3^{N} different measurement settings. For example a two-qubit state tomography requires the measurement of the expectation values of the observables $\{X, Y, Z\} \otimes \{X, Y, Z\}$. For more details concerning state tomography, the reader is referred to [42, 43].

Quantum process tomography

The main idea of quantum process tomography is to evaluate a process $\mathcal{E}$ by probing the process with a set of properly chosen input states $\{\rho_1, ..., \rho_{d^2}\}$, where d corresponds to the dimension of the state space ($d = 2$ for a single qubit). The input states are chosen in such a way that the density operators ρ_i form a basis set for any dxd-dimensional matrix. The next step is to apply the operation of interest $\mathcal{E}$ to each of the input states and finally performing a measurement of the operators $\{Z, X, Y\}$ with the corresponding projectors $\Pi = \{|0\rangle\langle 0|, |1\rangle\langle 1|, |+\rangle_x\langle +|_x, |-\rangle_x\langle -|_x, |+\rangle_y\langle +|_y, |-\rangle_y\langle -|_y\}$. From the experimental point of view it would be preferable to reveal the process $\mathcal{E}$ directly from experimentally available data. Therefore, assume the expansion of any complete positive map (CP map) $\mathcal{E}$ by a fixed set of basis elements E_i [21]:

$$\mathcal{E}(\rho) = \sum_{m,n} \chi_{m,n}\, E_m \rho E_n^\dagger. \tag{2.25}$$

The property of complete positivity restricts any physical quantum process to preserve the positive semidefiniteness of the density matrix as well as the trace of the mapped density operator. The elements E_i form a basis for the set of operators acting on the state space and will be chosen to be the Pauli matrices $\{\mathbb{1}, X, Y, Z\}$ for each qubit. In the previous section the operator sum representation was used to describe a quantum process. The Kraus operators of a certain process can be expanded in terms of the set of Pauli matrices. The expansion coefficients $\chi_{m,n}$ are necessary, since the basis is fixed for any process acting on the system. Consequently, the matrix χ contains the whole information about the quantum process $\mathcal{E}$. This particular representation of a quantum process is known as *chi-matrix representation* [21]. The χ-matrix is a d^2xd^2-dimensional positive Hermitian matrix. For a single qubit, χ contains $d^4 - d^2 = 12$ independent parameters (4 input states x 3 measurements for the state tomography). In general, the number of experimental settings scales with 12^{N}, where N is the number of qubits, which is experimentally unfavorable. A different method based on ancilla assisted process tomography is described in Chapter 4 and allows a reduction of the experimental settings to 4^{N}.

The reconstruction of the χ-matrix directly from the experimentally obtained data by linear inversion is described in Ref. [21]. This method is straightforward but has the difficulty of potentially yielding an unphysical result, as for example negative eigenvalues or $tr(\rho_{out}^2) > 1$ of the output state ρ_{out} due to measurement errors. The same problem arises for the reconstruction of quantum states and can be overcome by the maximum-likelihood (ML) method as described in Ref. [44]. The idea is to find the quantum state, which describes the measurement results as closely as possible and simultaneously fulfills the requirements for a physical density matrix ρ (i.e. positive semidefiniteness and $tr(\rho) = 1$). The ML-method incorporating the required constraints for complete positivity and trace preservation of the quantum process can be formulated similar to the ML approach for reconstructing quantum states [44]. The main idea is based on the isomorphism between the CP map $\mathcal{E}$ and a positive semidefinite operator S. The CP map $\mathcal{E}$ transforms an input state ρ_{in} of the Hilbert space H to an output state ρ_{out} associated with the Hilbert space K, whereas the operator S acts on the higher-dimensional Hilbert space $H \otimes K$. In other words, the quantum process is equivalent to a higher-dimensional density operator, which enables the reconstruction of the χ-matrix using the ML approach analog to quantum state reconstruction. The equivalence of the quantum process $\mathcal{E}$ and the density operator S is also known as Choi-Jamiolkowski isomorphism [44].

The construction of the Choi-Jamiolkowski matrix S is illustrated in Fig. 2.4 and is based on the following approach: Assume an entangled state $|\psi\rangle_{AB}$ on the Hilbert state $H \otimes H$, which can be expressed in the following way:

$$|\psi\rangle_{AB} = \sum_{j=1}^{d} |j\rangle_A |j\rangle_B , \tag{2.26}$$

with the dimensions $d = dim(H) = dim(K)$ of the input and output Hilbert space. The Choi-Jamiolkowski matrix S is defined by applying the process $\mathcal{E}$ only to one part of the entangled state $|\psi\rangle_{AB}$:

$$S = \mathbb{1}_A \otimes \mathcal{E}_B(|\psi\rangle_{AB} \langle\psi|). \tag{2.27}$$

Therefore S corresponds to an operator acting on the Hilbert space $H \otimes K$. The quantum process is only applied to the system part B of the maximally entangled state and the subsystem A is unchanged by the identity operator. The output state ρ_{out} can be calculated by multiplying the matrix S with the input state ρ_{in}^T and partially tracing over the input Hilbert space H [44]:

$$\rho_{out} = \mathrm{Tr}_H(S\rho_{in}^T \otimes I). \tag{2.28}$$

Thus, the output density matrix S of the process acting on one of the two maximally entangled subsystems can be directly used as a superoperator to calculate the transformation from the input state ρ_{in} to output state ρ_{out}. The constraint of $\mathcal{E}$ being a trace preserving map is incorporated in the Choi-Jamiolkowski matrix S by the requirement that $\mathrm{Tr}_K(E) = I_H$ [44]. As an example consider the identity operation $\mathbb{1}$ and a single qubit bit flip X. For the two cases the S matrices can be calculated easily and lead to the maximally entangled Bell state $|\phi^+\rangle$ for the identity operation and $|\psi^+\rangle$ for the bit flip. The two matrices are plotted in Fig. 2.5.

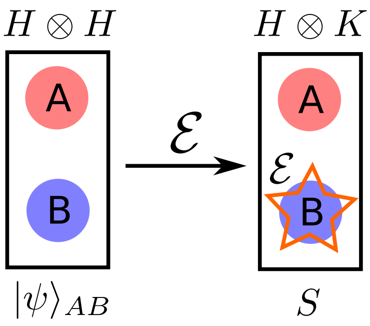

Figure 2.4: Choi-Jamiolkowski isomorphism: The Choi-Jamiolkowski state S is realized by applying the process $\mathcal{E}$ to one part of the maximally entangled state $|\psi\rangle_{AB}$.

As already described above, the experimental procedure for the reconstruction of a quantum process is to prepare a set of input states ρ_m and perform for each of the input states a set of measurements described by the operators Π_{ml}. For the standard process tomography the measurement operators correspond to the projectors $\{|0\rangle\langle 0|, |1\rangle\langle 1|, |+\rangle_x\langle +|_x, |-\rangle_x\langle -|_x, |+\rangle_y\langle +|_y, |-\rangle_y\langle -|_y\}$ used for the state tomography. The reconstruction method is applicable for any set of measurement settings (state preparation and measurement operators) allowing the calculation of the χ matrix. For example in Chapter 4 the χ matrix is reconstructed for the case

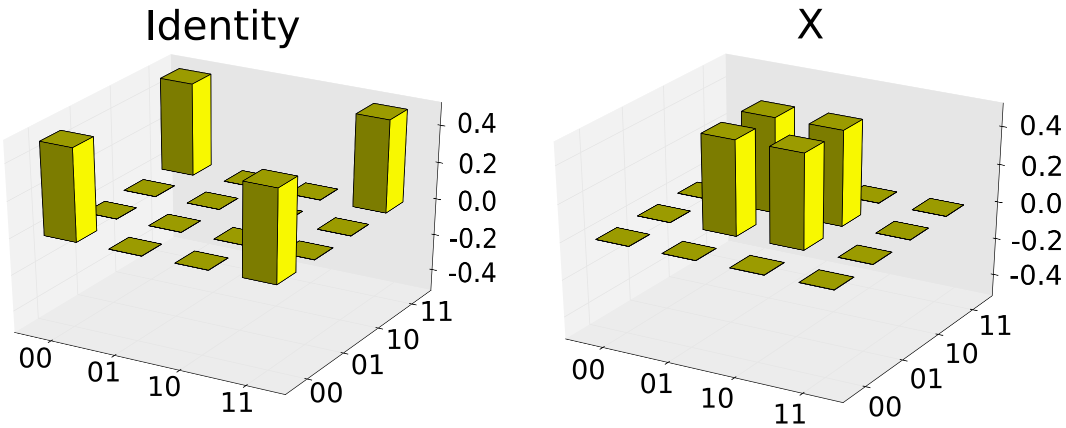

Figure 2.5: Choi-Jamiolkowski matrix: Illustration of the theoretically expected Choi-Jamiolkowski matrix S for the identity $\mathbb{1}$ and the bit-flip operation X.

of Bell state measurements. The Choi-Jamiolkowski isomorphism enables the reconstruction of a physical matrix S by maximizing the following log-likelihood function [44, 45]:

$$L(f_{ml}, p_{ml}(S)) = \sum_{m,l} f_{ml} ln(p_{ml}) - \mathrm{Tr}[\Lambda S], \tag{2.29}$$

where f_{ml} corresponds to the probability of measuring the projectors Π_{ml}[1], $p_{ml} = \mathrm{Tr}(\Pi_l \Pi_l^\dagger \rho_m)$ is given by the theoretically expected probabilities dependent on the matrix S and $\Lambda = \lambda \otimes I_K$. As already mentioned before, the same approach is used for the reconstruction of quantum states. The second term $\mathrm{Tr}[\Lambda S]$ is a Lagrange multiplier and takes the trace preservation of the process into consideration, fulfilling $\mathrm{Tr}_K(E) = I_H$. It can be proven that the log-likelihood function L is maximized if the following equation is satisfied [44, 45]:

$$S = \Lambda^{-1} K S, \text{ with } K = \sum_{m.l} \frac{f_{ml}}{p_{ml}} \rho_m^T \otimes \Pi_{ml}. \tag{2.30}$$

Using the hermiticity of S it follows that $S = SK\Lambda^{-1}$, which can be inserted again in Eqn. 2.30 and leads to $S = \Lambda^{-1} KSK \Lambda^{-1}$. The matrix Λ is calculated by tracing over the Hilbert space K and leads to $\Lambda = \sqrt{\mathrm{Tr}_K[KSK]}$. Eqn. 2.30 and the expression for λ allows the maximization of the log-likelihood function iteratively by starting from an unbiased density matrix $S^0 = \frac{I_{H \otimes K}}{2}$. Therefore S^0 is inserted in the right side of Eqn. 2.30, which leads to new matrix S^1 considering λ. This iterative procedure can be repeated until S converges to a final density operator. The requested condition of positive semidefiniteness and trace preservation is fulfilled after each iteration step. Please note that the creation of the maximally entangled state $|\psi_{AB}\rangle$ by expansion of the Hilbert space is a theoretical concept of the Choi-Jamiolkowski isomorphism and does not have to be realized experimentally. The described procedure can also be applied to entangled

---

[1] i.e. corresponds to $\{|0\rangle\langle 0|, |1\rangle\langle 1|, |+\rangle_x\langle +|_x, |-\rangle_x\langle -|_x, |+\rangle_y\langle +|_y, |-\rangle_y\langle -|_y\}$ for standard process tomography

input states (see Sec. 4). The S matrix resulting from the iterative ML algorithm has to be mapped to the χ matrix, which is described in Appendix B.

Chapter 3

Experimental setup

In the following chapter, the experimental setup used to realize the presented experiments will be explained. Here, the main focus is on the detailed description of implementing the Raman-sideband cooling technique as well as on improvements of the existing setup.

3.1 ^{40}Ca^{+} as a quantum bit

The experimental setup described here is a prototype of a small scalable quantum information processor, which is based on a string of ^{40}Ca^{+} ions confined in a linear macroscopic Paul trap [46, 39]. Since parts of the experimental setup are already described in Refs. [46, 39], the following sections will only provide a brief overview about the setup and a detailed description of the improvements carried out within this PhD project.
Our qubit is encoded in the ground and metastable states of a single ^{40}Ca^{+} ion. The required quantum gates, state initialization, detection of the quantum state and cooling of the motion is performed with precise laser pulses on or close to resonance with the optical transition connecting the two qubit states and will be described in the following sections. ^{40}Ca^{+} has one valence electron and therefore shows a level structure similar to the hydrogen atom. Additionally, the laser wavelengths required for cooling, detecting and manipulating the ions can be generated with commercial diode laser systems. In Fig. 3.1 a simplified level scheme of the ^{40}Ca^{+} ion, including the most relevant energy levels, is shown.

The optical qubit is encoded in the $4^2S_{1/2}$ ground state and the $3^2D_{5/2}$ excited state. More precisely, the ground- and excited states split up into $2J + 1$ Zeeman sublevels ($J = (1/2, 5/2)$ for the ($4^2S_{1/2}$, $3^2D_{5/2}$) states) by a constant magnetic field, which defines the direction of the quantization axis. The magnetic field strength is in the order of 4 G, which induces a splitting of the corresponding energy levels of about 2.7 MHz/G for the $4^2S_{1/2}$ state and 1.6 MHz/G for the $3^2D_{5/2}$ state. Our preferred choice of encoding the two-level system $\big(|0\rangle, |1\rangle\big)$ is the $4^2S_{1/2}$ $(m_j = -1/2) = |1\rangle \rightarrow 3^2D_{5/2}$ $(m_j = -1/2) = |0\rangle$ transition, as shown in Fig. 3.1. The most obvious source of decoherence for optical qubits is the natural lifetime of the excited state. In the case of ^{40}Ca^{+}, the excited state $3^2D_{5/2}$ has a natural lifetime $\tau = 1.17$ s [47], which is approximately a factor of 10^5 larger than the typical gate-operation times of about 10 μs. In addition to the qubit transition, multiple other optical transitions need to be addressed; an overview of the individual transition wavelengths as well as their purpose is

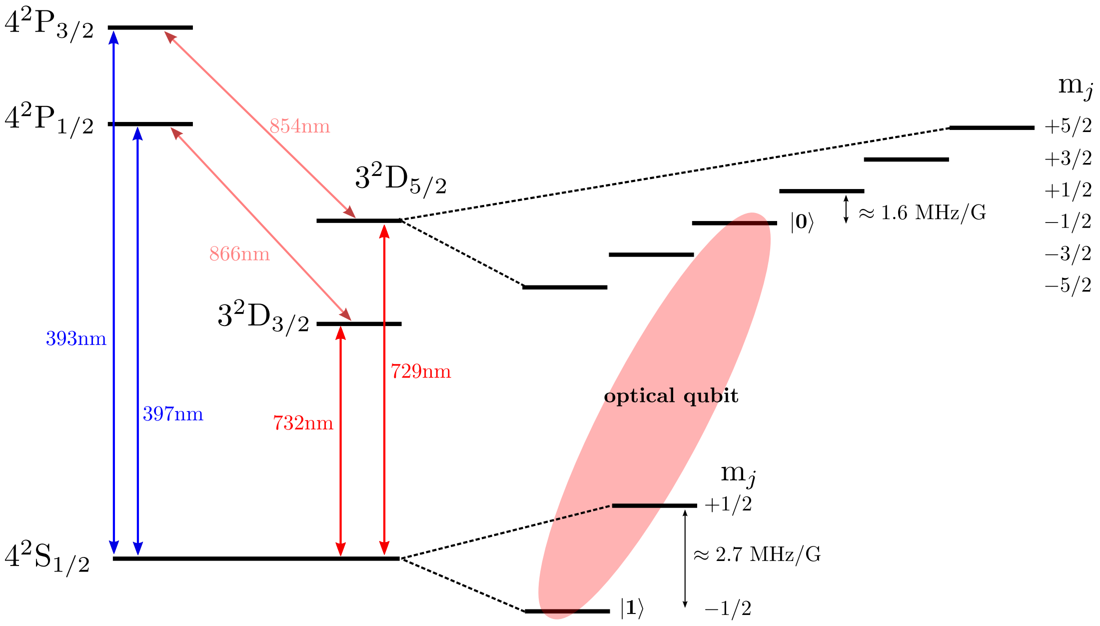

Figure 3.1: Schematic representation of the relevant level schemes of ^{40}Ca^{+}: The optical qubit is encoded in the Zeeman states $4^2S_{1/2}\ (m_j = -1/2) = |1\rangle$ and $3^2D_{5/2}\ (m_j = -1/2) = |0\rangle$. The $4^2S_{1/2} \rightarrow 4^2P_{1/2}$ transition at a wavelength of 397 nm is used for state detection and Doppler cooling (see main text for detailed explanation). The 866 nm and 854 nm light is used for repumping from the $3^2D_{5/2}$ and $3^2D_{3/2}$ state to the $4^2S_{1/2}$ ground state.

presented in Table 3.1.

Transition	Transition Wavelength	Purpose	AOM Frequ. shift
$4^2S_{1/2} \rightarrow 4^2P_{1/2}$	397.69990 nm	state detection and Doppler cooling	+80 MHz
$4^2S_{1/2} \rightarrow 3^2D_{5/2}$	729.14732 nm	coherent manipulation	+520 MHz
$3^2D_{5/2} \rightarrow 4^2P_{3/2}$	866.21460 nm	repumping during detection	+360 MHz
$3^2D_{3/2} \rightarrow 4^2P_{1/2}$	854.20958 nm	qubit reset and quenching for sideband cooling	+460 MHz
$4s^1S_0 \rightarrow 4p^1P_1$	422.67235 nm	Photoionization	–
$4p^1P_1 \rightarrow$ continuum	375 nm	Photoionization	–

Table 3.1: Required wavelengths for the ^{40}Ca^{+}qubit: Wavelengths, as shown at the wavemeter of the required transitions used for detection, cooling, repumping and state manipulation of the ^{40}Ca^{+}qubits (see also Ref.[46]). All wavelengths are measured with the WS7 wavemeter from High Finesse. The WS7 wavemeter has an accuracy of 10 MHz and therefore the wavelength numbers are reference values for typical experimental procedures. The actual applied laser frequency is shifted from the given value by the AOM frequency.

3.1.1 Laser systems

The requirements on the different laser systems depend on their role, where cooling and repumping lasers need to be stabilized to approximately 1 MHz and the qubit laser is required to be stabilized to ≤ 10 Hz. Frequency stability is achieved by stabilizing each laser to a reference cavity using the Pound Drever Hall (PDH) locking technique [48].

Ti-sapphire laser system at 397 nm:
The Ti:sapphire laser system from Coherent corresponds to a vertically mounted ring-laser including a Ti:sapphire crystal, which is pumped by a diode pumped solid state laser (DPSS) (Verdi V10) at a wavelength of 532 nm. The output of the Ti:sapphire laser at a wavelength of 794 nm and a pump power of 8 W is in the order of 650 mW. The output of the Ti:sapphire laser is frequency doubled to 397 nm by a commercial frequency doubling system[1]. The resulting maximum output power at 397 nm is in the order of 120 mW, which corresponds to a doubling efficiency of approximately 20%. A detailed description of the Ti:sapphire ring laser system is given in Ref. [49].

Ti:sapphire laser system at 729 nm:
The laser system used for coherent manipulation of the optical qubit is a Ti:sapphire laser at a wavelength of 729 nm. Since the natural linewidth of the optical qubit transition is 136 mHz and the coherence time of our quantum system is directly given by the laser linewidth, the required linewidth is in the order of 1 Hz. This demanding task can be accomplished by locking the Ti:sapphire laser to a reference cavity with a finesse of $F \approx 480000$. The achieved linewidth is in the order of 1 Hz over a time period of 1 second and 40 Hz over 2 hours. A detailed description of the locking procedure as well as technical details about the reference cavity is given in Refs. [49, 50].

Diode laser systems at 866 nm and 854 nm:
Optical repumping during the detection process is realized by a Toptica[2] diode laser system at 866 nm with an output power of about 30 mW. The light from the diode laser is amplified by a tapered amplifier (TA)[3] and directly coupled to an optical polarization maintaining (PM) single-mode fiber. The residual light power at the fiber output is on the order of 160 mW at a TA current of 1284 mA.

The required laser light at 854 nm for resetting the qubit and quenching the $3^2D_{5/2}$ state for sideband cooling is generated by a DL 100 Toptica diode laser system with a maximum output power of about 30 mW. Both laser systems are stabilized to reference cavities and exhibit a residual linewidth of less than 200 kHz.

---

[1] Spectra Physics SC-Block, SB550 102

[2] Toptica DL pro - Tunable Diode Laser

[3] semiconductor amplifier TA pro

Diode laser systems at 375 nm and 422 nm:

The ^{40}Ca$^+$ions are generated by an isotope selective two-step photoionization process from the $4s^1S_0$ ground state of neutral calcium to the excited state $4p^1P_1$ at a wavelength of 422 nm followed by ionization with 375 nm light. A detailed description of the ionization procedure can be found in Ref. [51]. The frequency of the 422 nm diode laser is controlled by a grating integrated in Littrow configuration, whereas the 375 nm diode laser is free running. The optical power of both laser systems is on the order of about 8 mW.

3.1.2 Qubit initialization and state detection

A typical experimental sequence consists of four steps: (1) Doppler cooling and state initialization (2) sideband cooling of the motional axial modes (3) coherent operations (4) state detection. Fig. 3.2(a) shows the pulse sequence of one experimental cycle. The first step is the cooling of the trapped ^{40}Ca$^+$ions on the $4^2S_{1/2} \leftrightarrow 4^2P_{1/2}$ dipole transition to a mean vibrational quantum number $\bar{n} \approx 12$ phonons using the Doppler cooling method followed by initializing the ion in the $4^2S_{1/2}$ ground state [52, 10]. State initialization is performed by repumping the population from the $3^2D_{5/2}$ state by the 854 nm laser and optical pumping from the $4^2S_{1/2}$ $(m_j = +1/2)$ to the $4^2S_{1/2}$ $(m_j = -1/2)$ via σ_- polarized 397 nm light (see Fig. 3.2(b)). As an alternative, the optical pumping from the $4^2S_{1/2}$ $(m_j = +1/2)$ state can be carried out in a frequency selective way, shelving the population from the $4^2S_{1/2}$ $(m_j = +1/2)$ state to the $3^2D_{5/2}$ $(m_j = +3/2)$ state by the 729 nm laser and simultaneously pumping the $3^2D_{5/2}$ population to the $4^2S_{1/2}$ $(m_j = -1/2)$ ground state by 854 nm light (see Fig. 3.2(c)). The latter approach has the advantage of not being sensitive to the polarization and therefore is very useful when the direction of the magnetic field is changed (e.g. to compensate for the electric quadrupole shift).

In the second step, the motion of the ion is cooled using a resolved sideband cooling technique on the qubit transition. This method enables the cooling of the ions to a mean phonon number of $\bar{n} \leq 0.1$. Within the current work, this cooling method was extended by a sideband cooling technique using Raman beams on the qubit transition, which will be explained in Sec. 3.7. In the third step, the coherent operations are applied on the $4^2S_{1/2} \rightarrow 3^2D_{5/2}$ qubit transition using the narrow linewidth 729 nm laser. Finally, the population of the $4^2S_{1/2}$ and $3^2D_{5/2}$ state of each individual qubit is detected. This can be achieved by exciting the $4^2S_{1/2} \leftrightarrow 4^2P_{1/2}$ transition at the end of the sequence. If the ion is in the state $4^2S_{1/2}$ the population is transferred to the $4^2P_{1/2}$ state and decays back to the $4^2S_{1/2}$ state, while emitting light. The emitted light is detected by a photomultiplier tube[4] and by a CCD camera[5]. During the 397 nm detection pulse, the 866 nm repumping beam is applied to the ion continuously to avoid population loss into the $3^2D_{3/2}$ state. If the ion is in one of the $3^2D_{5/2}$ Zeeman levels it remains dark after the detection pulse. This measurement method, also known as electron shelving, projects any state of the qubit onto the σ_z eigenstates $(|0\rangle, |1\rangle)$ (see Ref. [46] for further details).

---

[4] HAMAMATSU H10682-210

[5] Andor iXon Ultra 897

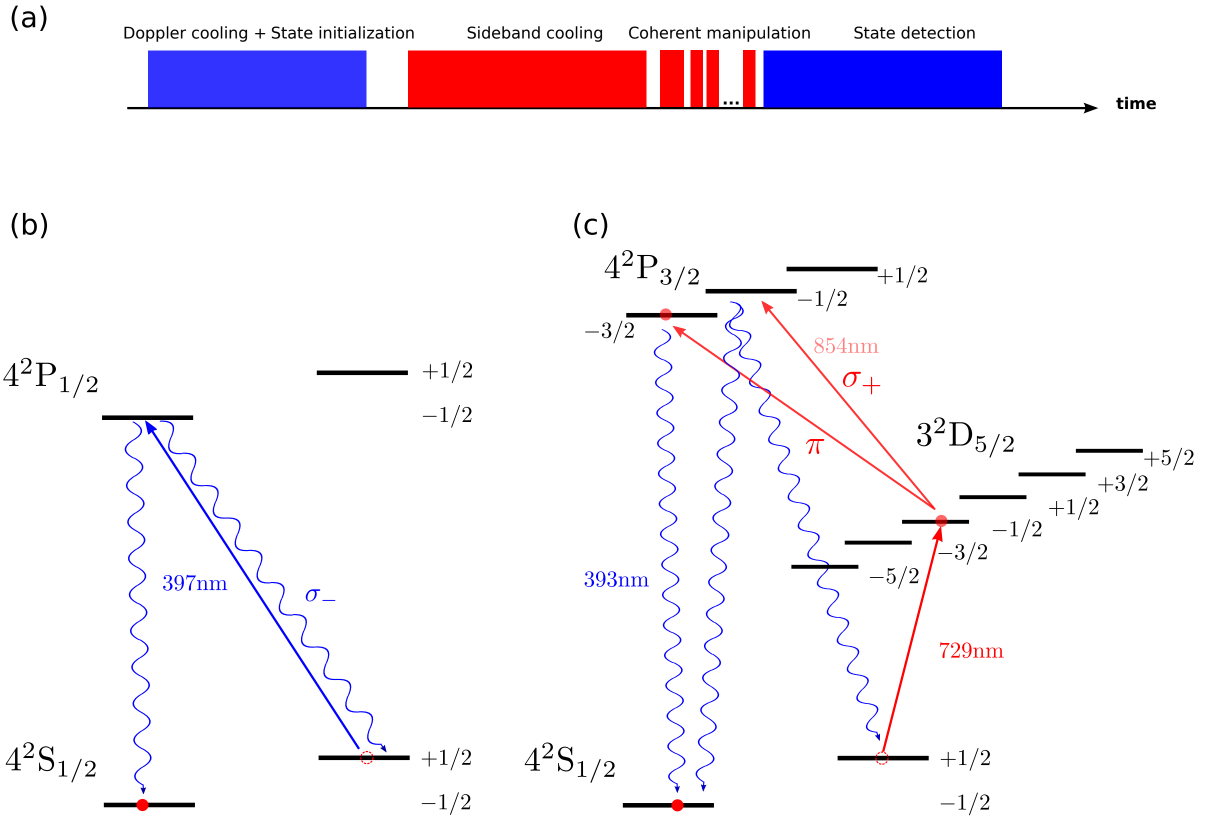

Figure 3.2: Experimental cycle and optical pumping schemes: Illustration of one experimental cycle (a) consisting of Doppler cooling and state initialization, sideband cooling of the motional state, coherent manipulation of the qubit and finally state detection using electron shelving. Optical pumping during the state initialization can be performed in two ways: (b) shelving the population from the $4^2S_{1/2}$ state polarization selective via σ_- light to the $4^2P_{1/2}$ state and (c) frequency selective pumping using the $4^2S_{1/2}$ $(m_j = +1/2) \rightarrow 3^2D_{5/2}$ $(m_j = -3/2)$ transition followed by optical pumping to the $4^2S_{1/2}$ state.

3.2 Laser-ion interaction

As already mentioned, the ^{40}Ca$^+$ions are confined to a string in a linear Paul trap by electric fields [53]. The design of the linear Paul trap used in our experimental setup is shown in Fig. 3.3. The trap consists of two tip electrodes separated by 5 mm along the axial z-direction and four radio frequency (RF) electrodes with a distance of 1.6 mm [39]. More precisely, the trapping potential along the axial direction is generated by a positive voltage on the order of 1 kV to 1.5 kV and can be well described by a harmonic trapping potential. The radial confinement is realized by a time-varying potential with a frequency of 23 MHz and a voltage amplitude of several 100 V.

The motion of the ion can be described by 3D harmonic oscillations around the minimum of the trapping potential in the axial and radial (secular motion) direction with typical frequencies of $\omega_z = (2\pi)1$ MHz and $\omega_r = \omega_x = \omega_y = (2\pi)3$ MHz respectively. The secular motion of the ion is modulated by a harmonic oscillation at the trap-drive frequency (23 MHz), the so-called

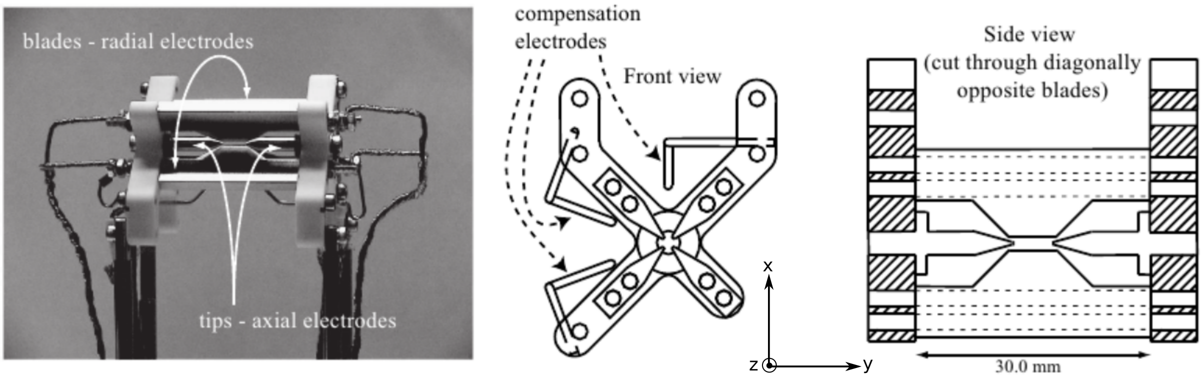

Figure 3.3: Linear Paul trap design: Drawing of the linear Paul trap used to confine a string of $^{40}\text{Ca}^{+}$ ions [39]. The picture was taken from Ref. [46].

micromotion. The micromotion can be compensated along the x- and y direction by shifting the ion to the minimum of the trap potential by DC voltages applied on two compensation electrodes (see Fig. 3.3). A detailed analysis of the equations of motion of a particle confined in a harmonic potential is presented in Ref. [54]. In the following, we will only consider a quantum mechanical description of the motion in the axial direction, neglecting the micromotion and the radial degrees of freedom. For the complete quantum mechanical description of an ion stored in a trap the harmonic motion of the particle has to be considered. In our case we make use of the axial center-of-mass (COM) mode to enable coupling of the ions, which is essential for the generation of entangled states (see Sec. 3.6). The combined system is composed of the qubit, which is described by a two-level system and the quantum mechanical oscillator, illustrated in Fig. 3.4.

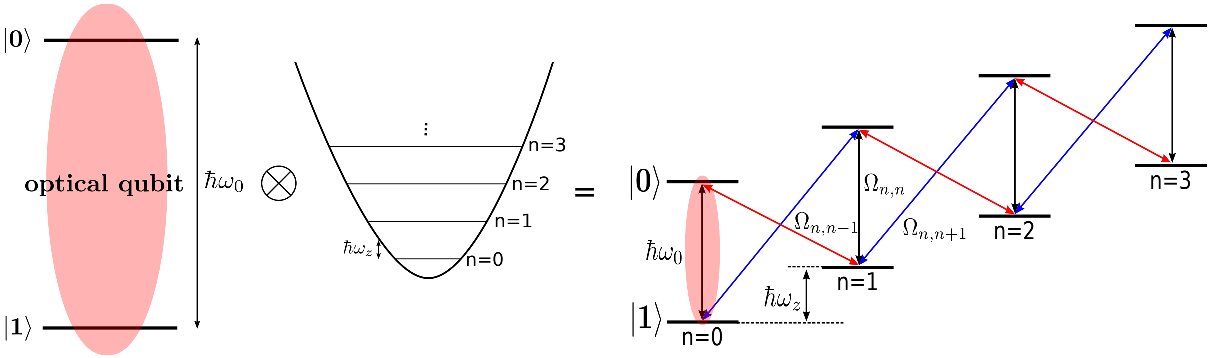

Figure 3.4: Two level system coupled to a harmonic oscillator: Coupling of a two level system with the ground state $|1\rangle$ and excited state $|0\rangle$ to a harmonic oscillator with the oscillation frequency ω_z. The wave function of the joined system $|\psi\rangle \otimes |n\rangle = \sum_n c_n |\psi, n\rangle$ contains besides an arbitrary state $|\psi\rangle$ of the two-level system also a motional part with the harmonic oscillator eigenstates $|n\rangle$. The model of the combined system illustrates the coupling to the carrier with the Rabi frequency $\Omega_{n,n}$, as well as to the red- and blue-sidebands with the coupling strengths $\Omega_{n,n-1}$ and $\Omega_{n,n+1}$, respectively.

A useful illustration of the composite system is the level scheme shown Fig. 3.4, which reveals that not only transitions between the two-qubit levels $|0\rangle$ and $|1\rangle$ can be driven by a laser field, but also transitions between states with different motional numbers n, as shown in Fig. 3.4. The interaction between light and the joint system of a trapped ion can be expressed by the following Hamiltonian H [54]:

$$\begin{aligned} H &= H_0 + H_I && (3.1)\\ H_0 &= \hbar\omega_z(a^\dagger\, a + 1/2) + 1/2\hbar\omega_0\sigma_z && (3.2)\\ H_I &= 1/2\hbar\Omega(e^{i\eta(a+a^\dagger)}\sigma^+ e^{-i\nu_L t} + e^{-i\eta(a+a^\dagger)}\sigma^- e^{i\nu_L t}), && (3.3)\end{aligned}$$

where H_0 corresponds to the Hamiltonian of the internal two-level system and the quantum mechanical harmonic oscillator with $a, a^\dagger$ the annihilation and creation operators and the Pauli operator σ_z. The Hamiltonian H_I describes the interaction with the laser field and $\sigma^+ = |e\rangle\langle g|, \sigma^- = |e\rangle\langle e|$. Here, the frequencies ω_0, ω_z and ν_L correspond to the two-level resonance frequency, the axial trap frequency and the laser frequency, respectively. The coupling strength of the light field with the two-level system is given by the Rabi frequency Ω. The parameter η, named Lamb-Dicke parameter, describes the ratio of the laser wavelength λ to the spatial expansion of the ground-state wave packet of the harmonic oscillator Δx_0[6]:

$$\eta = k\sqrt{\frac{\hbar}{2m\omega_z}} = \frac{2\pi}{\lambda}\Delta x_0. \tag{3.4}$$

In the case of $\eta^2(2n+1) \ll 1$ with the motional quantum number n of the harmonic oscillator state, the spatial extension of the ion is small compared to the wavelength of the laser field, which is known as the Lamb-Dicke regime. In the Lamb-Dicke regime the interaction Hamiltonian H_I can be simplified by the following (cut off) Taylor expansion:

$$e^{\pm i\eta(a+a^\dagger)} \approx 1 \pm \eta(a + a^\dagger). \tag{3.5}$$

The Lamb-Dicke approximation leads to a suppression of the coupling between states with a difference in the motional quantum number of more than two quanten of motion. The coupling strength $\Omega_{n,n}$ to the carrier transition between the states $|0,n\rangle$ and $|1,n\rangle$ is in second order Lamb-Dicke approximation dependent on the motional quantum number n:

$$\Omega_{n,n} = \Omega(1 - n\eta^2).$$

Detuning the resonance laser frequency by ω_z enables the coupling between the states $|0,n\rangle$ and $|1,n+1\rangle$, which is referred to as blue-sideband transition (see Fig. 3.4). In contrast to the excitation of the blue sideband, setting the laser frequency to $\omega_0 - \omega_z$ will drive transitions from $|0,n\rangle$ to $|1,n-1\rangle$, known as red-sideband respectively. The corresponding coupling strength for the blue- and red-sidebands is given by the following equation [54]:

$$\begin{aligned} \Omega_{n,n+1} &= \Omega\eta\sqrt{n+1} && \text{blue sideband transition}\\ \Omega_{n,n-1} &= \Omega\eta\sqrt{n} && \text{red sideband transition}\end{aligned}$$

---

[6] If the laser and the direction of the axial motion form an angle ϕ, then the Lamb-Dicke paramter is modified to $\frac{2\pi}{\lambda}\Delta x_0\cos(\phi)$.

The coupling strength to the red- and blue-sideband is weaker by η than to the carrier transition given the same laser light intensity. In our system, we assume that the Lamb-Dicke approximation is valid, as typical values for the Lamb-Dicke parameter in our setup are in the order of $\eta = 0.06$.

3.3 Optical setup

The geometry of the vacuum vessel, containing the linear Paul trap in the center, is sketched in Fig. 3.5. The different laser beams described in the previous sections are aligned with respect to the trap axis in various directions. The quantization axis is defined by the superposition of the magnetic field $\vec{B}_\sigma$ and $\vec{B}_D$ generated by two coils, illustrated in Fig. 3.5(a). By changing the current of the Doppler (B_D) and σ (B_σ) magnetic field coils the magnitude and direction of the quantization axis can be aligned. An additional magnetic field $\vec{B}_{grad}$ is used to compensate for magnetic field gradients along the ion string and one coil (B_{grad}) on the bottom side of the vessel compensates for vertical bias fields (e.g. earth magnetic field). Typical values for the magnetic field currents are $(I_\sigma, I_D, I_{grad}, I_{vert}) = (1.7, -0.4, -0.3, 0.1)$ A, which results in an effective magnetic field of 3.8 G. A detailed description of the magnetic field calibration is given in Ref. [49]. The Doppler beam as well as the 866 nm and 854 nm repumping laser beams are overlapped by a single mode photonic crystal fiber and aligned perpendicular to the quantization axis. The photoionization beams (375,422) nm are aligned counterpropagating. For the purpose of optical pumping the σ^- polarized 397 nm laser beam is aligned along the quantization axis. The beams used for Raman sideband cooling are overlapped with the Doppler- and σ^- beam, as shown in Fig. 3.5(a). The detailed structure of the optical setup for the UV beams is illustrated in Fig. 3.5(b). It is important to note that the quality of optical pumping (σ^- beam) and Raman cooling (σ^+ beam) strongly depends on the polarization of the light. Therefore it is advisable to use high-quality polarizing beam cubes (PBS) at the output of the fiber[7].

We use two 729 nm beams for the coherent manipulation of the qubits, aligned from two different directions onto the trap (see Fig. 3.5(a)): (a) The global beam is aligned with an angle of $22.5°$ with respect to the trap axis, which leads to an effective Lamb-Dicke factor of $\eta_{global} = 0.06$ [46]. The purpose of the global beam is the realization of collective coherent operations (see Sec. 3.5) on the entire ion string as well as entangling operations (see Sec. 3.6). Due to the fact that the global beam has an angle with respect to the ion string, the beam is elliptically shaped to guarantee equal intensity and coupling strength on all ions. A more detailed treatment is given in Sec. 3.5. (b) A tightly focused beam is aligned with an angle of $67.5°$ with respect to the trap axis and is used to perform operations on individual ions. In contrast to the global beam, the aim of the addressed laser beam is the realization of ac-Stark shifts on single qubits, which will be explained further in Sec. 3.4. The Lamb-Dicke factor $\eta_{addr} = 0.03$ of the addressed beam is lower compared to the global beam, which leads to a reduction of the coupling strength to the motional sidebands.

---

[7] Here we used Glan-Thompson Polarizers (GTH5-B) from Thorlabs with an extinction ratio of $10^5 : 1$.

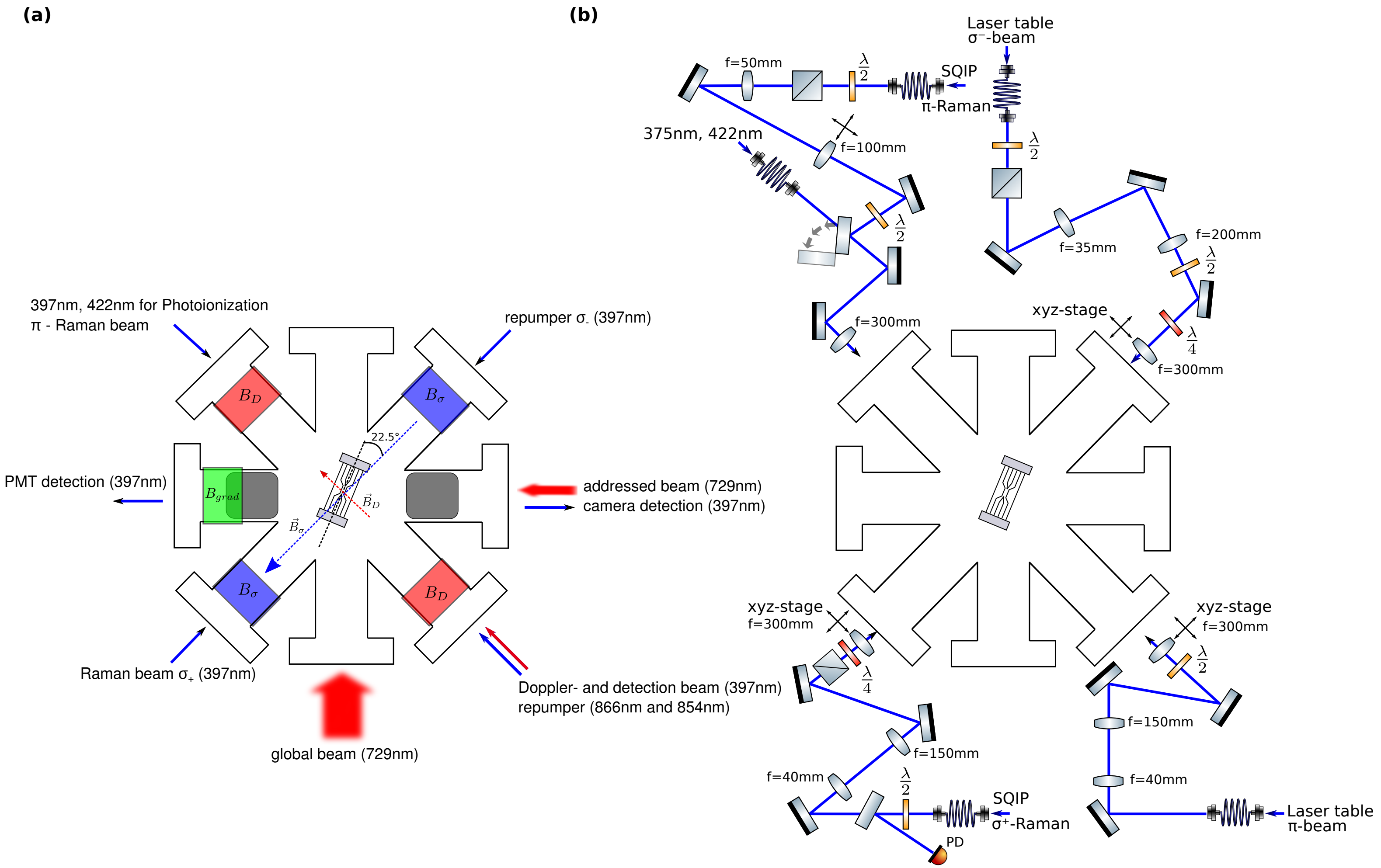

Figure 3.5: Optical setup: Schematic representation of the optical setup around the vacuum vessel. (a) Alignment of the used laser beams and magnetic field coils with respect to the trap. (b) Detailed schematics of UV and IR optics.

3.4 Addressed single qubit operations

Single qubit operations are an essential constituent of the set of quantum operations forming a universal set of gates. The aim of the addressed gates is to perform rotations around the z-axis of the Bloch sphere without changing the population of the state, which is shown in Fig. 3.6(a). The rotation around the z-axis is equivalent to changing the phase of a quantum state and can be experimentally realized by shining in laser light with the frequency ω_L, detuned by Δ from the resonance frequency, as illustrated in Fig. 3.6(b). Using the optical Bloch equations, it can be shown that the interaction of an off-resonant laser field with a two-level system leads effectively to an ac-Stark shift of the ground- and excited states, depending on the strength of the applied electric field and the detuning [55–57]. With the assumption of $\Delta \gg \Omega$, the shift δE of the energy levels with respect to the uncoupled system is given by:

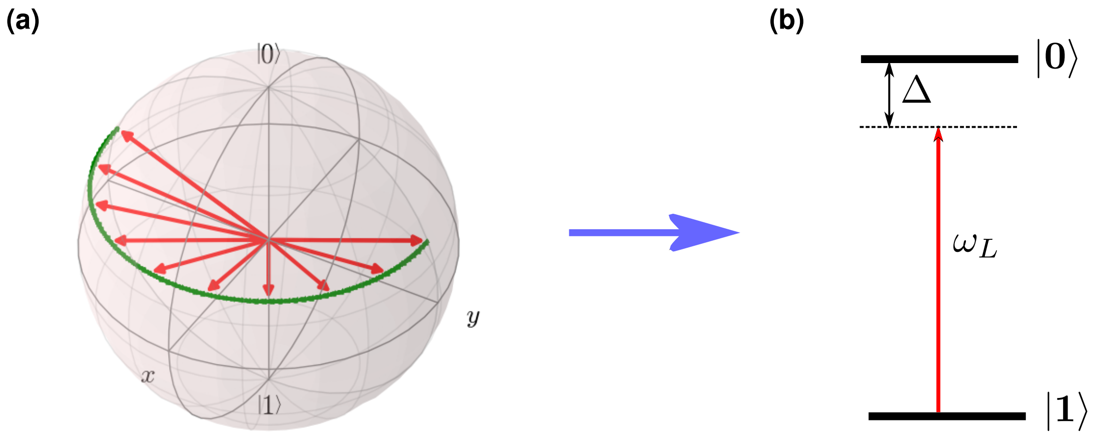

Figure 3.6: Single qubit phase rotation: Phase rotation of an arbitrary state on the Bloch sphere (a) can be achieved by (b) coupling the ground- and excited state of a two-level system with a laser field detuned by the frequency Δ from the resonance frequency $\omega_L + \Delta$.

$$\delta E = \pm \frac{\hbar \Omega^2}{4\Delta}, \tag{3.6}$$

with the Rabi-Frequency Ω in case of resonant excitation. Considering an arbitrary state $|\psi\rangle$ on the Bloch sphere, the ac-Stark shift of the levels effectively leads to a time dependent phase-shift and therefore corresponds to a rotation of the Bloch vector around the z-axis with the rotation frequency $\frac{\Omega^2}{4\Delta}$ (see Fig. 3.6(a)). Therefore, the rotation of the state vector $|\psi\rangle$ can be formulated in terms of a unitary operation U_Z as

$$U_Z(\theta)|\psi\rangle = e^{-i\frac{\theta}{2}\sigma_z}|\psi\rangle = |\psi'\rangle, \tag{3.7}$$

with the rotation angle θ:

$$\theta = \Omega_{AC} t \quad \text{and} \quad \Omega_{AC} = \frac{\Omega^2}{4\Delta}. \tag{3.8}$$

In the case of addressing one out of several ions, the unitary operator U_Z has to be reformulated and is given by the following operator:

$$U_Z^{(j)}(\theta) = e^{-i\frac{\theta}{2}\sigma_z^{(j)}}, \text{ with } \sigma_z^{(j)} = \mathbb{1}\otimes ... \otimes \mathbb{1}\otimes \sigma_z \otimes \mathbb{1} = \mathbb{1}^{j-1}\otimes\sigma_z\otimes\mathbb{1}^{N-j} \tag{3.9}$$

where the index j identifies the ion being addressed and N corresponds to the total number of ions. For example assume the addressing of the second ion $(j = 2)$ out of a two-ion string $(N = 2)$, then $U_Z^{(2)}(\theta)$ is given by:

$$U_Z^{(2)}(\theta) = e^{-i\frac{\theta}{2}\sigma_z^{(2)}} = \cos(\theta/2)\mathbb{1}^2 - i\sin(\theta/2)(\mathbb{1}\otimes\sigma_z) =$$

$$= \begin{pmatrix} \cos(\theta/2)-i\sin(\theta/2) & 0 & 0 & 0 \\ 0 & \cos(\theta/2)-i\sin(\theta/2) & 0 & 0 \\ 0 & 0 & \cos(\theta/2)-i\sin(\theta/2) & 0 \\ 0 & 0 & 0 & \cos(\theta/2)+i\sin(\theta/2) \end{pmatrix}$$

Please note that the unitary operator $U_Z^{(j)}(\theta)$ corresponds to a $2^N \times 2^N$ dimensional matrix. The notation of an addressed single qubit operation in the experimental control software on ion j with a rotation angle θ is defined as Rzred(θ,j).

3.4.1 Addressing single ions - optical setup

A simplified illustration of the optical setup used to perform operations on individual ions is shown in Fig. 3.7. All components of the addressing system are outside the vacuum chamber. The light at $729\,\mathrm{nm}$ is guided by a polarization maintaining single-mode optical fiber from the experiment table to the addressing setup close to the vacuum chamber and collimated by a 60FC-4-M5-10 fiber collimator from *Schaefter and Kirchhoff*. Afterwards, the polarization of the beam is adjusted by a PBS in combination with a $\lambda/2$ plate and guided through the *electro-optical deflector* (EOD)[8] illustrated in Fig. 3.7.

Electro optical deflector

The EOD is the basic element of the addressing setup and enables the controlled deflection of the laser beam. The functionality of the EOD is based on the principle of gradient scanners and is illustrated in Fig. 3.8(a). The incident wave is propagating along the z-direction of a crystal, whereas a linear gradient of the index of refraction is generated along the x-direction perpendicular to the direction of propagation. This effectively leads to an increasing retardation of the wavefront transverse to the propagation direction and finally to a bending of the rays towards increasing index of refraction. The total deflection angle θ can be calculated by the optical path difference Δz along the crystal with the length L:

$$\theta = \frac{\Delta z}{D} = \frac{\Delta n L}{D}. \tag{3.10}$$

Here, it was assumed that $\sin(\theta) \approx \theta$ due to the small deflection angle. The required linear gradient of the index of refraction is technically realized by making use of the electro-optical

---

[8] Leysop LTB - 1 mm aperture

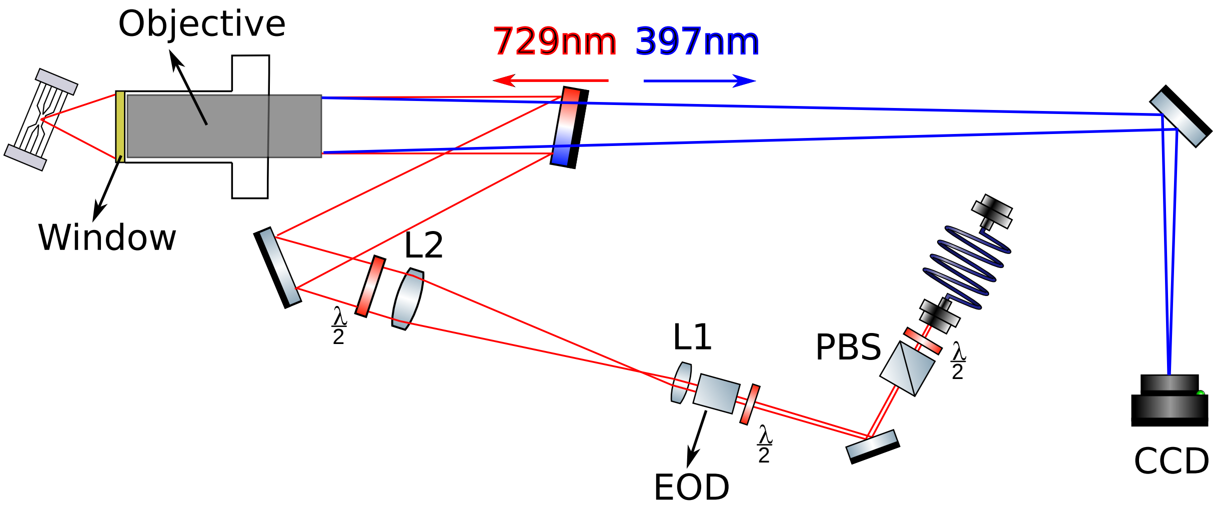

Figure 3.7: Addressing setup: Schematic representation of the addressing setup used to perform single qubit operations around the z-axis of the Bloch sphere. The beam is expanded by a telescope, formed by the lenses L1 and L2 and finally focused to a narrow spot at the position of the individual ions. Additionally, the objective is imaging the fluorescence picture of the ion string to the CCD camera. The position of the beam can be switched within the sequence by an electro optical deflector (EOD). See main text for detailed information.

Pockels effect of certain crystals, as for example Lithium Niobate. The Pockels effect leads to a modulation of the index of refraction by applying an electric field along the optical axis of the crystal. Here, we assume that the polarization of the incident beam matches the optical axis along the x-direction. Therefore, the modification of the index of refraction Δn can be expressed as:

$$\Delta n = n_0^3 r_{xx} E,$$

with the unmodified ordinary index of refraction n_0 and the Pockels coefficient r_{xx} along the x-direction. Fig. 3.8(b) shows a picture of the used EOD, which clearly illustrates the hyperbolic-shaped crystal with the attached electrodes. Due to the special crystal shape, a DC voltage V_0 applied to the electrodes creates an electric quadrupole field. The electric potential ϕ in the x, y plane of the crystal (see Fig. 3.8(a)) can be written as:

$$\phi(x, y) = -\frac{V_0}{2R^2}(x^2 - y^2),$$

with the radius of curvature R. The gradient Δn along the x-direction is then given by:

$$\Delta n = n_0^3 r_{xx} \Delta E_x = n_0^3 r_{xx}(-\nabla\phi(x, y)\vec{e_x})\Delta x = n_0^3 r_{xx}\frac{V_0}{R}$$

and therefore the total deflection angle θ can be written as:

$$\theta = n_0^3 r_{xx}\frac{V_0}{R}\frac{L}{D}. \tag{3.11}$$

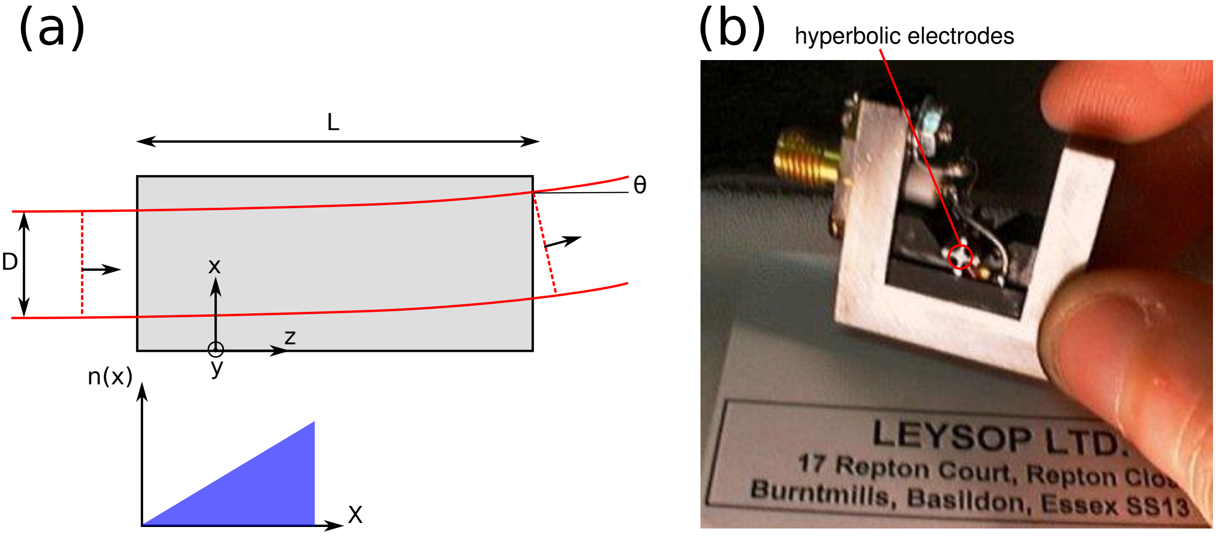

Figure 3.8: EOD: (a) Schematic representation of the crystal with the dimensions D $=1\,\mathrm{mm}$ and L $=11\,\mathrm{mm}$. (b) Picture of the electro-optical deflector (EOD) with the hyperbolic-shaped crystal (source: The University of St.Andrews Microchip Laser Research Group).

For a Lithium Niobate crystal, typical values are $n_0 = 2.3$ and $r_{xx} = 10^{-10}\mathrm{m/V}$. For a crystal length of L $=11\,\mathrm{mm}$ and a DC voltage of $500\,\mathrm{V}$ the total deflection angle is $\theta \approx 6\,\mathrm{mrad}$ under the assumption that the whole aperture is illuminated ($R = D = 1\,\mathrm{mm}$).

The figure of merits for any beam deflector are the switching speed and the resolution N, which is defined by the ratio of the total deflection angle θ and the beam divergence $\delta\theta$ of the incident beam [58]. A Gaussian beam with the beam diameter D at the crystal surface and a wavelength λ the resolution N, which is also named *number of resolvable spots*, is given by:

$$N = \frac{\theta}{\delta\theta} = \frac{\Delta n \pi}{4}\frac{L}{\lambda}, \tag{3.12}$$

with the beam divergence angle $\delta\theta = \frac{4\lambda}{\pi D}$. The switching speed of the EOD is limited by the high-voltage amplifier[9] used to apply the DC voltage to the electrodes of the crystal. The current of the amplifier is limited to $40\,\mathrm{mA}$ and therefore limits the charging time of the crystal with an intrinsic capacity C (see Ref. [46] for more information). The time until the position of the beam has settled after applying a step function is on the order of $20\,\mu\mathrm{s}$ - $30\,\mu\mathrm{s}$, depending on the deflection angle. The characteristic parameters of the EOD are listed in Table. 3.2.

---

[9] TreK Model 623B

Aperture R	$1\,\mathrm{mm}$
Dimensions	25x25x11 mm
Total deflection angle θ	$5\,\mathrm{mrad}$
Capacity C	$50\,\mathrm{pF}$
switching Speed	$50\,\mathrm{kHz}$
DC Voltage V_0	$\pm\,2\,\mathrm{kV}$
Optical loss @ $729\,\mathrm{nm}$	$\leq 2\%$

Table 3.2: Summary of the characteristic parameters of the used EOD.

3.4.2 Optical design of the addressing- and imaging system

After passing through the EOM, the addressing beam is expanded by two lenses L1 (f=$25\,\mathrm{mm}$)[10] and L2 (f=$200\,\mathrm{mm}$) [11] (see Fig. 3.7), which form a telescope with a magnification of 8. Furthermore, the beam is focused ideally to a diffraction-limited spot through the objective[12](see Fig. 3.9). The optical addressing setup, shown in Fig. 3.9, was designed with the optic simulation software *Zemax-OpticStudio*. With the *physical optics* toolbox in Zemax, the setup can also be simulated for a Gaussian input beam. The beam waist at the input of the telescope is $0.46\,\mathrm{mm}$, as measured by a beam profilometer after collimating the beam with the used fiber collimator. It is advisable to measure deviations from an ideal Gaussian beam directly after the fiber collimator with a wavefront sensor, since deformations of the wavefront can be induced by the collimation lens of the fiber collimator. The lens L2 is mounted on a motorized XYZ translation stage[13] used to steer the beam onto the position of the ion. The maximum displacement in all directions is $1\,\mathrm{cm}$.

The objective consists of 5 optical elements and was designed to minimize aberrations arising from the vacuum window. Since the details about the vacuum window of our setup is not known, we assumed for the simulations fused silica window with a thickness of $6\,\mathrm{mm}$ (see Fig. 3.9). The simulations show that the actual material of the window does not seem not be critical. The characteristic parameters of the addressing setup are listed in Table 3.3. The minimal spot size is defined by the diffraction limited Airy disc radius, which is $1.53\ \mu$m with a numerical aperture of $NA = 0.29$.

Besides the task of single ion addressing, the objective was also designed to simultaneously image the fluorescence light of the ion string onto the CCD camera[14] (see Fig. 3.7). The separation of the emitted fluorescence beam at $397\,\mathrm{nm}$ and the addressing beam at $729\,\mathrm{nm}$ is performed by a dichroic mirror (beam splitter). Before assembling the addressing system, the position of the objective was adjusted with respect to the fluorescence image of the ions on the camera. Therefore, according to the simulations, the camera was placed at a distance of about $1550\,\mathrm{cm}$ from the objective and the distance from the objective to the ion string was aligned by focusing the image onto CCD camera.

---

[10] Thorlabs AC127-025-B

[11] Thorlabs AC508-200-B

[12] Silloptics S6ASS2241

[13] Newport NSA12 motorized actuator and 460A translation stage

[14] Andor iXon

beam waist at the collimator	$0.46\,\mathrm{mm}$
focal length of L1	$25\,\mathrm{mm}$
focal length of L2	$200\,\mathrm{mm}$
distance between L1 and L2	$130\,\mathrm{mm}$
effective focal length	$66\,\mathrm{mm}$
numerical aperture NA	0.29
diffraction limited spot size (Airy-fringe radius)	$1.53\,\mu\mathrm{m}$

Table 3.3: Summary of the characteristic parameters of the addressing setup and the objective.

As a first approach, the objective was mounted on a XYZ translation stage[15] to optimize the fluorescence image of a single ion on the camera. With these 3 degrees of freedom, it proved difficult to align the objective along the optical axis without inducing any tilt, which leads to optical aberrations dominated by *coma* and *astigmatism*. Tilting the objective manually without a precision rotation stage seemed to be impossible due to the high sensitivity and confined space around the inverted viewport. Therefore, two rotational stages[16] were mounted on the translation stage, which allow tilting of the objective along the horizontal and vertical plane. An example of a typical fluorescence picture of a two-ion crystal is shown in Fig. 3.10(a), clearly indicating a significant tail to the left. The image defect of this picture can be identified by the optical aberration *coma*.

Since it is practically difficult to distinguish between an improvement of the image when tilting the objective and a mismatch of the focus (z-position), a useful method to find the correct alignment of the objective and correct for optical aberrations is to defocus the objective. The camera picture of a single ion out of focus is shown in Fig. 3.10(b). Fig. 3.10(c) illustrates a qualitative simulation of the picture by tilting the objective in x- and y-direction of about 2°. Both, the ion picture and the simulation show that tilting the objective leads to an inhomogeneous illumination of the diffraction ring on the upper left side. Therefore, the aberrations can be corrected by optimizing the homogeneous illumination of the ring by iteratively shifting and tilting the objective. Fig. 3.10(d) shows the two-ion crystal picture after the optimization procedure.

An important parameter for the characterization of the objective is the optical magnification, which can be quantified via the camera image of a two-ion crystal (see Fig 3.11). This is achieved in the following way:

The main idea is to measure the axial trap frequency ω_z of the COM mode of a two-ion crystal by spectroscopy on the qubit transition, which allows the calculation of the ion distance. According to Ref. [59] the distance d_{calc} of two ions in a harmonic trap potential is given by the following expression:

$$d_{calc} = \left[\frac{Z^2 e^2}{4\pi\epsilon_0 m \omega_z^2}\right]^{1/3} \times \frac{2.018}{N^{0.559}} \cos(\phi), \tag{3.13}$$

with the ion mass m, the electron charge e, the degree of ionization Z, the vacuum permittivity ϵ_0, the trap frequency ω_z, and the number of ions N. Note that ϕ considers the angle of the ion chain with respect to the optical axis of the objective. The magnification M is then given by the

---

[15] Opto Sigma TSD-655L

[16] OptoSigma Rotation Stage $65\,\mathrm{mm}$,124-0055

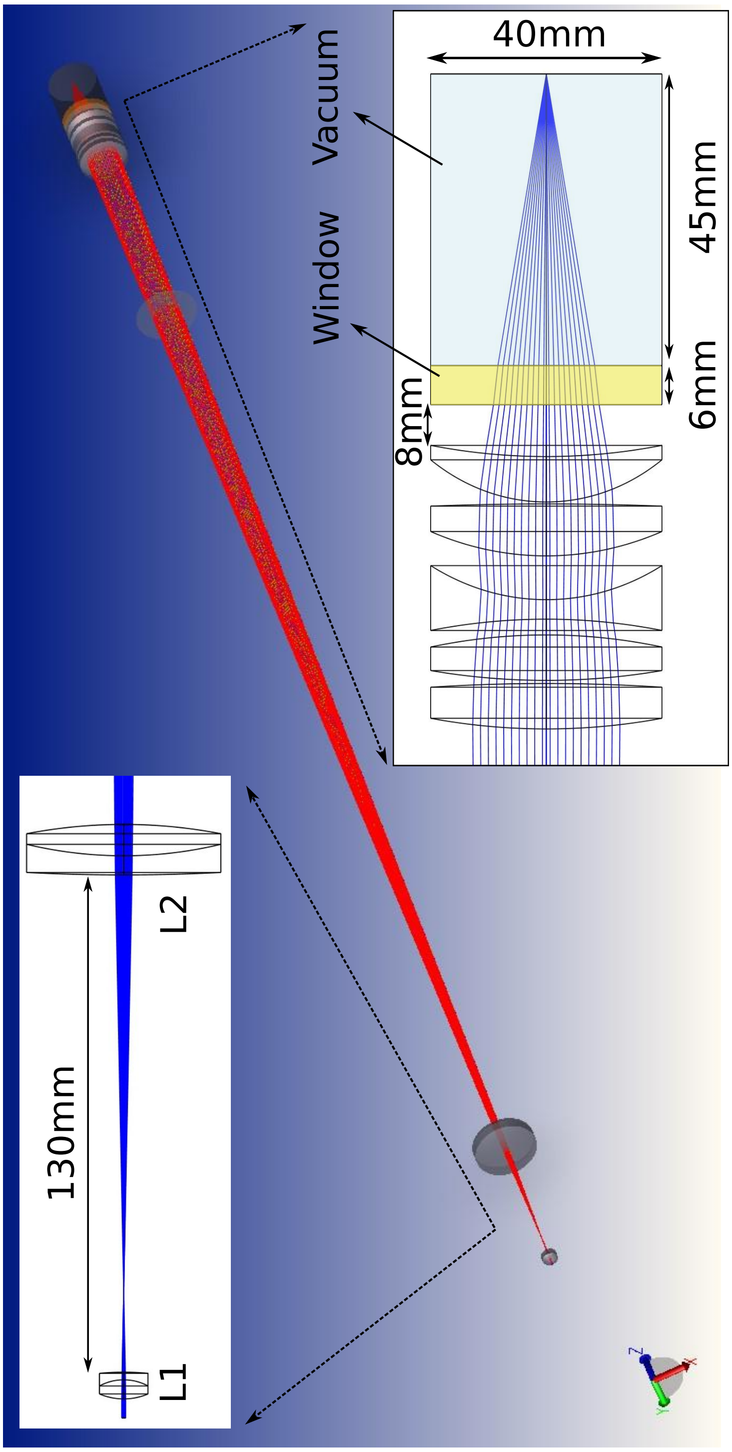

Figure 3.9: Zemax design of the addressing setup: Optical design of the addressing setup using the *Zemax-OpticStudio* software. The telescope and the z-position of the objective were optimized with respect to the size of the focal point. The vacuum window was simulated by a 6 mm fused silica glas.

ratio of the distance of the ions on the camera picture d_{cam} and the calculated distance d_{calc}:

$$M = \frac{d_{cam}}{d_{calc}} a_{pixel},$$

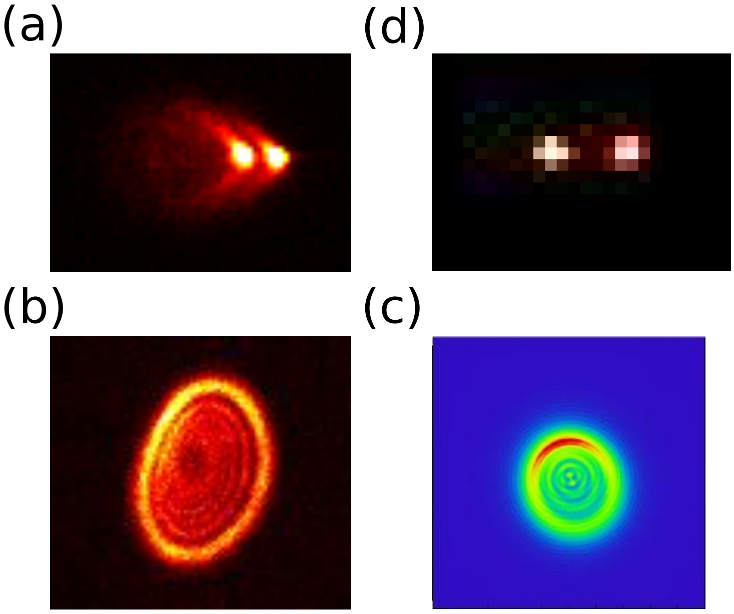

Figure 3.10: CCD camera image two ions:(a) Picture of a two-ion crystal taken with a CCD camera showing the optical aberration *coma*. (b) The inhomogeneous illumination of the diffraction ring indicates the optical aberration and can be used to optimize the fluorescence image. (c) Zeemax simulation of the camera picture by tilting the objective 2° in x- and y-direction. (d) Image of the two-ion crystal after the optimization procedure.

with the pixel size a_{pixel}. Fig 3.11(a,b) shows the measurement of the fluorescence counts summed along the cross section of the camera image for an endcap voltage of $1000\,\mathrm{V}$ ($\omega_z = (2\pi)1.209$ MHz) and $1500\,\mathrm{V}$ ($\omega_z = (2\pi)1.481$ MHz). A multiple Gaussian regression function for both endcap voltages (blue curves) leads to a distance $d_{cam} = (102.6 \pm 0.1)\mu\mathrm{m}$ ($d_{calc} = 4.96\mu\mathrm{m}$) for $1000\,\mathrm{V}$ and $d_{cam} = (89.8 \pm 0.1)\mu\mathrm{m}$ ($d_{calc} = 4.33\mu\mathrm{m}$) for $1500\,\mathrm{V}$. With a pixel size of $a_{pixel} = 16\,\mu\mathrm{m}$ and an angle $\phi = 22.5°$ the magnification of the objective is given by 20.7 ± 0.3. The imaging resolution is determined by the width (1/e) of the Gaussian regression function and is given by $(22 \pm 1)\mu\mathrm{m}$. Therefore, two ions with a distance of $(1.08 \pm 0.03)\mu\mathrm{m}$ can still be resolved by the imaging system.

3.4.3 Addressing of single ions

After adjusting the objective with respect to the fluorescence image of the ions on the camera, the addressing setup was assembled as illustrated in Fig. 3.7 without the EOD. The focal point of the $729\,\mathrm{nm}$ beam at the position of the ions was optimized by adjusting the distance of the objective to the ion and subsequently realigning the beam onto the ions with the dichroic mirror. Moving the z-position of the objective is slightly affecting the focal position of the fluorescence image, which can be compensated by changing the distance of the camera to the objective. The aligment of the addressed beam is optimized by applying the laser light continuously to the ion string and detecting the excitation on the qubit transition. If the laser beam is properly aligned with respect to the ions, then the qubit transition is saturating and the detection count rate of the

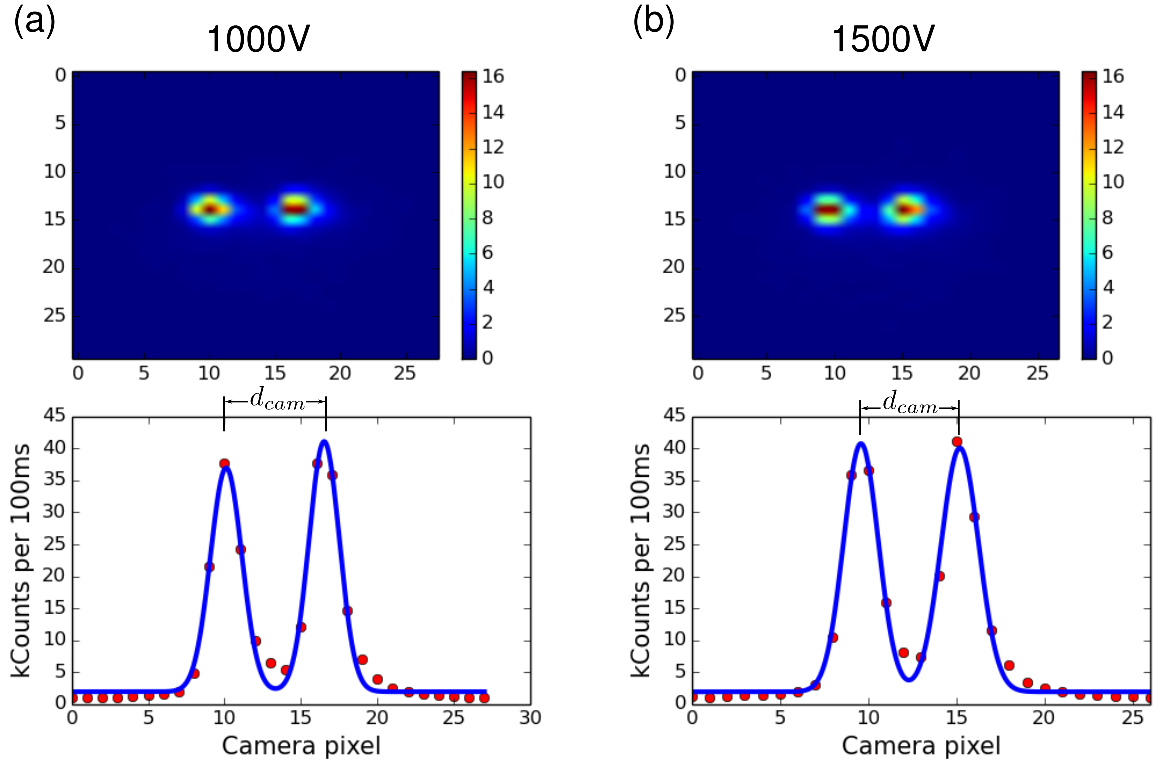

Figure 3.11: Objective magnification measurement: Measurement of the objective magnification using the camera picture of a two-ion crystal at an endcap voltage of (a) $1000\,\mathrm{V}$ and (b) $1500\,\mathrm{V}$. The magnification can be obtained by the ratio of the ion separation d_{cam} of the camera image and the distance d_{calc} of the ions in the trap. The ion separation in the trap is determined by the axial trap frequency ω_z. The camera images were all obtained with an exposure time of $100\,\mathrm{ms}$.

PMT will drop to 50% of the initial value[17]. This regime is not advantageous to optimize the addressing beam alignment, because the qubit transition is saturating and therefore the count rate can not be reduced further. The count rate is increased by repumping the population back to the ground state using the 854 nm laser, which allows the optimized positioning of the addressed beam with respect to the ion string. An improvement of the beam alignment will result in a reduction of the detection count rate. Increasing the 854 nm laser power is used to adjust the count rate back to the previous value. This procedure can be iteratively repeated until the count rate can not be reduced further. An improvement of the focal point can be observed when the optimization with the dichroic mirror becomes more sensitive. The next step is the adjustment of the distance between the telescope lens L1 and L2 using the motorized translation stage of L2. From experience, it is advisable to change the z-position of L2 iteratively and re-optimize the x- and y position for each step, since a slight angle between the beam and the lens will couple the x- and y position with z. The beam profile at the focal point is obtained by scanning the beam across the ion string via the motorized translation stage and measuring the excitation probability of each single ion with the CCD camera. Fig 3.12(a) shows a scan of the lens L2

---

[17] Typical optical power used for the optimization procedure is on the order of 2 mW.

across a three-ion crystal with an axial frequency $\omega_z = (2\pi)1.209$ MHz at an endcap voltage of $1000\,\mathrm{V}$. The width of the addressed beam at the focal point is measured via a Gaussian beam profile fitted to the excitation profile of Fig 3.12. Since the units of the abscissa are given by the step size of the motorized translation stage, the axis has to be calibrated. This is done similar to the method used for measuring the objective magnification using the dependence of the ion distance on the axial trap frequency. The width of the beam at the focus is defined by the waist ω_0 at which the Gaussian regression function is $1/e^2$ of its maximum value. The measurement of the beam waist results in $\omega_0 = 1.6\ \mu$m. *Zemax* simulations lead to an expected waist of $\omega_{sim} = 1.3\ \mu$m at the position of the focal point. Considering that the distance of the objective to the ions is not known exactly and that aberrations lead to an increase of the width, the measured value is in good agreement with the expected simulated result. In optical systems, the minimal achievable focus is given by the Airy disc radius R_{airy}, which arises from diffraction off the aperture of an optical system [58]. The radius of the Airy disc is defined as the distance from the maximum to the first diffraction minimum. Here, with the used optical system the minimal expected Airy disc radius $R_{airy} = \frac{1.22\lambda}{2NA} = 1.53\,\mu\mathrm{m}$, with the maximal numerical aperture $NA = 0.29$ (see Table 3.3). Assuming a sinc-type regression function and fitting the data shown in Fig 3.12(a) leads to a radius $R_{airy} = 2.37\,\mu\mathrm{m}$. The measured radius is bigger than expected from the diffraction limit because the aperture of the EOD limits the initial beam waist and therefore also the beam size at the objective, which reduces the effectively used numerical aperture to $NA = 0.18$. Considering the reduced numerical aperture, the calculated Airy disc radius is $2.47\,\mu\mathrm{m}$, which is again in good agreement with the measured value. Since the measured waist is still smaller than the minimal distance of a 7-ion crystal ($3\,\mu\mathrm{m}$ at $700\,\mathrm{V}$ endcap voltage) it is not necessary to further decrease the beam waist. A possibility to illuminate the whole objective would be to increase the divergence of the Gaussian beam via the telescope, but this would also lead to an increase of spherical aberrations. The optimal way to decrease the beam waist further is to use an EOD with a larger aperture and expand the initial beam to a collimated Gaussian beam with a waist of $20\,\mathrm{mm}$. Fig 3.12(b) demonstrates the addressing of a

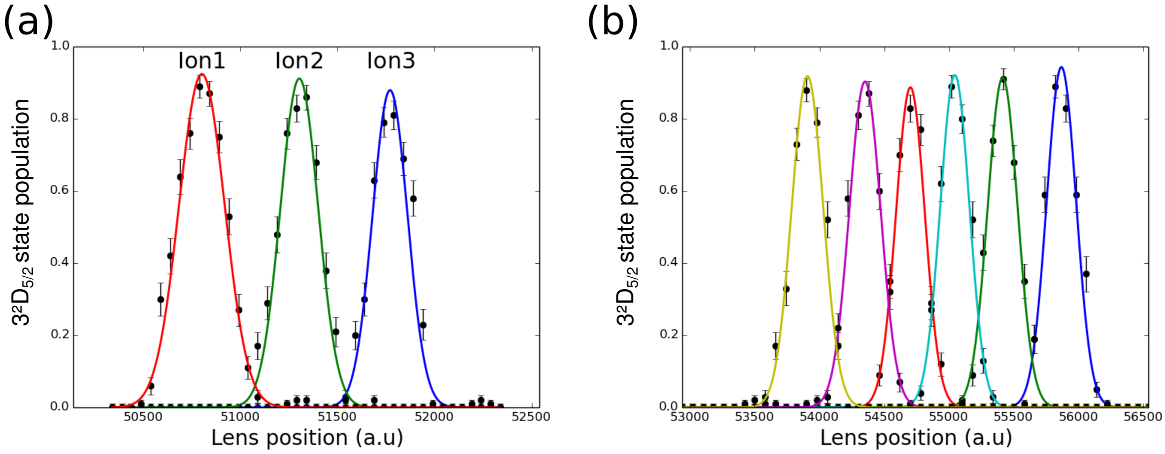

Figure 3.12: Addressing Excitation probability of the $3^2D_{5/2}\ (m_j = -1/2)$ state when scanning across a (a) three and (b) six-ion crystal with a tightly focused laser beam. The excitation of the individual ions leads to the possibility of single-ion addressing. The measured beam waist at the focus is about $1.6\,\mu$m.

six-ion crystal at a tip-voltage of $700\,\mathrm{V}$.

By including the EOD, the same excitation pattern as shown in Fig. 3.12(a,b) is observed when scanning the control voltage of the EOD. Fig. 3.13(a) shows the excitation profile of the individual ions as a function of the control voltage. Therefore, each ion can be addressed during the sequence by setting the corresponding EOD control voltage. In Fig. 3.13(b) the control voltage is set to $-0.1\,\mathrm{V}$(100 V at the EOD) and coherent Rabi oscillations are performed on the third ion. Besides the Rabi oscillations on the addressed ion, excitation on the neighbouring ions 2 and 4 are observed, caused by optical aberrations. The crosstalk on the i-th ion when addressing ion j is quantified by the ratio ϵ_{ij} of the Rabi frequencies Ω_i and Ω_j respectively. Hence, $\epsilon_{ij} = \frac{\Omega_i}{\Omega_j}$ with $\epsilon_{ij} = 1$ for $i = j$. Nevertheless, the crosstalk for the six ions is maximally 3%, which is reasonable and can be reduced further by addressing error correction, which is described within the next section.

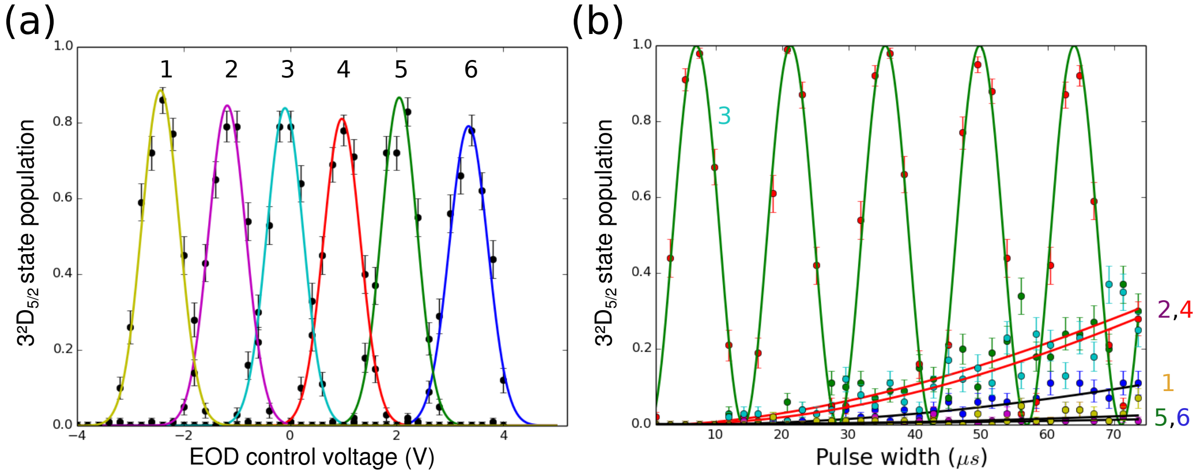

Figure 3.13: Addressing of single ions: (a) Addressing profile of a six-ion crystal with a distance of about $3\,\mu\mathrm{m}$ by scanning the voltage applied to the EOD. (b) Rabi oscillations on the third ion with crosstalk to the neighbouring ions of about 3%.

3.4.4 Addressing error correction

Addressing of a single ion is leading to residual light on the neighbouring ions due to the finite size of the focused beam and especially due to optical aberrations, indicated by the excitation of ion 2 and 4 in Fig. 3.13(b). Ideally, the aim of the addressing beam is to realize the operation $U_z^{(j)}(\theta) = e^{-i\frac{\theta}{2}\sigma_z^{(j)}}$ on the j-th ion and the identity operation on the remaining ions. Due to the addressing error (crosstalk) ϵ, the effective operation is of the form $U_z^{(j)}(\theta) = e^{-i\sum_i \frac{\theta}{2}\epsilon_{ij}\sigma_z^{(i)}}$, with the addressing error matrix ϵ_{ij}. The question arises if the addressing error can be reduced further. One method, which is called addressing error correction is to split the operation on the addressed ion into a specific sequence of multiple operations. As an example let us consider a bit-flip on ion 1 in a two-ion crystal. The procedure is graphically illustrated in Fig. 3.14 on the Bloch sphere for both ions. The aim is to achieve only a π-rotation on ion 1 and ideally leaving the neighbouring ion 2 unaffected. Both ions are initially in the state $|1\rangle$, which corresponds to the south pole of the Bloch sphere. Applying the π-rotation directly on ion 1 would lead to a rotation of $\epsilon\pi$ on ion 2, with the addressing error $\epsilon = 0.3\ (30\%)$. The π-rotation is split into three pulses, which are pointed out by the paths on the Bloch sphere with numbers (1) to (3). The first rotation (1) is a $\pi/2$ pulse around the y-axis on the first ion, which rotates ion 2 by an angle of $\epsilon\pi/2$. The next step (2) is a π-rotation around the z-axis on ion 1 by an off-resonant ac-Stark pulse, which rotates the Bloch vector of ion 1 to the state $|-\rangle_x = 1/\sqrt{2}(|0\rangle - |1\rangle)$. The important fact is that the error induced on ion 2 during the ac-Stark operation on ion 1 scales with ϵ^2, since the Rabi frequency $\Omega_{ac} = \frac{\Omega^2}{4\Delta}$ scales quadratically with the resonant Rabi frequency Ω. The final step (3) is again a $\pi/2$-rotation around the y-axis with a phase shift of π with respect to the first rotation (1). Ion 2 again is affected by the addressing error and is rotated back similarly to step (1). Therefore, ion 2 is effectively rotated by $\epsilon^2\pi$ instead of $\epsilon\pi$ by splitting a single addressing pulse into a sequence of three pulses (Fig. 3.15). This method implies a significant improvement of the addressing error. The addressing error correction protocol is demonstrated experimentally by performing Rabi oscillations on a single ion. In Fig. 3.15(a) resonant Rabi oscillations on one ion out of a two-ion crystal are shown. After four oscillations of the first ion, excitation on the second ion occurs. The ratio of the corresponding Rabi frequencies corresponds to an addressing error $\epsilon_{1,2} = 2\%$. The same measurement is repeated following the described addressing error method and is shown in Fig. 3.15(b). It is obvious that still after 15 oscillations no excitation on the second ion is visible, resulting in a reduced addressing error on the order of 10^{-4}. The technique of addressing error correction can be extended by splitting the rotation into more steps, which would lead to a further reduction of the addressing error. At this stage this is not necessary, since the errors on the resonant transition are at a level where a single addressing

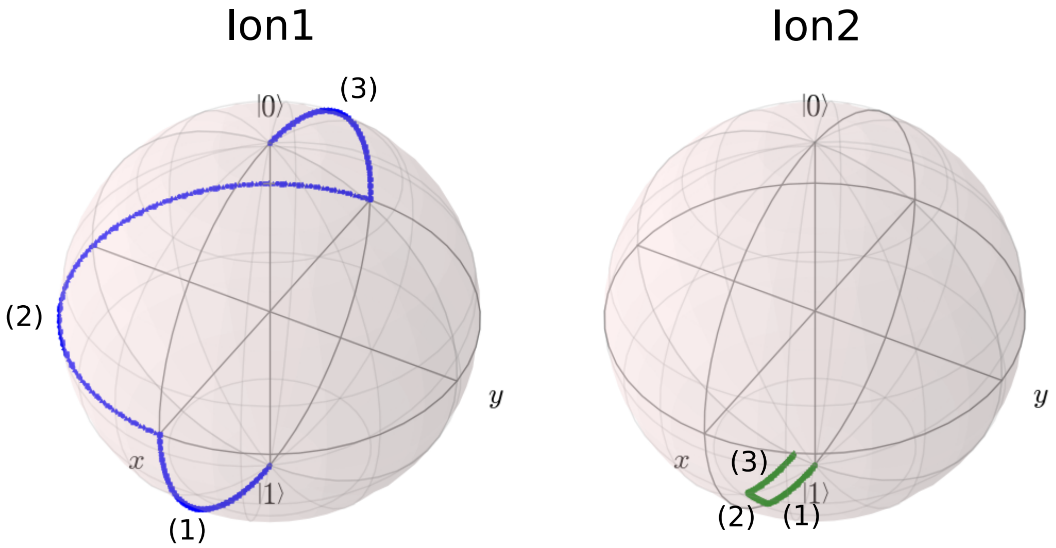

Figure 3.14: Graphical representation of the addressing error correction protocol: The π-rotation is split into two resonant $\pi/2$-rotations (1,3) and one π-rotation around the z-axis (2). The effective rotation of the neighbouring ion 2 scales with ϵ^2 (for this example, $\epsilon = 30\%$) and therefore leads to a significant reduction of the crosstalk to the neighbouring ions. In this example, the addressing error on ion 2 would be 9% instead of 30%.

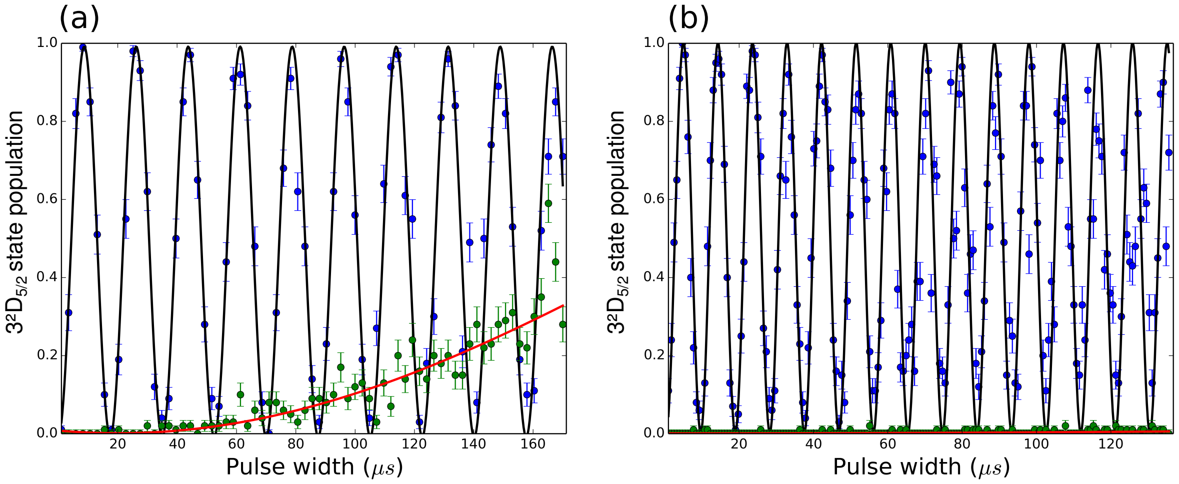

Figure 3.15: Addressing error correction: Experimental demonstration of the addressing error correction protocol by addressing a single ion out of a two-ion crystal. (a) Addressing ion 1 without addressing error correction leads to a crosstalk of $\epsilon_{1,2} = 2\%$. (b) Using addressing error correction, the effective addressing error can be reduced substantially to about $4 \cdot 10^{-4}$.

error step leads to a significant improvement. However, the addressed ion gets more sensitive to intensity fluctuations of the laser.

3.4.5 Spatial light modulator for improved addressing

If the addressing errors of resonant carrier excitation are sufficiently small, these can be further reduced by using addressing error correction. On the one hand, it is experimentally expensive to lower the addressing errors on the carrier to a level of $\approx 3\%$. On the other hand, addressing error correction lowers the crosstalk but requires three pulses per operation instead of one pulse and in addition is more sensitive to intensity fluctuations. Therefore it would be desirable to minimize the crosstalk between the ions to a limit where it becomes feasible to work without addressing error correction.

One promising method to achieve this goal would be the technique of spatial light modulators (SLMs). These devices are commonly used in projectors and for scientific applications, as for example optical tweezers, the generation of controllable holograms, the realization of optical lattices for ultracold atoms, the transport of Bose-Einstein condensates and correction of aberrations in microscopy [60]. We are not aware of an implementation of SLM devices for ion-trap based quantum systems. Here, a test setup for the usability of SLM devices for ion-trap based system is presented. In more detail, the capability of correcting addressing errors using SLMs will be discussed within this section.

The SLM devices are based on liquid crystal technologies and are mostly used as phase modulators. With modifications of the optical setup, they can also be used as amplitude modulators. The SLM we used is a refractive nematic Liquid Crystal on Silicon SLM[18]. The architecture of the used SLM is based on a layer structure design. The ground layer contains the corresponding

---

[18] Boulder Nonlinear Systems, HSP 256

image pixel electrodes (256 x 256 pixels). The liquid crystal layer is located between the ground layer and one transparent electrode. The voltage of each individual pixel can be controlled via a specific electronic circuit board. The last layer on top is a cover glass layer with anti-reflection coating, depending on the used wavelength[19]. The important characteristic of the liquid crystal used in SLMs for phase modulation is birefringence. This means that the index of refraction of an incoming beam depends on the orientation of the polarization vector with respect to the optical axis. If the polarization is perpendicular to the optical axis the beam sees an index of refraction n_0 (fast axis) and n_e (slow axis) for the polarization parallel to the optical axis. Light with arbitrary linear polarization with respect to the optical axis will split up into the ordinary and extra-ordinary beam, whereas the extra-ordinary beam effectively experiences a retardation with respect to the ordinary beam due to different velocities. Therefore, the phase Γ of the beam changes according to $\Gamma = 2\pi\Delta n\frac{d}{\lambda_0}$, with the thickness of the liquid crystal layer d and the difference of the index of refraction Δn. The maximum phase shift is given by $2\pi(n_0 - n_e)\frac{d}{\lambda}$. The main effect behind the controlled phase shift in an SLM is that the orientation of the molecules, which define the optical axis are changing by applying an electric field. Therefore the index of refraction n_e of the extra-ordinary beam also changes with the tilting angle θ. Effectively, the phase shift can be expressed by $\Gamma(\theta) = 2\pi(n_0 - n_e(\theta))\frac{d}{\lambda}$. A more detailed description of SLMs can be found in Ref. [61].

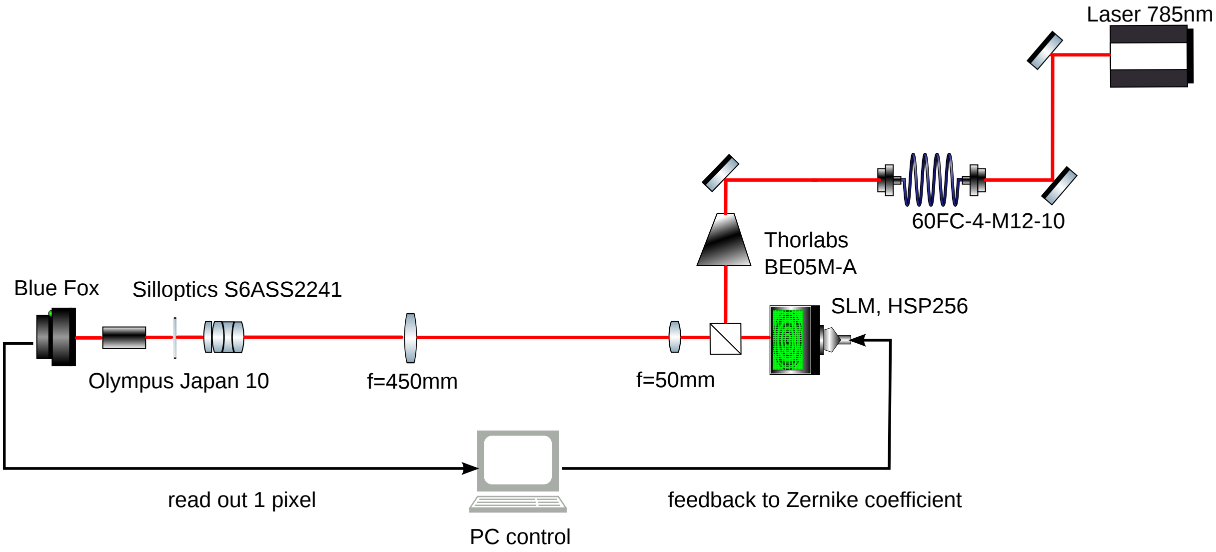

Figure 3.16: Correcting aberrations using a SLM device: Optical test setup to demonstrate the usability of SLMs for the correction of aberrations of the wavefront by iteratively changing the Zernike coefficients of the beam via electronic feedback to the SLM.

The optical test setup is shown in Fig. 3.16. As a light source we used a grating stabilized diode laser at a wavelength of 785 nm. The spatial mode of the emitted light is cleaned by an optical fiber and then enlarged by a telescope with a magnification factor of 5[20]. The SLM is illuminated by a 50:50 beam splitter, which makes it more convenient to align the SLM, and the

---

[19] See Boulder Nonlinear Systems for a more detailed description.

[20] Thorlabs BE05M-A

reflected light from the SLM is expanded again with a telescope by a factor of 9. The collimated beam passes the Silloptics objective followed by a glass plate with a thickness of 10 mm. The size of the beam at the position of the focal point would be too small to be imaged directly with a CCD camera. Therefore, we placed a calibrated objective[21] with a magnification of 10 at the focal point to enable the imaging with a commercial CCD camera[22]. The procedure used to correct the beam aberrations is to change the Zernike coefficients of the wavefront via the SLM and optimize for each coefficient the illumination of the center pixel of the CCD camera. The feedback to the Zernike coefficients is realized by the SLM control software, which calculates the required control voltages for each coefficient. The result of the correction procedure is shown in Fig. 3.17. In Fig. 3.17(a) the camera image as well as a cross section along the X- and Y direction of the pattern of the initial beam are shown. After the correction procedure, which takes about five minutes, the shape of the beam results in a diffraction limited spot with an Airy-disc radius of about $1.6\,\mu\mathrm{m}$, as shown in Fig. 3.17(b). The setup was assembled at the Division of Biomedical Physics located at the Medical University of Innsbruck with the support of Dr. Gregor Thalhammer.

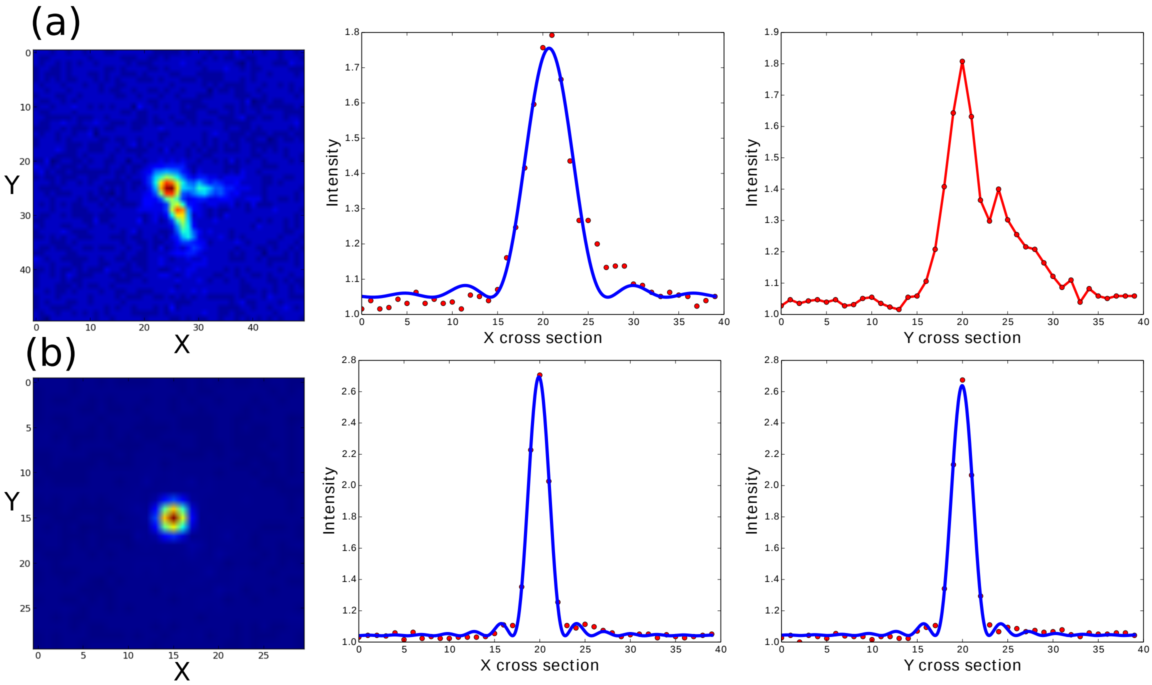

Figure 3.17: Optimization procedure of the optical aberrations using a LCoS-SLM: In (a) the beam profile of the uncorrected beam is shown and (b) illustrates the camera pattern after 12 optimization cycles. The result is a diffraction limited spot with an Airy-disc radius of $1.6\,\mu\mathrm{m}$, revealed from the blue regression curves.

This setup demonstrates the capability of using SLM devices for the correction of optical aberrations in our setup. One technical issue, which can be problematic for the addressed pulses is

---

[21] Olympus Japan 10

[22] CCD mvBlueFox-220

the modulation of the control voltage applied on each pixel. Due to electromechanical effects, the SLM can degrade by applying DC voltages over a longer time period. Therefore, the control voltages are typically square wave signals with a frequency of about 6 kHz. This can lead to a amplitude modulation of the reflected beam, which would directly affect the intensity stability of the addressed beam. The intensity fluctuations of the used SLM model were measured at the Division of Biomedical Physics by realizing a diffraction grating and measuring the relative intensity fluctuations of the 1st order beam. The measurement results show fluctuations of less than 0.1% at the characteristic modulation frequency, which would be below the intrinsic intensity fluctuations of the laser light. In principle, this problem could be overcome by utilizing deformable mirrors, which can also be used as phase modulators but with static control voltages[23].

3.5 Collective operations

As already shown in Fig. 3.5(a), collective operations are performed with a wide laser beam illuminating simultaneously the entire ion string. In contrast to the addressed beam, which is used to enable σ_z rotations on individual ions, the purpose of the global beam is the realization of resonant excitation on the qubit transition. Ideally, the dynamics of global operations is equal for each ion and can be represented by rotations of the Bloch vector around the X and Y axis. Therefore, the collective operations can be expressed in terms of a unitary operator $U(\theta,\phi)$ [21]:

$$U(\theta,\phi) = e^{-i\frac{\theta}{2}[\cos(\phi)S_x+\sin(\phi)S_y]} \tag{3.14}$$

with $S_{x,y} = \sum_{i=1}^{N} \mathbb{1}^{i-1} \otimes \sigma_{x,y} \otimes \mathbb{1}^{N-i}$ the sum of Pauli operators acting on the i-th qubit. The rotation angle $\theta = \Omega t$ is given by the Rabi frequency Ω and the excitation time t, ϕ corresponds to the phase of the light field. Experimentally, ϕ is controlled by setting the phase of the radio frequency (RF) source applied to the acoustic optical modulators (AOM) [55]. The operation in Equ. 3.14 is represented as RcarX$(\theta,\phi) = U(\theta,\phi+\pi,8)$, where X is an index for the desired transition. We use an elliptical shape of the laser beam to approximate constant illumination of the entire ion string, since the global beam and the ion trap span an angle of 22.5° (see Fig. 3.5(a)). If we assume an ion string of up to ten ions with an axial frequency of 900 kHz, then the total length of the ion string is about 27.4 μm and the projection along the elongated horizontal beam axis is 10.5 μm. The ellipticity of the global beam is realized by a pair of cylindrical lenses, which form a telescope with a magnification of 5 along the vertical direction. The beam diameter (FWHM) along the elongated main axis is typically around 100 μm and about 20 μm in the other direction. With the given parameters the maximum relative difference of the coupling strength along the ion string consisting of ten ions is about 0.7%. This can be measured by comparing the Rabi times of each individual ion, as shown in Fig. 3.18 for six- and seven ions.

Let us now consider the damping of these oscillations. In Fig. 3.18 (a,c), Rabi oscillations are performed after cooling the axial COM mode at a trap frequency of $\omega_z^{COM} = 1014$ kHz and Fig. 3.18 (b,d) shows the same oscillations with additionally cooling the axial breathing

---

[23] Thorlabs - deformable mirror devices

($\sqrt{3}\omega_z^{COM}$) and egyptian mode ($\sqrt{29/5}\omega_z^{COM}$). A detailed analysis of the oscillation frequencies and direction of the normal modes is given in Ref. [59]. The results clearly show an improvement of the contrast with additional sideband cooling the two higher axial modes. The main reason for the damping characteristics is that the coupling strength Ω_0 of the resonant carrier transition depends on the motional states[24]. This means that the occupation of the motional Fock states of the higher axial modes leads effectively to an alteration of the coupling strength of the ion to the light and therefore causes fluctuations of the resonant Rabi frequency. This fact can also be used to estimate the phonon occupation of the motional states [62]. A larger damping of the outermost ions is observed in Fig. 3.18 (a,c) without additional cooling, which can be explained by a larger contribution of the oscillation amplitude of the outer ions to relevant modes (e.g. breathing mode). Therefore, cooling the breathing and egyptian mode leads to a significant improvement of the Rabi oscillations as demonstrated in Fig. 3.18 (b,d). Although the first three axial modes are cooled, the Rabi oscillations still show an effective damping after several oscillation periods (see Fig. 3.18 (d)). This decoherence could be further reduced by cooling all axial modes. In addition to the motional modes, fluctuations of the laser beam intensity ($\approx 1\%$) also causes dephasing. Cooling the higher axial modes leads to a more balanced coupling strength along the ion string, as the average coupling strength increases with decreasing phonon number. This fact is indicated by the measured Rabi frequency difference along the ion string of $1.32\%(1.65\%)$ for the 7(6) ions with cooling only the axial COM mode and $0.93\%(0.61\%)$ with additional SB-cooling.

---

[24] The carrier Rabi frequency is proportional to $(1-\eta^2 n)$, with the Lamb-Dicke factor η and the motional phonon number n.

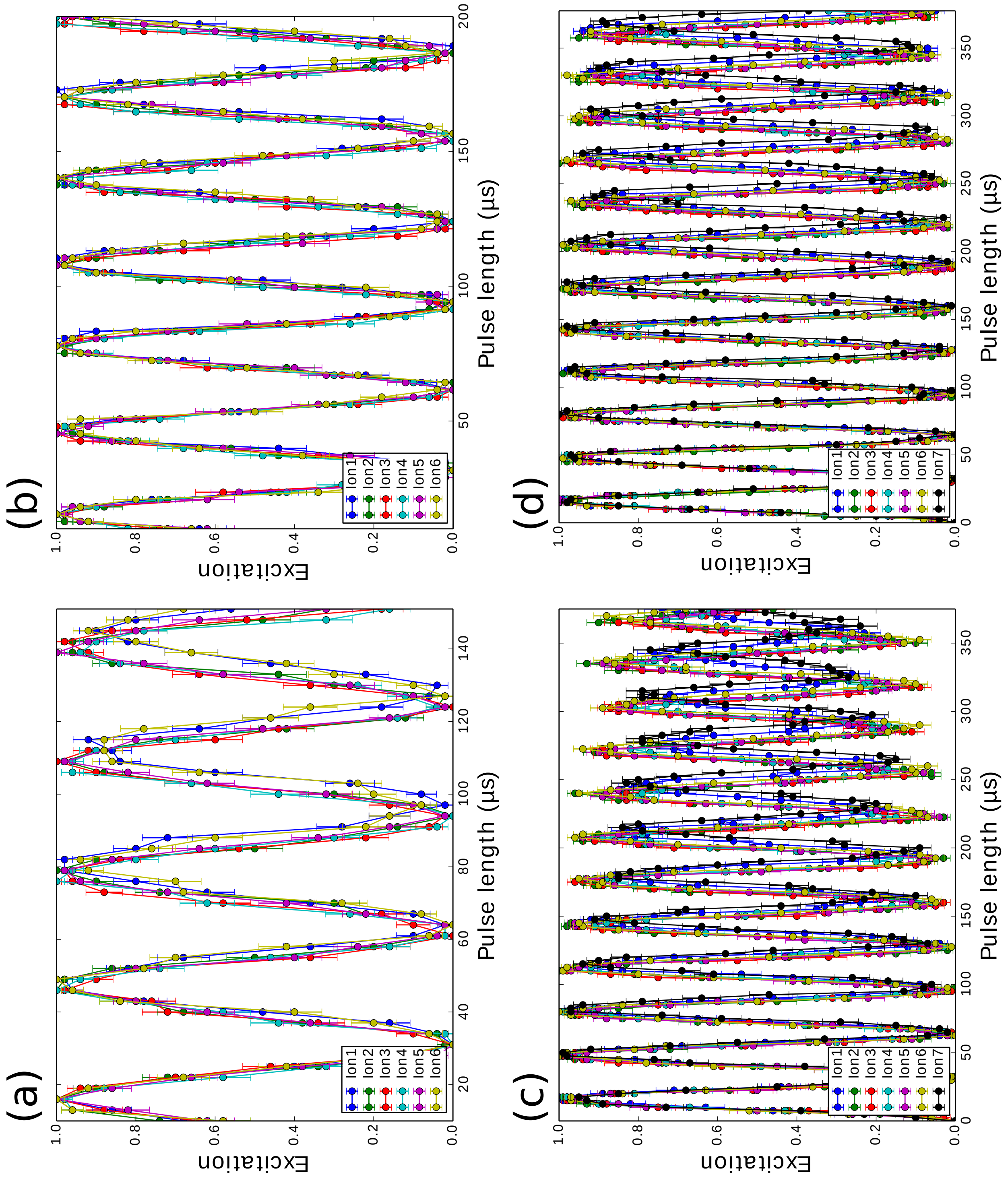

Figure 3.18: Collective Rabi oscillations: Rabi oscillations realized with the global beam on a string of 6 (7) ions. The influence of the higher motional states when only cooling the COM mode is illustrated in (a) and (c) by the decoherence of the Rabi contrast. In (b) and (d) the breathing and egyptian mode were cooled additionally and show clearly an improvement of the Rabi contrast.

3.6 Entangling operation

The implementation of multi-particle entanglement is the most challenging building block of a universal set of quantum gates. In our setup, an entangled state between multiple ions is realized by a method originally proposed by Mølmer and Sørensen [63]. In this method, correlated spin-flips between the states $|\downarrow\downarrow\rangle \rightarrow |\uparrow\uparrow\rangle$ and $|\uparrow\downarrow\rangle \rightarrow |\downarrow\uparrow\rangle$, with $|\downarrow\rangle = 4^2S_{1/2}\ (m_j = -1/2) = |1\rangle$ and $|\uparrow\rangle = 3^2D_{5/2}\ (m_j = -1/2) = |0\rangle$ are generated with an effective Hamiltonian $H \propto \sigma_\phi \otimes \sigma_\phi$, where $\sigma_\phi = \cos(\phi)\sigma_x + \sin(\phi)\sigma_y$. In Ref. [63] the realization of this effective Hamiltonian is described by coupling the $|00\rangle$ and $|11\rangle$ states via a two-photon transition making use of the axial COM-mode. The entire ion string is simultaneously excited by two different laser frequencies $\omega_\pm = \omega_0 \pm \delta$, red-and blue detuned from the resonant qubit transition frequency ω_0 by $\delta = \nu - \epsilon$ with the axial COM mode frequency ν and a detuning ϵ. Experimentally, this is accomplished by a copropagating bichromatic light field at the corresponding frequencies. A detailed description of the experimental setup used to realize the described entangling scheme is given in Ref. [64]. The analysis of the coupling between the bichromatic laser light and the ions is performed in Refs. [64, 63]. Within the Lamb-Dicke regime the propagator $U(t)$ describing the interaction can be solved analytically and is resulting in the unitary operation $U(t = \tau_{gate}) = \exp(i\tilde{\Omega}\tau_{gate}S_\phi^2)$ for a specific interaction time $t = \tau_{gate}$ and $S_\phi = \cos(\phi)S_x + \sin(\phi)S_y$. The effective Hamiltonian after the interaction time $t = \tau_{gate} = 2\pi/\epsilon$ is described by $H_{eff} = -2\hbar\tilde{\Omega}(\mathbb{1} + \sigma_\phi \otimes \sigma_\phi)$ and is up to some global phase identical to the collective spin-flip Hamiltonian described before [64] . The parameter $\tilde{\Omega} = (\eta\Omega)^2/\epsilon$ determines the effective coupling strength of the interaction. For a coupling strength $\tilde{\Omega} = \pi/(8\tau_{gate})$ the effective unitary operation is given by $U_{eff} = \exp(i\frac{\pi}{8}S_\phi^2)$, which maps the computational states $\{|00\rangle, |10\rangle, |01\rangle, |11\rangle\}$ to maximally entangled GHZ states, as for example $U_{eff}|00\rangle = 1/\sqrt{2}(|00\rangle - i|11\rangle)$. By adjusting the phase of the light field, the described unitary operation enables the deterministic creation of maximally entangled states and can be generalized by the following operator:

$$MS(\theta,\phi) = \exp\left(-i\frac{\theta}{4}\left[\sum_i(\sin(\phi)\sigma_y^{(i)} - \cos(\phi)\sigma_x^{(i)})\right]^2\right). \tag{3.15}$$

The choice of the gate time τ_{gate} restricts the optical power of the bichromatic laser beams as well as the detuning ϵ. In practice the optical power can be adjusted by measuring the Rabi time of each bichromatic laser beam on resonance with the qubit transition.

The main advantage of the Mølmer and Sørensen method is that the operation is independent of the motional state of the ions, which was already demonstrated in [64, 20] with a mean phonon number of $\overline{n} = 20$ and an entangled state with a fidelity of about 96%. However, the highest fidelity can be achieved by cooling the qubits into the motional ground state [64]. Additionally, the performance of the MS-gate is affected by systematic ac-Stark shifts of the respective qubit transition. For an ideal two-level system the ac-Stark shifts of the red- and blue detuned laser beams would cancel out each other. In practice, coupling to other $3^2D_{5/2}$ Zeeman states as well as coupling the qubit states $4^2S_{1/2}$ and $3^2D_{5/2}$ to the $4^2P_{1/2}$ and $4^2P_{3/2}$ levels leads to systematic ac-Stark shifts [65]. This systematic shift can be compensated by detuning both bichromatic beams. But this has the drawback of inducing a time-dependent phase evolution of the created entangled state, which complictates the calibration of the succeeding preparations. To overcome this problem, one can induce an additional ac-Stark shift on the qubit transition by unbalancing the power of the two bichromatic beams, respectively. A detailed discussion of the ac-Stark compensation methods is given in Ref. [64].

Ramsey experiments under entangling operations

In Ref. [66], the influence of correlated phase noise on a GHZ state was investigated with the result that any N-qubit GHZ state is N^2 more sensitive to phase noise than a single qubit. Therefore, the dominant error source affecting the performance of the entangling gate operation is dephasing. Optical qubits are subject to two dominant sources of dephasing: laser and magnetic field fluctuations. Both error sources lead to a time variation of the qubit transition frequency and therefore lowering the coherence of the qubit.

The coherence of our quantum system is investigated by Ramsey spectroscopy [67]. A Ramsey sequence consists of three steps[25]: (1) resonant global $\pi/2$-rotation $U(\pi/2, 0)$ on the qubit initially prepared in $|1\rangle$, which creates a coherent state $(|0\rangle + |1\rangle)/\sqrt{2}$. (2) a free evolution time t_R (Ramsey time) and (3) applying a second $\pi/2$-rotation $U(\pi/2, \phi)$ with a relative phase ϕ with respect to the first pulse. When scanning the phase ϕ for a given free evolution time t_R, the probability of measuring the excited state $p_{|0\rangle}$ is given by $p_{|0\rangle} = 1/2(1 + C(t_R)\cos\phi))$, whereas the contrast $C(t_R)$ corresponds to the oscillation amplitude. Therefore, the Ramsey contrast can be revealed directly from the measured amplitude as a function of phase [67, 49].

The important task at hand is to improve the coherence of the system, for which the dominant noise source has to be identified. This can be achieved by estimating the noise spectral density of the noise sources and modeling the coherence behaviour of that. One approach to address this problem is the spin echo method, originally used in NMR systems [68]. The idea is to interleave the two $U(\pi/2, 0)$ pulses with one $U(\pi, 0)$ pulse after the time $t_R/2$. Fig. 3.19 shows Ramsey contrast measurements using the spin echo technique on the $4^2S_{1/2}$ $(m_j = -1/2) \to 3^2D_{5/2}$ $(m_j = -1/2)$ transition for different settings of the 729 nm laser feedback control loop [49]. The blue diamonds illustrate the Ramsey contrast before changing the control loop settings. Different settings are distinguished by the noise spectrum of the in-loop Pound-Drever-Hall error signal shown by the curves in the inset of Fig. 3.19. The Ramsey contrast pattern features a dip at a Ramsey time $t_R \approx 100\mu$s, which indicates dominant frequency components of the laser in the region of 10 kHz. The coherence decay can be investigated theoretically assuming a certain laser spectrum $S(\omega)$ and fitting the resulting coherence $C(t_R)$ to the measured data points (blue diamonds). The temporal course of the decoherence for the spin echo sequence can be calculated by the following equation [69, 46]:

$$C(t_R) = \exp\left[-t_R^2 \int_0^\infty S(\omega)^2 \underbrace{\mathrm{sinc}(\omega t_R/4)^2 \sin(\omega t_R/4)^2 d\omega}_{g_{n=1}(\omega,t)}\right] \tag{3.16}$$

with the power spectral density (PSD) $S(\omega)^2$ and a weighting function $g_{n=1}(\omega, t)$, where n specifies the number of interleaved spin echo pulses. Here, we show the usability of this method for identifying the dominant noise source. For the noise spectrum $S(\omega)$ we assume typically a

---

[25] Here, for simplification the example is illustrated on a single qubit but can directly be applied on a larger system.

narrow Lorentzian profile $L(\omega) = \frac{\Gamma^2}{\Gamma^2+\omega^2}$ with overlapping Gaussian noise profiles $G^{(\omega_0,\sigma)}(\omega) = \exp -(\omega-\omega_0)^2/\sigma^2$:

$$S(\omega) = a\Big[L(\omega) + b\,G^{(10kHz,4kHz)}(\omega) + c\,G^{(2.9kHz,30Hz)}(\omega) + d\,G^{(1kHz,200Hz)}(\omega)\Big], \tag{3.17}$$

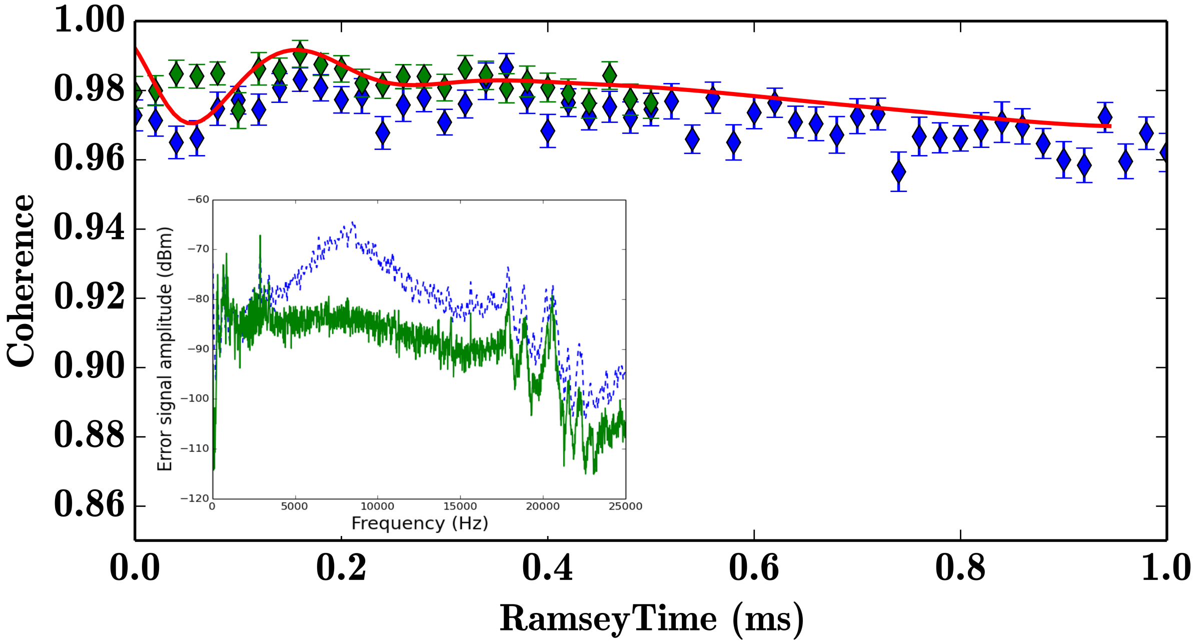

Figure 3.19: Coherence decay measurement: Measurement the coherence decay using the spin echo method for two different settings of the feedback loop electronics of the 729 nm laser. The blue and green curve of the inset show the noise spectrum of the in-loop error PDH error signal and the blue (red) diamonds correspond to the coherence measurement respectively.

where $G^{(10kHz,4kHz)}(\omega)$ corresponds to the dominant noise peak at around 10 kHz, which is indicated by the oscillating behaviour, a narrow Peak at 2.9 kHz, which arises from the Etalon lock (see Ref. [49]) and a peak at 1 kHz, which could be induced by acoustic noise and explains the contrast loss up to 1 ms. In Fig. 3.19 the contrast decay according to equation 3.17 with the fitted parameters $[a = 36.5\ \sqrt{\text{Hz}}, \Gamma = 3\ \text{Hz}, b = 5.3, c = 4.2, d = 1.5]$ is shown by the red curve. The coherence loss, indicated by the dip in Fig. 3.19 caused an infidelity of the entangling gate in the order of 10%. After optimizing the parameters of the feedback loop[26] the noise around 10 kHz could be reduced by 20 dBm (green curve of the inset). The coherence decay measurement after the optimization (green diamonds) clearly indicates that the oscillation vanishes and therefore significantly improves the fidelity of the MS gate ($\approx$96% for four ions).

This phenomenological approach is helpful to reveal problems of the laser and magnetic field current feedback parameters or noise arising from electronic crosstalk (e.g. ground loops). Further investigation of the sensibility of the ion to specific frequency noise components is not

---

[26] In that case, the gain settings of the feedback loop to the electro-optical modulator as well as to the intracavity Piezo were adjusted. A detailed description of the different feedback loops is presented in Ref. [49].

possible with this approach. Nevertheless, the described spin echo technique can be advanced to a more complex scheme, which allows the measurement of the noise spectrum $S(\omega)$ with a single qubit (see Ref. [69]). This method involves multiple spin echo pulses and can be interpreted as a single qubit spectrum analyzer. This step is necessary to further explore the sensitivity of the ion to specific frequency components and can be used to systematically investigate different error sources and improve the coherence of the system. This example demonstrates the importance of the laser performance for the coherence of our system. Within the next section a new generation of a Ti:sapphire laser system for the coherent manipulation of the qubits is introduced.

3.6.1 Improved Ti:sapphire laser system

During the course of this thesis, a new Ti:sapphire laser system from Msquared[27] was installed that is supposed to outperform the current laser system in following properties: Laser output power, Intrinsic frequency noise, Mechanical stabililty and Intensity stability. The system consists of a diode-pumped solid-state (DPSS) laser system[28] at 532 nm, which pumps the Ti:sapphire laser. The maximum pump power is 15 W, which leads to a maximum output power after the Ti:sapphire laser of 4 W at 729 nm and a peak power of 4.8 W at 780 nm. The emitted light from the crystal is enhanced by a resonator including two frequency selective elements: (a) a birefringent Lyot-Filter enables course frequency adjustment over a free spectral range (FSR) of 0.5 nm (b) an Etalon filter allows for fine tuning of the frequency. The Etalon is held on the maximum emission power by a control loop realized by a lock-in detector at a modulation frequency of 19 kHz. This ensures single-frequency-mode operation of the laser system. Furthermore, the resonator includes two piezo-electrical elements (Piezo), which are used to stabilize the laser frequency to a ultra-stable reference resonator with a Finesse of 490.000. The frequency response of the fast Piezo is flat up to 30 kHz and has a 90° phase shift at 50 kHz with a resonance at 105 kHz. The fast Piezo has a frequency gain of 35 MHz/V, whereas the slow Piezo with a bandwith of only 100 Hz shows a frequency gain of 25 GHz/V. In the following section the stabilization of the Msquared laser to our high finesse resonator will be described in detail.

Fig. 3.20 shows an illustration of the experimental setup used to stabilize the Ti:sapphire laser onto the high finesse resonator. Part of the laser output light is split up by a polarizing beamsplitter (PBS) and guided through an optical multimode fiber to the High Finesse WS-7 wavemeter. After the PBS (100 mW) the laser light is passing through an acousto-optical modulator (AOM) (“noise eater”), which is used as a high bandwidth frequency control. Part of the first order diffracted light is sent to a 50:50 beamsplitter, overlapped with light from another narrow linewidth laser system [70] and sent to a photodiode (PD), which provides a beat measurement. The light transmitted through the PBS is coupled into a polarization maintaining single-mode fiber, which is guided to the high finesse resonator. There it is necessary to cancel phase noise induced in the optical fiber by acoustic noise affecting the fiber medium. The phase noise cancellation technique was originally described in Ref. [71].

Stabilization of the laser to the resonator is realized via the Pound-Drever-Hall (PDH) locking technique introduced in Ref. [48]. The error signal is applied to the input of two different

---

[27] Msquared - SolsTis SA PSX R

[28] Sprout High Power CW 532 nm DPSS Lasers Sprout-G Series

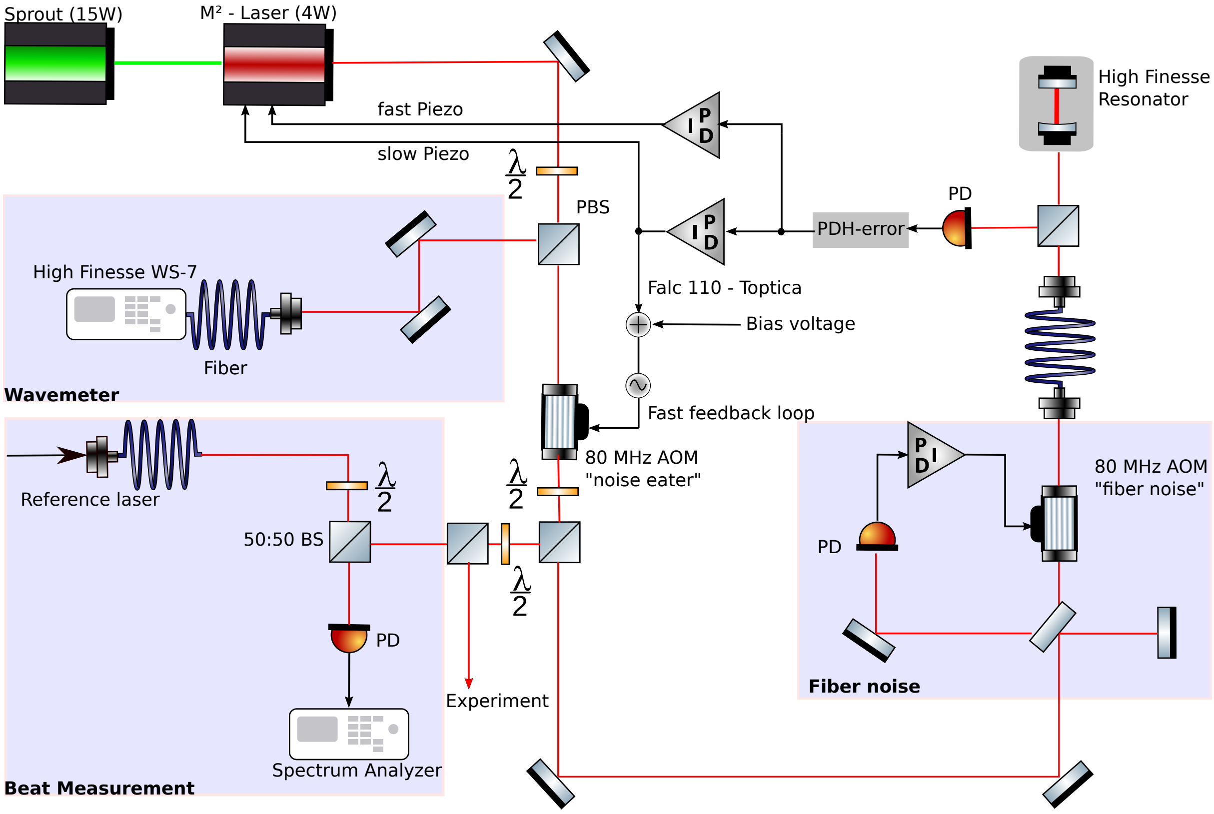

Figure 3.20: Laser locking scheme: Schematic illustration of the experimental setup for locking the next generation qubit laser to an optical resonator with a finesse of 490.000. The PDH error signal is applied to the fast and slow internal piezo as well as to a noise cancellation AOM. The fiber noise cancellation setup is necessary for cancelling phase noise of the fiber to the reference cavity.

proportional-integral-derivative controllers (PID controllers), each acting on a different actuator. The fast branch of the feedback is realized by shifting the frequency of an AOM - “noise eater” (see Fig. 3.20), which exhibits a bandwidth of 1.5 MHz.[29] The feedback signal to the AOM is generated by a Toptica Falc 110 PID controller, which has a bandwidth limit of 10 MHz and several integrating circuits. The actuating variable for the noise cancelling AOM is the driving frequency, which has to be biased by the AOM center frequency of 80 MHz. The corresponding electronic circuit is shown in Appendix A. The feedback to the slow piezo is realized by the unlimited integrator of the Falc PID controller to compensate slow frequency drifts induced by temperature changes. The drift of the laser directly after switching on the Etalon lock was obtained from the beat measurement and is on the order of 470 kHz/min. The third feedback loop is applied to the fast Piezo, which is mainly required to compensate acoustic noise up to 3 kHz. The dominant frequency noise is in the acoustic domain, which results in a high gain in the lower kHz frequency regime. The laser system is mounted on a vibration isolation platform integrated in an acoustically shielded box to lower the acoustic noise coupling into the laser. The acoustic box leads to a suppression of more than 30 dBm for frequencies larger than 100 Hz. More details concerning the acoustic box will be given in the master thesis of Roman Stricker. All adjustments of the PID controllers are described in detail in Appendix A.

---

[29] The bandwith is limited by the speed of sound in the crystal and the beam diameter.

The measurement of the laser linewidth is performed by beating the laser light with an independent ultra-stable diode laser system described in the master thesis of Lukas Postler [70]. Hence, the linewidth of both lasers can be benchmarked. The beat measurement is realized by overlapping both lasers onto a photodiode with a bandwidth of 1 GHz. Note that the light from the other narrow laser system is guided through a 20 m long optical fiber and therefore phase noise cancellation has to be integrated, which is not shown in Fig. 3.20. Fig. 3.21(a) shows the beat measurement of the free running (including Etalon lock) Msquared laser with the diode laser at a residual bandwidth of 1 kHz and averaging over 20 measurements. This results into a total measurement time of 20 ms. A gaussian fit to the beat measurement gives a linewidth of 125(2) kHz, which is significantly lower than the intrinsic linewidth of the previously used Ti:sapphire laser of about 500 kHz [49].

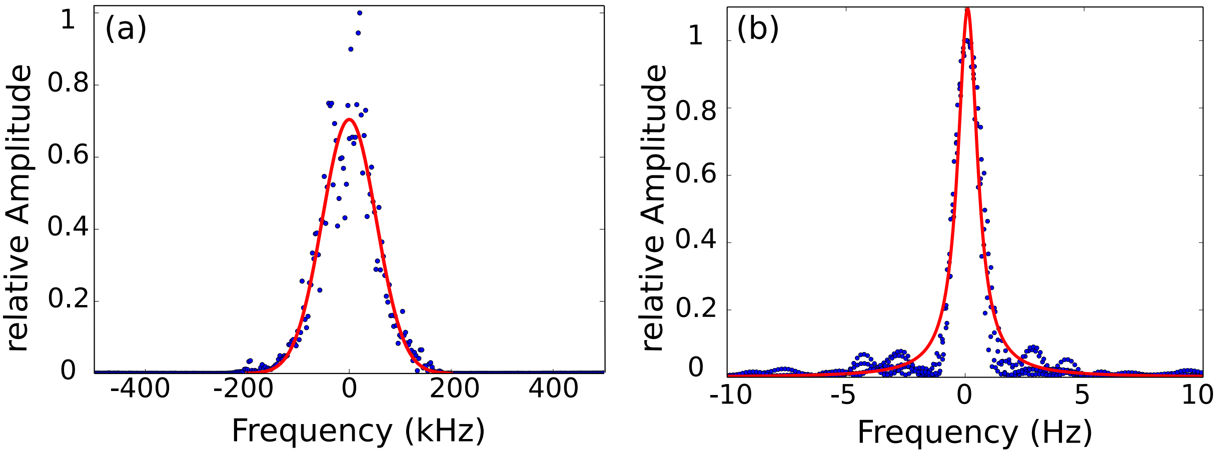

Figure 3.21: Laser linewidth measurement: Beat measurement of the Msquared laser with the diode laser locked to a high finesse cavity. (a) Beat measurement of the free running (Etalon lock) Msquared laser with a diode laser locked to a high finesse cavity over a measurment time of 20 ms and 1 kHz residual bandwidth. The FWHM linewidth of the gaussian fit function is 125(2) kHz. (b) Overlap of five single beat measurement with a resolution bandwidth of 1 Hz (1s measurement time). The offset of the individual measurements was corrected and the resulting lorentzian fit leads to a linewidth of 1.01(1) Hz.

In Fig.3.21(b) the beat measurement was performed with locking the Msquared laser to the high finesse cavity. The measurement shows the overlap of five single beat measurements with a residual bandwidth of 1 Hz (1 s measurement time), whereas the frequency offset of each measurement was corrected. The lorentzian fit leads to a FWHM linewidth of 1.01(1) Hz. The result corresponds to a convolution of the frequency profiles of both lasers, which implicates that the linewidth of the two lasers can be estimated to be around 500 mHz, since $\Delta = \Delta_{Msquared} + \Delta_{diode}$ for two lorentzian laser profiles under the assumption that both lasers contribute equally to the measured linewidth.

As already pointed out above, the spectrum of the error signal reveals important information about the laser performance and is therefore compared with the error signal of the current Ti:sapphire laser system. Fig. 3.22 shows the measurement of the error signal of both laser systems. The signals were measured with an audio analyzer (SR1). The error signal of the Msquared laser system (blue curve) shows a significant reduction of the noise level for the entire frequency domain up to 100 kHz and almost 45 dBm suppression up to 20 kHz The dominant narrow peak at 13 kHz corresponds to the modulation frequency of the Etalon locking branch.

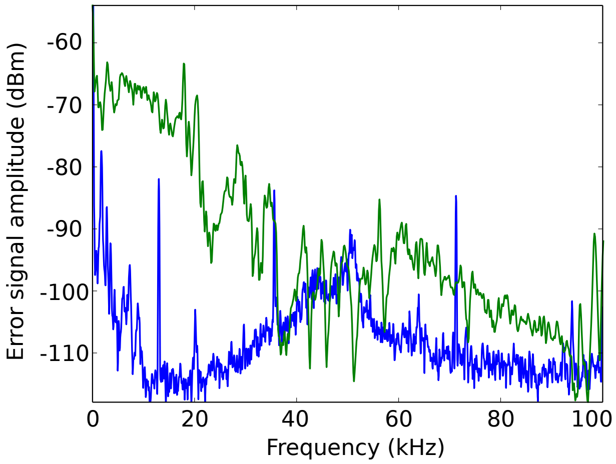

Figure 3.22: Comparison of the currently used Ti:sapphire laser (green) with the Msquared laser system (blue) locked to the high finesse resonator by measuring the Fourier spectrum of the in-loop error signal.

Fig. 3.23 shows Ramsey contrast measurements on the $4^2S_{1/2}$ $(m_j = -1/2)\rightarrow$ $3^2D_{5/2}$ $(m_j = -1/2)$ transiton for the Msquared laser (green diamonds) and the previously used laser system (blue diamonds). The measurement clearly shows an improvement of the coherence for the Msquared laser. The coherence at a Ramsey time of 10 ms is about 97%, whereas the coherence with the current laser system is about 88%. The improvement of the coherence for timescales lower than 5 ms is related to the low laser noise level for frequencies larger than 200 Hz. Low frequency noise ($\leq$200 Hz) leads to an enhanced coherence decay for timescales larger than 5 ms. The new laser system shows also an improved performance in the low frequency domain, as indicated by the Ramsey contrast measurements in Fig. 3.23. Besides the study of the coherence, further investigations of the fidelity of single- and muti-qubit gate operations have to be accomplished using randomized benchmarking [72]. First single-qubit randomized benchmarking results of the global beam did already show an improvement of the gate fidelity by a factor of 20 using the Msquared laser system and resulting in an infideltiy of $6.2(2) \times 10^{-4}$ for resonant global operations on a single qubit. Further investigations will also be accomplished within the master thesis project of Roman Stricker. Another parameter, which is crucial for the gate operation fidelity is the stability of the laser intensity. The intrinsic laser intensity stability without active stabilization was measured with a photodiode and is on the order of 0.1%. This is already an enormous improvement compared to the existing setup, which exhibits intensity fluctuations up to 10% (see master thesis of Roman Stricker).

3.7 Implementation of Raman-sideband cooling

As already pointed out in the previous sections, cooling the motion of the ions close to the motional ground state is mandatory for the realization of high fidelity gates. In previous experi-

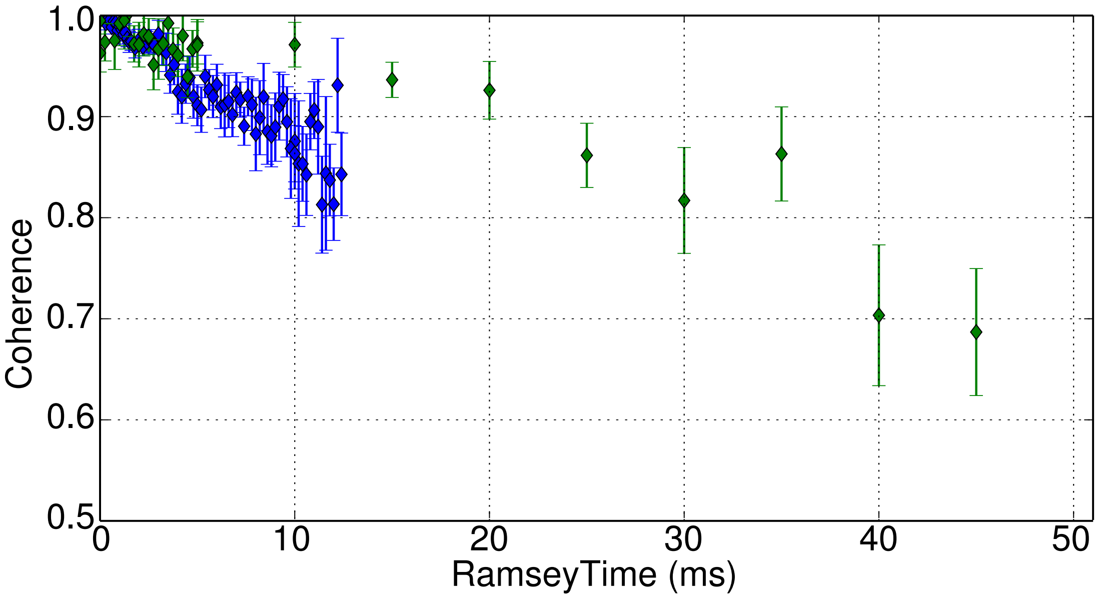

Figure 3.23: Ramsey contrast measurement: Msquared laser system performance compared to the previously used Ti:sapphire laser system by measuring the Ramsey contrast on the $4^2S_{1/2}$ $(m_j = -1/2)\rightarrow$ $3^2D_{5/2}$ $(m_j = -1/2)$ transiton. The Msquared laser system (green diamonds) shows a clear improvement of the coherence compared to the old Ti:sapphire laser (blue diamonds).

ments, this task has been achieved by resolved sideband cooling on the $4^2S_{1/2}$ $(m_j = -1/2)\rightarrow$ $3^2D_{5/2}$ $(m_j = -5/2)$ transiton [73]. Here, the implementation of resolved sideband cooling on the $4^2S_{1/2} \rightarrow 4^2P_{1/2}$ Raman transition is described. After summarizing the resolved sideband cooling technique, the Raman cooling scheme is introduced with emphasis on coherent Rabi oscillations on the Raman transition as well as the measurement of the cooling parameters - cooling rate and minimal phonon number.

3.7.1 Resolved Sideband cooling

Sideband cooling (SB-cooling) of a two-level system in a harmonic potential is illustrated in Fig. 3.24(a). The two-level subspaces for the different vibrational levels $\{|n-1\rangle, |n\rangle, |n+1\rangle\}$ are split by the trap frequency ω_z. Two important aspects are assumed: (1) the condition of resolved motional sidebands, which implies that $\Gamma \ll \omega_z$ with the linewidth Γ of the excited state and (2) fulfilling the Lamb-Dicke condition, which allows us to consider only transitions with $\Delta n = 0, \pm 1$.

A detailed description of the SB-cooling dynamics is given in [74, 52]. The important parameters describing the cooling dynamics are the cooling rate and the steady state phonon number. Here, we follow the approach of a rate equation model to calculate the cooling rate and the mean steady state phonon number. When exciting the two-level system with laser light detuned by the frequency $\Delta \leq 0$ from the resonant carrier frequency ω_0, different processes lead to an increase (heating) and a decrease (cooling) of the phonon number, as indicated in Fig. 3.24(a) where each cycle consists of a stimulated absorption process followed by a spontaneous decay to the electronic ground state. The excitation probability of the upper level $|e, n\rangle$

without changing the motional state is given by $P(\Delta) = \frac{\Omega_0^2}{4\Delta^2+\Gamma^2}$, whereas the probability of exciting the red- and blue sideband transition is given by $\Gamma\eta^2 n P(\Delta)$ and $\Gamma\eta^2(n+1)P(\Delta)$ respectively. Fig. 3.24(b) shows a simple illustration of the corresponding cooling rates $R_-^{(1,2)}$ as well the heating rates $R_+^{(1,2)}$. With the corresponding excitation probability the cooling- and heating rates can be calculated to:

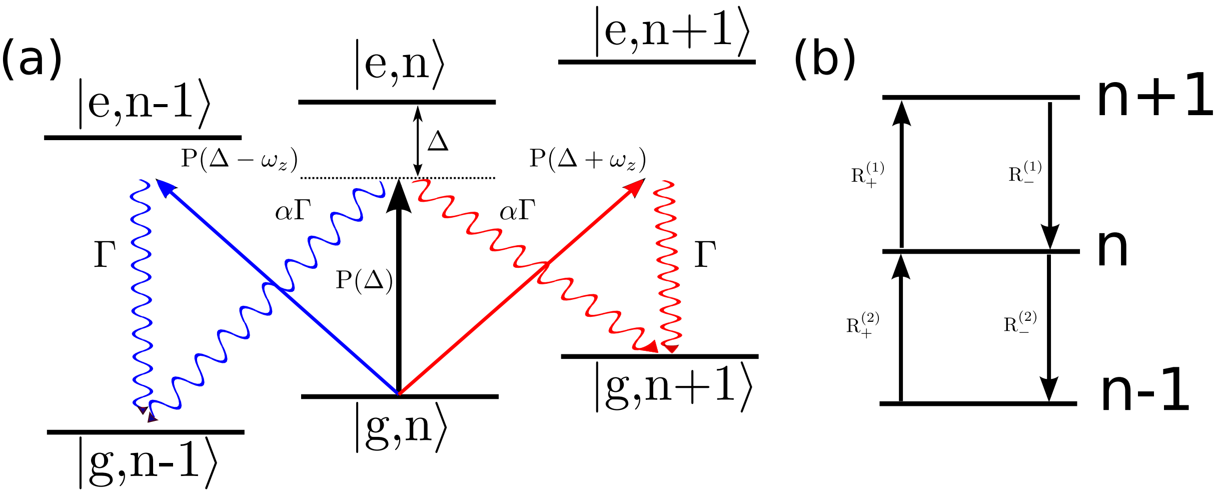

Figure 3.24: Resolved sideband cooling: (a) Heating and cooling processes of a two-level system in a harmonic potential. (b) Rate model for the cooling dynamics with the cooling rates $R_-^{(1,2)}$ and the heating rates $R_+^{(1,2)}$. If the laser frequency is detuned close to the red sideband ($\Delta = \omega_z$), then the cooling rate is larger than the heating rate, which effectively leads to cooling of the motional mode.

$$\begin{aligned}
R_+^{(1)} &= \Gamma\eta^2(n+1)\{P(\Delta-\omega_z)+\alpha P(\Delta)\}\\
R_-^{(1)} &= \Gamma\eta^2(n+1)\{P(\Delta+\omega_z)+\alpha P(\Delta)\}\\
R_+^{(2)} &= \Gamma\eta^2 n\{P(\Delta-\omega_z)+\alpha P(\Delta)\}\\
R_-^{(2)} &= \Gamma\eta^2 n\{P(\Delta+\omega_z)+\alpha P(\Delta)\}.
\end{aligned}$$

Please note that the spontaneous decay rate Γ from the state $|e,n\rangle$ to the states $|g,n\pm1\rangle$ is modified by a factor $\alpha < 1$, which considers the spread of the population to the different motional modes[30]. The rate coefficients $R_\pm^{(1)}$ scale with $(n+1)$ and $R_\pm^{(2)}$ with n respectively. Therefore, the rate equation for the population p_n of the motional state with n phonons is given by the following equation:

$$\frac{dp_n}{dt} = \{-\big[(n+1)A_+ + nA_-\big]p_n + (n+1)A_-p_{n+1} + nA_+p_{n-1}\}, \tag{3.18}$$

with the rate coefficients $A_+ = \Gamma\eta^2\{P(\Delta-\omega_z)+\alpha P(\Delta)\}$ and $A_- = \Gamma\eta^2\{P(\Delta+\omega_z)+\alpha P(\Delta)\}$. A more general solution of this equation is given in Ref. [74], but here it is sufficient

---

[30] In the case of a dipole transition $\alpha = 2/5$.

to consider only the lowest vibrational levels $\{|n=0\rangle, |n=1\rangle\}$, since we are interested in the cooling dynamics close to the motional ground state. This simplifies Equ. 3.18 to the following expression:

$$\frac{dp_0}{dt} = \{-A_+ p_0 + A_- p_1\}.$$

With $\bar{n}(t) = \langle n \rangle = \sum_{n=0}^{\infty} n p_n = p_1(t)$ and $p_0(t)+p_1(t) = 1$, the solution of the inhomogeneous linear differential equation of first order is given by:

$$p_1(t) = \bar{n}_0 \exp(-Rt) + \frac{\beta}{R}[1 - \exp(-Rt)], \tag{3.19}$$

with the cooling rate $R = (A_- - A_+)$, the heating rate $\beta = A_+$ and the phonon number $\bar{n}_0$ at the time $t = 0$. This yields a steady state phonon number of $\bar{n}(t \rightarrow \infty) = \frac{\beta}{R}$. The cooling parameters R and $\bar{n}$ can be calculated from the excitation probability distribution $P(\Delta)$ while considering that $\Gamma \ll \omega_z$:

$$\begin{aligned} R &= A_- - A_+ \approx \frac{\Omega^2 \eta^2}{\Gamma} && (3.20) \\ \bar{n}(t \rightarrow \infty) &= \frac{A_+}{A_- - A_+} \approx \frac{\Gamma^2}{\omega_z^2}\left(\frac{1}{16} + \frac{\alpha}{4}\right). && (3.21) \end{aligned}$$

This means that on one hand, a narrow linewidth of the upper state leads to a lower minimal achievable steady state phonon number $\bar{n}(t \rightarrow \infty)$. On the other hand, the cooling rate R is limited by the spontaneous decay rate Γ and is saturating when the coupling strength $\eta\Omega$ is equal to Γ. Therefore a very narrow cooling transition will reduce the cooling rate. For example in the case of SB-cooling using only the quadrupole transition, the maximum cooling rate would be in the order of $(2\pi)0.16s^{-1}$ and therefore not practical for any experimental implementation. To overcome this problem, the transition is broadened by exciting further to a third level via a dipole transition with a smaller lifetime [73].

Using the $4^2S_{1/2} \rightarrow 4^2P_{1/2}$ dipole transition instead of the quadrupole transition would enable higher cooling rates due to the stronger coupling of the laser field to the dipole transition and the larger scattering rate. Furthermore, the Lamb-Dicke parameter for the Raman-transition is almost a factor of two larger compared to the quadrupole transition at 729 nm. But one has to consider that increasing the cooling rate also implies a larger mean phonon number. Besides the cooling rate, there is one major advantage of using the Raman cooling technique. The dipole transition at 397 nm is far detuned from the quadrupole transition and therefore the coherence of the stored quantum states is not affected by the Raman cooling beams. This opens the possibility of in-sequence laser cooling, which was already successfully used for the implementation of the Shor algorithm [75] and the correction of a quantum measurement on a single qubit [76].

3.7.2 The Raman transition

The Raman transition is realized by two laser beams coupling to a Λ-system formed by the Zeeman sublevels of the $4^2S_{1/2} \rightarrow 4^2P_{1/2}$ dipole transition. The Λ-system for the Raman transition is generated by the $4^2S_{1/2}$ $(m_j = -1/2) = |1\rangle$, $4^2S_{1/2}$ $(m_j = +1/2) = |2\rangle$ and $4^2P_{1/2}$ $(m_j = +1/2) = |3\rangle$ Zeeman sublevels, as shown in Fig. 3.25. Transition between these levels $\{|1\rangle, |2\rangle, |3\rangle\}$ with the energies $\{0, \hbar\omega_{21}, \hbar\omega_{31}\}$ are driven by two off-resonant laser beams. The first laser beam with the frequency ω_1 drives the $|1\rangle \rightarrow |3\rangle$ transition, whereas the levels $|3\rangle$ and $|2\rangle$ are coupled by a laser field with frequency ω_2. The selection rules for the dipole transitions ($\Delta m = 0, \pm 1$) require σ_+ polarization of the first laser beam and π polarization of the second laser light field.

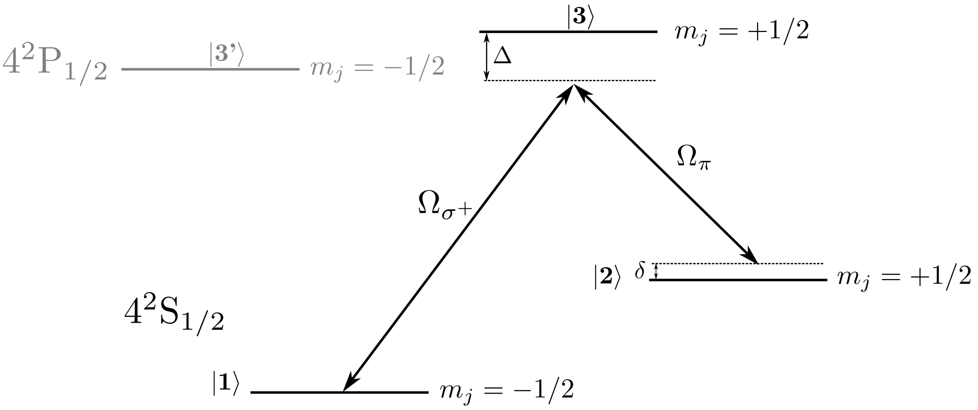

Figure 3.25: Raman transition: The Raman transition consists of Zeeman levels of the $4^2S_{1/2}$ ground state and the $4^2P_{1/2}$ $(m_j = +1/2)$ state forming a Λ-system system. Two Raman beams detuned by Δ from the $4^2P_{1/2}$ $(m_j = +1/2)$ level are effectively coupling the two ground states. Resonant excitation of the Raman transition is observed if the frequency difference bewtween the two Raman beams is equal to the ground state splitting. The effective Rabi frequency is given by $\Omega_{eff} = \frac{\Omega_\pi \cdot \Omega_{\sigma+}}{2\Delta}$. The Zeeman level $4^2P_{1/2}$ $(m_j = -1/2) = |3'\rangle$ is greyed out as it is not of importance here, but will be considered within the next sections.

The time evolution of the states can be described by solving the Schrödinger equation, which leads to a system of three coupled differential equations. A detailed theoretical description of the Λ-system is given in Ref. [77]. Here, the detuning Δ of the two laser beams from the upper level $|3\rangle$ is typically several GHz and therefore $\Delta \gg \Omega_{\sigma+}, \Omega_\pi, \Gamma, \delta$ holds, with the Rabi frequencies $\Omega_{\sigma+}, \Omega_\pi$, the natural linewidth Γ of the state $|3\rangle$ and the detuning $\delta = \omega_1 - \omega_2 - \omega_{31}$ from the resonance. As a result of this, the wavefunction amplitude of state $|3\rangle$ is small and varying at much faster timescales ($\propto 1/\Delta$) compared to the amplitude of $|1\rangle$ and $|2\rangle$. This allows the adiabatic elimination of the upper state $|3\rangle$ and effectively reduces the Λ-system to a two level system, consisting of states $|1\rangle$ and $|2\rangle$. The effective coupling between $|1\rangle$ and $|2\rangle$ is given by $\Omega_{eff} = \frac{\Omega_{\sigma+}\Omega_\pi}{2\Delta}$ [77]. So far the system was introduced as a three level system, which is a simplification, since the two beams can also couple to the $4^2P_{1/2}$ $(m_j = -1/2)$ state and induce additional frequency shifts, which will be discussed within the next sections. Before the realization of coherent Raman oscillations and the characterization of the effective Rabi frequency Ω_{eff} is discussed, the experimental system is described in detail.

The Raman laser setup

The optical setup for the σ_+- and π Raman beams at the experimental table is shown in Fig. 3.5. The two laser beams were generated with a laser diode system[31]. The detailed optical setup as well as the logic control of the pulses is shown in Fig. 3.26. The laser system consists of a diode laser at 794 nm with an output power of 30 mW, which is amplified by a tapered amplifier (TA) to a maximal power of 500 mW. The amplified light is coupled into a second harmonic generation (SHG) module, generating light at 397 nm and a nominal output power of maximal 100 mW. The laser frequency is stabilized by standard Pound-Drever-Hall locking technique with respect to a reference cavity (details about the cavity system can be found in the PhD thesis of Mathias Brandl) with a free spectral range of 1.5 GHz. The laser frequency can be tuned adjusting the cavity length with a piezoelectric crystal. The light at the output of the SHG is split by a polarizing beam cube into two optical paths (σ_+ and π). Each of the two paths are frequency shifted by 2×80 MHz using an AOM in double pass configuration. The AOMs are used for switching the optical beams within the sequence, controlling the frequency and power respectively. Finally, the beams are guided to the experiment with 25 m long single mode and polarization maintaining fibers. The coupling efficiencies of the fibers are about 35%. The control logic for the two AOMs is shown in the box of Fig. 3.26.

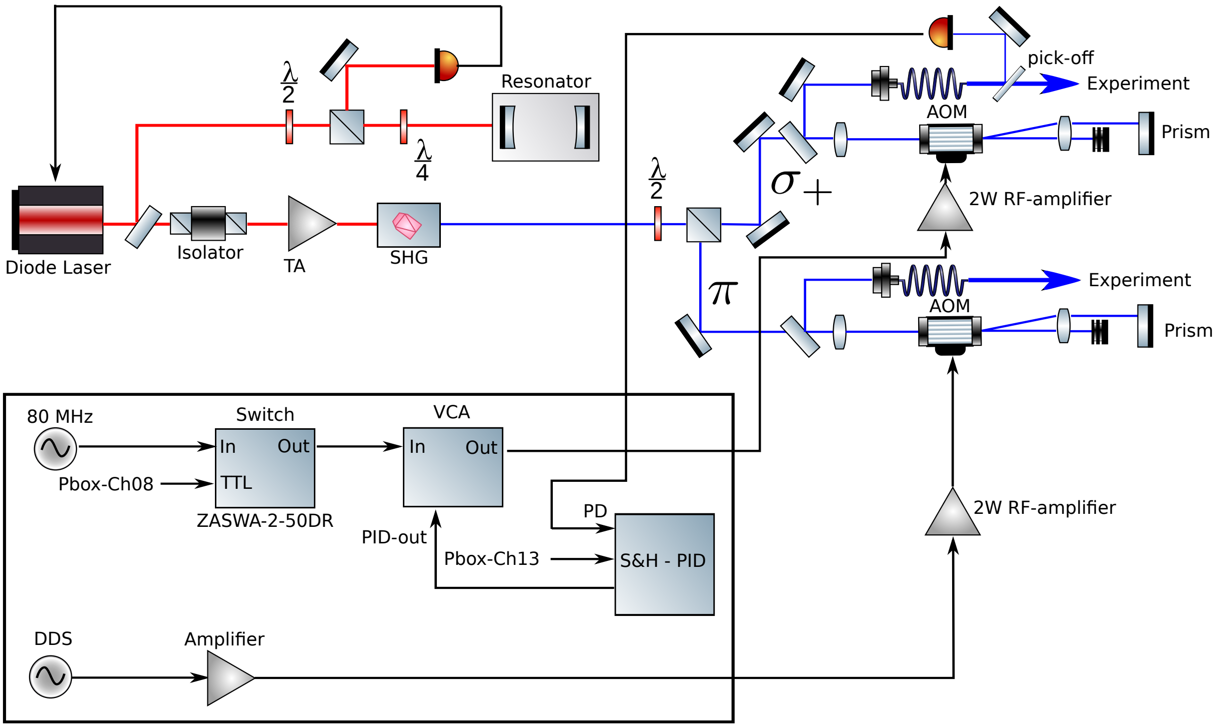

Figure 3.26: Raman cooling setup: Optical setup used for the realization of Ramana sideband cooling. The two Raman beams (σ_+ and π) are generated by a diode laser system at 794 nm in combination with a tapered amplifier (TA) and a SHG module. The laser system is stabilized to a resonator with a finesse of about 10.000. The frequency and optical power of the laser beams is controlled by two AOMs in double pass configuration with the control logic shown in the inset box.

---

[31] Toptica DL-Pro with tapered amplifier and SHG

Driving the Raman transition resonantly requires that the difference frequency of the two Raman beams match the energy gap of the two ground state Zeeman levels (see Fig. 3.25). Therefore, the frequency of the AOM controlling the σ_+ Raman beam is set up to a fixed value of 80 MHz using a frequency synthesizer. The π beam instead is scanned by the second direct digital synthesis (DDS) output of the pulse generator (Pbox)[32] with respect to the frequency of the σ_+ AOM. The σ_+-pulses within the sequence are generated by a RF-switch[33] with the control TTL signal provided by channel 08 of the Pbox. The output of the RF-switch is applied to a voltage controlled attenuator[34] (VCA) stabilizing the optical power of the σ_+ light. The output voltage of a sample and hold PID regulator is applied to the control voltage input of the VCA with the aim to stabilize the intensity of the σ_+ beam between each sequence. The intensity of the beam is measured with a photodiode (PD) directly behind the output of the fiber coupler (see Fig. 3.26).

Coherent Raman operations

The first step towards the realization of Raman sideband cooling was to measure the Rabi frequency of the individual beams. This was accomplished by investigating the optical pumping process from the ground state $|1\rangle$ to the state $|2\rangle$, which enables the optimization of the σ_+- and π polarization as well as the characterization of the individual coupling strength $\Omega_{\sigma+}$ and Ω_π respectively. The pulse sequence used to perform the presented experiments is schematically illustrated in Fig. 3.27.

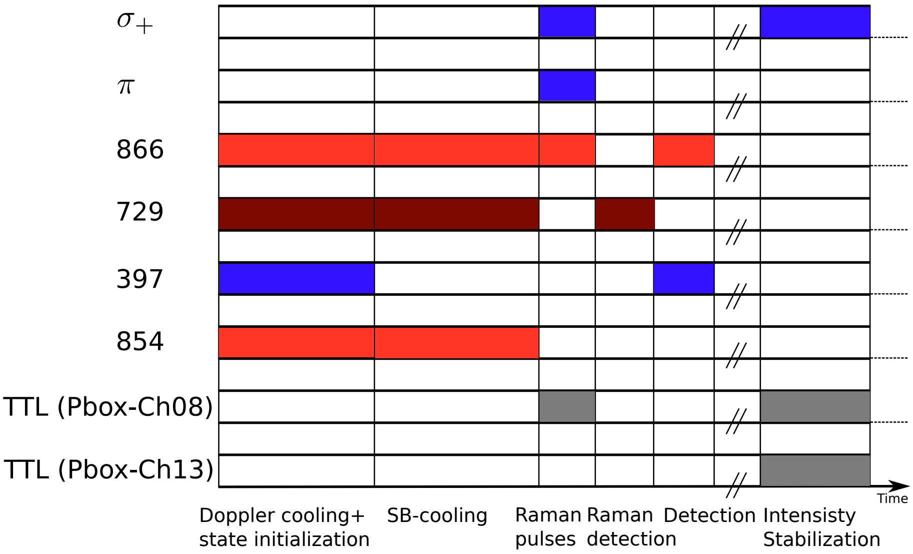

Figure 3.27: Raman sequence: Schematic diagram of the pulse sequence used to realize optical pumping as well as coherent Rabi oscillations on the Raman transition.

---

[32] The TTL signals, which are used to control the RF-switches are generated by the pulse generator (Pbox). A detailed description of the Pbox is given in Ref. [55]

[33] ZASWA-2-50DR

[34] mini circuits ZX73-2500+

The schematics in in Fig. 3.27 shows the sequence of laser pulses within one experimental cycle. The first two steps include Doppler cooling, state preparation and sideband cooling of the axial COM mode. The next step involves state manipulation using the Raman beams. Here, the light beams are switched on simultaneously, which requires the TTL signal generated by Pbox-Ch08 to be high. During this time the 866 repump laser has to be switched on, otherwise population gets transferred to the $3^2D_{3/2}$ state. The induced qubit dynamics of the Raman pulses is detected by population transfer from state $|1\rangle$ to state $|2\rangle$. This is achieved by mapping the remaining population of state $|1\rangle$ to the $3^2D_{5/2}$ $(m_j = -1/2)$ qubit state using the 729 nm laser and subsequent detection of the $3^2D_{5/2}$ state population.

As a first measurement, the coupling strength of the individual Raman beams was measured by applying each Raman beam separately to the ion for a time period T, following the sequence in Fig. 3.27. The detuning of both laser fields from the upper level is $\Delta = 4$ GHz. The measured population of the state $|1\rangle$ as a function of the excitation time T fot the σ_+ and π beam is shown in Fig.3.28. The σ_+-beam leads to off-resonant excitation of the state $|3\rangle$ and subsequent decay to the state $|1\rangle$ with rate $2\Gamma/3$ and to state $|2\rangle$ with the rate $\Gamma/3$. Therefore, the population of state $|1\rangle$ is completely pumped to the dark state $|2\rangle$, which can be seen clearly in Fig.3.28(a). The same measurement was performed with the π-beam applied to the ion for time T. In that case, the population of the state $|1\rangle$ is pumped via the $4^2P_{1/2}$ $(m_j = -1/2) = |3'\rangle$ state to level $|2\rangle$ with the decay rate $2\Gamma/3$, but also the same process is pumping back from $|2\rangle$ to the ground state $|1\rangle$. This dynamics effectively leads to a steady state population of the two ground states of 50%, which is confirmed by the measurement result in Fig. 3.28(b).

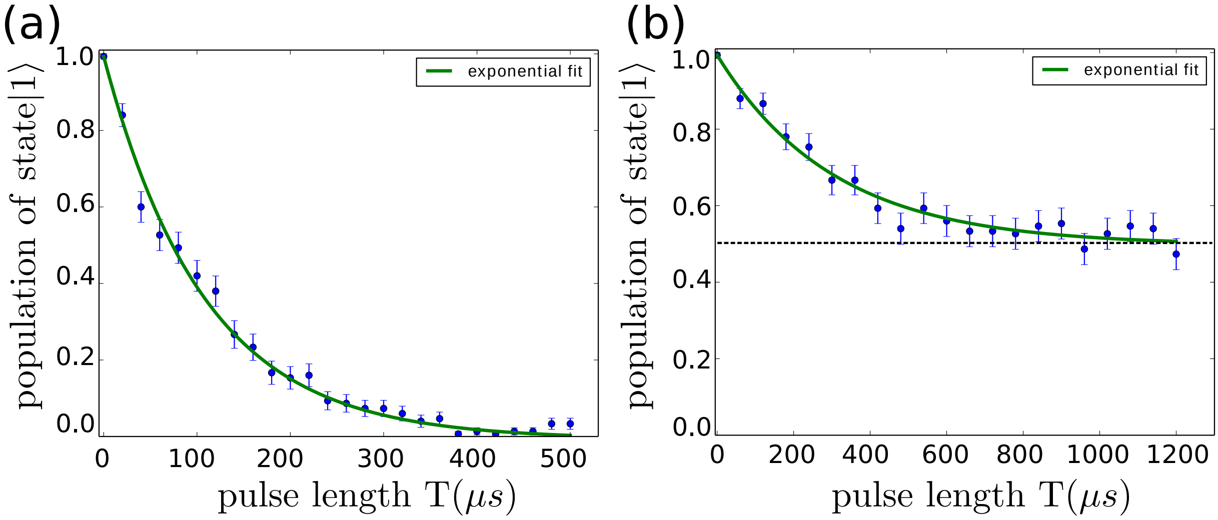

Figure 3.28: Optical pumping: Measurement of the Rabi frequency $\Omega_{\sigma+}$ (a) and Ω_{π} (b) via optical pumping. In (a) only the σ^+ Raman beam was applied to the ion, whereas in (b) the π beam was exciting the $|1\rangle \rightarrow |3'\rangle$ transition for a time T. For each case the population of the state $|1\rangle$ was measured as a function of the excitation time T. The measured decay rate of the pumping process enables the calculation of the Rabi frequencies (see main text) and additionally the calibration of the effective Rabi frequency Ω_{eff} without performing coherent Rabi oscillations.

Both processes can be described theoretically by an exponential decay of the population $p_{|1\rangle}$ with the effective decay rates $R^{\sigma+}$ and R^{π}:

$$p_{|1\rangle} = \exp(-R^{\sigma+}t), \text{with } R^{\sigma+} = \frac{\Gamma}{3}\left(\frac{\Omega_{\sigma+}}{2\Delta}\right)^2 \quad (3.22)$$

$$p_{|1\rangle} = \exp(-R^{\pi}t) + \frac{1}{2}, \text{with } R^{\pi} = \frac{2\Gamma}{3}\left(\frac{\Omega_{\pi}}{2\Delta}\right)^2. \quad (3.23)$$

Therefore, the decay rates $R^{\sigma+}$ and R^{π} can be revealed from fitting the corresponding exponential regression curves (Fig. 3.28(a,b)) to the measured data. With the fitted decay rates $R^{\sigma+} = 9.2(3) \cdot 10^3 s^{-1}$ and $R^{\pi} = 3.3(2) \cdot 10^3 s^{-1}$, the detuning $\Delta = 4$ GHz and a natural linewidth of $\Gamma = (2\pi)20.7$ MHz, we obtain the Rabi frequencies $\Omega_{\sigma^+} = (2\pi)116.6$ MHz and $\Omega_{\pi} = (2\pi)49.4$ MHz. Out of that result, the effective Rabi frequency Ω_{eff} can be calculated and yields $(2\pi)720$ kHz. The optical power typically used to obtain the measured Rabi frequencies is on the order of 500 μW.

After characterizing the individual Raman beams, the Raman transition was driven with both beams simultaneously. First, a spectrum was measured by applying the sequence in Fig. 3.27 and scanning the frequency of the π-Raman beam with respect to the σ_+-beam. The result of the Raman spectrum measurement is shown in Fig. 3.29(a). The spectrum was measured with a pulse length of 2.5 μs. The spectrum clearly indicates the carrier of the $|1\rangle \rightarrow |2\rangle$ Raman transition at a centre frequency of -390.299 MHz and the red- and blue SB detuned by ± 1.158 MHz from the carrier. Please note that the control frequency of -380 MHz corresponds to the physical DDS output frequency of 80 MHz. The carrier is shifted about 680 kHz from the expected transition frequency, which arises from a differential ac-Stark shift caused by the σ_+-beam and will be discussed within the next section.

Finally, coherent Rabi oscillations on the Raman transition were realized by setting the frequency of the π-beam to the center frequency (-390.299 MHz), which corresponds to an effective frequency shift of 10.3 MHz relative to the σ_+-beam frequency[35] and scanning the duration T of both pulses. Fig. 3.29(b) shows the coherent Rabi oscillations on the $4^2S_{1/2}$ to $4^2P_{1/2}$ Raman transition. The Rabi oscillations reveal coherent oscillations between the two ground states $|1\rangle$ and $|2\rangle$ including an exponential decay characteristics. The Rabi time $T_{2\pi}$ as well as the decay time τ extracted by fitting the following regression function (green curve) to the measured population $p_{|1\rangle}(t)$:

$$p_{|1\rangle}(t) = \left[\frac{A}{2}\cos(2\pi t/T_{2\pi} + B)\exp-(t/\tau)\right] + C,$$

with the oscillation period $T_{2\pi}$ = 4.78(2) μs, the amplitude $A = 1.03(2)$, the offset $C = 0.50(1)$, the phase B = -0.32(4) and the decay time τ =18(1) μs. The main reason for the decay of the Rabi oscillations is off-resonant excitation of the upper Raman state $|3\rangle$, which has an intrinsic lifetime of only 7.7 ns. Due to the detuning of 1.56 GHz and typical Rabi times on the order of (2π)50 MHz the excitation probability $(\Omega/2\Delta)^2$ of the upper state is on the order of 10^{-4}, which decreases the effective lifetime. Further increasing of the detuning Δ would lower the excitation probability of state $|3\rangle$ and therefore enhance the coherence time.

---

[35] Please note that the AOMs used to shift the π- and σ_+-laser beam frequency are in double pass configuration. Therefore, the shift of the π-beam AOM is 5.15 MHz with respect to the σ_+ AOM (80 MHz).

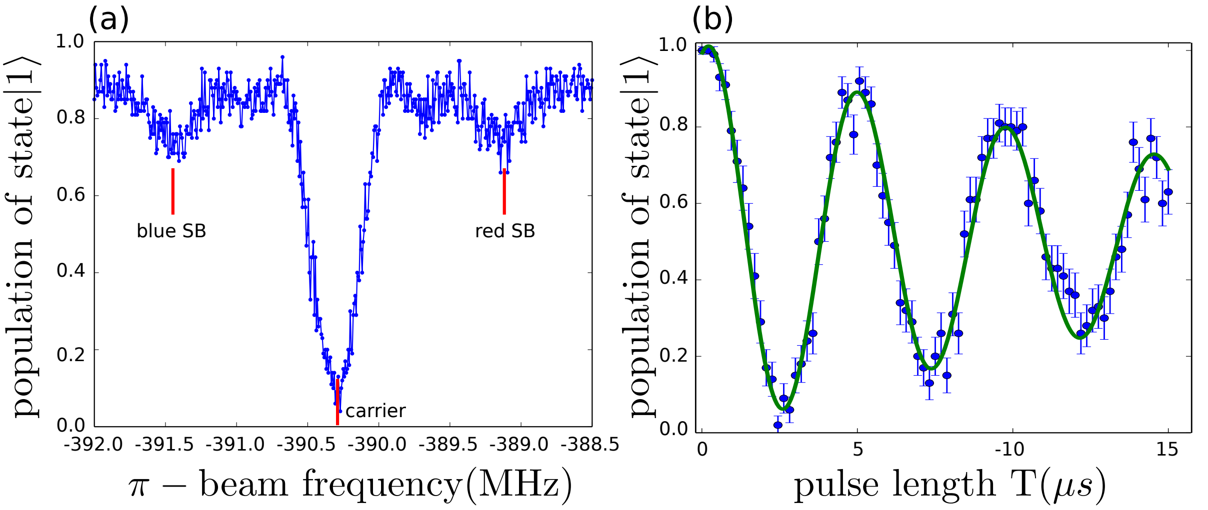

Figure 3.29: Coherent Raman operation: Measurement of the Raman spectrum (a) and coherent Rabi oscillations on the Raman transition (b) of a single ion. The spectrum was measured by scanning the relative frequency of the two Raman beams and measuring the population of state $|1\rangle$. The center frequency as well as the red and blue sidebands are indicated by the red lines. By setting the frequency resonant to the Raman transition, coherent Rabi oscillations were realized. The effective Rabi frequency Ω_{eff} and the decay time τ were obtained from the sinusoidal regression function (green curve) and lead to $\Omega_{eff} = (2\pi)209.2$ kHz and τ =18(1) μs. Both measurements were performed with a detuning $\Delta = 1.56$ GHz.

3.7.3 Raman sideband cooling

Within this section, the measurement of the characteristic cooling parameters, as the cooling rate R and the mean phonon number $\bar{n}$ are presented. Additionally, two methods used to obtain the mean phonon number are discussed. As already mentioned before, it was observed that the Raman spectrum is shifted depending on the power of the σ_+-laser beam. In the following section, the characterization of the effective ac-Stark shift is presented.

ac-Stark shift measurement

At the beginning of Sec.3.7, the Raman process was described in a pure three level system, which could be simplified to a two level system ($|1\rangle\,, |2\rangle$) coupled by the two Raman beams with an effective coupling strength Ω_{eff}. This point of view is not entirely true, since the upper $4^2P_{1/2}\,(m_j = -1/2) = |3'\rangle$ state was not considered. In the case of the three level system, the ground state splitting between the two residual Raman levels $|1\rangle$ and $|2\rangle$ is changed by light shifts depending on the intensity of the σ_+- and π-beam. Considering the present $4^2P_{1/2}\,(m_j = -1/2)$ state, the π-Raman beam drives not only the $|2\rangle \rightarrow |3\rangle$ transition but also the transition from $|1\rangle$ to $|3'\rangle$ (as shown in Fig. 3.30). This leads to the fact that the differential light shift is canceled, assuming that the Zeeman splitting of the two ground states ($\approx$10 MHz) is small compared to the detuning Δ $\geq$1.5 GHz. Therefore, the frequency difference of the two Raman levels is shifted only due to the coupling of the σ_+ laser field to the $|1\rangle \rightarrow |3\rangle$ transition. The differential light shift δ_{ac} is given by $\delta_{ac} = \frac{\Omega^2_{\sigma+}}{4\Delta}$ and depends on the intensity $I_{\sigma^+} \propto \Omega^2_{\sigma^+}$ of the σ_+ beam and the detuning Δ. The intensity fluctuations of the σ_+ laser beam

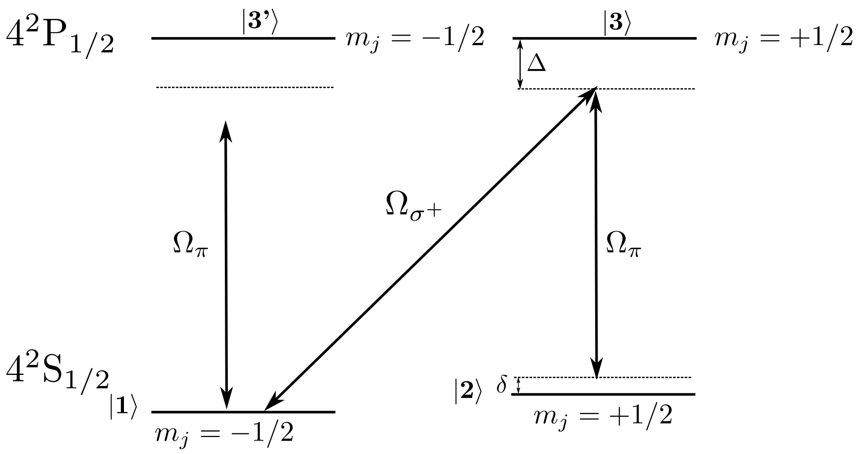

Figure 3.30: Complete Raman scheme: Schematic representation of the Raman level scheme including the $4^2P_{1/2}$ $(m_j = -1/2) = |3'\rangle$ state. In contrast to the three level system, coupling of the σ_+-beam to the $|1\rangle \to |3\rangle$ transition leads to an effective differential light shift between the two ground states, whereas the ac-Stark shifts induced by the π-beam is cancelled out assuming that the ground state Zeeman splitting is small compared to the detuning Δ.

were measured with a photodiode after the optical fiber to the experiment (see Fig. 3.26) and are on the level of 7% on a timescale of minutes, which dominantly results from polarization drifts in the optical fiber. For example with the parameters obtained from the decay measurements in Fig. 3.28, the expected light shift from the resonance is about 850 kHz and agrees with the value observed in the spectrum (see Fig. 3.29(a)). The ac-Stark shift was characterized

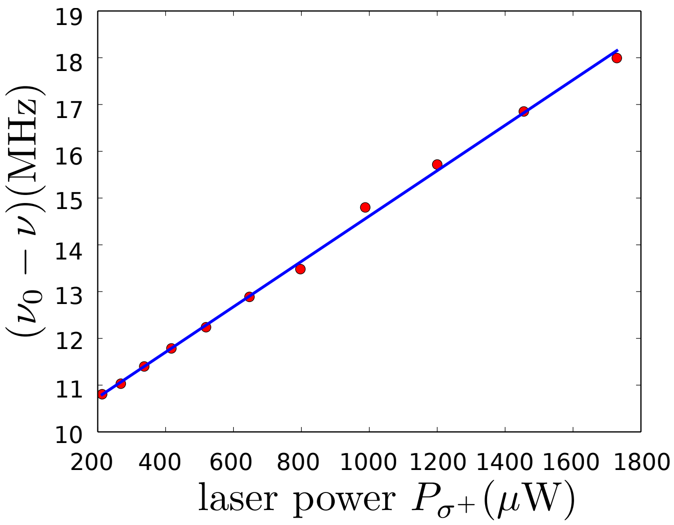

Figure 3.31: ac-Stark shift measurement: The relative shift with respect to the expected center frequency ν_0 as a function of the laser power $P_{\sigma+}$. The obtained sensitivity of the ac-Stark shift is about 5 kHz/μW.

by measuring the frequency shift of the carrier transition as a function of the σ_+ laser beam power. The difference of the fitted center frequency ν and the expected unperturbed carrier frequency at ν_0 = -389.610 MHz is plotted in Fig. 3.31 as a function of the optical power P_{σ^+}. The measurement result reveals a clear linear dependence between the induced ac-Stark shift and the optical power. The linear fit function in Fig. 3.31 results in a sensitivity (slope of the linear function) of about 5 kHz/μW. Fluctuations on the order of 7 % at an optical power of 500 μW lead to relative frequency fluctuations of about 175 kHz. The intensity fluctuations were actively compensated for with the sample and hold stabilization described above (see Fig. 3.26). Changing the power of the π-beam did not lead to any differential light shifts.

Raman sideband cooling - Experimental results

The scheme used for Raman sideband cooling is shown in Fig. 3.32. The three level system is defined by the two ground states $|1\rangle$, $|2\rangle$ and the upper state $|3\rangle$. The cooling process can be described in a similar way as the two-state sideband cooling process on the quadrupole transition. A detailed theoretical description is given in Ref. [78]. Consider the ion initially prepared in the ground state $|1\rangle$. The π beam is detuned red by the axial trap frequency $\delta = \omega_z$ from the Raman carrier (see Fig. 3.29) which leads to a population transfer from the $|1, n\rangle$ ground state to the $|2, n-1\rangle$ state. This Raman transition on the red-SB acts similar to the excitation process of the two-level sideband cooling process (see Fig. 3.24) with the effective Rabi frequency $\eta_R \Omega_{eff}$. Here, the Lamb-Dicke factor η_R for the Raman transition is given by $\eta_R = \frac{2\pi}{\lambda} |\Delta\vec{k}| x_0 cos(\alpha)$ and depends besides the wavelength and the ground-state wave packet expansion x_0 on the difference $\Delta\vec{k} = e_{\vec{k}1} - e_{\vec{k}2}$ between the wave vectors of the two Raman beams and the angle α between the vector $\Delta\vec{k}$ and the direction of the axial motional modes. Therefore, cooling of the axial mode is only possible if the effective k-vector difference $\Delta\vec{k}$ includes a projection along the motional mode and is maximized if the Raman beams are counter-propagating along

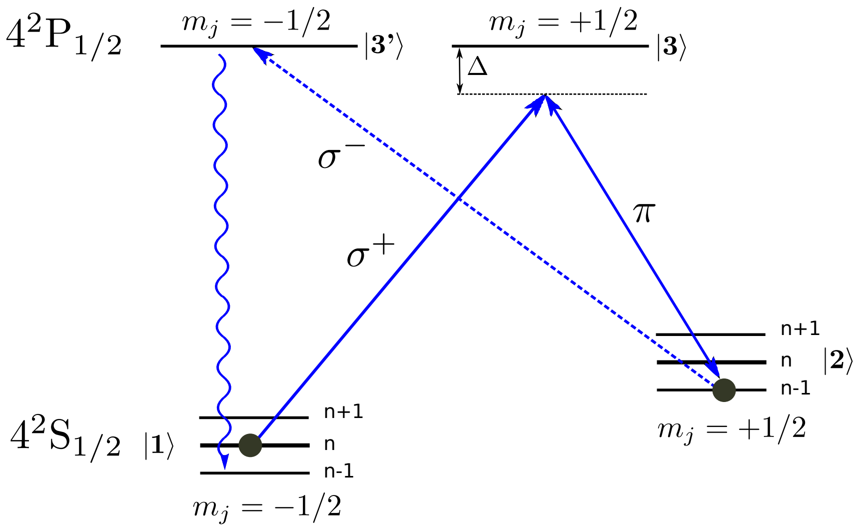

Figure 3.32: Three beam Raman cooling scheme: Schematic representation of the three beam Raman cooling scheme. Population from the $|1, n\rangle$ state is transferred by exciting the red SB Raman transition to the $|2, n-1\rangle$ state and simultaneously pumped back to the ground state $|1, n-1\rangle$ by the σ_- laser beam.

the motional mode direction. The population of the $|2, n-1\rangle$ state is pumped by a third σ_--polarized laser beam via the upper level $|3'\rangle$ back to the initial state $|1, n-1\rangle$, which closes the cooling cycle and can be compared to the decay of the two-level SB-cooling scheme. This Raman cooling process involves three laser beams (two Raman beams and one repump laser) and therefore is denoted as three-beam Raman cooling. The pulse sequence used for Raman SB-cooling is shown in Fig. 3.33. During the three-beam Raman cooling sequence both Raman beams as well as the 397 nm σ_- beam are switched on simultaneously within the cooling time T. Again, the 866 nm repump laser has to be on during the whole cooling process. After the Raman cooling sequence the σ_- beam is switched on for a short time interval of 50 μs to pump remaining population of the state $|2\rangle$ back to the initial state $|1\rangle$. The cooling performance can be analyzed by two different methods, denoted as A1 and A2 in Fig. 3.33 followed by detection. After repeating this sequence with the number of cycles (100-200) the σ_+ beam intensity stabilization is applied.

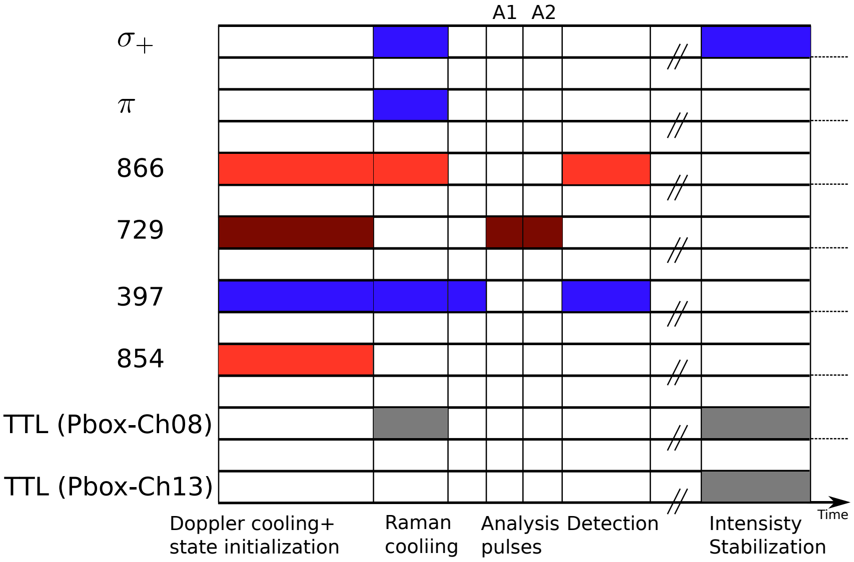

Figure 3.33: Raman cooling sequence: Schematic diagram of the pulse sequence used to realize the described Raman SB-cooling process. The main cooling part consists of simultaneously turning on the two Raman beams as well as the 397 nm σ_- laser beam. The two different analysis pulses A1 and A2 correspond to red- and blue SB pulses respectively and are used to measure the mean phonon number.

At the first stage, the performance of the Raman cooling sequence can be optimized by applying a red SB-pulse of about 800 μs on the qubit transition after the cooling step followed by detection. The closer the motional state of the ion to the ground state $|1, n=0\rangle$, the lower the excitation on the red SB. To quantify the mean phonon number $\bar{n}$, two different methods are introduced:

Excitation ratio:

A simple method for the determination of the mean phonon number is to measure the excitation when driving the red- and blue SB. It can be shown that the ratio of the red SB excitation p_{rsb}

to the excitation on the blue SB p_{bsb} is only dependent on the mean phonon number [73, 52]:

$$R = \frac{p_{rsb}}{p_{bsb}} = \frac{\bar{n}}{\bar{n}+1},$$

assuming that the same excitation length and power is used for each SB transition and off-resonant excitations are negligible. The ratio R can be extracted by scanning over the red- and blue resonance and revealing the excitation amplitudes of p_{rsb} and p_{bsb}.

Blue SB oscillations:

A more sensitive method, which was used in the presented work is to coherently excite the blue SB on the $4^2S_{1/2} \rightarrow 3^2D_{5/2}$ transition. The idea is that the coupling strength of the blue SB transition depends on the motional state. Therefore, the coherent dynamics corresponds to a superposition of Rabi oscillations with different Rabi frequencies $\Omega_{n,n+1}$. More detailed, the excitation probability p_{bsb} on the blue SB is given by [73, 52]:

$$p_{bsb}(t) = \sum_{n=0}^{\infty} \frac{\bar{n}^n}{(\bar{n}+1)^n} \frac{1}{2}\{1 - \cos(\Omega_{n,n+1}t)\}, \tag{3.24}$$

and depends on the phonon occupation probability of the n-th motional state $p(n) = \frac{\bar{n}^n}{(\bar{n}+1)^n}$ assuming a thermal distribution. The idea is to fit the excitation probability $p_{bsb}(t)$ with the mean phonon number $\bar{n}$ as free parameter. Fig. 3.34 shows a measurement of the mean phonon number $\bar{n}$ of the axial COM mode of a three ion crystal for different cooling times T. The measurement was performed with Raman SB-cooling (red squares) and two-level SB cooling on the qubit transition (blue stars) respectively. The mean phonon number was measured by Rabi oscillations on the blue SB of ion 1 out of three ions, as shown in the inset of Fig. 3.34. The population of the two remaining ions was spectroscopically decoupled in the $3^2D_{5/2}$ $(m_j = -5/2)$ state. The experimentally obtained oscillations on the blue SB with the corresponding fit result (green curve) at a cooling time of T= 200 μs leads to a mean phonon number of $\bar{n} \approx 0.44$. The result clearly shows the exponential decay behaviour of the cooling dynamics as expected by Equ. 3.19. A fit of Equ. 3.19 results in the characteristic cooling rate $R \approx 19$ μs for Raman SB-cooling and $R \approx 228$ μs for the two-level SB cooling. In case of the Raman cooling process, the minimal phonon number $\bar{n} \approx 0.44$ is achieved after a cooling time of T= 200 μs and for the two-level SB-cooling method the minimal phonon number is about 0.068 after a cooling time of 7 ms. Therefore, Raman SB-cooling allows us to cool a string of three ions to a mean phonon number of $\bar{n} = 0.44$ within 200 μs, which is sufficient for in-sequence cooling. The typically used cooling time in Ref. [76, 75] was about 200 μs for sympathetically cooling a three and five ion crystal via one ion.

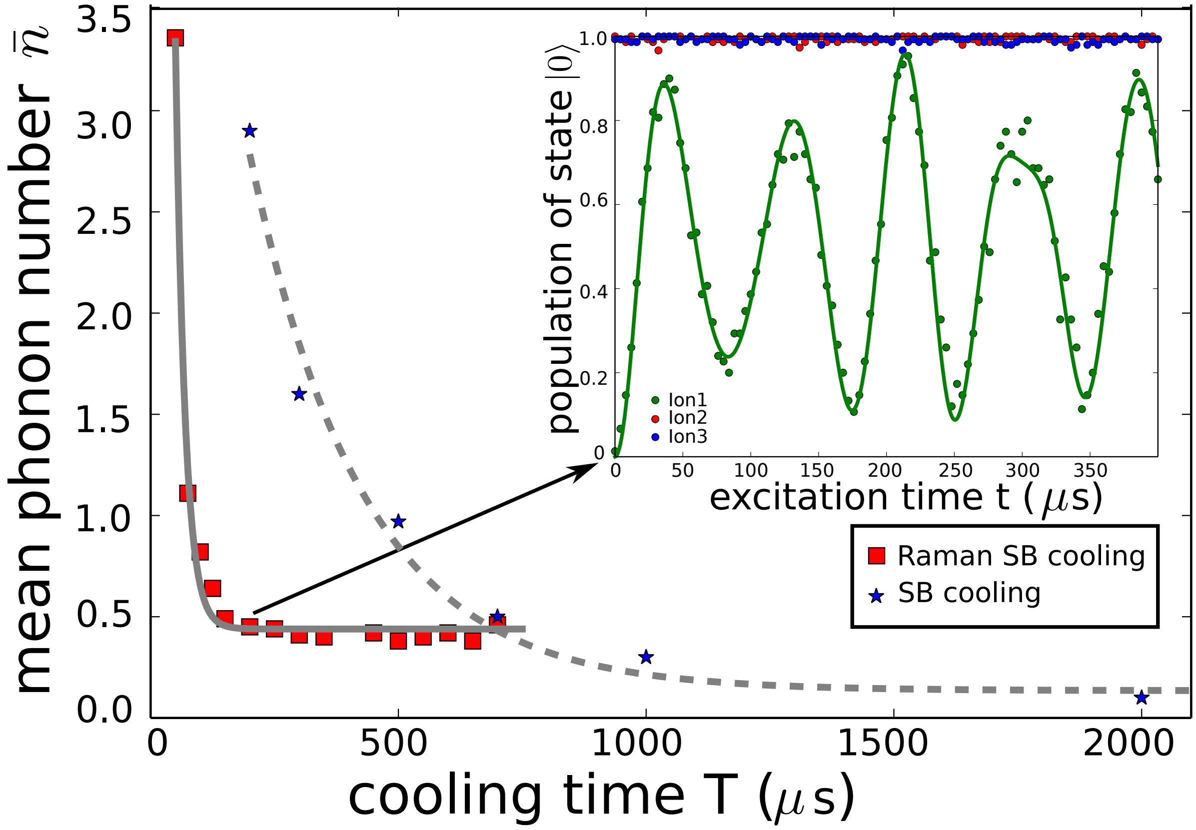

Figure 3.34: Raman SB-cooling: Experimental result of the mean phonon number $\bar{n}$ as a function of the cooling time T for the three beam Raman SB-cooling (red squares) and the two-level SB-cooling (blue stars). Using Raman cooling, a steady state phonon number of about 0.44 could be reached after T=200 μs, whereas SB-cooling via the quadrupole transition reaches a lower phonon number of about 0.07 after 7 ms. Both measurements were applied on one ion out of a three ion crystal. The inset figure demonstrates blue SB oscillations on ion 1 with the aim of revealing the mean phonon number $\bar{n}$ (see main text). The experimental parameters for the Raman cooling are $\Delta = 1.56$ GHz, $R^{\sigma+} \approx 110$ μs and $R^{\sigma+} \approx 292$ μs.

Chapter 4

Direct Characterization of Quantum Dynamics[1]

4.1 Introduction

Characterizing quantum dynamics is an important primitive in quantum physics, chemistry, and quantum information science for determining unknown environmental interactions, estimating Hamiltonian parameters, and verifying the performance of engineered quantum devices. This has led to a major effort in developing tools for the full characterization of quantum processes, known as quantum process tomography (QPT). As already pointed out in Sec. 2, the standard approach for QPT is resource intensive, requiring 12^N experimental configurations for a system of N qubits [21, 80], where each experimental configuration consists of the preparation of 4^N input probe states and a full state tomography for each of the imput states. An alternative method, ancilla assisted process tomography (AAPT), for the tomography of unknown quantum processes using additional qubits (ancilla qubits) was proposed in Refs. [81, 82]. As the name suggests, this method uses ancilla qubits but is restricted to joint separable measurements. Here, the number of experimental configurations is still 12^N [83, 81, 84]. The advantage of non entangled AAPT compared to the standard QPT (SQPT) is that only a single input state is required.

However, the use of many-body interactions to ancilla qubits in the preparation and/or measurements can significantly decrease the number of experimental configurations to anywhere from 4^N to a single configuration depending on the nature and complexity of quantum correlations [84]. Using two-body interactions only, DCQD (Direct Characterization of Quantum Dynamics) requires up to 4^N experimental configurations for full quantum process tomography. It is furthermore possible to estimate certain physical parameters with only one experimental setting. Examples are the characterisation of the relaxation times T_1 and T_2 [85, 86]. Prior experimental efforts in this direction include a partial implementation of DCQD [87, 88], an ancilla-assisted process tomography [81, 83]. Simultaneously to the presented work, an effort to efficiently implement DCQD in a photonic system [89] has been undertaken.

Alternatively, efficient gate-fidelity estimation methods such as randomized benchmark-

---

[1] Text paragraphs, pictures and data of the following chapter are based on the original work Ref. [79] and presented in a more detailed way.

ing [72], or tomographic methods such as selective and efficient QPT [90, 91] and compressed sensing for quantum process tomography [92–94] have been developed to overcome the exponential increase of the required experimental configurations. Generally, these methods are tailored to estimate a polynomial number of effective parameters, such as gate fidelities [72] or they require a priori knowledge about the quantum system to make a sparse quantum process/Hamiltonian assumption [94].

Within this chapter, the implementation of the DCQD technique and extensions in our system of trapped $^{40}\mathrm{Ca}^{+}$ ions is described in detail [79]. The experimental tomography of single-qubit processes with only four experimental configurations using DCQD, and alternatively with just a single configuration using a generalized measurement (GM) is demonstrated. In addition, we quantify the relaxation times T_1 and T_2 in our system with a single configuration. This technique can also characterize more realistic environments affecting not only the probe but also the ancilla qubit collectively.

The estimation of the dynamical parameters T_1 and T_2 (longitudinal and transverse relaxation times [21]) is a task involving two non-commuting observables (e.g. σ_x and σ_z) that cannot be measured simultaneously. These parameters describe the influence of noise on atomic-, molecular- and spin-based systems induced by the interaction with the environment. An alternative approach based on DCQD, henceforth called Direct Characterization of Relaxation Times (DCRT), enables the measurement of both T_1 and T_2 *simultaneously* with a single experimental configuration [95].

4.2 Direct characterization of quantum dynamics

Following the χ matrix representation of a quantum process, as introduced in Sec. 2, we consider only processes which can be described by a completely positive, linear and trace-preserving map E mapping the input state ρ onto the output state ρ'. For a single qubit this can be written as

$$E : \rho \rightarrow \rho' = \sum_{m,n=1}^{4} \chi_{m,n}\, \sigma_m\, \rho\, \sigma_n^{\dagger}, \tag{4.1}$$

with σ_m, σ_n being the Pauli operators $\{\mathbb{1}, \sigma_x, \sigma_y, \sigma_z\}$ and χ a positive Hermitian matrix containing the complete information about the process. In standard quantum process tomography the process is applied to all four input states and subsequently followed by full state tomography of each output state, which for a trace preserving map consists of three measurements, resulting in $4 \times 3 = 12$ experimental configurations.

In contrast, the DCQD method requires input states that entangle the system qubit S and the ancilla qubit A. The DCQD tomography technique is illustrated in Fig. 4.1(a). The unknown quantum process E is applied on the system qubit A and finally a single Bell state measurement (BSM), which is described in Sec. 2, is performed on the collective system (see Fig. 4.1(a)). The four different input states $\rho_i = |\psi_j\rangle\langle\psi_j|$ and the Bell state basis $|\Psi^{\pm}\rangle$ and $|\Phi^{\pm}\rangle$ are defined in Table 4.1 and in lead to $4 \times 1 = 4$ experimental configurations. According to Sec. 2 the probabilities $p_{i,j}$ of measuring the Bell-state projectors $P_i = \{|\Phi^{\pm}\rangle\langle\Phi^{\pm}|, |\Psi^{\pm}\rangle\langle\Psi^{\pm}|\}$ for each input state ρ_j are determined by the following relations [85, 96]:

$$\begin{aligned} p_{i,j} &= \mathrm{Tr}(P_i\, E(\rho_j)) = \sum_{m,n=1}^{4} \chi_{m,n}\, \Lambda^{i,j}_{m,n} \\ \text{with} \quad \Lambda^{i,j}_{m,n} &= \mathrm{Tr}(P_i(\sigma_m \otimes \mathbb{1})\rho_j(\sigma_n \otimes \mathbb{1})^\dagger). \end{aligned} \tag{4.2}$$

Equation 4.2 can also be written in a vector form:

$$\begin{bmatrix} p_{1,1} \\ p_{1,2} \\ \vdots \\ p_{4,4} \end{bmatrix} = \begin{pmatrix} \Lambda^{1,1}_{1,1} & \Lambda^{1,1}_{1,2} & \dots & \Lambda^{11}_{16,16} \\ \vdots & \vdots & \vdots & \vdots \\ \vdots & \vdots & \vdots & \vdots \\ \Lambda^{4,4}_{1,1} & \Lambda^{4,4}_{1,2} & \dots & \Lambda^{44}_{16,16} \end{pmatrix} \begin{bmatrix} \chi_{1,1} \\ \chi_{1,2} \\ \vdots \\ \chi_{4,4} \end{bmatrix}, \tag{4.3}$$

which is equivalent to the following equation:

$$\boldsymbol{p} = \boldsymbol{\Lambda}(\rho_i, P_j) \cdot \boldsymbol{\chi}, \tag{4.4}$$

with the vector $\boldsymbol{p}$ containing the measured probabilities $p_{i,j}$, the predefined 16x16 matrix $\boldsymbol{\Lambda}$ and $\boldsymbol{\chi}$, which is the process matrix in vector form. For a given set of input states and measurement operators the process vector $\boldsymbol{\chi}$ can be obtained directly by linear inversion of the matrix $\boldsymbol{\Lambda}$, yielding $\boldsymbol{\chi} = \boldsymbol{\Lambda}^{-1} \cdot \boldsymbol{p}$. The matrix $\boldsymbol{\Lambda}$ contains the information about the chosen measurement bases and input states. The set of input states ρ_j and the Bell-state projectors P_i have to be chosen such that the 16 equations in Eq. (2) are linearly independent, which ensures that $\boldsymbol{\Lambda}$ is invertible (Table 4.1). The invertibility of $\boldsymbol{\Lambda}$ is fulfilled if det($\boldsymbol{\Lambda}$) $\neq 0$.

Input states $\rho_j = \lvert\psi_j\rangle\langle\psi_j\rvert$	Bell-state basis
$\lvert\psi_1\rangle = \lvert 00\rangle + \lvert 11\rangle$	$\lvert\Phi^+\rangle = \lvert 00\rangle + \lvert 11\rangle$
$\lvert\psi_2\rangle = \alpha\lvert 00\rangle + \beta\lvert 11\rangle$	$\lvert\Psi^+\rangle = \lvert 01\rangle + i\lvert 10\rangle$
$\lvert\psi_3\rangle = \alpha\lvert ++\rangle_x - \beta\lvert --\rangle_x$	$\lvert\Psi^-\rangle = \lvert 01\rangle - i\lvert 10\rangle$
$\lvert\psi_4\rangle = \alpha\lvert ++\rangle_y - \beta\lvert --\rangle_y$	$\lvert\Phi^-\rangle = \lvert 00\rangle - \lvert 11\rangle$

Table 4.1: Input states and measurement basis: Input states and BSM basis used for the implementation of DCQD ($\lvert\pm\rangle_x = \frac{\lvert 0\rangle \pm \lvert 1\rangle}{\sqrt{2}}$, $\lvert\pm\rangle_y = \frac{\lvert 0\rangle \pm i\lvert 1\rangle}{\sqrt{2}}$). The determinant of Λ in Eq. (2) is maximized for $\alpha = \cos(\frac{3\pi}{8})$ and $\beta = \exp(i\frac{\pi}{2})\sin(\frac{3\pi}{8}))$ to ensure the invertibility [96]. The BSM is realized by a measurement with the projectors $P_i = \{\lvert\Phi^\pm\rangle\langle\Phi^\pm\rvert, \lvert\Psi^\pm\rangle\langle\Psi^\pm\rvert\}$.

The reconstruction method can be illustrated more intuitively by the following example: Assume the preparation of the input state $\rho_1 = \lvert\Phi^+\rangle\langle\Phi^+\rvert$ given in Table 4.1. If the process E corresponds to the identity $\mathbb{1}$ the output state $E(\rho_1) = \lvert\Phi^+\rangle\langle\Phi^+\rvert$ and therefore the expectation value of the BSM projector $P_1 = \lvert\Phi^+\rangle\, \langle\Phi^+\rvert$ is 1 which is equivalent to detecting both ions in the state $\lvert 11\rangle$ after the BSM in the basis $\lvert\Phi^+\rangle$ (see Sec. 2). In the case of the bit-flip process on qubit S the output state is mapped onto the state $\lvert 01\rangle$ by the BSM and therefore the probability of measuring the projector $P_2 = \lvert\Psi^+\rangle\, \langle\Psi^+\rvert$ is 1. The considerations are similar for a phase-flip, or bit- and phase-flip processes. Therefore, the diagonal elements of the process matrix $\chi_{i,i}$ corresponding to the $\mathbb{1}$, σ_x, σ_y, and σ_z process are obtained by the first input state ρ_1 in combination with one BSM, $\chi_{i,i} = \mathrm{Tr}(P_i\, E(\rho_1))$. The off-diagonal elements of the χ matrix are measured by the preparation of the three non-maximally entangled input states $(|\psi_2\rangle, |\psi_3\rangle, |\psi_4\rangle)$ followed again by one BSM [97]. The free parameters α and β of the three non-maximally input states (see Table 4.1) are determined by maximizing the determinant of $\mathbf{\Lambda}$. The realized parameters $(\alpha, \beta) = (\cos(\frac{3\pi}{8}), \exp(i\frac{\pi}{2})\sin(\frac{3\pi}{8}))$ lead to the maximum value det($\mathbf{\Lambda}$) = 1.

(a) DCQD - scheme

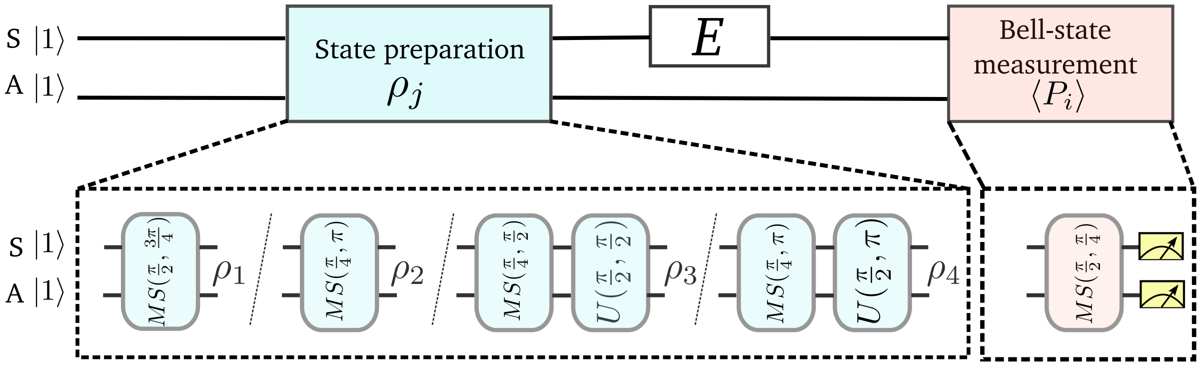

(b) GM - scheme

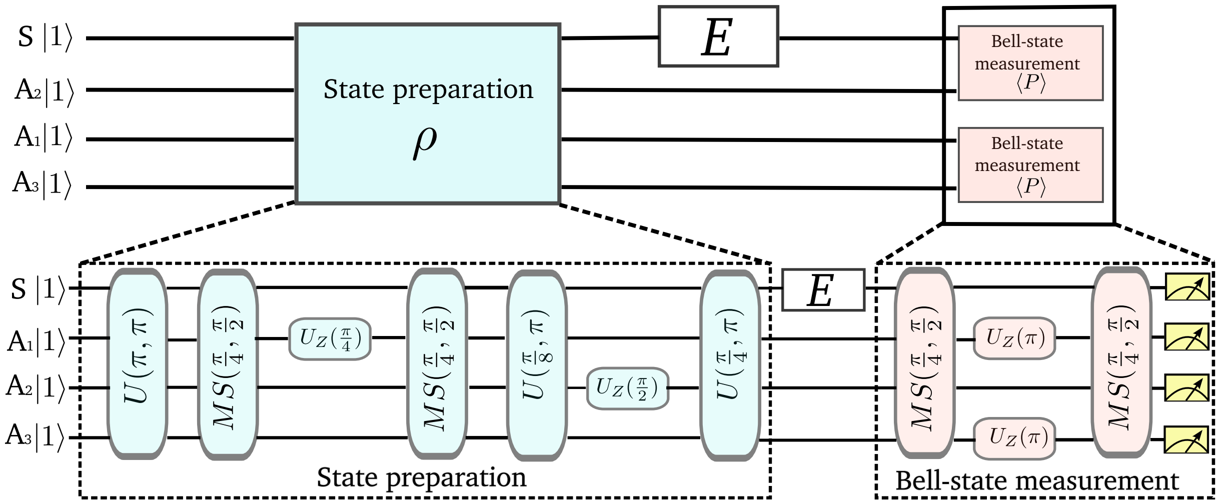

Figure 4.1: Schematics and pulse sequence for the DCQD- and GM-scheme: Procedure to characterize a single-qubit process with DCQD and a GM. In DCQD (a) each experimental configuration consists of the preparation of one of four input states ρ_j entangled between the system ion S and the ancilla ion A. The process E is applied on S followed by a BSM on the output state $E(\rho_j)$, which consists of a single MS operation followed by a projection onto the computational basis. (b) Generalized measurement via many body interactions (see text). (picture also shown in Ref. [79])

4.3 Generalized method

Full QPT of a single-qubit process is also possible with a single experimental configuration by using additional ancillas and a generalized measurement (GM). Here, we expand the dimension of the Hilbert space $H_A \otimes H_S$, with the system Hilbert space H_S and the ancilla Hilbert space H_A, such that the dimension of the total Hilbert space is equal to the number of free parameters in the process matrix χ [84]. For a single-qubit process one has to determine all 16 superoperator elements $\chi_{m,n}$ which leads to an 8-dimensional ancilla Hilbert space. Therefore we used three ancilla qubits A_1, A_2 and A_3 to quantify a full process E acting on the system qubit S. This GM is realized by entangling the system and ancilla qubits using many-body interactions [63, 98], then applying the process E on S and finally performing simultaneously a BSM on the pairs SA_2 and SA_{13}, which is illustrated in Fig. 4.1(b).

4.4 Experimental realization of DCQD

Our experiments were realized on a system consisting of $^{40}\text{Ca}^+$ ions confined to a string in a linear Paul trap [46]. A detailed description of the setup is presented in Chapter 3. The BSM is experimentally realized by a maximally entangling operation $MS(\frac{\pi}{2}, \frac{\pi}{4})$, which maps from the Bell-state basis to the computational basis $\{|00\rangle, |01\rangle, |10\rangle, |11\rangle\}$, followed by individual-ion-resolving fluorescence detection with a CCD camera [46]. We demonstrate the DCQD method by characterizing the full quantum process of the complete set of unitary rotations σ_x, σ_y and σ_z as well as controlled non-unitary processes such as amplitude- and phase-damping. For the complete quantum process tomography using DCQD it was considered that the process of interest only acts on the system qubit. To minimize the crosstalk between the ancilla qubit(s) and the system qubit S, all unitary operations were performed with the refocusing technique, described in Sec. 3.4.4. The controlled realization of phase- and amplitude damping on the system qubit S is described in detail in Appendix D.

Fig. 4.2(a,b) shows the reconstructed χ matrices for σ_x and σ_y rotations. As described in Chapter 2 a single-qubit process can also be visualized by transforming the ensemble of pure states on a Bloch sphere. In this Bloch sphere representation, decohering processes map the unit Bloch sphere (shown as a transparent mesh) to an ellipsoid of smaller volume [21]. Implemented amplitude- and phase-damping processes taking place with a 60% probability ($\gamma = 0.6$) are shown in this representation in Fig. 4.2(d,f). For each input state the experiment was repeated up to 250 times for statistical averaging. All processes were reconstructed with a maximum likelihood algorithm using the Choi-Jamiolkowski isomorphism as described in Chapter 2 to ensure trace preservation and positivity of the χ matrix [43]. The fidelity F of a process describes the overlap between the measured χ_{meas} and the ideal superoperator χ_{id}. According to the relation between a quantum process and the Choi-Jamiolkowski matrix, described in Chapter 2, the process fidelity is calculated by $F = \left(tr\left(\sqrt{\sqrt{S_{id}}S_{meas}\sqrt{S_{id}}}\right)\right)^2$ with the corresponding Choi-Jamiolkowski matrices S_{id} and S_{meas} obtained from the maximum likelihood algorithm [43, 99, 100]. Table 4.2 shows the estimated fidelities for the implemented DCQD and for SQPT. The uncertainty in the fidelity was estimated by parametric bootstrapping based on projection noise in our measurement [101](see Chapter. 2).

We also demonstrated the reconstruction of a full quantum process with a single experimental setting and 3 ancillas. Figure 4.1(b) shows the sequence to implement the GM method, which proceeds as follows. First, we create an entangled input state using maximally and non-maximally entangling Mølmer - Sørenson interactions in combination with global and addressed single-qubit rotations. After applying the process E on S we perform a pairwise

Target process	DCQD, F (%)	SQPT, F (%)
$\mathbb{1}$	97.5 ± 0.6	98.1 ± 1.3
σ_x	96.5 ± 1.0	98.1 ± 1.3
σ_y	96.6 ± 1.4	97.5 ± 1.4
amplitude damping	95.3 ± 1.9	95.2 ± 2.7
phase damping	97.4 ± 0.8	95.7 ± 0.8

Table 4.2: Measured single qubit processes: Calculated process fidelities F between implemented and target processes as characterized with DCQD and SQPT. All processes were measured with a total of 1000 experimental cycles, which correspond to 1000/4 cycles per experimental configuration for DCQD and 1000/(4×3)∼84 for SQPT. The SQPT of the phase damping process was measured with a total of 3000 experimental cycles.

BSM on the combined output state by implementing two non-maximally entangling operations $MS(\frac{\pi}{4})$ and two addressed AC-Stark pulses $U_Z^{(1)}(\pi)$ and $U_Z^{(3)}(\pi)$, which separate the entangled system $H(S, A_1, A_2, A_3)$ into a product state of two subsystems $H(A_1, A_3) \otimes H(S, A_2)$. These operations are equivalent to two pairwise maximally entangling gates $MS(\frac{\pi}{2})$ acting on the two subsystems $H(A_1, A_3)$ and $H(S, A_2)$. The 16 results of the measurement are directly linked to the 16 superoperator elements $\chi_{m,n}$ by a matrix Λ similar to Eq. (2). Using this technique we reconstructed unitary processes $\{\mathbb{1}, \sigma_x = U(\pi, 0), \sigma_y = U(\pi, \frac{\pi}{2}), \sigma_z = U_z^{(1)}(\pi)\}$ acting on a single qubit with a fidelity of $\{99.70 \pm 0.02, 97.30 \pm 0.29, 99.80 \pm 0.01, 99.40 \pm 0.02\}\%$. The process fidelities were obtained by comparing the ideal process with the measured one applied on experimentally created state (measured by full state tomography). All processes were measured with a total of 5000 samples.

The presented QPT measurements were characterizing engineered processes, but we are also able to characterize phase and amplitude damping that occurs naturally in our system due to laser-and magnetic field fluctuations and spontaneous decay [18, 46]. The dynamical parameters T_1 and T_2 can be determined simultaneously with only the first input state ρ_1 being subject to the DCQD scheme if the damping processes act collectively on both qubits (as in our experimental system [18]). This method, named DCRT above, consists of preparing the first input Bell state $\rho_1 = |\Phi^+\rangle\langle\Phi^+|$, exposing both qubits to the damping processes for time t and a final BSM, which yields the diagonal elements $\chi_{i,i}$ of the process matrix.

The dynamics is described by a global thermalization process acting on the entire system for the time t. The evolution of the density matrix is described by the two parameters T_2 and T_1 as discussed in Chapter 2. As described in Appendix C and assuming Markovian noise the dynamical parameters can then be estimated from:

$$\begin{aligned} e^{-\frac{N^2 t}{T_2}} &= \chi_{1,1} - \chi_{4,4} && (4.5) \\ &= \mathrm{Tr}\left\{\left[|\Phi^+\rangle\langle\Phi^+| - |\Phi^-\rangle\langle\Phi^-|\right] \mathrm{E}\left(|\Phi^+\rangle\langle\Phi^+|\right)\right\}, \\ 1 + 2e^{-\frac{2t}{T_1}} - 2e^{-\frac{t}{T_1}} &= 1 - 2(\chi_{2,2} + \chi_{3,3}), && (4.6) \end{aligned}$$

with N the number of ions. From the two equations it becomes obvious that the relaxation times T_2 and T_1 depend only on the digonal elements of the process matrix χ. In particular, T_2 only depends on $\chi_{1,1}$ and $\chi_{4,4}$, which corresponds to the probability that no error or phase

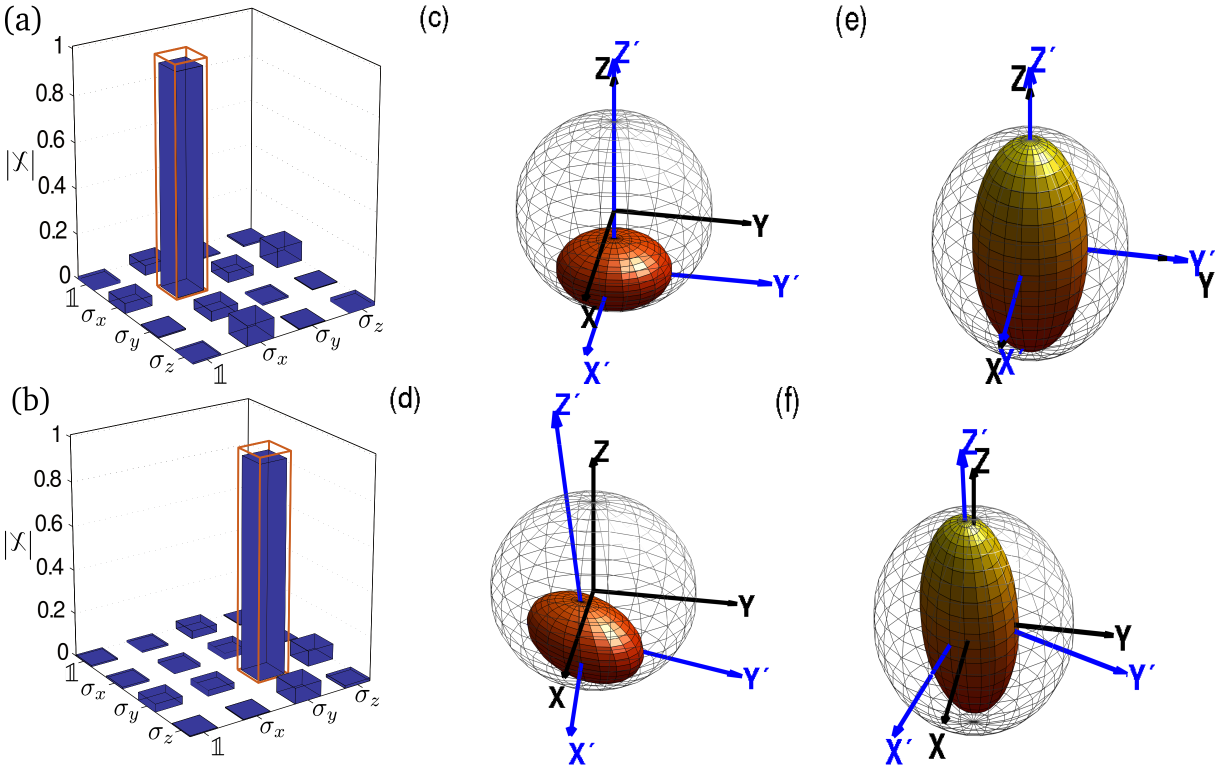

Figure 4.2: Representation of measured processes: Experimental results of DCQD for unitary and decoherence processes. (a-b) Results of the measured superoperator χ for the rotation operations $U(\pi, 0)$ in (a) and $U(\pi, \pi/2)$ in (b). Ideally, the target processes have only nonzero elements at positions indicated by the orange-bordered bars. (c-d) Bloch sphere representation of the ideal (c) and measured (d) amplitude damping process with 60% probability. (e-f) Bloch sphere representation of the ideal (e) and measured (f) phase damping process with 60% probability. Bloch sphere axes in black evolve into the spheroid primed axes in blue. A slight imperfection due to residual light on the ancilla ion can be observed as a rotation of the spheroids in the measured decohering processes.(picture also shown in Ref. [79])

flips occur on the entire system, whereas T_1 can be revealed from $\chi_{2,2}$ and $\chi_{3,3}$, corresponding to the occurrence of bit-flips. A fit of DCRT measurements $\chi_{i,i}$ to Eqns. (4.5-4.6) at different times t thus yields T_1 and T_2 using a single experimental configuration. We explored this DCRT technique in our experimental system. The measurement results of the decoherence estimation are shown in Fig. 4.3(a). The green dots show the difference between the diagonal elements $\chi_{1,1}$ and $\chi_{4,4}$ as a function of the waiting time t. The spontaneous decay of the system is shown in Fig. 4.3(b) by plotting $1 - 2(\chi_{2,2} + \chi_{3,3})$ as a function of time. For every waiting time t the experiment was repeated 250 times. The exponential fit (green line) of Eqn. (4.5) to the data was estimated with $N = 2$ (collective dephasing) and yields T_2^{DCRT}=18.8(5) ms.

We can compare the DCRT technique with two traditional methods that use product input states: Ramsey-contrast measurements for phase-decoherence estimation and direct spontaneous decay measurements if the timescales T_1 and T_2 are not similar [102]. The Ramsey-contrast measurement is realized by initializing the ion in the state $(|0\rangle + |1\rangle)/\sqrt{2}$ by a global rotation $U(\frac{\pi}{2}, 0)$, followed by a waiting time t and finally applying a second rotation $U(\frac{\pi}{2}, \phi)$ in which the phase ϕ is varied. The observed contrast as a function of ϕ corresponds to the remaining phase coherence. Spontaneous decay measurements, instead, consist of preparing both ions in the excited state $|0\rangle$ and measure its decay as a function of time. The results of these Ramsey-contrast (spontaneous-decay) measurements are shown in Fig. 4.3(a) (Fig. 4.3(b)) as red diamonds (blue triangles). The measured relaxation times corresponding to the traditional methods are called T_1^{trad} and T_2^{trad}. The Ramsey-contrast measurements (red diamonds) were carried out on a single ion and yield a coherence time of T_2^{trad}=19.4(8) ms. The green dotted line in Fig. 4.3(a) corresponds to the single-qubit coherence decay estimated from DCRT and shows good agreement with the single-ion Ramsey-contrast measurement. Therefore the DCRT technique enables the characterization of the phase decoherence of the collective system (green line) and also gives a conclusion about the phase decoherence of a single ion (green dotted line). An exponential fit of the decay data of Fig. 4.3(b) to Eq. (4.6) gives the characteristic lifetime $\mathrm{T}_1^{DCRT} = 1130(47)$ ms for the DCRT technique (green line) and $\mathrm{T}_1^{trad} = 1160(30)$ ms for the traditional method (blue dotted line), which are in good agreement with previously measured values [103] of 1148(18) ms.

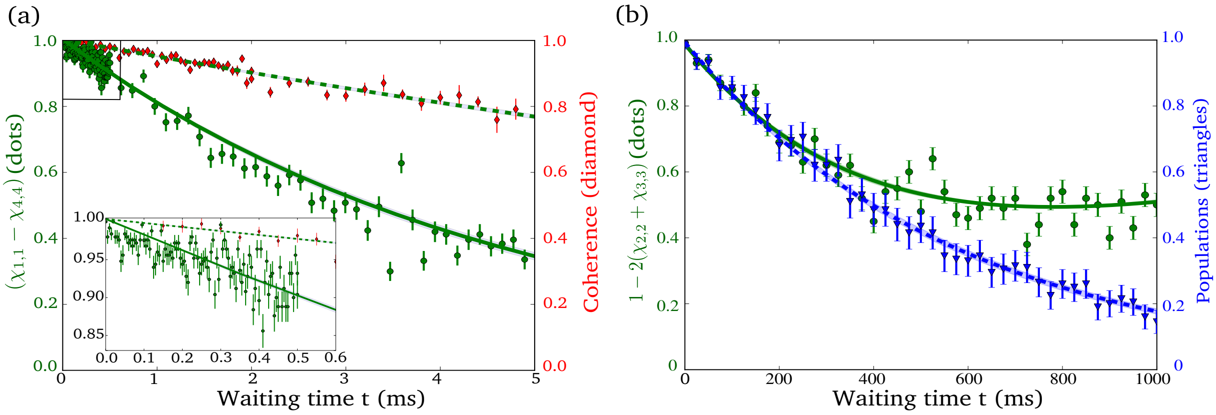

Figure 4.3: Measurement of the relaxation times: Simultaneous measurement of phase decoherence (a) and the spontaneous decay (b) of a two-qubit system. The DCRT technique (green dots) is compared to a Ramsey-contrast measurement (red diamonds) and a spontaneous decay measurement (blue triangles) (see text). The measurement using the DCRT method in (a) was carried out on the entangled two-qubit system ($\exp(-\frac{4t}{T_2^{DCRT}})$ scaling) whereas the red diamonds were measured on a single qubit with the Ramsey-contrast technique ($\exp(-\frac{t}{T_2^{trad}})$ scaling). The shaded areas correspond to the envelope of the curves with the decay times $T_{1,2}^{DCRT,trad} \pm \Delta T_{1,2}^{DCRT,trad}$, considering the statistical errors $\Delta T_{1,2}^{DCRT,trad}$. The relaxation time measurements, using the DCRT method and, in comparison, the traditional Ramsey-contrast and spontaneous decay measurement, yield: T_2^{DCRT}=18.8(5) ms, T_2^{trad}=19.4(8) ms, $\mathrm{T}_1^{DCRT} = 1130(47)$ ms and $\mathrm{T}_1^{trad} = 1160(30)$ ms. (picture also shown in Ref. [79])

In summary, we have experimentally demonstrated two different approaches for the full characterization of single-qubit quantum processes, lowering the required experimental configurations from 12 to 4 using DCQD and a single configuration via the GM method. The reconstruction of coherent and incoherent processes was shown with fidelities of $\geq 97\%$ using DCQD. In particular, we have observed a lower statistical uncertainty of the fidelity of some of the processes compared to the SQPT.

Experimentally, a reduced number of experimental configurations implies a substantial reduction of measurement time for a full QPT using DCQD as compared with SQPT. As supporting evidence in the reduction of measurement time of DCQD as compared with SQPT, let us consider, for example, the performed simulation with 6 qubits [104], where the simulation would be completely characterized by process tomography. The most important point to note is that in our laboratory the time it takes to change an experimental configuration is almost two orders of magnitude slower ($\approx$ 1 s) than that of one experimental cycle ($\approx$ 40 ms). To compare the performance of the two process tomography methods, we consider that for each method we use the same number of copies or instances of the process and call this the total number of cycles. If the time to change experimental configurations were zero, under this conditions, both methods would take the same time. However, this is not the case and we will distribute the total number of cycles among the required experimental configurations for each method. Therefore, the total number of cycles is equal to the number of cycles per experimental configuration times the required total number of experimental configurations.

The DCRT technique, based on the DCQD protocol, was used as a powerful tool to characterize the noise in our system by measuring the relaxation times T_1 and T_2 simultaneously with one experimental setting. This technique indicates good agreement with traditional methods as Ramsey-contrast and spontaneous decay measurement. In principle, there is an improvement of a factor of two in the measurement time if T_1 is of the same order of magnitude as T_2, which is not the case for our setup. In contrast, spin-based solid state systems are collectively affected by noise and $T_1 \approx T_2$, which would lead to a significant improvement of the measurement time [105]. Another application of DCRT could be for biological systems where dissipative dynamics play a crucial role [106, 107]. The same measurement procedure can also be used as a tool to quantify Hamiltonian parameters efficiently, which can not be realized with other currently known techniques besides full QPT [95, 86]. Furthermore, DCQD offers the capability to reveal the non-Markovian properties of system-bath interactions [86, 108].

Chapter 5

Characterization of spatial correlations

The evolution of a quantum system is inevitably affected by noise processes. Therefore, it is one of the main tasks for each quantum computer architecture to reveal the different noise sources and investigate tools to characterize such processes. In the following, we will discuss a method to quantify spatial correlations in noise acting on a quantum register. The encoding of quantum information using quantum error correction codes provide the possibility to perform arbitrary long quantum computation if the error threshold theorem is fulfilled - the error rate has to be lower than a certain value. Theoretical assumptions used to calculate the error threshold are mostly rather simple and based on spatially uncorrelated noise models, and Markovian noise (i.e. temporally uncorrelated noise) [21]. In practice this simplified assumptions are not fulfilled, which would strongly affect the error threshold. Fortunately, it has been proven theoretically in Ref. [109] that the concept of fault tolerant quantum computation and the calculation of an experimentally reasonable error threshold is still possible under spatial correlated noise if the noise is weak enough and the correlation length is short compared to the system size.

For the realization of fault tolerant quantum computation in any quantum architecture, the main questions will be: How strong are the spatial correlations for any quantum dynamics and how big is the correlation length compared to the separation of the qubits? If the qubit separation distance is bigger compared to the correlation length, then can the noise considered to be spatially uncorrelated? A method recently proposed by Angel Rivas and Markus Müller allows to quantify spatial correlations of quantum dynamical processes [36]. Within this chapter we demonstrate the experimental implementation of the proposed technique and show that this method can be employed as a useful toolbox to investigate spatial correlations.

5.1 Theoretical model

The model proposed in Ref. [36] provides a measure of the spatial correlations between two subsystems A and B of a larger system. The advantage of this method is that the measure does not depend on any a priori knowledge about the underlying dynamics. The general idea of the method is based on the Choi-Jamiolkowski isomorphism described in Sec. 2.2. The dynamics of the quantum system (e.g. a certain unitary operation or noise processes) can be described by the Choi-Jamiolkowski state ρ^{CJ} embedded in a higher dimensional Hilbert space. The correlation measure of the dynamics is then based on the quantum mutual information of the state ρ^{CJ}.

The introduced measure can already be motivated by the classical mutual information. Assume two random variables X and Y with the joint probability distribution $p(x, y)$. The mutual information of X and Y is given by the following equation [21]:

$$H(X : Y) = H(X) + H(Y) - H(X, Y) = \sum_{x,y} p(x, y) \log\left(\frac{p(x, y)}{p(x)p(y)}\right), \tag{5.1}$$

with the marginal entropies $H(X) = \sum_y p(x, y)$, $H(Y) = \sum_x p(x, y)$ and the joint entropy $H(X, Y) = \sum_{x,y} p(x, y) \log(p(x, y))$ following the definition of the Shannon entropy [21]. An intuitive picture is that the mutual information corresponds to the correlation between the two variables X and Y or in other words, how much information they have in common. It can be seen clearly that if the two variables X and Y are completely independent, which means that $p(x, y) = p(x)p(y)$, then the mutual information $H(X : Y) = 0$. The quantum mechanical analogon to the classical Shannon entropy is given by the Von Neumann entropy, whereas the density matrix corresponds to the probability distribution.

The Von Neumann entropy S of a quantum state ρ is given by the following expression:

$$S(\rho) = -\mathrm{tr}(\rho \log(\rho)) = -\sum_i \lambda_i \log(\lambda_i), \tag{5.2}$$

with λ_i the eigenvalues of ρ. Note that the entropy for an eigenvalue $\lambda_i = 0$ is given by $0 \log(0) = 0$, since $\lim_{n\to 0} n \log(n) = 0$. The quantum mechanical mutual information can be defined similar to the classical case using the Von Neumann entropy. Assume the joint Hilbert space $H_A \otimes H_B$ of the two subsystems A and B. The mutual information $I(\rho_{AB})$ of the quantum system is given by:

$$I(\rho_{AB}) = S(\rho_A) + S(\rho_B) - S(\rho_{AB}). \tag{5.3}$$

The marginal entropy of the subsystems A and B is defined by tracing over the corresponding system: $S(\rho_A) = \mathrm{tr}_B(\rho_{AB})$ and $S(\rho_B) = \mathrm{tr}_A(\rho_{AB})$. The mutual information of the quantum state ρ_{AB} is a measure of the correlations between the subsystems A and B. If the joint state can be written as a product state $\rho_{AB} = \rho_A \otimes \rho_B$, then the mutual information is 0.

The quantum dynamics can be directly linked to a quantum state by the Choi-Jamiolkwski isomorphism. Therefore the correlations of a quantum dynamical process correspond to the correlations of the Choi-Jamiolkowski state ρ^{CJ}, which can be quantified by the mutual information as defined above. Analog to the definition of the Choi-Jamiolkowski state introduced in Sec. 2.2 the quantum system S=AB is expanded by the ancillary system S'=A'B', as illustrated in Fig. 5.1. Further assume a maximally entangled state $|\psi_{SS'}\rangle$ between the system S' and S [36]:

$$|\psi_{SS'}\rangle = \frac{1}{d} \sum_{k,l=1}^{d} |k\rangle_A |l\rangle_B \otimes |k\rangle_{A'} |l\rangle_{B'}, \tag{5.4}$$

with the dimensions dim(H_A) = dim(H_B) = d. Please note that this state is equal to the product of the maximally entangled states between AA' and BB', which correspond to the Choi-Jamiolkowski states of the system AA' and BB'. The Choi-Jamiolkowski state ρ_S^{CJ} is realized

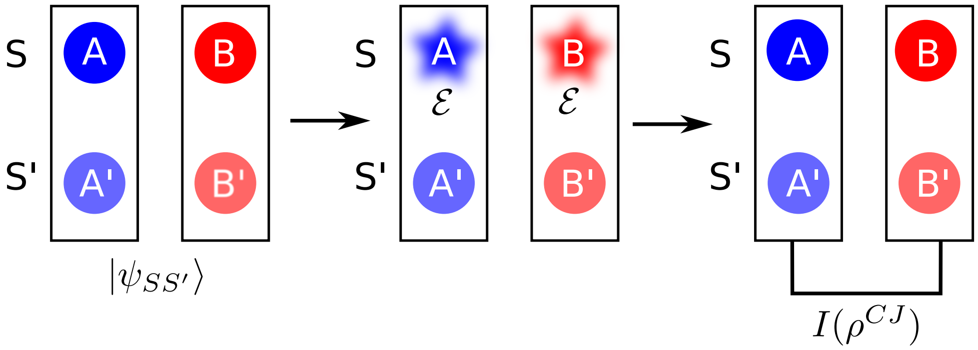

Figure 5.1: Schematics of quantifying spatial correlations: The characterization of the spatial correlations of a quantum process is based on the Choi-Jamiolkowski isomorphism. The system S is expanded by the ancillary system S' and a maximally entangled state $|\psi_{SS'}\rangle$ between the system S and S' is realized (left). The process of interest $\mathcal{E}_S$ is acting on the system S (middle). If the process is inducing correlations in the system S=AB, then the total system SS' becomes correlated with respect to AA' and BB', which is quantified by the mutual information of the Choi-Jamiolkowski state.

by applying the process $\mathcal{E}_S$ on the principle system S and the identity operation $\mathbb{1}_{S'}$ on the system A'B' (see Sec. 2.2):

$$\rho_S^{CJ} = \mathcal{E}_S \otimes \mathbb{1}_{S'}(|\psi_{SS'}\rangle\langle\psi_{SS'}|). \tag{5.5}$$

If the quantum map $\mathcal{E}_S$ introduces correlations between A and B the Choi-Jamiolkowski state ρ_S^{CJ} exhibits correlations with respect to the subsystems AA' and BB'. The amount of spatial correlations $\bar{I}(\mathcal{E}_S)$ of the quantum process $\mathcal{E}_S$ is defined by the quantum mutual information I of the state ρ_S^{CJ} [36]:

$$\bar{I}(\mathcal{E}_S) := \frac{1}{4\log(d)}\Big[S(\rho_S^{CJ})_{AA'} + S(\rho_S^{CJ})_{BB'} - S(\rho_S^{CJ})\Big]. \tag{5.6}$$

From the definition of the classical mutual correlations it was obvious that the correlations are 0 for independent probability distributions ($p(x,y) = p(x)p(y)$). The measure introduced for quantum maps can be interpreted similar to the classical counterpart. The introduced measure fulfills three important and necessary properties, which are proven in Ref. [36]:

- The quantity $\bar{I}(\mathcal{E}_S) \geq 0$. $\bar{I}(\mathcal{E}_S) = 0$ if and only if the process $\mathcal{E}_S$ is uncorrelated, which is fulfilled if $\mathcal{E}_S = \mathcal{E}_A \otimes \mathcal{E}_B$.
- In the framework of resource theory, one essential law for the useful measure of correlations is that the mutual information is not increased by composition with uncorrelated dynamical maps [21]. In Ref. [36] it is proven that this theorem is fulfilled for the introduced measure.
- The maximum value of $\bar{I}(\mathcal{E}_S) = 1$ can only be achieved if the quantum map $\mathcal{E}_S$ corresponds to a unitary operation $\mathcal{E}_S(\rho) = U_S \rho U_S^\dagger$ with $U_S U_S^\dagger = \mathbb{1}$.

An interesting example of the spatial correlations that arise between the systems A and B is the CNOT operation introduced in Chapter 2. Although the CNOT gate can be used to generate highly correlated entangled states the spatial correlation only reaches 0.5. A reason for this is that the creation of correlations induced by the CNOT operation depends on the input state of the system. For example the two qubit state $|0\rangle + |1\rangle \otimes |0\rangle$ is mapped onto a maximally entangled state $|00\rangle + |11\rangle$ by the CNOT operation, whereas the input state $|0\rangle + |1\rangle \otimes |0\rangle + |1\rangle$ is left unchanged. The SWAP operation is an example of a unitary map inducing the maximum amount of spatial correlations.

5.2 Spatial correlations in an ion-trap-based quantum computer

In this section we present an application of the described method to quantify spatial noise correlations to real noise dynamics. As a first test of the method, we investigated the spatial correlations of real-noise dynamics acting in our ion-trap based quantum system [46]. The quantum bit is encoded in the $S_{1/2}(m_j = -1/2)$ and $D_{5/2}(m_j = -1/2)$ Zeeman levels of $^{40}\text{Ca}^+$ ions. Therefore, frequency fluctuations of the laser which excites this qubit transition as well as magnetic field fluctuations at the position of the ions cause a loss of coherence. Since the magnetic field is de-facto constant over the spatial extension of the linear ion chain and coherent operations are performed in our setup with a global laser beam illuminating the whole ion chain simultaneously it is expected to induce noise that is strongly correlated in space. Here we investigate whether the degree of spatial correlations in our system can be quantified and verified by simulations or analytical calculations.

5.2.1 Quantum Process of a two-qubit system

Each dynamical process can be described by a complete positive and trace-preserving map $\mathcal{E}$ acting on a system S with initial state ρ_S. The output state $\mathcal{E}(\rho_\text{S})$ for a single qubit process can be written in the following form [21]:

$$\mathcal{E}(\rho_\text{S}) = \sum_{i,j=1}^{d^2} \chi_{i,j} \sigma_i \rho_\text{S} \sigma_j^\dagger, \tag{5.7}$$

with $\{\sigma_0 = \mathbb{1}, \sigma_1 = \sigma_x, \sigma_2 = \sigma_y, \sigma_3 = \sigma_z\}$ the set of Pauli operators and $d = \dim(\mathcal{H}_\text{A}) = \dim(\mathcal{H}_\text{B}) = 2$. Thus, the $d^2 \otimes d^2$ dimensional matrix χ contains the whole information about the process for a given basis. Similarly, in the case of a two-qubit process the output state can be written in the same form:

$$\mathcal{E}(\rho_\text{S}) = \sum_{i,j=1}^{d^4} \chi_{i,j} (\sigma_i \otimes \sigma_j) \rho_\text{S} (\sigma_i \otimes \sigma_j)^\dagger. \tag{5.8}$$

In the framework of standard process tomography, the evaluation of the full process matrix χ requires 12^N measurements settings (with N the number of qubits) [21]. For example in the case of a two-qubit process tomography 16 different input states are required, followed by implementing the (unknown) quantum process and finally performing a full state tomography (9 measurement settings) for each input state. Similar to the reconstruction of quantum states (quantum state tomography) it has to be guaranteed that the evaluated process matrix is physical, i.e. fulfills complete positivity and trace preservation. The most commonly used method for the reconstruction of quantum states is the Maximum Likelihood (ML) reconstruction method proposed in Ref. [45]. By mapping the quantum process onto a higher dimensional state ρ^{CJ} via the Choi-Jamiolkowski isomorphism, all techniques available for the reconstruction of a quantum state can be applied in a one-to-one manner to the state ρ^{CJ}.

The Choi-Jamiolkowski isomorphism is outlined at the example of a process tomography of a two-qubit system $\mathrm{S} = \mathrm{AB}$. An additional auxiliary system $\mathrm{S}' = \mathrm{A}'\mathrm{B}'$ of the same dimension is added to S and the combined system is initialized in the maximally entangled state $|\Phi_{\mathrm{SS}'}\rangle$:

$$
\begin{aligned}
|\Phi_{\mathrm{SS}'}\rangle &= 1/d \sum_{k,l=1}^{2} |kl\rangle_{\mathrm{AB}} \otimes |kl\rangle_{\mathrm{A}'\mathrm{B}'} && (5.9)\\
&= 1/2\{|1_{\mathrm{A}}1_{\mathrm{B}}1_{\mathrm{A}'}1_{\mathrm{B}'}\rangle + |1_{\mathrm{A}}0_{\mathrm{B}}1_{\mathrm{A}'}0_{\mathrm{B}'}\rangle + |0_{\mathrm{A}}1_{\mathrm{B}}0_{\mathrm{A}'}1_{\mathrm{B}'}\rangle + |0_{\mathrm{A}}0_{\mathrm{B}}0_{\mathrm{A}'}0_{\mathrm{B}'}\rangle\}. && (5.10)
\end{aligned}
$$

Then, the actual physical map $\mathcal{E}$ applied to the system S, the identity operation $\mathbb{1}_{\mathrm{S}'}$ on the mathematical auxiliary system S' leading to the d^4-dimensional Choi-Jamiolkowski state ρ^{CJ}:

$$
\rho_{\mathrm{S}}^{\mathrm{CJ}} = \mathcal{E} \otimes \mathbb{1}(|\Phi_{\mathrm{SS}'}\rangle\langle\Phi_{\mathrm{SS}'}|). \tag{5.11}
$$

This state contains the entire information about the dynamical process $\mathcal{E}$. Finally, the amount of spatial correlations $\bar{I}$ of the quantum process can be calculated directly from ρ^{CJ}, as described in Sec. 5.1.

5.2.2 Measurement of spatial correlations of real noise

The experimental characterization of the spatial correlations of real noise in our system has been carried out by the following procedure (see inset of Fig. 5.2): In between the preparation of the required input states for the process tomography and the state tomography pulses, a waiting time T was included. During the waiting time, the initially prepared state is prone to dephasing increasing with the waiting time T. Therefore, given that the noise - as argued above - is expected to act in a spatially correlated way, an increase of the mutual correlation measure $\bar{I}$ as a function of the waiting time T is expected. In Fig. 5.2(a) the experimentally determined spatial correlation measure $\bar{I}$ is plotted for different waiting times T. The data shows that the spatial correlations increase rapidly with increasing waiting time, and converge to a certain value for longer waiting times. Averaging of the correlations for $T \geq 40$ ms leads to an estimation of this saturation value around 11.5% ($\bar{I} = 0.115$). In order to obtain further understanding of this temporal behavior we numerically simulated the measurements, and derived an analytical solution within a simple model.

For the simulation of a perfectly correlated phase damping process on the two-qubit system we assume a random phase-kick process with equal strength on both qubits. This process can be written as

$$
\mathcal{E}(\rho) = \int_{-\infty}^{\infty} f(\theta,\sigma)U(\theta)\rho U^{\dagger}(\theta)d\theta, \tag{5.12}
$$

where $U(\theta)$ corresponds to a σ_z rotation on the whole system with a rotation angle θ, and where $f(\theta, \sigma)$ represents the probability distribution of θ. Since the spatial correlation measure $\bar{I}$ is calculated from the Choi-Jamiolkowski state, we write the expression in the operator-sum representation:

$$\begin{aligned} \mathcal{E}(\rho) &= \int_{-\infty}^{\infty} f(\theta,\sigma)\big[\sum_{i,j}\chi_{i,j}(\theta)(\sigma_i\otimes\sigma_j)\rho(\sigma_i\otimes\sigma_j)^\dagger\big]d\theta = \\ &= \sum_{i,j}\int_{-\infty}^{\infty} f(\theta,\sigma)\chi_{i,j}(\theta)(\sigma_i\otimes\sigma_j)\rho(\sigma_i\otimes\sigma_j)^\dagger. \end{aligned} \tag{5.13}$$

It can be shown that the χ-matrix describing this process contains in total 16 nonzero elements. If one furthermore assumes a noise probability distribution $f(\theta, \sigma)$ with an even parity, which implies that $f(\theta, \sigma) = f(-\theta, \sigma)$ the number of nonzero elements reduces to 8, which can be characterized by 3 parameters

$$\begin{aligned} \chi'_{(0,0,0,0)} &\equiv C_c, \\ -\chi'_{(0,0,3,3)} = \chi'_{(0,3,0,3)} = \chi'_{(0,3,3,0)} = \chi'_{(3,0,0,3)} = \chi'_{(3,0,3,0)} = -\chi'_{(3,3,0,0)} &\equiv C_{sc}, \\ \chi'_{3,3,3,3)} &\equiv C_s, \end{aligned}$$

with $[C_c, C_s, C_{sc}]$ defined as

$$\begin{aligned} C_c &= \int_{-\infty}^{\infty} f(\theta,\sigma)\cos(\theta/2)^4 d\theta \\ C_s &= \int_{-\infty}^{\infty} f(\theta,\sigma)\sin(\theta/2)^4 d\theta \\ C_{sc} &= \int_{-\infty}^{\infty} f(\theta,\sigma)\sin(\theta/2)^2\cos(\theta/2)^2 d\theta. \end{aligned}$$

In the case of a Gaussian spectral noise density $f_{\text{Gauss}}(\theta, \sigma)$ of the rotation angle θ:

$$f_{\text{Gauss}}(\theta,\sigma) = \frac{1}{\sqrt{2\pi}\sigma}e^{-\frac{\theta^2}{2\sigma^2}}, \tag{5.14}$$

the parameter σ corresponds to the width of the Gaussian curve and determines the dephasing probability. For a value of $\sigma = \pi$ rad, 95% of the rotation angle θ is within the interval $[-\pi, \pi]$ and therefore corresponds already to complete dephasing [1]. The integrals can be readily solved analytically, yielding

$$\begin{aligned} C_c &= 1/8[3 + e^{-2\sigma^2} + 4e^{-\sigma^2/2}] \\ C_s &= 1/8[3 + e^{-2\sigma^2} - 4e^{-\sigma^2/2}] \\ C_{sc} &= 1/8[1 - e^{-2\sigma^2}] \end{aligned}$$

Fig. 5.2(b) shows the results of the numerical simulation of the spatial correlation for the Gaussian noise probability distribution f_{Gauss} as a function of the width σ. In comparison, the

---

[1] The unitary operation $U(\theta = \pi)$ corresponds to a phase-flip on the entire system

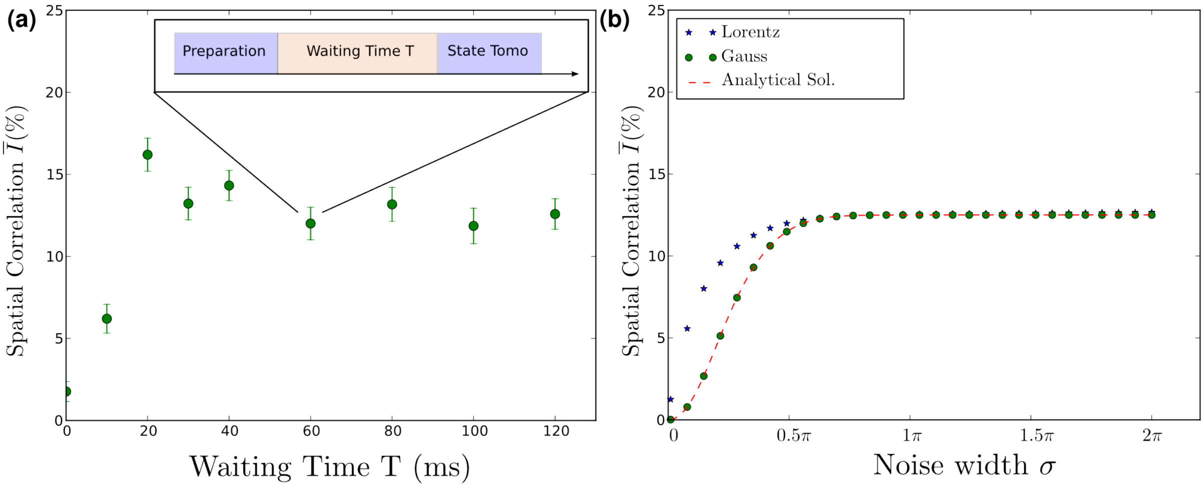

Figure 5.2: Measured and simulated spatial correaltions for real noise dynamics: (a) Measurement of the spatial correlation of a dephasing process caused by laser- and magnetic field fluctuations. (b) Simulation of the experimental data for a Gaussian (blue stars) and Lorentzian (green dots) noise probability distributions as well as a analytically derived solution for the spatial correlations for comparison (red dotted curve).

same simulation was performed assuming a Lorentzian noise probability distribution $f_{\text{Lorentz}} = \frac{1}{\pi}\frac{\sigma}{\theta^2+\sigma^2}$ (blue stars). It can be seen that the numerical simulation with the Gaussian noise distribution is in agreement with the measured data in Fig. 5.2(a). In Fig. 5.2(b) the correlations level out exactly at a value of 12.5% (resulting from the analytical solution for long waiting times, $C_c = C_s = 3/8$ and $C_{sc} = 1/8$ for $\sigma \to \infty$), which is within our experimental accuracy in agreement with the experimental result. For smaller timescales the initial increase of the correlations depends on the intrinsic noise probability distribution of the particular physical system, whereas the saturation value is independent of the noise distribution and only originates from the fact that the phase noise is perfectly correlated. The experimentally obtained data in Fig. 5.2(a) and the simulations in Fig. 5.2(b) are not plotted in the same graph, since the relation between T and the parameter σ has to be evaluated. For the characteristic behavior of the spatial correlations in our system and the validation of the noise model, the relation between the two parameters is not important. Fig. 5.3 shows the analytical solution and the experimentally obtained χ-matrix for a waiting time T $=$ 100 ms. The agreement provides further evidence that on the experimentally explored time scales the dominant noise in our system is correlated phase-noise.

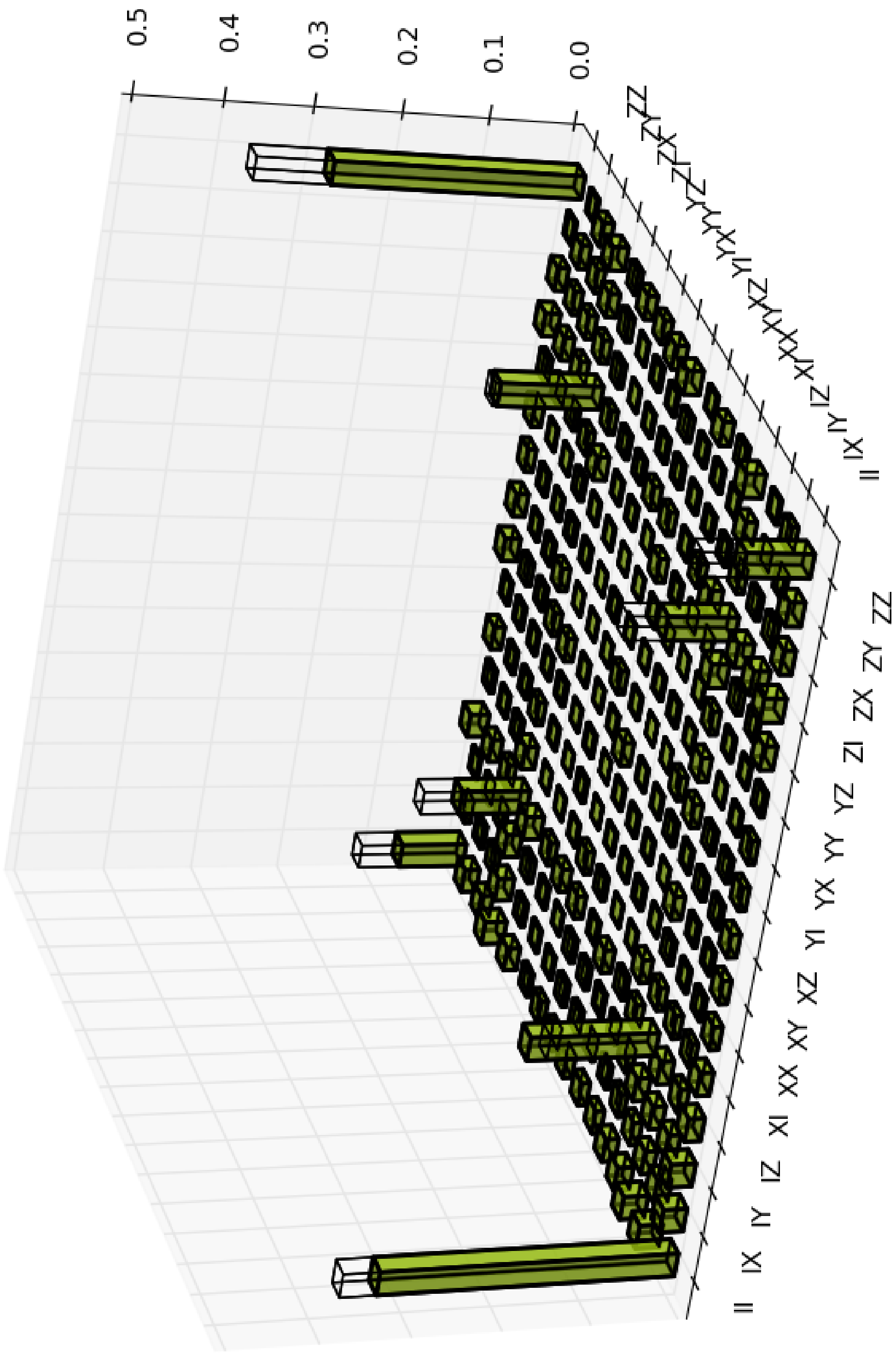

Figure 5.3: Measured process matrix in comparison with the simulated noise process: Measured two-qubit process matrix for a waiting time of $T = 100$ ms (green bar). The agreement with the analytical χ-matrix (black frame) confirms the fact that the real noise in our system is dominantly given by correlated phase noise.

Chapter 6

Quantum computations on a topologically encoded qubit

Within this chapter, the fundamental ingredient for the realization of a quantum computing device - *quantum error correction* (QEC) - is discussed. The basic elements of quantum error correction are summarized in the first section with the emphasis on the stabilizer formalism of QEC codes including the properties of Calderbank, Shor, Steane (CSS) codes. In the second section, the fundamental concept of *fault tolerant quantum computation* (FTQC) is introduced. The subsequent section is providing a detailed introduction to the field of topological QEC codes within the framework of FTQC. Furthermore, the Kitaev toric code as the first topological QEC code is described to give an introduction to the basic elements of topological QEC codes. At the end of the chapter, the so called tolopological color-codes and some of their central properties are introduced as well as the experimental implementation of a minimal two-dimensional color code in our ion trap based quantum computer is provided.

6.1 Quantum error correction

6.1.1 Introduction

The concept of error correction was invented within the broad field of classical computation. For example think about a classical bit 0 or 1, which is sent from the sender to the receiver through some channel (cable, radio waves, glass fiber, ...). In principle, the classical channel can be noisy and cause errors affecting the transmitted information, the bit. In classical information the typical error is a bit-flip error 0→1 (1→0). The reliable transmission of information is only possible if the corrupted bits are detected and corrected before further processing. The main method to address this task is based on *redundancy*. The main idea is to copy each information bit several times and send the whole information through the noisy channel. The receiver sees a series of bits and performs in the simplest case a *majority voting*. Assume the information bit initially was 0. Then the first step (encoding step) is to create a copy of the information bit 0→000 [1]. Note that using three bits for the encoding step is the simplest possible case. The bit string is sent through the channel, which might cause a flip on one of the three bits, say

---

[1] If the information bit is in 1, then the encoding is similar 1→111

e.g. the second bit. Therefore the information at the receiver will be 010. The receiver has to decide which bit was flipped by the majority voting. Since the majority is 0, the receiver would guess that the original information bit was 0 and if necessary correct the error. This code is also known as the *repetition code*. Now assume that two bit-flip events occurred, leading to the bit string 110. The result after the majority voting would be 111, which finally would cause an error and therefore the method did fail. It becomes apparent that the method is failing if two or more bit-flip errors occur. In the case of an independent and equal strength single bit-flip error probability p, the failure probability p_f of the code is given by the probability of two and three bit-flip errors $p_f = 3p^2(1-p)+p^3$ [2]. Without encoding and correction the error probability is p and therefore the error correction code makes the transmission more reliable if $p_f < p$, which is satisfied if $p < 0.5$. Therefore the classical error correction procedure works only if the single bit-flip error probability is below a certain value. Using more bits in the encoding will make the error correction code more robust.

It is certainly the case that each quantum information architecture is prone to errors affecting the quantum states (e.g. due to decoherence, faulty operations, preparation and measurements). The errors affecting a quantum system are more complex compared to the classical bit-flip error. Besides bit-flip errors mapping the state $|0\rangle \rightarrow |1\rangle$ ($|1\rangle \rightarrow |0\rangle$) we also have to consider phase-flip errors $|0\rangle \rightarrow |0\rangle$ ($|1\rangle \rightarrow -|1\rangle$), which are not possible in classical computation. This implies that reliable quantum information processing will only be realizable with the investigation of quantum error correction codes. The question arises if the described classical error correction method can be directly converted to quantum systems. Note that the principle of the classical repetition code is to make several copies of the bit. Assume that there exists any operation which generates a copy of the state $|\psi\rangle$ and $|\phi\rangle$: $|\psi\rangle \rightarrow |\psi\rangle \otimes |\psi\rangle$ and $|\phi\rangle \rightarrow |\phi\rangle \otimes |\phi\rangle$. The operation applied to the superposition of the two states leads to $|\psi\rangle + |\phi\rangle \rightarrow |\psi\rangle + |\phi\rangle \otimes |\psi\rangle + |\phi\rangle$. Due to the linearity of quantum mechanics, this has to be equal to $|\psi\rangle + |\phi\rangle \rightarrow |\psi\rangle\,|\psi\rangle + |\phi\rangle\,|\phi\rangle$, which is not fulfilled for arbitrary states $|\phi\rangle$ and $|\psi\rangle$. This simple example is a proof of the *no-cloning theorem*, indicating that there exists no code which is able to perfectly copy an arbitrary quantum state [24]. Nevertheless, there exists a possibility to avoid the obstacle of copying the quantum state by distributing the information over a larger quantum register using entanglement. The first pioneering work towards the realization of a quantum error correction code was accomplished by Peter Shor in 1995 with the nine-qubit Shor code [110]. Before we describe the Shor code in more detail, let us consider the simplest QEC codes, the three-qubit bit-flip and phase-flip code, which form the basic elements of the Shor code. Assume a general quantum state $|\psi\rangle = \alpha\,|0\rangle + \beta\,|1\rangle$ with $|\alpha|^2 + |\beta|^2 = 1$. The goal of the three-qubit bit-flip code is to protect the coherent state $|\psi\rangle$ against a bit-flip error. This code can be interpreted as the quantum version of the classical repetition code and is shown in Fig. 6.1.

The first encoding step of the bit-flip code consists of two CNOT operations on the qubit pairs q1q2 and q1q3. The state after the encoding step is given by:

$$\alpha\,|0\rangle + \beta\,|1\rangle \rightarrow \alpha\,|000\rangle + \beta\,|111\rangle := \alpha\,|0\rangle_L + \beta\,|1\rangle_L\,. \tag{6.1}$$

The two states $|0\rangle_L$ and $|1\rangle_L$ are called the *codeword basis states*. The state space, which is spanned by the superposition of the two codeword basis states is called the *code space* and

---

[2] Here, the assumption of independent and equal strength bit-flip errors was made. In general, each error correction code (classical or quantum) assumes a certain error noise model and is designed to tackle errors according to the specific noise model.

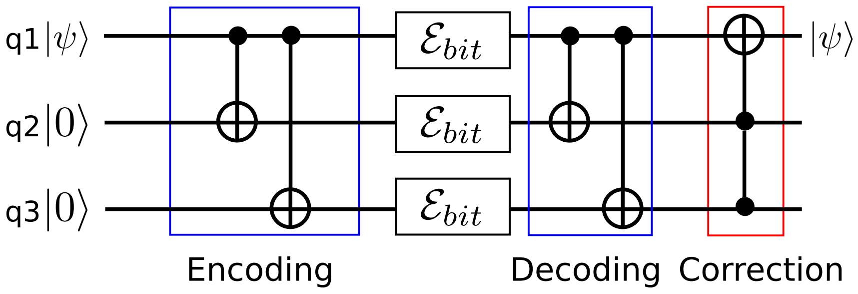

Figure 6.1: Three qubit repetition code: The schematic of the simplest QEC code able to correct single bit-flip errors. Here, the information of a single qubit q1 is distributed over three qubits by generating a highly entangled state $|\psi\rangle_L$ (encoding). After the decoding step, the state of the two qubits q1 and q2 is $|00\rangle$ if no error occurred on q1 and $|11\rangle$ if q1 was affected by a bit-flip error. In the latter case, the CCNOT (Toffoli) operation corrects the bit-flip error.

the state $|\psi\rangle_L = \alpha|0\rangle_L + \beta|1\rangle_L$ after the encoding is called the *logical qubit*. This notation is used throughout the whole chapter. Assume that after the encoding step, the logical qubit is affected by three independent single-qubit bit-flip channels $\mathcal{E}_{bit}$ with the single-qubit bit-flip probability p. At the end of the sequence, the encoding process is reversed followed by the correction step. If the state $|\psi\rangle$ was left unchanged, the state after the decoding step is $|\psi\rangle_{dec} = \alpha|000\rangle + \beta|100\rangle = |\psi\rangle \otimes |00\rangle$ and the last CCNOT gate (Toffoli gate [111]) does not change the state $|\psi\rangle$. In the case of a bit-flip error on the first qubit, the state $|\psi\rangle_{dec} = \alpha|111\rangle + \beta|011\rangle = |\psi\rangle \otimes |11\rangle$ consists of the product state $X|\psi\rangle \otimes |11\rangle$. Now the second and third qubit are in the state $|11\rangle$ instead of $|00\rangle$, which leads to a bit-flip of state $X|\psi\rangle$ induced by the last correction step (Toffoli gate). Therefore the bit-flip error on the state $|\psi\rangle$ is corrected successfully. The success probability of the correction depends on the bit-flip probability p and is - as in the case of the classical three-bit repetition code- given by $1 - 3p^2 + 2p^3$. The three-qubit bit-flip code presented in Fig. 6.1 corrects bit-flip errors appearing on the state $|\psi\rangle$. After the decoding step, the qubits q2 and q3 are in the state $|00\rangle$ if no error on q1 appears and $|11\rangle$ if q1 is flipped. What happens if the second or the third qubit is flipped by the error channel? If q2 is flipped from $|0\rangle$ to $|1\rangle$ the state after the decoding step is $|\psi\rangle \otimes |10\rangle$ and if q3 was affected by a bit-flip the state ends up in $|\psi\rangle \otimes |01\rangle$. Therefore, it becomes obvious that the information about the occurrence and location of a bit-flip error on the logical state $|\psi\rangle_L$ is determined by the state of q2 and q3. After the correction step, q2 and q3 have to be reset for repeating of the whole error correction step, as demonstrated in Ref. [112]. Let us focus on the question how the complete logical state $|\psi\rangle_L$ can be recovered. If we could reveal the information about the location of the bit-flip error, then the logical state could be recovered with absolute accuracy at least if only a single bit-flip error occurs. The problem is that the direct measurement of q2 and q3 would destroy the coherence of the logical state. A more sophisticated method to readout the information is to use two ancilla qubits A1 and A2, as shown in Fig. 6.2.

The main idea is to map the information about the error on the ancilla qubits followed by a measurement in the computational basis. The measurement result of each ancilla qubit leads to two outcomes $\{|0\rangle, |1\rangle\}$. In total we receive two bits of information, which is enough to encode the four possible errors (no error, bit-flip on q1, bit-flip on q2 and bit-flip on q3). The first step

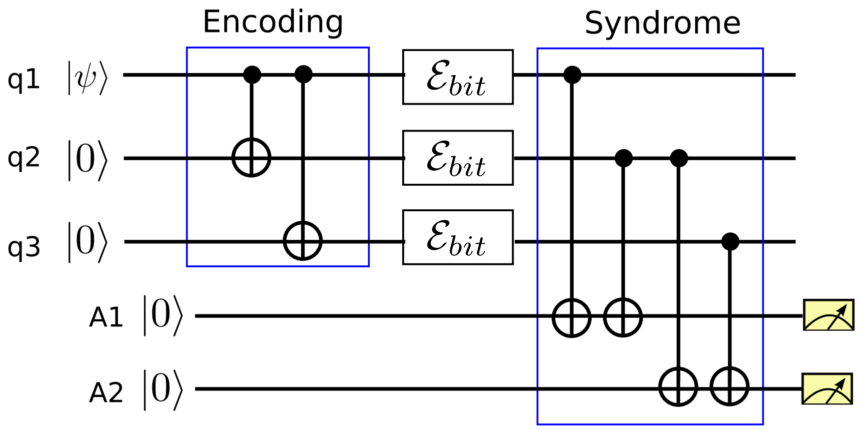

Figure 6.2: Three qubit syndrome measurement: Quantum circuit for the error syndrome measurement of the three-qubit bit-flip code. The information about the error syndrome is mapped by four CNOT operations (Syndrome) on two ancilla qubits A1 and A2. The measurement of the ancilla qubits results in four different outputs, corresponding to the eigenvalues of Z_1Z_2 and Z_2Z_3.

is to apply a CNOT operation on the qubits q1, q2 and the ancilla qubit A1. Assume that no error occurred on the logical qubit $|\psi\rangle_L$, then the final state after the two first CNOT operations (see Fig. 6.2) is $|\psi\rangle_L \otimes |00\rangle$. In the case of a bit flip on q1, the final state would end up in $(\alpha|100\rangle + \beta|011\rangle) \otimes |10\rangle$. The measurement of the ancilla qubit A1 would yield different outcomes, depending if an error appeared on q1 or q2. Therefore, the occurrence of a bit-flip error on q1 or q2 would result in a measurement of A1 in the state $|1\rangle$ and if no error occurred, A1 would remain in $|0\rangle$. This procedure is equivalent of measuring the eigenvalues of the operators $Z_1Z_2 = Z \otimes Z \otimes \mathbb{I}$. The states of the two qubits q2 and q3 are compared by measuring the eigenvalue of the operator $Z_2Z_3 = \mathbb{I} \otimes Z \otimes Z$ accomplished by the last two CNOT operations. The four different outputs of the eigenvalues contain the whole information about the different error scenarios, which is also referred to as *error syndrome measurement*. The error syndrome of the three-qubit bit-flip code is summarized in Table 6.1.

Error	$Z \otimes Z \otimes \mathbb{I}$	$\mathbb{I} \otimes Z \otimes Z$	output state
no error	+1	+1	$(\alpha|000\rangle + |111\rangle) \otimes |00\rangle$
bit flip on q1	-1	+1	$(\alpha|100\rangle + \beta|011\rangle) \otimes |10\rangle$
bit flip on q2	-1	-1	$(\alpha|010\rangle + \beta|101\rangle) \otimes |11\rangle$
bit flip on q3	+1	-1	$(\alpha|001\rangle + \beta|110\rangle) \otimes |01\rangle$

Table 6.1: Error syndrome of the three qubit QEC: Complete error syndrome of the three-qubit bit-flip code. The complete information about the error syndrome is obtained by measuring the eigenvalues of the two operators $Z \otimes Z \otimes \mathbb{I}$ and $\mathbb{I} \otimes Z \otimes Z$. This is realized by mapping the eigenvalues to the ancilla qubits A1 and A2 followed by a non-destructive measurement (see Fig. 6.2).

The measurement of the ancilla qubits can be realized in our system by a non-destructive way, which is also known as *quantum non demolition measurement* (QND) and demonstrated in Ref. [113]. As mentioned above, only correcting for bit-flip errors will certainly not be enough since a quantum state can also be perturbed by phase-flip errors. The three-qubit bit-flip code can be transformed to the three-qubit phase-flip code. Instead of the logical states $|0\rangle_L = |000\rangle$ and $|1\rangle_L = |111\rangle$ used for the bit-flip code, let us think about encoding the logical qubit $|\phi\rangle_L = \alpha\,|+++\rangle + \beta\,|---\rangle$ with $|\pm\rangle = \frac{1}{\sqrt{2}}(|0\rangle \pm |1\rangle)$. A bit-flip on one of the qubits would not change the logical state but for example a phase-flip on the first qubit would result in the state $\alpha\,|-++\rangle + \beta\,|+--\rangle$. The basis change from $\{|0\rangle, |1\rangle\}$ to $\{|+\rangle, |-\rangle\}$ can be performed by applying a Hadamard operation H after the encoding procedure of Fig. 6.1:

$$H(\alpha\,|000\rangle + \beta\,|111\rangle) \rightarrow (\alpha\,|+++\rangle + \beta\,|---\rangle). \tag{6.2}$$

The error syndrome measurement described in Fig. 6.2 can also be mapped to the basis $\{|+\rangle, |-\rangle\}$ by applying the Hadamard H before the CNOT operations (see Fig. 6.2). The basis transformation followed by measuring the ancilla qubits can be interpreted as a syndrome measurement of the observables $X_1X_2 = X \otimes X \otimes \mathbb{I}$ and $X_2X_3 = \mathbb{I} \otimes X \otimes X$, since $H^{\otimes 3}Z_1Z_2(H^{\otimes 3})^\dagger = X_1X_2$ as well as $H^{\otimes 3}Z_2Z_3(H^{\otimes 3})^\dagger = X_2X_3$. The encoding of the three-qubit phase-flip code and the syndrome measurement is illustrated in Fig. 6.3.

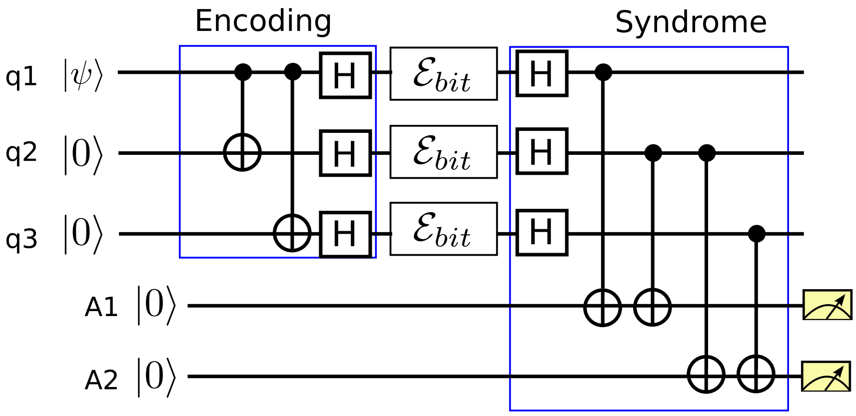

Figure 6.3: Three-qubit phase-flip code: Quantum circuit for the encoding and error syndrome measurement of the three-qubit phase-flip code. The phase-flip code is directly obtained from the bit-flip code by transformation of the basis $\{|0\rangle, |1\rangle\}$ to the $\{|+\rangle, |-\rangle\}$ basis. The error syndrome measurement is performed by measuring the eigenvalues of X_1X_2 and X_2X_3 (see text).

The combination of the three-qubit bit-flip code and the three-qubit phase flip code forms the nine-qubit Shor code, which has the capability to correct single-qubit bit-flip and phase-flip errors [21]. The encoding is demonstrated in Fig. 6.4. The outer layer of the code (q1,q4,q7) is encoded by the three-qubit-phase flip code and each qubit is again encoded by the three-qubit bit-flip code using two additional qubits respectively. This layer structure is also known as *concatenation*.

Arbitrary errors

It was mentioned before that quantum states can be corrupted by bit-flip and phase-flip errors. The nine-qubit QEC code is able to detect and correct both error types, the bit- and phase-flip error on a single qubit. However, the errors on a single qubit can be much more complex

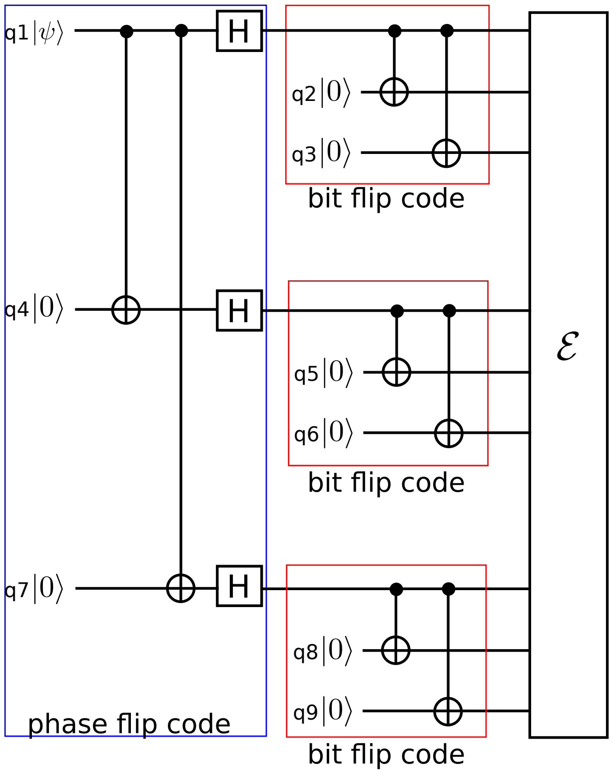

Figure 6.4: Nine-qubit Shor code: Circuit of encoding a single logical qubit in nine physical qubits by concatenation of the three-qubit phase-flip and bit-flip code.

than a discrete flip from $|0\rangle$ to $|1\rangle$ or from $|+\rangle$ to $|-\rangle$ and vice versa. In Sec. 2 continuous rotations on a single-qubit were introduced. The question arises, if such operations can be corrected with the described QEC codes. What about the important dephasing process (phase damping), dominating the loss of coherence? Is it possible to correct any arbitrary single- qubit error under the assumption of being able to correct bit -and phase-flip errors? To answer this question, consider the description of a general quantum process $\mathcal{E}$ acting on the encoded qubit $\rho_L = |\psi\rangle_L \langle\psi|$:

$$\mathcal{E}(\rho_L) = \sum_i E_i \rho_L E_i^\dagger. \tag{6.3}$$

The operators E_i can be expanded by the set of the Pauli operators $\{\mathbb{1}, X, Y, Z\}$ [21]:

$$E_i = a_{i0}\mathbb{1} + a_{i1}X + a_{i2}Y + a_{i3}Z, \tag{6.4}$$

which was already used for the χ-matrix representation of quantum processes. For example assume a rotation $R_x(\theta)$ about the X axis on qubit q1 with a rotation angle θ. This rotation can be expressed by the Pauli operators:

$$R_x^{(q1)}(\theta) = e^{-i\frac{\theta}{2}X^{(q1)}} = \cos(\theta/2)\mathbb{1}^{\otimes 3} - i\sin(\theta/2)(X \otimes \mathbb{1}^{\otimes 2}). \tag{6.5}$$

Following the encoding and syndrome measurement described in Fig. 6.2 for the three-qubit bit-flip code, the output density matrix after the error (rotation) is given by:

$$\mathcal{E}(\rho_L) = R_x^{(q1)}(\theta)\rho_L(R_x^{(q1)}(\theta))^\dagger. \tag{6.6}$$

Note that the last two qubits are used for the syndrome measurement. After performing the error syndrome mapping demonstrated in Fig. 6.2, the state results in:

$$\mathcal{E}(\rho_L) = \cos(\theta/2)^2 \rho_L \otimes |00\rangle\langle 00| + \sin(\theta/2)^2 \left[X \otimes \mathbb{1}^{\otimes 2} \rho_L \mathbb{1}^{\otimes 2} \otimes X\right] \otimes |10\rangle\langle 10| . \tag{6.7}$$

Therefore, the state remains unchanged with the probability $\cos(\theta/2)^2$, which for each case leads to the state $|00\rangle$ of the ancilla qubits. With the probability $\sin(\theta/2)^2$ the qubit is affected by a bit-flip, which results in the syndrome output $|10\rangle$ and finally will be corrected. This approach can be applied to an arbitrary process, as for example dephasing on qubit q1 can be expressed by the Kraus operators (see Sec. 2):

$$E_1 = \sqrt{1-p}\mathbb{1}^{\otimes 3}, \; E_2 = \sqrt{p} Z \otimes \mathbb{1}^{\otimes 2}. \tag{6.8}$$

The argumentation is completely analogous to the rotation error. Therefore we summarize that any QEC code, which is able to correct a discrete set of errors (no error $\mathbb{1}$, bit-flip X, bit-and phase-flip Y, phase-flip Z) has the capability to correct arbitrary errors without any further efforts. This fact is of fundamental importance for quantum error correction.

6.1.2 Some general properties

Here, some notations and properties used to describe different QEC codes are presented [21]:

- Logical operators: Logical operators are operators acting on the logical qubit $|\psi\rangle_L$. The logical X operation denoted as $\bar{X}$ maps the state $|0\rangle_L$ to $|1\rangle_L$ and vice versa. The logical Z operation denoted as $\bar{Z}$ acts on the logical state similar as Z on the physical qubit, $\bar{Z}|0\rangle_L = |0\rangle_L$ and $\bar{Z}|1\rangle_L = -|1\rangle_L$. Besides the logical $\bar{X}$ and $\bar{Z}$ operation, further logical gates are required to perform arbitrary operations on the logical qubit, e.g. the logical Hadamard $\bar{H}$, the logical phase gate $\bar{S}$, the logical T-gate $\bar{T}$ and the logical two-qubit CNOT gate. As an example, the logical Hadamard operation maps the state $|0\rangle_L$ to a coherent superpositon state $\frac{1}{\sqrt{2}}(|0\rangle_L + |1\rangle_L)$, analog to the Hadamard applied to the physical qubit. Within the following chapters the logical operations on the encoded qubit will play a major role.

- Distance d: A QEC code that is able to correct t errors has a code distance $d = 2t+1$. The code distance is also equivalent to the minimal weight of the logical $\bar{X}$ and $\bar{Z}$ operator. The weight of an operator is given by the number of qubits it acts non-trivially on (no identity). For example the operator $X \otimes Y \otimes X$ has weight 3, whereas the operator $\mathbb{I} \otimes \mathbb{I} \otimes \mathbb{I}$ has weight 0.

- A quantum code that encodes k logical qubits using n physical qubits and with a code distance d is written in the following form: [[n,k,d]]. For example the nine-qubit Shor code is a [[9,1,3]] code, since one logical qubit is encoded by nine physical qubits and has the capability to correct one arbitrary single qubit error.

- The construction of a good QEC code is not at all a trivial task. So far we have discussed the nine-qubit Shor code consisting of the simplest three-qubit codes. But besides that, there are many other different QEC codes, where each QEC code has different properties as for example the complexity of encoding, syndrome measurement and correction, the number of qubits, the robustness against errors and so forth. However, there are concrete restrictions concerning the capability of a QEC code, motivated by the fact that it is not possible to encode many logical qubits in a small number of physical qubits and aiming to protect many errors. The *Quantum Singleton bound* states that any [[n,k,d]] QEC has to satisfy the following condition [21]:

$$n \geq 4t + k. \tag{6.9}$$

This means that there exists no QEC code, which is able to encode one logical qubit in less than five physical qubits and being able to correct arbitrary single qubit errors. For the nine-qubit Shor code the condition is fulfilled, since $9 \geq 4 + 1$. In principle the number of physical qubits n could be even lower. Within the next chapter, QEC codes are described, showing the capability of detecting and correcting arbitrary single-qubit errors with only seven and five qubits. The five-qubit QEC code is saturating the Singleton bound $(5 = 4 + 1)$ and therefore represents the smallest QEC code being able to correct arbitrary single-qubit errors [114].

6.1.3 Stabilizer codes

In the previous section, the QEC codes were described by the codewords defining the logical code space. But there is a more elegant and powerful description of QEC codes using the *stabilizer formalism*. The main idea is to describe the codes not explicitly by the vector states, but rather by certain operators. This leads to an efficient description of the QEC codes. Furthermore, the syndrome measurement as well as operations on the logical qubit can be described by the stabilizer formalism.

The stabilizer formalism can be illustrated by a simple example. Assume the GHZ state $|\psi\rangle = \frac{1}{\sqrt{2}}(|000\rangle + |111\rangle)$. The GHZ state is the unique state which fulfills the three conditions:

$$\begin{aligned} Z_1 Z_2 |\psi\rangle &= |\psi\rangle \\ Z_2 Z_3 |\psi\rangle &= |\psi\rangle \\ X_1 X_2 X_3 |\psi\rangle &= |\psi\rangle . \end{aligned}$$

This is why the set of operators $\{Z_1Z_2, Z_2Z_3, X_1X_2X_3\}$ is said to stabilize this state. A more precise definition of the stabilizer is the following: Assume that the group S is a subgroup of the Pauli group [3] containing a set of n-qubit Pauli operators $P^{(n)}$. The group S is said to be the *stabilizer* of the vector space V if for all elements $P_k^{(n)}$ and states $|\psi\rangle_j \in V$ the following constraint holds:

$$P_k^{(n)} |\psi\rangle_j = |\psi\rangle_j \ \forall\, k, j. \tag{6.10}$$

In other words, each element of the vector space V is stabilized by the elements of the stabilizer group. It is important to note that S can only be a stabilizer of a non-trivial vector space if the following two conditions are fulfilled: (a) The element $-\mathbb{1} \notin S$ and (b) all elements of S

---

[3] The Pauli group of one qubit contains the elements $\{\pm\mathbb{1}, \pm i\mathbb{1}, \pm X, \pm iX, \pm Y, \pm iY, \pm Z, \pm iZ\}$

have to commute with each other. If $-\mathbb{1}$ was an element of S, then $-\mathbb{1}\,|\psi\rangle = |\psi\rangle$ would have to be fulfilled, which is a contradiction. To prove condition (b) assume two stabilizer operators A and B of S. Then it follows that $A\,|\psi\rangle = |\psi\rangle$ and $B\,|\psi\rangle = |\psi\rangle$. For the case of anti-commuting operators $AB = -BA$, it follows that $AB\,|\psi\rangle = |\psi\rangle = -BA\,|\psi\rangle = -\,|\psi\rangle$, which leads also to a contradiction. Only the trivial element $|\psi\rangle = 0$ would repeal the contradiction.

Consider again the example of the GHZ state. Besides the three operators Z_1Z_2, Z_2Z_3 and $X_1X_2X_3$ the state is also stabilized by the operator Z_1Z_3, $X_1X_2X_3$ and the identity. Therefore we define the stabilizer group $S = \{\mathbb{1}, Z_1Z_2, Z_2Z_3, Z_1Z_3, X_1X_2X_3\}$ of the state $|\psi\rangle = \frac{1}{\sqrt{2}}(|000\rangle + |111\rangle)$. Please note that the operators are acting on a three-qubit state. The elements of the stabilizer S can be defined by only three operators Z_1Z_2, Z_2Z_3 and $X_1X_2X_3$ of S, since $Z_1Z_2Z_2Z_3 = Z_1Z_3$ and $(Z_1Z_2)^2 = \mathbb{1}$. This subgroup of S is called the generator group of S. The elements g_j of a group G, which is a subgroup of S, are called generators of the group G, if all elements of S can be written as a product of elements in G [21]. Therefore the group $G = \{Z_1Z_2, Z_2Z_3, X_1X_2X_3\}$ generates the stabilizer S.

A QEC code is called an [n,k][4] *stabilizer code*, if the codeword basis states are stabilized by the stabilizer S, which is generated by $n-k$ independent and commuting generator elements g_j [21]. The idea of the stabilizer formalism is explained by the previous example of the [3,1] bit-flip code. The code space is spanned by the two states $|000\rangle$ and $|111\rangle$. Using the previous definition, the stabilizer is generated by $3-1=2$ generators. The two operators $g_1 = Z_1Z_2$ and $g_2 = Z_2Z_3$ are generating the stabilizer $S = \{\mathbb{1}, Z_1Z_2, Z_2Z_2, Z_1Z_3\}$ of the bit-flip code. Please note that any superposition of the basis states is also stabilized by S. What happens if we apply the errors $E = \{\mathbb{1}, X_1, X_2, X_3\}$ on the logical qubit? The errors lead to a transformation of the generators $\{g_j\}$ to $Eg_jE^\dagger$.

Error E	generators $\{g_j\}$
no error-$\mathbb{1}$	$\{Z_1Z_2, Z_2Z_3\}$
bit flip on q1-X_1	$\{-Z_1Z_2, Z_2Z_3\}$
bit flip on q2-X_2	$\{-Z_1Z_2, -Z_2Z_3\}$
bit flip on q3-X_3	$\{Z_1Z_2, -Z_2Z_3\}$

Table 6.2: Three-qubit stabilizer code: The two gerators $g_1 = Z_1Z_2$ and $g_2 = Z_2Z_3$ of the three-qubit bit-flip code are mapped by the different errors (left column) to the generators listed in the right column. The different generators indicate the principle of uniquely detecting different errors (see main text).

Table. 6.2 shows the generators of the three-qubit bit-flip code affected by the correctable errors E. There is a unique structure of the transformed generators, which allows the clear distinction of the error syndromes. If we compare this result with the described error syndrome measurement in the previous section it becomes clear that the measured operators in Table. 6.1 are identical with the signs of the transformed generators. The error syndrome of an $[n,k]$ stabilizer code is uniquely defined by measuring the eigenvalues of the $n-k$ independent generators. This implies that the three-qubit bit -and phase-flip code belongs to the class of stabilizer codes. Since the nine-qubit Shor code can be constructed by concatenation of the two different

---

[4] Similar to the definiton used before, n corresponds to the number of physical qubits and k is equal to the encoded logical qubits.

three-qubit codes, it can also be described by the stabilizer formalism. In the original work of Ref. [110], the code is described by the state vector notation. The eight stabilizer generators of the nine-qubit Shor code are listed in Table 6.3.

generator	Operator
g_1	$ZZ\mathbb{1}\mathbb{1}\mathbb{1}\mathbb{1}\mathbb{1}\mathbb{1}\mathbb{1}$
g_2	$\mathbb{1}ZZ\mathbb{1}\mathbb{1}\mathbb{1}\mathbb{1}\mathbb{1}\mathbb{1}$
g_3	$\mathbb{1}\mathbb{1}\mathbb{1}ZZ\mathbb{1}\mathbb{1}\mathbb{1}\mathbb{1}$
g_4	$\mathbb{1}\mathbb{1}\mathbb{1}\mathbb{1}ZZ\mathbb{1}\mathbb{1}\mathbb{1}$
g_5	$\mathbb{1}\mathbb{1}\mathbb{1}\mathbb{1}\mathbb{1}\mathbb{1}ZZ\mathbb{1}$
g_6	$\mathbb{1}\mathbb{1}\mathbb{1}\mathbb{1}\mathbb{1}\mathbb{1}\mathbb{1}ZZ$
g_7	$XXXXXX\mathbb{1}\mathbb{1}\mathbb{1}$
g_8	$\mathbb{1}\mathbb{1}\mathbb{1}XXXXXX$

Table 6.3: Nine-qubit Shor code generators: Generators of the nine-qubit Shor code.

The occurrence of any single qubit error X, Z and in combination Y can be detected by a change of the expectation value of one or several of the eight generators from +1 to -1. The unique detection of error syndromes in a stabilizer code leads to a certain constraint of the errors:

- Any error described by the operator E can only be detected by the syndrome measurement if E anti-commutes with at least one of the generators g. Therefore the acting of the error E onto one state of the code space $|\psi\rangle_L$ results in $E|\psi\rangle_L = Eg|\psi\rangle_L = -gE|\psi\rangle_L$, which leads to $g(E|\psi\rangle_L) = -(E|\psi\rangle_L)$. The logical state after the error is a -1 eigenstate of at least one, but in general more generators g.

Every logical operator $\bar{L}$, as for example $\bar{X}$ and $\bar{Z}$ should not map any logical state to a state outside the code space. Making use of the same argumentation as before, this implies that every logical operator $\bar{L}$ has to commute with every element of the stabilizer S and therefore with each of the generators g. The simplest logical Pauli operators, which are constructed for every stabilizer code are given by $\bar{X} = X_1X_2...X_n$ and $\bar{Z} = Z_1Z_2...Z_n$. Within the next chapter, the construction of more complex logical operators required for computational tasks is presented.

The investigation of theoretical concepts in the field of QEC has led to a variety of QEC codes. Another prominent QEC code belonging to the group of stabilizer codes is the seven-qubit Steane code [25]. The Steane code is a $[[7,1,3]]$ code and similar to the Shor code is able to correct arbitrary single-qubit errors by encoding a logical qubit in seven physical qubits. At the same time, Raymond Laflamme discovered the smallest possible QEC using only five physical qubits, which is capable of detecting and correcting arbitrary single-qubit errors [114]. The generators of the seven-qubit Steane and the five-qubit QEC code are listed in Table. 6.4.

A closer look at Table 6.4 shows that the generators of the Steane code are either X-type (g_1, g_2, g_3) or Z-type (g_4, g_5, g_6) Pauli operators. The X-type generators enable the detection of phase-flip errors, whereas the Z-type generators detect bit-flip errors. This feature of the seven-qubit Shor code enables the independent detection and correction of phase- and bit-flip

Steane code	Operator	five qubit code	Operator
g_1	$\mathbb{1}\mathbb{1}\mathbb{1}XXXX$	g_1	$XZZX\mathbb{1}$
g_2	$\mathbb{1}XX\mathbb{1}\mathbb{1}XX$	g_2	$\mathbb{1}XZZX$
g_3	$X\mathbb{1}X\mathbb{1}X\mathbb{1}X$	g_3	$X\mathbb{1}XZZ$
g_4	$\mathbb{1}\mathbb{1}\mathbb{1}ZZZZ$	g_4	$ZX\mathbb{1}XZ$
g_5	$\mathbb{1}ZZ\mathbb{1}\mathbb{1}ZZ$		
g_6	$Z\mathbb{1}Z\mathbb{1}Z\mathbb{1}Z$		

Table 6.4: Steane code and five-qubit code: Generators of the seven-qubit Steane code and the five-qubit QEC.

errors, which is a general property of so called CSS (Calderbank-Shor-Steane) codes [115, 116]. In contrast, the generators of the five-qubit code do not show this advantageous property (see Table 6.4), because the five-qubit code does not belong to the class of CSS codes [21]. This fact is also reflected in the complexity of the operations on the logical qubit, which will play an important role for the concept of FTQC discussed within the next section.

6.2 Fault tolerant quantum computation

The necessity of quantum error correction was motivated in the previous section by protecting a single qubit against arbitrary errors. So far, the general picture was to encode the logical qubit, perform the syndrome measurement, correct the error if necessary and finally apply the decoding step. This procedure is useful when storing quantum information or transmit the information through some noisy channel. But the most powerful application of QEC would be the protection of the quantum information against errors occurring during the computation [21]. The main problem is that any building block used to perform quantum computation is faulty and cannot be implemented perfectly. The quantum computation scheme shown in Fig. 6.5 is illustrating this fact. The state preparation (1) at the beginning of the computation is already faulty, for example due to imperfection in the polarization of the repumping lasers. The implementation of coherent unitary operations (2) can only be performed with a certain fidelity, as

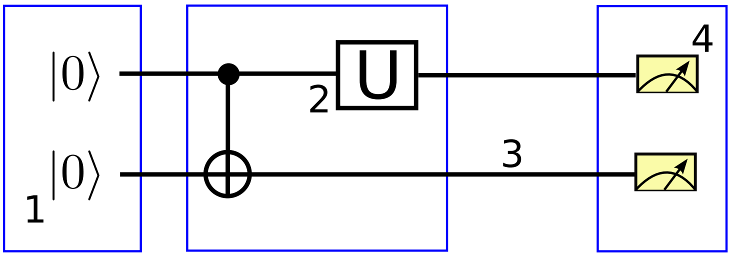

Figure 6.5: Quantum circuit: Illustration of an arbitrary quantum circuit consisting of (1) state preparation and initilaization, quantum operations (2) and measurements in a certain basis (4). Each of this elemementary building block is faulty. Even between the individual gates, the system is affected by decoherence processes (3).

described in Chapter 3. Even between the different operations (3), the coherence of the quantum state is affected by non-unitary processes as dephasing and spontaneous decay, which induce errors. The measurement of the qubits' information at the end of the computation exhibits some amount of infidelity, for example due to spontaneous decay during the measurement process or background counts. Following the general idea of QEC described in the previous section, the qubit information would be encoded, followed by error detection and correction and finally decoding the information. This procedure would be repeated periodically. The bad news is that this procedure alone would not be sufficient to overcome the faulty operations during the computation. The reason is illustrated by the following example [21]: Assume the encoding step of the three-qubit bit-flip code, illustrated in Fig. 6.6(a). In the case of an ideal encoding procedure,

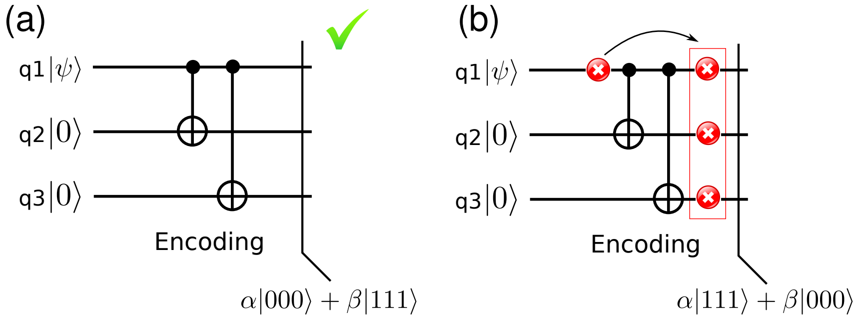

Figure 6.6: Error propagation: Non-fault-tolerant encoding of the three-qubit bit-flip code. (a) Ideal case of the encoding procedure, resulting in the state $\alpha\,|000\rangle+\beta\,|111\rangle$. (b) A single-qubit bit-flip error on qubit q1 leads to a propagation of the error onto qubit q2 and q3.

the state at the output yields $\alpha\,|000\rangle+\beta\,|111\rangle$. If qubit q1 is affected by a bit-flip error before the encoding step, consisting of the two CNOT operations, then the final state at the output of the encoding procedure results in $\alpha\,|000\rangle+\beta\,|111\rangle$, which effectively corresponds to a three-qubit bit-flip error (see Fig. 6.6(b)) . Therefore the CNOT operations did lead to a propagation of the single-qubit bit-flip error onto the whole register. The propagation of errors caused by operations is the main problem of protecting a logical qubit during quantum computation. The good news is that arbitrary long quantum computation is still possible even with faulty gates. The basic idea is to perform the quantum computation directly on the encoded qubit without the necessity of decoding. All operations on the logical qubits have to be performed in such a way that errors appearing on the individual qubits do not cause multiple errors in any of the other logical qubits. This basic concept behind this idea is called *fault tolerant quantum computation* (FTQC). Fig. 6.7 represents the circuit shown in Fig. 6.5 within the framework of fault tolerant quantum computation [21]. The logical qubits are encoded in several physical qubits in a fault tolerant way. After some time fault tolerant (FT) error correction is performed on each logical qubit followed by the FT logical operations (CNOT,U) and finally a FT detection of the logical qubits. This scheme works only if all building blocks are implemented in a fault tolerant way, preventing the uncontrolled propagation of errors, and if the error probability per gate is below a certain *error threshold*.

A more detailed definition of fault tolerant quantum operation on logical qubits is the following: A quantum operations on the logical qubit is called fault tolerant, if the failure of one component used to perform the logical operation causes at most one error in the output of each

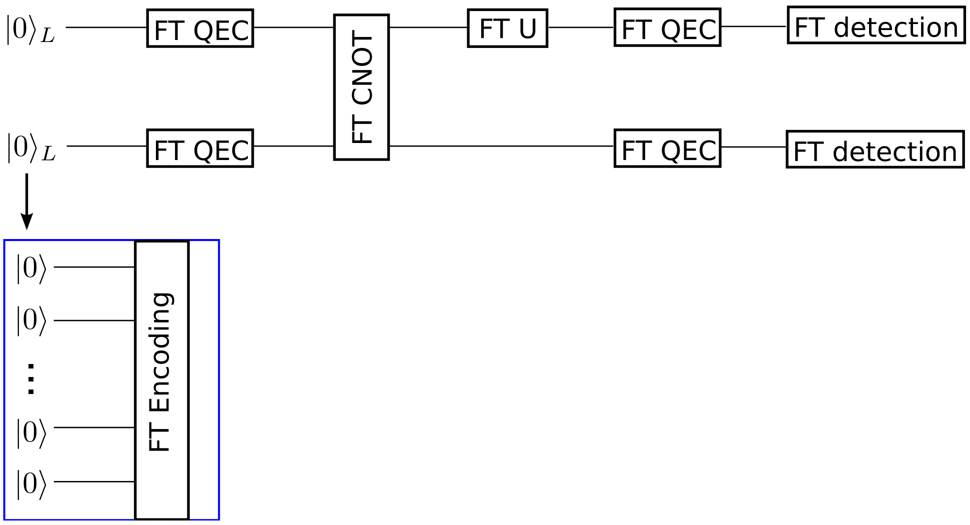

Figure 6.7: FTQC scheme: Illustration of FTQC between two logical qubits $|0\rangle_L$. The main idea is to perform all elementary building blocks (see Fig. 6.5) on the encoded qubit. If the operations on the logical qubit are implemented in such a way that errors on the physical qubits are not propagating along the whole system (fault tolerant), then arbitrary long quantum compution will be possible, if the error probability is below a certain threshold.

logical qubit [117, 21]. For example a failure in one of the physical gates implementing the fault tolerant unitary operation U in Fig. 6.7 corresponds to the perfectly implemented operation up to one error on a single qubit at the output. If more errors would appear on the logical qubit, quantum error correction would fail and resul in the accumulation of errors. This definition of fault tolerance is the same for the state preparation, detection and error correction building block (see Fig. 6.7). For any fault tolerant quantum code, there exists a threshold p_{th}, such that if the error rate per physical gate p is lower than p_{th} ($p < p_{th}$) arbitrary long quantum computations is feasible [21, 117]. The performance of any QEC code depends on the construction of the code. This means that the way of encoding, the implementation of logical gates, the syndrome measurement and correction of errors determines if the code is fault tolerant. Similar to that, the error threshold p_{th} depends strongly on the implementation of the different building blocks and the underlying noise model. There are different approaches for the construction of fault tolerant codes, showing different error thresholds. In the following, two different approaches will be discussed - *concatenated codes* and *topological codes*. Besides that, a property of the Steane code will be explained, which allows the fault tolerant implementation of logical gates.

6.2.1 Transversality and FT quantum operations

As motivated above, the basic idea of FTQC is to encode the logical qubit and perform a universal set of fault tolerant operations on the encoded qubit. The difficulty is to find a way to perform the logical operations in a fault tolerant way, which implies for logical single-qubit operations that a single-qubit error is not spreading out to other qubits. In the case of the logical two-qubit CNOT gate, fault tolerance requires that an error on a physical qubit does not spread out to more than one qubit in the other layer. Depending on the QEC code used to encode the logical qubit (Steane code, Shor code, five qubit code, ...) the implementation of fault tolerant gates will differ from each other in terms of the complexity. Here, a useful method is presented, allowing the construction of fault tolerant quantum operations. In particular, this method is demonstrated by implementing a set of logical single-qubit operations on the seven-qubit Steane code [116]. Analog to the quantum computation on the physical qubit introduced in Chapter 2, universal computation within the framework of FTQC requires the implementation of the logical Hadamard gate $\bar{H}$, the logical phase gate $\bar{S}$, the logical CNOT operation and the logical $\pi/8$-gate $\bar{T}$. The realization of the logical single-qubit operations in the Steane code is shown in Fig. 6.8.

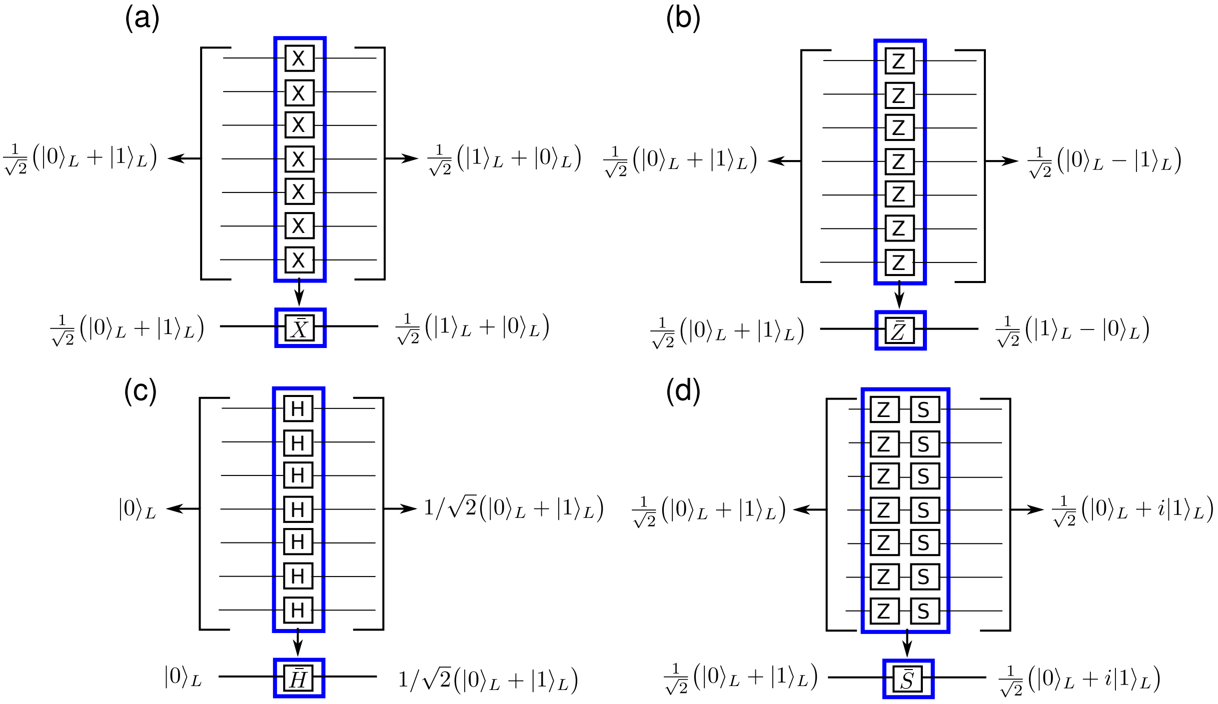

Figure 6.8: Transversal single-qubit gates: Transversal implementation of the $\bar{X}$, $\bar{Z}$, Hadamard $\bar{H}$ and phase gate $\bar{S}$ on one logical qubit encoded in the Steane code.

Fig. 6.8 reveals a clear archetype for the implementation of the logical $\bar{X}$, $\bar{Z}$, $\bar{H}$ and $\bar{S}$ gate-all operations on the logical qubit are performed by *bit-wise* operations on the individual physical qubits. This bit-wise implementation of a logical operation on an encoded qubit is called *transversality* [21]. For example assume the bit-wise implementation of the logical Hadamard $\bar{H}$ (Fig. 6.8(c)). If one single component of the whole block is affected by some error, then this error is not affecting other qubits, because the operations are performed on each qubit individually. Therefore, one individual error is causing only one error at the output of the whole block after the logical Hadamard operation. For example assume that one qubit is affected by a bit flip error X before the logical Hadamard operation is applied. Then the whole operation $HX = HXH^{\dagger}H$ is equivalent to ZH, which corresponds to a perfect Hadamard gate in combination with a phase-flip error. The transversal implementation of the logical phase gate $\bar{S}$ should transform the logical operator $\bar{Z}$ to $\bar{Z}$ and the operator $\bar{X}$ to $\bar{Y}$. This can be understood by the fact that the logical $\bar{S}$ gate transforms an eigenstate of the logical $\bar{X}$ operator to an eigenstate of the logical $\bar{Y}$ operator. Applying only S on each physical qubit would transform $\bar{X}$ to $-\bar{Y}$ with an additional phase-flip, which can be compensated by adding a transversal $\bar{Z}$ operation (see Fig. 6.8(d)).

So far, only transversal single-qubit operations on the logical qubit (see Fig. 6.8) were discussed. Fortunately, the implementation of the logical CNOT operation can also be performed transversely, as illustrated in Fig. 6.9 [21]. The transversal CNOT gate is implemented by pairwise CNOT operations between the physical qubits of each encoded block. Therefore, if one single component fails (e.g. an error on a single qubit) then only one error appears at the output of the whole block. The logical single-qubit operations $\bar{X}$, $\bar{Z}$ $\bar{H}$ and $\bar{S}$ as well as the logical two-qubit CNOT operation can be realized transversely in the seven-qubit Steane code. This group of gate operations is known as the Clifford group, which does not represent a universal gate set (see Chapter 2) but still enables the realization of interesting protocols such as quantum state distillation and quantum teleportation [118, 119]. This set of operations can be completed to a universal set of gates by complementing the set of Clifford gate operations by a non-Clifford operation, the logical $\bar{T}$-gate [21, 117]. As compared to the Clifford operations, the logical $\bar{T}$-gate ($\pi/8$-gate) can not be implemented transversely in terms of bit-wise operations on the physical qubits. Nevertheless, the fact that there exists no transverse implementation of the $\bar{T}$-gate does not imply that there exists no fault-tolerant realization. As already mentioned in the previous sections, the measurement of the stabilizers is mandatory to get the information about the er-

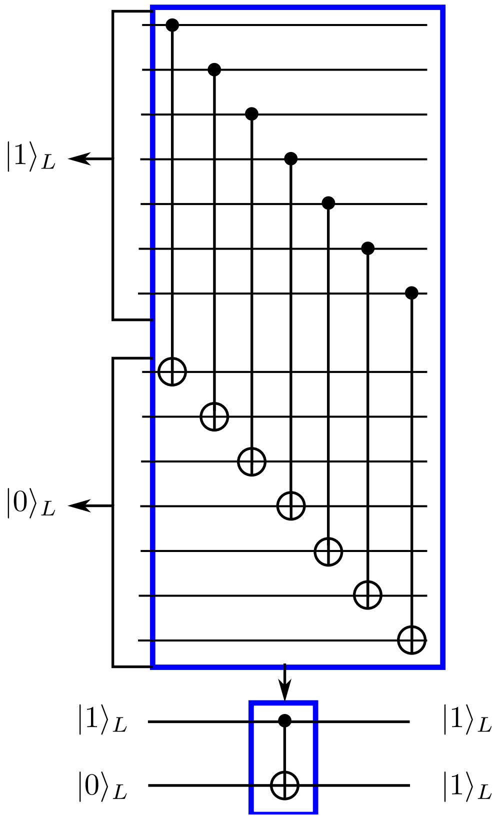

Figure 6.9: Transverse CNOT gate: Transversal implementation of the logical CNOT operation on two qubits encoded in the Steane code.

ror syndrome. Furthermore, the measurement of an operator can also be applied as a powerful technique for state preparation, which will be used for the fault tolerant implementation of the $\bar{T}$-gate. Before we describe the scheme, which is used to realize the $\bar{T}$-gate, the fault-tolerant measurement procedure will be discussed.

6.2.2 Fault-tolerant measurement

The measurement of an operator M is one of the main requirements for the realization of fault tolerant quantum computation. The main principle for measuring an operator M is to use an ancilla qubit initially in the state $|0\rangle^{(A)}$ and mapping the information about the eigenvalues of the operator to the ancilla qubit. The simplest circuit to perform this task is shown in Fig. 6.10(a). Assume the ancilla qubit (physical qubit) is initially prepared in the state $|0\rangle^{(A)}$ and the logical qubit, which is being measured, is in any arbitrary superposition state $|\psi\rangle_L = a\,|0\rangle_L + b\,|1\rangle_L$. The circuit consists of preparing the ancilla qubit in a superposition state, applying a conditional M-operation on the logical qubit, followed by a second Hadamard operation and finally measuring the ancilla qubit in the computational basis. The circuit can be understood better by considering a concrete example. Assume the measurement of the logical operator $\bar{Z}$ illustrated in Fig. 6.10(b). The mapping of the input state $|0\rangle^{(A)} \otimes |\psi\rangle_L = |0\rangle^{(A)} \otimes (a\,|0\rangle_L + b\,|1\rangle_L)$ via the circuit of Fig. 6.10(b) is explicitly shown:

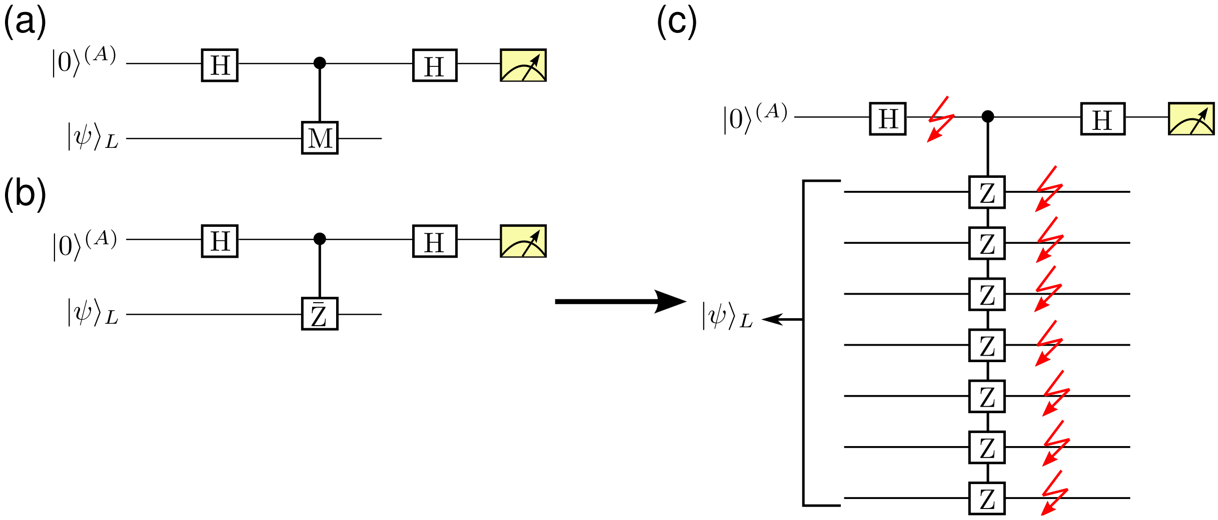

Figure 6.10: Measurement circuit: (a) Measurement of the operator M of the logical qubit $|\psi\rangle_L$ by mapping the information about the expectation value of M to the ancilla qubit initially prepared in the state $|0\rangle^{(A)}$. (b) Concrete example of measuring the logical operator $\bar{Z}$. Mapping the information about the expectation value to the ancilla qubit is not fault tolerant, as illustrated in (c). One error occurring on the ancilla qubit (red arrow) will lead to seven errors on the logical qubit.

$$|0\rangle^{(A)} \otimes (a\,|0\rangle_L + b\,|1\rangle_L) \xrightarrow{H^{(A)}} \frac{1}{\sqrt{2}}(|0\rangle^{(A)} + |1\rangle^{(A)}) \otimes (a\,|0\rangle_L + b\,|1\rangle_L) \xrightarrow{C\,\bar{Z}}$$

$$\frac{1}{\sqrt{2}}(a[|0\rangle^{(A)} + |1\rangle^{(A)}]\,|0\rangle_L + b[|0\rangle^{(A)} - |1\rangle^{(A)}]\,|1\rangle_L) \xrightarrow{H^{(A)}} a\,|0\rangle^{(A)}\,|0\rangle_L + b\,|1\rangle^{(A)}\,|1\rangle_L\,.$$

Therefore, measuring the ancilla qubit at the end of the sequence will yield with probability $|a|^2$ the eigenvalue +1 and with probability $|b|^2$ the eigenvalue -1. This is exactly the result which would be obtained by directly measuring the $\bar{Z}$ expectation value, since $\bar{Z}(a\left|0\right\rangle_L + b\left|1\right\rangle_L) = (+1)a\left|0\right\rangle_L + (-1)b\left|1\right\rangle_L$. In Fig. 6.10(c), the circuit of measuring $\bar{Z}$ of a logical qubit encoded in the seven-qubit Steane code is shown. Due to the transversality property of the Steane code, the controlled operation can be implemented by pair-wise operations. In the previous section it was shown that transversal gates are fault tolerant. But what is happening if a bit-flip error occurs on the ancilla qubit, which is illustrated in Fig. 6.10(c) by the red arrow? The single qubit error is spreading out on the whole logical block and effectively leads to seven bit-flip errors. Therefore, this implementation of measuring an operator will not be fault tolerant.

Nevertheless, there exists a possibility to make the circuit shown in Fig. 6.10 fault tolerant [21, 120]. The circuit diagram of a fault tolerant measurement is illustrated in Fig. 6.11 specifically for the measurement of the logical $\bar{Z}$ operator of a qubit encoded in the seven-qubit Steane code, but it can be generalized for any other transversal code.

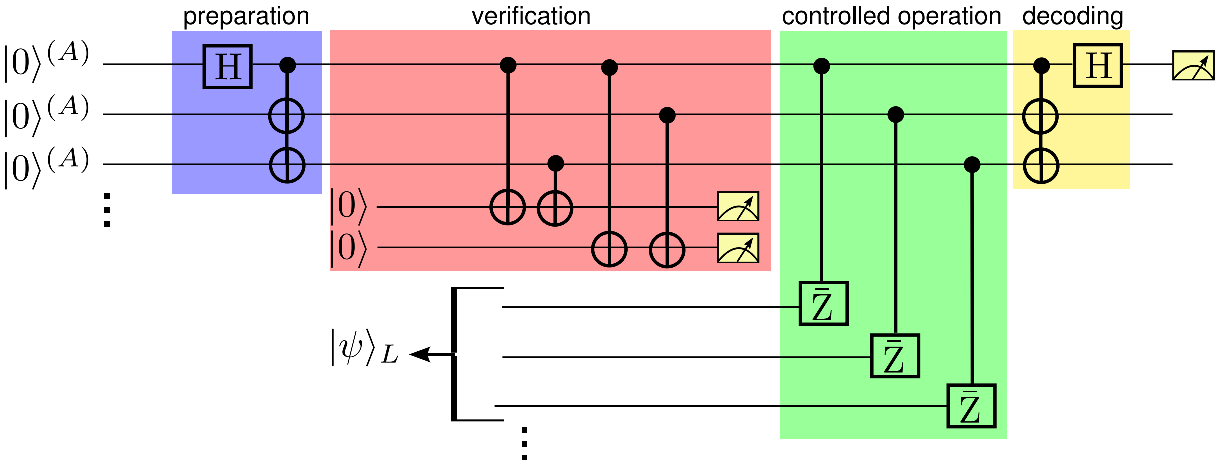

Figure 6.11: Fault tolerant measurement scheme: A fault tolerant implementation of measuring the logical operator $\bar{Z}$. Compared to the scheme in Fig. 6.10, the ancilla qubits are encoded in a GHZ state (preparation), followed by a verification step. The verification step checks if the GHZ state was corrupted by an error and leads to a repetition of the preparation step if neccesary. Then the controlled $\bar{Z}$ operation is implemented transversely, followed by reversing the preparation step and measuring the ancilla qubit. To deal with errors appearing on the ancilla qubits and corrupting the measurement results, the whole procedure is repeated several times and making a majority voting (see main text). Note that for simplicity only a subset of the required qubits is shown [21].

As already pointed out, the main problem are errors on the ancilla qubit spreading out and leading to multiple errors. Assume the logical qubit in the state $\left|\psi\right\rangle_L$ is encoded in seven physical qubits and there is one extra ancilla qubit in the state $\left|0\right\rangle_L^{(A)}$ for each of the seven qubits. Note that for simplicity only a part of the qubits involved is shown in Fig. 6.11. In general, 14 qubits would be required for the measurement scheme (7 ancilla qubits and 7 for the logical qubit). The basic idea to fight the measurement errors is to perform a verification procedure. The first step is to prepare the ancilla qubits in an entangled GHZ state $\frac{1}{\sqrt{2}}(|000\rangle + |111\rangle)$, indicated by the first (blue) circuit block. The verification is realized by measuring the parity operators Z_1Z_3

and Z_1Z_2 by mapping the information to two additional ancilla qubits and performing a measurement of the two qubits. Only if both ancilla qubits remain in the state $|0\rangle$, the ancilla qubits have been in the GHZ state and the measurement procedure will be carried on. If the verification procedure fails, which means that the parity measurement shows that the GHZ state was corrupted, then the preparation is repeated. The next step is the mapping of the measurement information onto the ancilla qubits by the controlled $\bar{Z}$ operations, as described in Fig. 6.10. As a reminder, the controlled operations are performed pair-wise in a fault tolerant way. The last step is to decode the information and measure the first ancilla qubit, which contains the information about the expectation value of the logical $\bar{Z}$ operator. But why is this procedure fault tolerant compared to using only one ancilla qubit? For example errors during the preparation or verification step can lead to multiple errors on the ancilla qubits. An important fact is that phase-flip errors occurring on the ancilla qubits during the whole procedure (preparation, verification, controlled operations and decoding) will not affect the encoded logical qubit but will result in a final measurement error. To overcome this problem, the whole measurement procedure will be repeated several times and a majority voting is performed on the output information. Similar to the previously described three-qubit code, the verification procedure together with the majority voting will lead to a failure probability of the measurement procedure of at most $O(p^2)$, with the failure probability p of a single component. With only one ancilla qubit as described before, the failure probability would scale with p. The same argument holds for errors occurring on the ancilla qubits during the decoding step. In case of the bit-flip errors, it can be revealed from the circuit diagram that one bit-flip error can maximally lead to one error on the logical qubit $|\psi\rangle_L$.

6.2.3 Implementation of the logical $\bar{T}$-gate

The realization of the $\bar{T}$-gate is based on injecting the state of interest from an ancilla qubit to the logical qubit using the set of Clifford operations, which can be implemented fault-tolerantly [21, 121]. The general scheme is shown in Fig. 6.12. The main task of the circuit is to apply

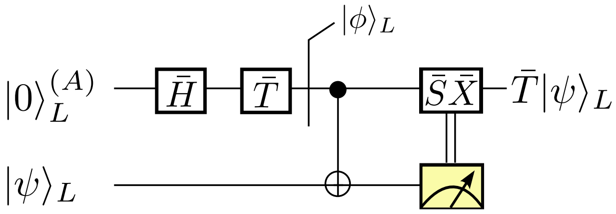

Figure 6.12: $\bar{T}$-gate implementation: Circuit diagram for the implementation of a logical $\bar{T}$-gate on an arbitrary logical state $|\psi\rangle_L = a\,|0\rangle_L + b\,|1\rangle_L$ using the technique of magic-state injection [121] (see main text).

the $\bar{T}$-gate on a general logical state $|\psi\rangle_L$ and generate the state $\bar{T}\,|\psi\rangle_L$. Assume the ancilla qubit starts in the logical state $|0\rangle_L^{(A)}$ and the logical qubit in an arbitrary superposition $|\psi\rangle_L = a\,|0\rangle_L + b\,|1\rangle_L$. The first step is to create the ancilla state $|\phi\rangle_L^{(A)}$ by applying the Hadamard operation $\bar{H}$ followed by the $\bar{T}$-gate, as shown in Fig. 6.12. The output state after these two operations is given by $|\phi\rangle_L^{(A)} = 1/\sqrt{2}(|0\rangle_L^{(A)} + e^{i\pi/4}\,|1\rangle_L^{(A)})$. The next step is to create a CNOT operation with the ancilla qubit acting as the control qubit. The whole system is resulting in the state:

$$1/\sqrt{2}\Big[\big(\alpha\,|0\rangle_L^{(A)} + \beta e^{i\pi/4}\,|1\rangle_L^{(A)}\big)\otimes|0\rangle_L + \big(\alpha e^{i\pi/4}\,|1\rangle_L^{(A)} + \beta\,|0\rangle_L^{(A)}\big)\otimes|1\rangle_L\Big]. \qquad (6.11)$$

Therefore, if the system qubit is found in the state $|0\rangle_L$ after the measurement, then the ancilla qubit will be in the state $\big(\alpha\,|0\rangle_L^{(A)} + \beta e^{i\pi/4}\,|1\rangle_L^{(A)}\big)$, which corresponds to the operation $\bar{T}\,|0\rangle_L^{(A)}$. In this case, the implementation of the logical $\bar{T}$ gate has been successful. If the measurement of the logical qubit reveals the state $|1\rangle_L$, then the ancilla qubit is projected to the state $\big(\alpha e^{i\pi/4}\,|1\rangle_L^{(A)} + \beta\,|0\rangle_L^{(A)}\big)$. In this case, the ancilla state can be transformed to the target state by applying the logical $\bar{S}$ gate followed by the logical $\bar{X}$ operation, which results in the state $e^{-i\pi/4}\big(\alpha\,|0\rangle_L^{(A)} + \beta e^{i\pi/4}\,|1\rangle_L^{(A)}\big)$. Therefore, up to some irrelevant global phase, the right target state is achieved. We know already that the logical CNOT operation, Hadamard $\bar{H}$, the phase gate $\bar{S}$, the logical $\bar{X}$ as well as the measurement procedure can be implemented in a fault tolerant way. But how does the realization of the $\bar{T}$- gate on the ancilla qubit used to prepare the injection state $|\phi\rangle_L^{(A)}$ work? We can make use of the fact that the injection state $|\phi\rangle_L^{(A)}$ is a +1 eigenstate of the operator $M = e^{-i\pi/4}\bar{S}\bar{X}$. Therefore, the state $|\phi\rangle_L^{(A)}$ can be prepared by measuring the operator M. The schematics of the corresponding measurement protocol is illustrated in Fig. 6.13(a). Fig. 6.13(b) shows the circuit of measuring the operator M by only using transverse Clifford operations on the logical qubit and the T-gate applied on the ancilla qubit. Here, we assume that there is only one ancilla qubit prepared in the state $|0\rangle^{(A)}$. The state of the joined system right before the measurement is given by:

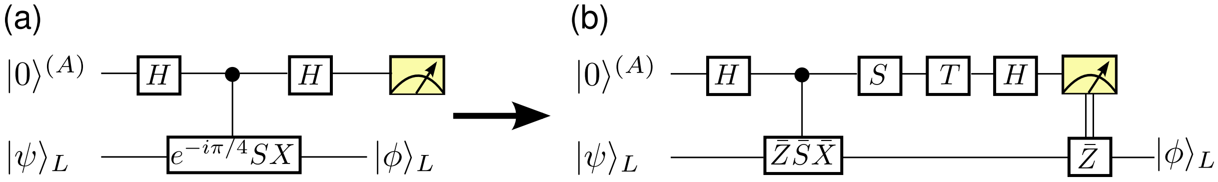

Figure 6.13: FT $\bar{T}$-gate implementation: (a) Realization of the magic state $|\phi\rangle_L$ on the ancilla qubit, required for the implementation of the logical $\bar{T}$-gate. The state $|\phi\rangle_L$ can be prepared by measuring the the operator $M = e^{-i\pi/4}\bar{S}\bar{X}$ on the logical qubit $|\phi\rangle_L$ following the measurement procedure illustrated in Fig. 6.10. (b) Decomposition of the measurement in (a) into transverse operations, enabling the fault tolerant implementation of the $\bar{T}$-gate.

$$1/\sqrt{2}\Big[\underbrace{\big(|0\rangle_L + e^{i\pi/4}\,|0\rangle_L\big)\otimes|0\rangle^{(A)}}_{|\phi\rangle_L} + \underbrace{\big(|0\rangle_L - e^{i\pi/4}\,|0\rangle_L\big)\otimes|1\rangle^{(A)}}_{\bar{Z}|\phi\rangle_L}\Big]. \qquad (6.12)$$

Therefore, measuring the state of the ancilla qubit projects the logical qubit to the right state $|\phi\rangle_L$ if the ancilla qubit is in the state $|0\rangle^{(A)}$. In the other case, where the ancilla qubit is measured in the state $|1\rangle^{(A)}$, the logical qubit will be in the wrong state $\bar{Z}\,|\phi\rangle_L$. The logical $\bar{Z}$ rotation can be easily corrected for by an additional $\bar{Z}$ rotation on the logical qubit. As already mentioned, it was assumed for simplicity that only one physical ancilla qubit is used for the measurement procedure, which does not provide fault tolerance. The scheme presented in Fig. 6.13(b) has to be realized following the verification protocol shown in Fig. 6.11.

6.2.4 Concatenated codes

In the previous section, a detailed introduction to fault tolerant quantum computation was presented with the main focus on the seven-qubit Steane code. It was already mentioned that the error threshold is different for various QEC codes. There is one class of QEC codes based on the idea of concatenation, which was already introduced in terms of the three-qubit code. The basic idea is to encode the logical qubit within multiple layers of a small QEC code, as for example the Steane code [25] or the five qubit QEC code [114]. An example of the concatenation of the Steane code is shown in Fig. 6.14. The error probability p of an operation on the physical qubit is reduced by encoding the information to cp^2, with a code specific constant c. If the encoding is recursively repeated for each qubit in the first layer encoding, then the error probability of an error occurring on the logical encoded qubit is reduced further to c^3p^4 [122, 21]. In general, concatenation of k steps reduces the error rate proportional to p^{2^k}. The concatenation method for the reduction of the failure probability is only successful if the overall failure probability of the encoded qubit is smaller than the error rate of the physical qubit, $cp^2 < p$. The noise threshold p_c is defined by the equality of the equation $cp_c^2 = p_c$. Concatenation of a QEC code reduces the effective error probability on the logical qubit exponentially with k, whereas the overhead in physical qubits scales exponentially with the number of concatenation steps. The provable error rates for concatenated quantum codes are typically on the order of 10^{-5} [123], which is at the limit of the experimentally realizable single-qubit gate fidelities (see Sec. 3.5).

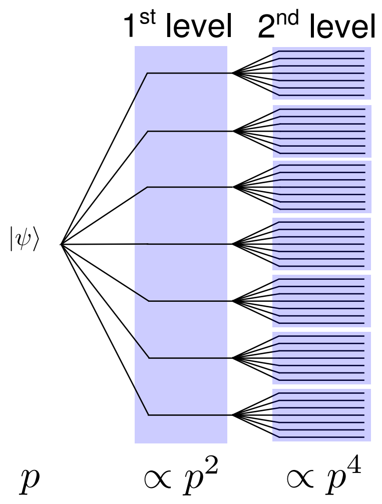

Figure 6.14: Concatenation: A qubit in the state $|\psi\rangle$ is encoded in multiple layers of an elementary QEC code. Here, the principle of concatenation is illustrated by the seven-qubit Steane code. Each layer of encoding reduces the probability of errors occurring on the logical qubit only if the single-qubit error probability is below a certain threshold (see main text).

6.3 Topological Quantum Codes[5]

The realization of FTQC with the Steane code and other different elementary codes, such as the five-qubit (non-CSS-type) code [29, 125] or the nine-qubit code proposed by Shor [26] is typically via concatenation (see Sec. 6.2.4). Concatenation requires a considerable overhead in qubits, which grows exponentially in the number of encoding layers used in the encoding hierarchy. Furthermore error detection and correction generally involves operations between far-distant qubits of the code. In topological quantum error correcting codes, protection of errors is achieved in a qualitatively different way: logical qubits are encoded in large lattice systems of physical qubits. Here, due to the topological nature of the codes, quantum error correction operations, such as measurements of the stabilizer or check operators defining the code space respect the spatial structure of the underlying lattice, i.e. they act on groups of physically neighboring qubits belonging for instance to the plaquettes of the lattice. Due to this locality property topological codes are ideally suited to be embedded in physical 2D architectures [126], where individual qubits and groups of few adjacent qubits can be addressed and manipulated locally [32, 127, 128]. Robustness of logical qubits is achieved by encoding logical qubits in larger and larger lattice structures. Roughly speaking, such large code structures can tolerate more and more errors occurring locally on physical qubits, before the logical quantum information, encoded in global (topological) properties of the many-qubit system, cannot be recovered after the occurrence of too many errors on the register. Provided that single-qubit errors occur with a low enough error rate, and the error syndrome formed by the stabilizer information can be measured with sufficient accuracy, quantum information stored in large topological codes can be protected from errors and processed fault-tolerantly [129]. The robustness and error thresholds have been studied analytically and numerically for various topological quantum codes, including color codes [35, 130–136], and Kitaev's toric code and related models [129, 137–144]. Here, threshold values are code-dependent and also strongly depend on the noise model considered, typically yielding error thresholds on the order of 10^{-2} to 10^{-1} for phenomenological noise models and somewhat lower threshold values on the order of 10^{-3} to 10^{-2} for circuit noise models, where errors are taken into account at the level of imperfections in the quantum circuitry which is required for the readout of the error syndrome.

6.3.1 The toric code

The concatenation of quantum codes provides a way to improve the robustness of a logical qubit. In 1996, A. Yu. Kitaev proposed the realization of fault tolerant quantum computation in a two-dimensional system, which established the field of *topological* quantum error correction [145]. Topology is a mathematical field, which describes objects by global properties instead of the detailed local structures. Thus, different objects with apparently completely different structures can share certain global topological features and being topologically equivalent. One example of such a topological equivalence is *homeomorphism*, which includes the continuous distortion of an object like stretching and bending. Two objects are homeomorphic if they can be mapped to another by continuous deformation. An example of two topologically equivalent objects in terms of homeomorphism is shown in Fig. 6.15(a). Although the coffee mug and the torus seem

---

[5] Some text extracts and pictures of this chapter are similar to Ref. [124].

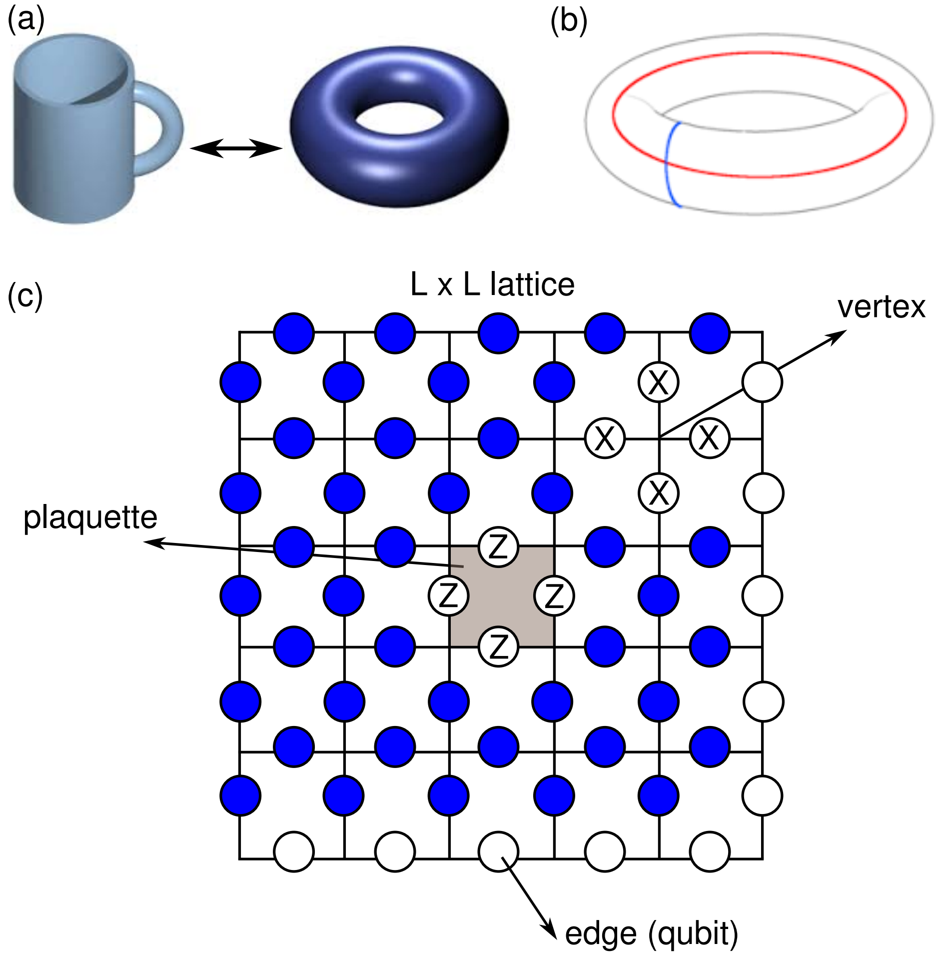

Figure 6.15: Kitaev toric code: (a) Topological quantum computation is based on the idea of encoding information in global properties of a topological system and therefore being robust against local errors. One example of two topologically equivalent objects are the coffee mug and the torus. The two objects can be mapped to each other by continuous deformation - the objects are said to be homeomorphic. (b) Illustration of the Kitaev toric code embedded on the surface of a torus with the logical $\bar{Z}_1$ and $\bar{X}_1$ operation (see main text). (c) The qubits are arranged on the edges of an LxL lattice with the plaquette and vertex operators forming the stabilizer generators.

to be completely different structures, they are topologically homeomorphic.

The basic idea of topological quantum codes is to encode the logical information in global topological properties, which are robust against local deformations (errors). The first topological quantum code proposed by Kitaev - Kitaev's *toric code* - consists of qubits arranged on a two-dimensional lattice wrapped around a torus to fulfil periodic boundary conditions assumed originally by Kitaev (see Fig. 6.15(b)). More precisely, the qubits are arranged on the edges of an L×L lattice, as shown in Fig. 6.15(c). The qubits at the boarder are not filled to illustrate the periodic boundary conditions. In total there are $N = 2L^2$ qubits on an L×L toric code. The Kitaev toric code belongs to the class of stabilizer codes, which requires the existence of stabilizer generators as well as logical $\bar{X}$ and $\bar{Z}$ operators for each encoded qubit. The toric code defines two different types of stabilizer generators, associated geometrically with *plaquettes* and *vertices*. The plaquette operators are products of Z-type operations acting on four qubits surrounding one particular plaquette, as highlighted in Fig. 6.15(c). The second type of stabilizer operators are tensor products of X-type Pauli operators acting on four qubits nearby to a vertex. In total there are L^2 plaquette and vertex operators. As already mentioned in the previous section, the stabilizer generators of a stabilizer code have to commute with each other. Operators, which are not adjacent mutually commute with each other, since all operators belong to different qubits. Neighboring plaquette and vertex operators are commuting, since they share one qubit with each other and each operator commutes trivially with itself. In the case of neighboring plaquette and vertex operators the situation is slightly different, since they share two different qubits. The X and Z operators are acting both on the two respective qubits. Although X and Z Pauli operators do not commute, the tensor product operators $X \otimes X$ and $Z \otimes Z$ are commuting with each other and therefore also adjacent vertex and plaquette operators commute.

How many logical qubits are encoded by the toric code? To answer this question we have to count the number of independent stabilizer generators. A trivial answer would be that there are L^2 plaquette and vertex operators, but the product of all plaquette operators (vertex operators) is resulting in the identity operation. Therefore, the plaquettes (vertices) do not form an independent set of generators. The solution is simply to remove one plaquette and vertex operator from the whole set. Therefore, with $L^2 - 1$ independent plaquette (vertex) operators and $2L^2$ qubits, the toric code encodes $2L^2 - 2(L^2 - 1) = 2$ logical qubits. This section provides only a summary of the toric code, since a more detailed discussion would be beyond the scope of the current work. Further details are presented in [145, 146, 123].

Each of the encoded logical qubits is associated with two logical operations $\bar{Z}$ and $\bar{X}$. It can be shown that the logical $\bar{Z}_1$ operation of the first encoded qubit corresponds to a closed loop of Z operations winding around the torus, as shown in Fig. 6.16 (red line). The logical $\bar{X}_1$ operation on the first qubit has to anti-commute with the logical $\bar{Z}_1$ operation. The logical $\bar{X}_1$ operation for the toric code is defined by a closed loop of X operations around the torus perpendicular to the $\bar{Z}_1$ loop but shifted from the original lattice edge by half a lattice cell (see Fig. 6.16 (green line)). The shifted lattice is also called *dual* lattice, which offers a convenient tool to describe the toric code. The vertex operators of the original lattice corresponds to plaquette operators in the dual lattice and vice versa. Obviously, the logical $\bar{Z}_1$ and $\bar{X}_1$ operation share only one qubit at the point of intersection and therefore anti-commute with each other. The two logical operations of the first encoded qubit are also illustrated by the red and blue loop around the torus in Fig. 6.15(b). The logical $\bar{Z}_2$ and $\bar{X}_2$ operation on the second encoded qubit are obtained by turning the $\bar{Z}_1$ and $\bar{X}_1$ operations by 90°.

Errors affecting the lattice qubits are detected by measuring the stabilizer generators, which is a unique feature of any stabilizer code. If no error occurred, then the eigenvalues of all vertex and plaquette operators are +1. Let us assume that a single qubit Z error occurs anywhere in the lattice. All plaquette operators will commute with the error, since $Z^2 = \mathbb{1}$. In contrast, the vertex operators directly adjacent to the affected qubit will not commute with the error operation, since Z and X Pauli operations anticommute. Therefore, a Z error will result in a -1 eigenvalue of the neighboring vertex operators. In the case of a string of Z errors only the vertex operators at the end of the error string are affected. An example of a string of a string of Z errors with the corresponding error syndrome is shown in Fig. 6.17(a). The appearance of a string of X errors in the dual lattice leads to a flip of the neighboring plaquette operators in the original lattice or

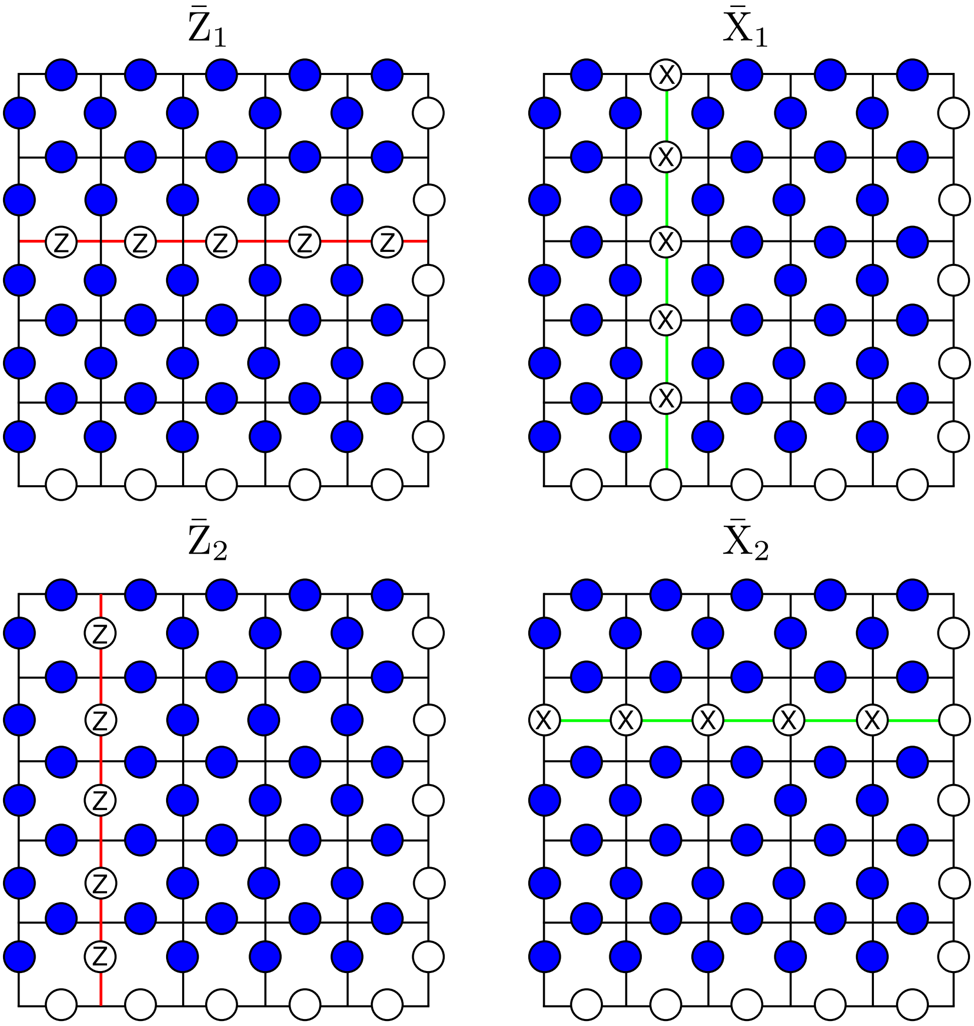

Figure 6.16: Logical operations: The logical operations $\bar{Z}_1$, $\bar{X}_1$ and $\bar{Z}_2$, $\bar{X}_2$ of the two encoded qubits are implemented by Z-and X-type string operators around the torus. The logical operations of the two encoded qubits are perpendicular to each other [146, 123].

of the vertex operator in the dual lattice, which is sketched in Fig. 6.17(b). In both cases, the error syndrome results in a flip of the eigenvalue of stabilizer generators at the end of the string.

The correction of errors can be performed by applying the inverse to the error operation E, or the same operation in the case of the Pauli Z and X operators. Here, the difficulty is to find the correction operation to a certain measured error syndrome, since different errors can lead to the same error syndrome. Therefore, the relation between the errors and the error syndrome is not unique. If the correction operation C obtained from the measured syndrome differs only by a stabilizer operator S from the real error E, meaning that $EC = S$, then the combination of the error chain E and the correction operation C will effectively generate a stabilizer operation and leaves the encoded qubit invariant [146]. This leads to a successful correction of the error. If the combined operation EC forms a closed loop around the whole torus corresponding to a logical operation, then the encoded qubit is not corrected successfully. The "guessing" of the right correction step given a certain syndrome measurement is performed by certain decoding

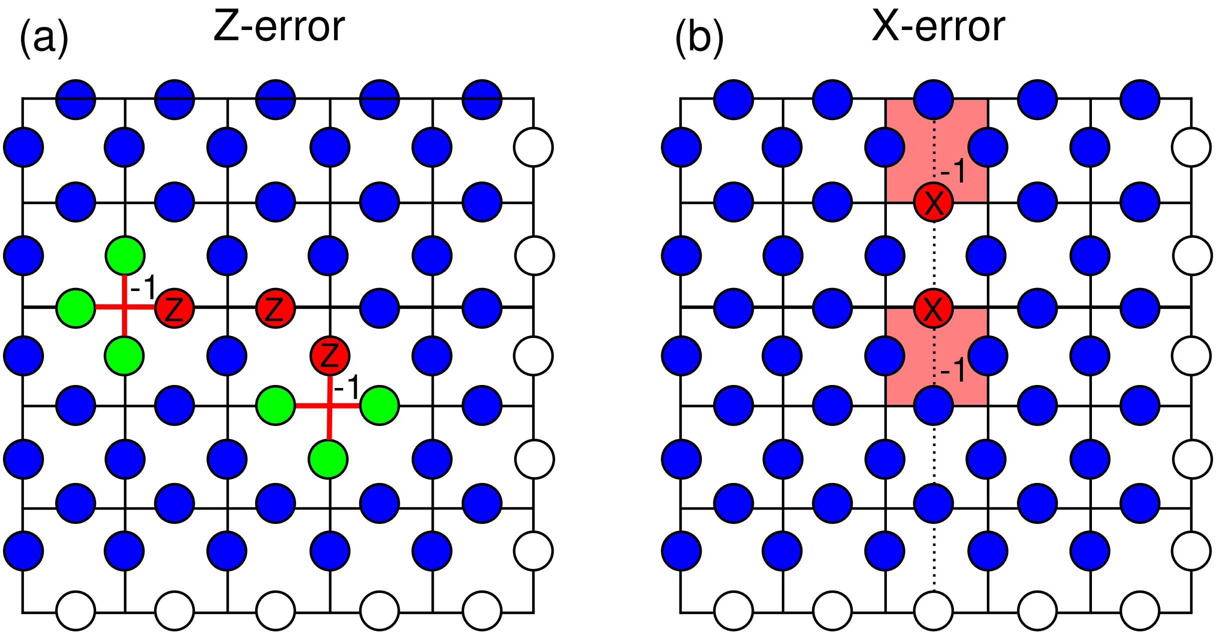

Figure 6.17: Error detection in the toric code: Error syndrome of Z-errors (phase-flip) and X-errors (bit-flip) in the toric code. (a) The appearance of Z-errors lead to a flip of the vertex operators at the end of the errors string, whereas bit-flip errors implicate a flip of plaquette operators in the original lattice connecting the error string (b) (see main text) [146, 123].

algorithms, as for example the minimum weight algorithm, which finds the minimum weight error string leading to the measured syndrome [146].

6.3.2 The surface code

One assumption for the originally proposed realization of the toric code was the periodic boundary condition. This assumption seems to be inconvenient from a practical perspective. Bravyi and Kitaev described the realization of the toric code on a lattice with boundaries, which promises to be a more realistic implementation [147]. Compared to the toric code, the surface code shows two different kind of boundaries - the rough and smooth boundaries, which is illustrated in Fig. 6.18. At the boundary of the lattice, the stabilizer generators are modified to act only on three instead of four qubits. As illustrated in Fig. 6.18, the surface code consists of two different kind of qubits - the data qubits (blue big dots) arranged on the edges of the 2D lattice and the syndrome qubits (red small dots), which are located between the data qubits. The stabilizer generators consist of the previously introduced Z-type plaquette operators and X-type vertex operators, which act on the four qubits respectively and commute with each other. The smallest instance of the surface code consists of 13 physical qubits, encoding one logical qubit with a code distance of 3 ([[13,1,3]]) [146, 123]. However, there exists a rotated surface code with distance d=3 that requires only 9 instead of 13 qubits [148]. Note that if the boundaries of the lattice are all equal, then there is effectively no logical qubit encoded. Here, the logical operators correspond to the topological property of deformable but non-contractible strings that connect opposite boundaries of the same type. This is similar to the Kitaev toric code, where

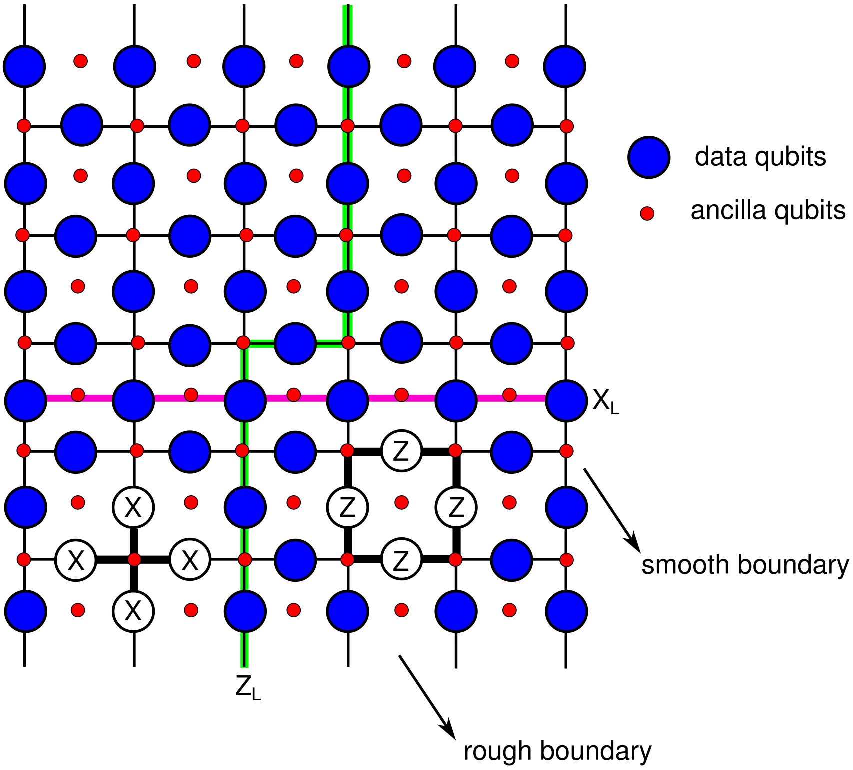

Figure 6.18: Surface code: Illustration of the surface code following the approach of Ref. [34]. The surface code consists of the data qubits (blue big dots) arranged on the edges of the lattice and the syndrome qubits (red small dots) adjacent to the data qubits. The stabilizer generators as well as the logical operators are defined similar to the toric code with the difference that the stabilizers at the boundaries are acting on three qubits [146, 123]. The syndrome qubits are used to prepare the logical qubit and reveal the syndrome by measuring the stabilizer generators.

logical operators are encoded in non-contractible loops around the torus [146, 123, 145]. The logical $\bar{Z}_L$ operator acting on the logical qubit corresponds according to Fig. 6.18 to a string of Z operators connecting the rough boundaries of the lattice. In contrast, the logical $\bar{X}_L$ operator is equal to a string of X operators connecting the smooth boundaries. In general, with $L^2 + (L-1)^2$ physical qubits arranged on a LxL lattice and encoding one logical qubit, the parameters of the surface code are $[[L^2 + (L-1)^2, 1, L]]$. A more detailed introduction to the surface code and the implementation of fault tolerant quantum computation is presented in Ref. [34]. The purpose of the syndrome qubits appearing in the surface code is the readout of the stabilizer generators by mapping the information of the generators to the syndrome qubits using the technique described in Sec. 6.2.2. Additionally, the syndrome qubits are used to prepare the logical qubit in the +1 eigenstate of the stabilizer generators [34].

As already pointed out in the introduction of the Steane code, the main goal is the fault tolerant implementation of a universal set of gates on the logical qubit. Here, a brief description of the main ideas for the realization of fault tolerant quantum computation on the surface code is given. The implementation of a universal set of gates requires arbitrary operations on one logical qubit as well as CNOT operations on two logical qubits. The Hadamard operation can be implemented "transversely" in the surface code with the drawback of rotating the whole lattice by 90°. The lattice can be rotated back to the original orientation, as described in Refs. [34, 146]. The implementation of the phase gate K as well as the T-gate to perform arbitrary single-qubit operations on the logical qubit can be realized with state injection. The basic idea of the state injection in the surface code is similar to the method described in Sec. 6.2.3 and will not be discussed here. A nice overview of state injection in the surface code is presented in [34, 148].

There are two substantially different ways of encoding a logical qubit in the surface code and performing multi-qubit operations [34, 146]. The first method is to encode several logical qubits within one lattice, whereas in contrast the second method is encoding one logical qubit in one lattice and using multiple lattices for computation.

As already mentioned before, the encoding of one logical qubit in one lattice requires two different boundaries (see Fig. 6.18). A qubit can also be encoded by creating a "hole" in the lattice. The expression "hole" does not mean that a set of qubits are removed physically from the lattice. A hole is created by just removing for example a subset of plaquette operators and the vertex operators acting on the qubits inside the hole. The induced hole is called "smooth hole", because the boundary of the hole is smooth (see Fig. 6.19(a)). The logical $\bar{Z}_S$ operator of the smooth hole qubit corresponds to the Z-loop around the hole and the $\bar{X}_S$ operator corresponds to the X-string connecting the hole region with the outer boundary of the lattice. In the case of two smooth holes forming one logical qubit, then the logical $\bar{X}_S$ operator connects the two boundaries of the hole, which is indicated in Fig. 6.19(a). The qubits inside the plaquette are disconnected from the lattice. The same procedure can of course be applied to the vertex operators, creating a rough qubit with the corresponding logical operators $\bar{Z}_R$ and $\bar{X}_R$ (see Fig. 6.19(b)). The CNOT operation between the smooth and rough qubit can be realized by moving the smooth qubit around the rough qubit, which is also known as *braiding* [34].

Encoding one logical qubit in one lattice is also known as planar logical qubit. One approach towards the implementation of a CNOT gate between two planar logical qubits are bit-wise CNOT operations between adjacent lattice qubits. A different method proposed in Ref. [148] is to merge and split the planar qubits, which also leads to the possibility of creating a CNOT operation. The splitting and merging of two lattices is also known as *lattice surgery* (see Fig. 6.19(b)). The main advantage of the braiding approach with respect to the transversal CNOT gate between two encoded qubits is that only nearest neighbor interaction is required. On the other hand, the braiding method needs more qubit overhead than the lattice surgery approach, also maintaining nearest neighbor interactions. In Ref. [148], the realization of a CNOT gate using lattice surgery is proposed with 53 physical qubits instead of 143 qubits using the braiding technique.

6.3.3 The color code

The color code belongs to the class of topological stabilizer codes and was originally proposed by H. Bombin and M. A. Martin-Delgado [128, 149]. In contrast to the Kitaev code, topological color codes offer the distinctive feature that the entire group of Clifford gate operations can be implemented transversely [21]. This versatile set of operations directly enables protocols for quantum distillation of entanglement, quantum teleportation and dense coding with topologi-

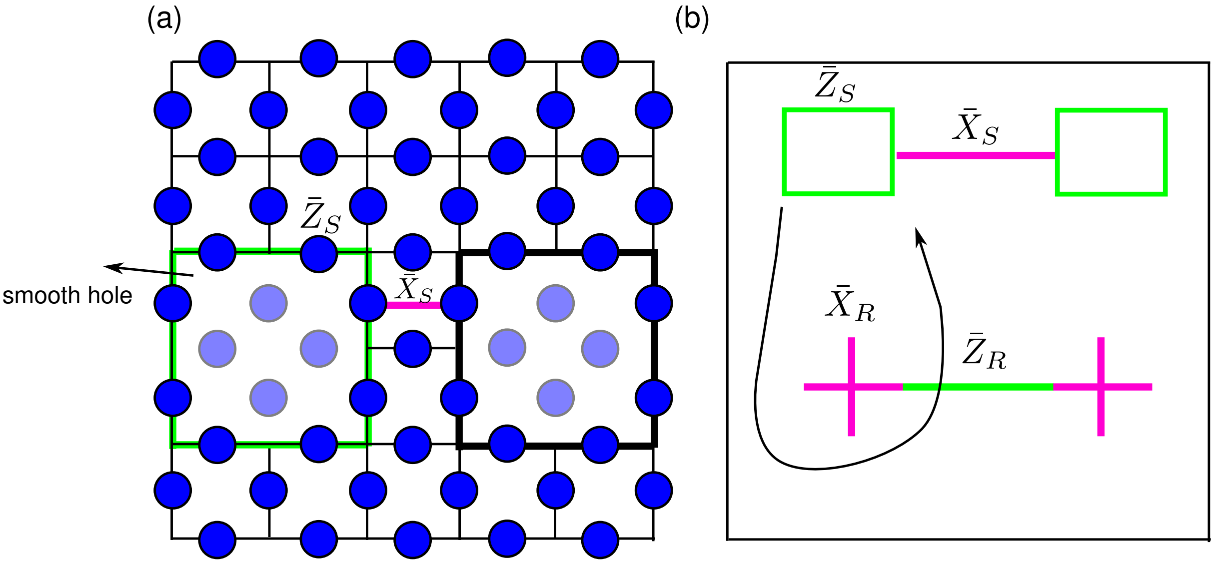

Figure 6.19: CNOT operation via braiding: (a) Illustration of a smooth hole qubit consisting of two smooth holes with the corresponding logical operators $\bar{Z}_S$ and $\bar{X}_S$. The holes are generated by removing a set of plaquette operators (in this case four). The same procedure can be done to create a rough qubit by removing vertex operators. In (b) the realization of a CNOT gate between a smooth and rough qubit is shown by moving the smooth qubit around the rough qubit. This procedure is known as braiding [34, 146].

cal protection [128]. Moreover, a universal gate set, enabling the implementation of arbitrary quantum algorithms, can be achieved by complementing the Clifford operations with a single non-Clifford gate [21]. For color codes in two-dimensional (2D) architectures [128], such an additional gate can be realized by magic-state injection [121], which was already described in Sec. 6.2.3. Remarkably, 3D color codes enable the implementation of a universal set of gates on the logical qubit only using transversal operations and without the need of magic-state injection, which is not possible within the Kitaev code [149]. Furthermore, 3D gauge color codes allow the implementation of single-shot error correction protocols, as proposed in Ref. [150].

Two-dimensional color codes are topological quantum error-correcting codes that are constructed on underlying 2D lattices [128] for which three links meet at each vertex and three different colors are sufficient to assign color to all polygons (plaquettes) of the lattice such that no adjacent plaquettes sharing a link are of the same color. The smallest, fully functional 2D color code involves seven qubits and consists of a triangular, planar code structure formed by three adjoined plaquettes with one physical qubit placed at each vertex. The minimal instance of the color code is demonstrated in Fig. 6.20(a). As all stabilizer codes, the color code is defined by a set of commuting stabilizer operators $\{S_i\}$, each having eigenvalues +1 or -1. More precisely, the code space hosting logical or encoded quantum states $|\psi\rangle_L$ is fixed as the simultaneous eigenspace of eigenvalue +1 of all stabilizers, $S_i\,|\psi\rangle_L = +\,|\psi\rangle_L$ [151, 21]. In color codes, there are two stabilizer operators associated with each plaquette, which for the seven-qubit color

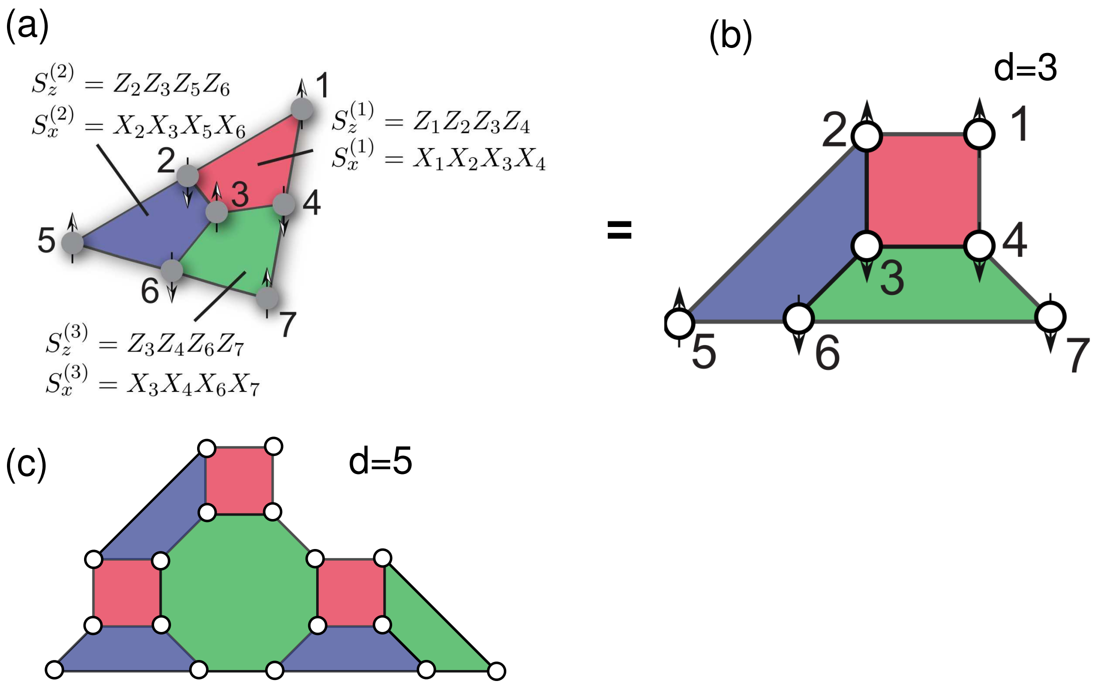

Figure 6.20: Two-dimensional color code: (a) One logical qubit is embedded in seven physical qubits forming a 2D triangular planar code structure of three plaquettes. The code space is defined via six stabilizer operators $S_x^{(i)}$ and $S_z^{(i)}$, each acting on a plaquette which involves four physical qubits. (b) The same quantum code as in (a) with a different visual representation of the plaquettes. (c) The minimal instance with distance d=3 can be sclaced up to the distance d=5 color code that can correct at least arbitrary errors on any of the 17 qubits. (picture also shown in Ref. [124])

code (see Fig. 6.20(a)) results in the set of four-qubit X and Z-type operators

$$\begin{aligned} S_x^{(1)} &= X_1X_2X_3X_4, & S_z^{(1)} &= Z_1Z_2Z_3Z_4, \\ S_x^{(2)} &= X_2X_3X_5X_6, & S_z^{(2)} &= Z_2Z_3Z_5Z_6, \\ S_x^{(3)} &= X_3X_4X_6X_7, & S_z^{(3)} &= Z_3Z_4Z_6Z_7. \end{aligned} \tag{6.13}$$

Here, X_i, Y_i and Z_i denote the standard Pauli matrices acting on the i-th physical qubit with the computational basis states $|0\rangle$ and $|1\rangle$ [21]. The stabilizers in Equ. (6.13) impose six independent constraints on the seven physical qubits and thus allows the encoding of one logical qubit. The logical basis states $|0\rangle_L$ and $|1\rangle_L$ spanning the code space are entangled seven-qubit states and given as the eigenstates of the logical operator $Z_L = Z_1Z_2Z_3Z_4Z_5Z_6Z_7$, where $Z_L\,|0\rangle_L = |0\rangle_L$ and $Z_L\,|1\rangle_L = -\,|1\rangle_L$ [128]. Fig. 6.20(b) shows a slightly different illustration of the minimal color code instance with distance d=3. This representation clearly shows the construction of the two-dimensional color code consisting of 17 qubits and with distance d=5 (Fig. 6.20(c)).

The seven-qubit color code with distance d=3 has the capability to detect and correct single-qubit errors. As for all stabilizer codes, errors on the physical qubits are detected by measuring the expectation values of the stabilizer generators - syndrome measurement. A single-qubit error on the encoded logical qubit shown in Fig. 6.20(a) leads to a sign flip of the eigenvalue of

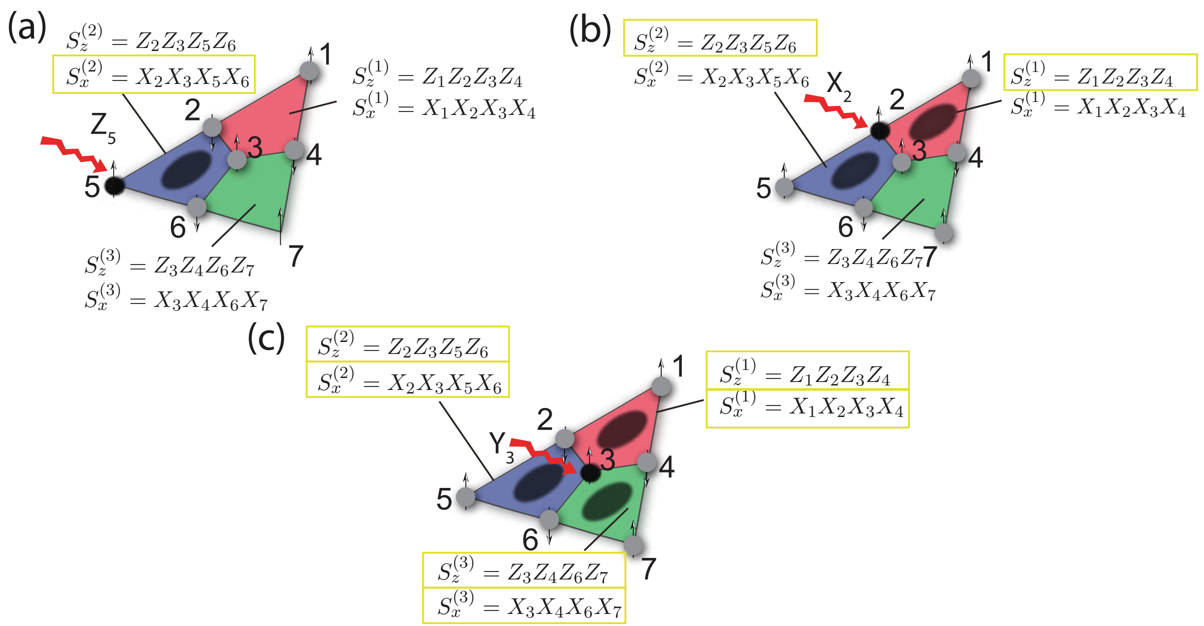

Figure 6.21: Error detection: Different errors occurring on the logical qubit (red arrow) affects the corresponding plaquettes (black-shaded ellipse) and induces a sign change of the eigenvalues of different plaquette operators (yellow boxes). (a) Phase-flip error on qubit 5 induces a sign change of the $S_x^{(2)}$ operator, whereas a bit-flip error on qubit 2 (b) leads to a change of the Z-type stabilizers $S_z^{(1)}$ and $S_z^{(2)}$. (c) A combined X-and Z-type error (Y error) on qubit 3 manifests itself in negative eigenvalues of all 6 plaquette operators. (picture also shown in Ref. [124])

at least one plaquette operator from +1 to -1. An example of three different errors affecting the logical qubit encoded in the seven-qubit color code is demonstrated in Fig. 6.21. Fig. 6.21(a) shows a phase-flip error on qubit 5 (red arrow), which affects the stabilizer of the second (blue) plaquette (visualized by the black-shaded ellipse) and leads to a negative eigenvalue of the $S_x^{(2)}$ plaquette operator (visualized by the yellow box). A bit-flip error on qubit 2 is affecting both Z-type stabilizers of the first (red) and second (blue) plaquette and manifests itself by negative eigenvalues of the $S_z^{(1)}$ and $S_z^{(2)}$ (see Fig. 6.21(b)). Fig. 6.21(c) shows a combination of a bit-flip and phase-flip error on qubit 3, which induces a sign change of all 6 plaquette operators. The examples illustrated in Fig. 6.21 indicate that Z-type errors manifest themselves in a violation of the X-type stabilizers and X-type errors in a violation of the Z-type stabilizers, which reveals the CSS character of the topological color code.

As described above, errors in the Kitaev code show up by a sign flip of the vertex (plaquette) operators at the end of the errors string (see Sec. 6.3.1). The appearance of errors in the color code is demonstrated by a larger 2D color code system with distance d=11 (see Fig. 6.22), able to correct 5 errors. In the left part of the lattice, a scenario is shown where, a sequence of single-qubit errors of the same type, e.g. bit-flip errors (indicated by red wiggled arrows), affects four physical qubits (marked by black filled circles). This physical error chain results in an error chain (white dashed line), where the (equally-colored) plaquettes at the two end points of the chain are in -1 eigenstates of the corresponding ($S_z^{(i)}$) stabilizer operators - these stabilizer

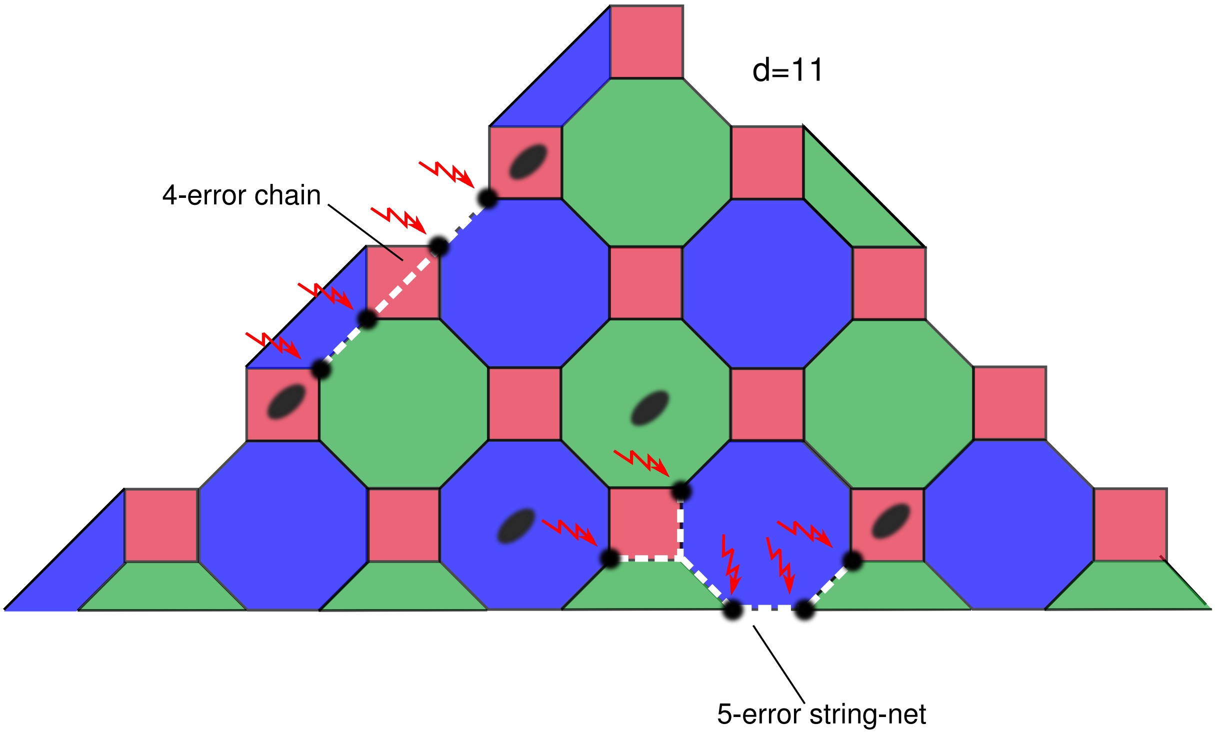

Figure 6.22: Branching of error string nets: The occurrence of an error string is illustrated in the left part of the figure by the 4-error chain. The four errors (indicated by red wiggled arrows) induce a flip of the eigenvalues of the corresponding plaquette operators at the end of the error string, visualized by the black-shaded ellipses. A different scenario is shown in the lower part of the figure by inducing 5 physical errors. These errors result in an error string-net, which undergoes branching and affects three different plaquettes (three endpoints of the string-net). This distinctive feature of the color code cannot be observed in the Kitaev code. (picture also shown in Ref. [124])

violations are indicated as black-shaded ellipses on the red plaquettes. This behaviour is similar to the occurrence of errors in the Kitaev code. A distinctive feature of color codes compared to the Kitaev code is that sequences of physical errors (such as the combination of 5 physical errors shown in the right part of the lattice) cannot only be connected by chains, but also result in error string-nets (dashed white line) that undergo branching [128, 149]. In the displayed example, the string-net has three endpoints terminating at the three plaquettes of different colors, which will display stabilizer violations (-1 eigenvalues) of the associated plaquette operators in the syndrome measurement.

Chapter 7

Experimental implementation of the color code[1]

This chapter presents a detailed description of encoding a topological qubit within seven physical qubits, building the minimal instance of a topological color code. Furthermore, the realization of transversal Clifford operations on the encoded logical qubit, being a fundamental requirement for FTQC, is shown. The details concerning the experimental system and operations are addressed in Chapter 3. Main parts of the presented results are also discussed in [124].

7.1 Encoding of the logical qubit

The code space hosting logical states $|\psi\rangle_L$ is fixed as the simultaneous eigenspace of eigenvalue +1 of the six $S_x^{(i)}$ and $S_z^{(i)}$ stabilizer operators, defined in Sec. 6.3.3. The initial preparation of the logical state $|0\rangle_L$ (encoding) is realized deterministically by applying the quantum circuit illustrated in Fig. 7.1 to the seven-ion system. The first initialization step of the seven-qubit system in the logical $|0\rangle_L$ state consists of converting the state of the 7 qubits, initialized by optical pumping in the state $|1111111\rangle$, into the state $|1010101\rangle$. This state fulfills the Z-type stabilizer constraints, as it is a +1 eigenstate of three $S_z^{(i)}$-stabilizers as well as of the logical operator Z_L. In the remaining three steps, the subsets of four qubits belonging to each of the three plaquettes of the code, are sequentially entangled to also fulfill the stabilizer constraints imposed by the three operators $S_x^{(i)}$. This is achieved by spectroscopically decoupling the ions hosting inactive qubits (e.g. qubits 5, 6, and 7) not participating in the plaquette-wise entangling operation, shown in Fig. 7.1.

Spectroscopically decoupling and recoupling

For the experimental initialization of the encoded qubit in the logical state $|0\rangle_L$, the main resource is an entangling operation acting on a subset of four out of seven qubits. Fig. 7.2A shows a more detailed circuit diagram of the sequence used for encoding. In the first step an entangling operation $MS(\pi/2, 0)$ is to be applied to ions 1, 2, 3, 4 without affecting the ions

---

[1] Text paragraphs, pictures and data of the following chapter are based on the original work Ref. [124] and presented in a more detailed way.

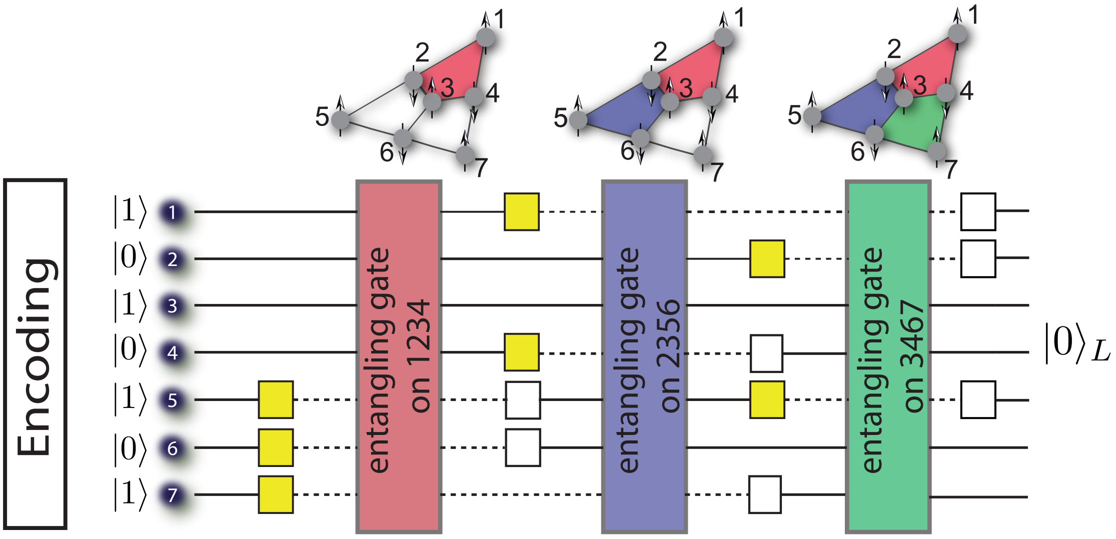

Figure 7.1: Initialization of a topological encoded qubit: Encoding of the logical qubit is achieved by coherently mapping the input state $|1010101\rangle$ onto the logical state $|0\rangle_L$, using a quantum circuit that combines plaquette-wise entangling operations with de- and recoupling pulses (yellow and white squares, respectively). Dashed (solid) lines denote decoupled or inactive (recoupled or active) qubits (picture also shown in Ref. [124]).

5, 6 and 7. However, as the laser beam of the entangling MS gate operation illuminates the entire ion string, an entangling operation on a subset of ions can be achieved in two different ways: One can resort to refocusing techniques, as originally pioneered in NMR systems [152]. Here, partially entangling *global* MS gate operations are interspersed with single-qubit ac-Stark shifts, which eventually lead to an effective decoupling of (subsets of) ions from the entangling dynamics of the remaining ions (see e.g. [153] for more information). However, in the present case, such decoupling of 3 ions, using refocusing pulses, from the entangling dynamics of the remaining 4 qubits belonging to one plaquette of the quantum code, would require a large overhead in terms of (partially entangling) MS gate operations and addressed, single-ion refocusing pulses. Thus, in the present experiment we pursue an alternative approach, where we decouple ions *spectroscopically* from the dynamics induced by the global MS gate operation. To this end, we coherently transfer and store the quantum state of qubits (say 5, 6 and 7) encoded in the states $S_{1/2}(m_j = -1/2)$ and $D_{5/2}(m_j = -1/2)$, which do not participate in the entangling dynamics of qubits 1, 2, 3, and 4, in a subset of the remaining Zeeman levels.

The latter has the advantage that the entangling operation, acting only on the subset of 4 qubits in a 7 ion string, can be realized with a fidelity of 88.5(5)%, as determined by a 4-qubit state tomography of the created 4-qubit GHZ state, $(|0101\rangle + |1010\rangle)/\sqrt{2}$. Besides imperfections in the entangling operation, this value thus also includes the effect of small imperfections in the preparation of the initial product state $|1010\rangle$. The fidelity of the entangling operation on 4 out of 7 ions is substantially higher than the fidelity with which a seven-qubit GHZ state can be created by a global entangling operation (acting on all 7 ions). From population and parity measurements we estimate the fidelity for a 7-ion entangling operation to be about 84%. Generating the required entangling operation on 4 out of 7 qubits would require two of theses operations and therefore lead to poor performance. In Fig. 7.2, the decoupling (DEC) steps, highlighted as colored boxes (DEC) are illustrated by a reduced level scheme of the relevant Zeeman states. The decoupling sequence can be adapted, so that – depending on the internal state of the physical qubit – only a minimal number of decoupling pulses have to be applied. For example, the decoupling of qubits 5 and 6 (blue and red box) before the first entangling operation is realized as follows: The population of qubit 5 (initially entirely in state $S_{1/2}(m_j = -1/2)$) is transformed to the $D_{5/2}(m_j = -5/2)$ state via a pulse sequence of 3 coherent single-qubit operations: a resonant $\pi/2$-pulse $U^{(5)}(\pi/2, \theta)$ with arbitrary, but fixed phase θ on qubit 5, followed by a Z rotation $U_Z^{(5)}(\pi)$ and finally another resonant $U^{(5)}(\pi/2, \theta - \pi)$ rotation with phase $\theta - \pi$. Effectively, this sequence realizes a π-flop (i.e. complete population transfer) between the computational basis state $S_{1/2}(m_j = -1/2)$ and the storage state $D_{5/2}(m_j = -5/2)$. This population transfer could in principle also be performed by a single resonant $U^{(5)}(\pi, \theta)$ pulse. The reason for splitting this up into 3 addressed pulses is to minimize errors on neighboring ions, which is described in Sec. 3.4.4

Similarly, spectroscopic decoupling of ions with population being entirely in the $D_{5/2}(m_j = -1/2)$ state is achieved by transferring the electronic population first to the $S_{1/2}(m_j = 1/2)$ ground state and subsequently to the $D_{5/2}(m_j = -3/2)$ state, as shown in the red box of Fig. 7.2B. This sequence requires in total 3 single-qubit operations: $U^{(6)}(\pi/2, \theta)$, $U_Z^{(6)}(\pi)$ and $U^{(6)}(\pi/2, \theta - \pi)$ on the $D_{5/2}(m_j = -1/2) \rightarrow S_{1/2}(m_j = 1/2)$ transition, and a similar 3-pulse sequence on the $S_{1/2}(m_j = 1/2) \rightarrow D_{5/2}(m_j = -3/2)$ transition, respectively. Therefore, decoupling and also recoupling (REC) of one qubit with populations in (and coherences between) both computational basis states requires in total 9 single-qubit operations with a pulse length of about 10 μs per pulse (see green box in Fig. 7.2B). It should be noted that although this requires resonant operations on the addressed laser beam, no phase coherence between this beam and the global laser beam is required, as the phase of the addressed beam drops out after recoupling.

The MS gate operation, applied to the remaining active qubits (say, qubits 1, 2, 3, and 4) creating the four-qubit GHZ-type entangled state. Under this operation, for instance in the first step the state $|1010101\rangle$ is mapped onto the superposition $|1010101\rangle \pm i|0101101\rangle$ (see e.g. [153]). The $\pm\pi/2$ phase shift of this state with respect to the target state $|1010101\rangle \pm |0101101\rangle$ can be compensated for at any later instance during the remaining encoding sequence. To this end, after the encoding sequence we apply an ac-Stark shift compensation pulse $U_Z^{(1)}(\pm\pi/2)$ on qubit 1 located at the corner of the first (red) plaquette, which does not participate in entangling operations of the other two plaquettes. Thus, the four-qubit entangling operation in combination with the phase compensation pulse creates the $|1010101\rangle + |0101101\rangle$ superposition state after the first step of the encoding sequence. The successful preparation of this intermediate state is indicated by the measurement of electronic populations in the $2^7 = 128$ computational basis states and the stabilizer operators, as shown in Fig. 7.3(A). Here, the data shows the two dominant expected populations, as well as the GHZ-type coherence as signaled by the non-vanishing expectation value of $S_x^{(1)}$.

In the second and third step, similarly, entanglement between the qubits of the second (blue) and third (green) plaquette is created, which is reflected (see Fig. 7.3B and C) by the appearance of electronic populations in the four and eight expected computational basis states, respectively, as well as by the step-wise build-up of non-vanishing coherences $\langle S_x^{(2)} \rangle$ and $\langle S_x^{(3)} \rangle$. After the third step and the application of the three phase compensation pulses the encoding of the sys-

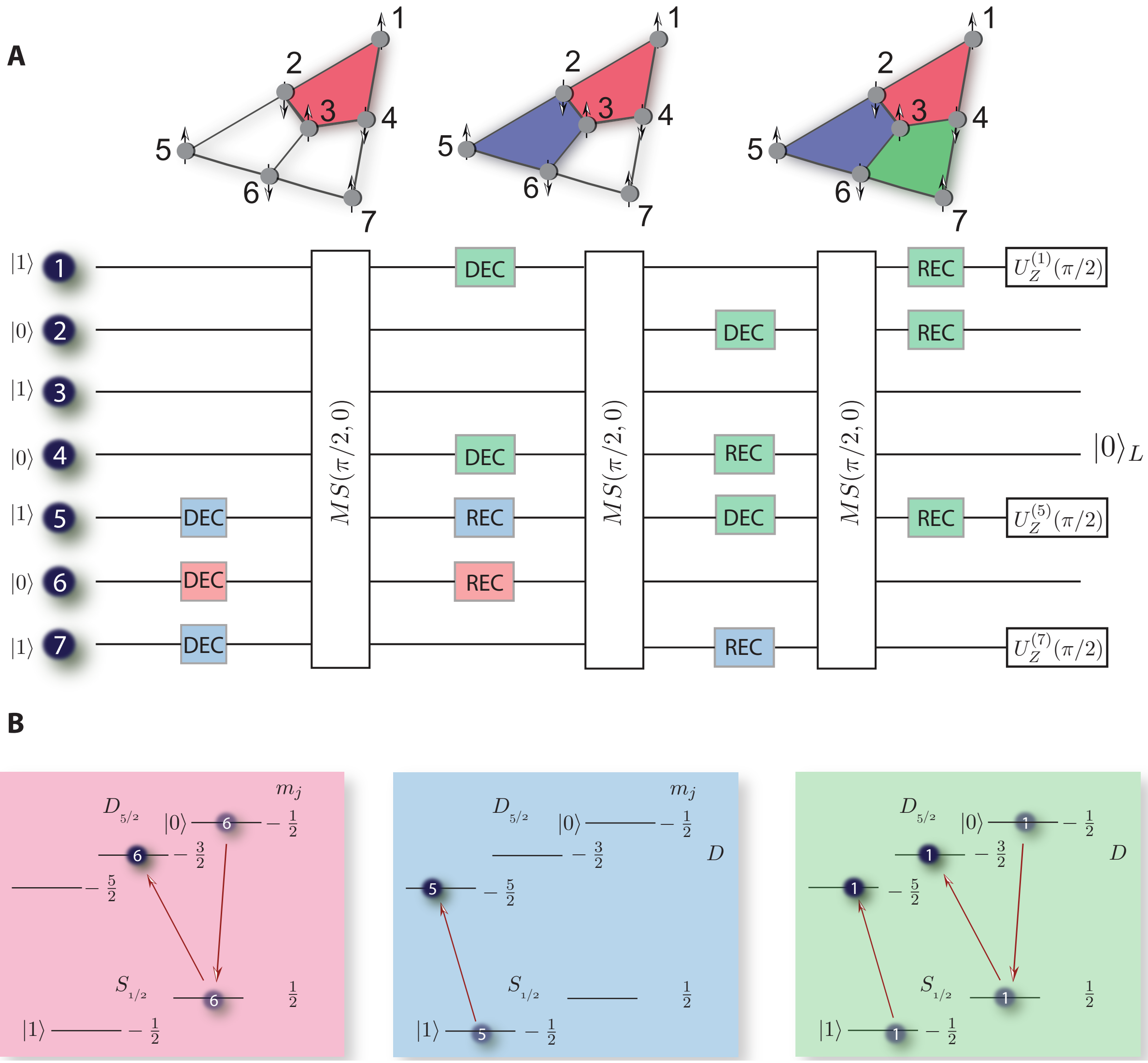

Figure 7.2: Spectroscopically decoupling and encoding: (**A**) Circuit diagram of the encoding step - preparation of the seven-qubit system in the logical state $|0\rangle_L$. The encoding consists of three steps, where consecutively all three colored (red, green, blue) plaquettes are prepared by applying an entangling MS gate on the subset of qubits involved in the plaquette under consideration (e.g. qubits 1, 2, 3 and 4 for the plaquette), starting in the initial product state $|1010101\rangle$. (**B**) The qubits, which do not participate in a particular plaquette, are not affected by the entangling operation by means of spectroscopic decoupling pulses (DEC). Here, their quantum state is stored in additional electronic levels, by coherently transferring the electronic population of the $S_{1/2}(m_j = -1/2)$ and $D_{5/2}(m_j = -1/2)$ qubit states to the Zeeman“storage" states $\{D_{5/2}(m_j = -5/2), D_{5/2}(m_j = -3/2)\}$ by a sequence of up to 9 addressed single qubit rotations. The working principle of the decoupling and recoupling (REC) pulses is illustrated in (B) and described in detail in the main text. (picture also shown in Ref. [124]).

tem in the logical state $|0\rangle_L = |1010101\rangle + |0101101\rangle + |1100011\rangle + |0011011\rangle + |1001110\rangle + |0110110\rangle + |1111000\rangle + |0000000\rangle$ is signaled by positive (ideally +1) values of all six stabilizer and the logical Z_L operator.

The described three-step sequence realizing plaquette-wise entangling operations to prepare the system in the state $|0\rangle_L$ works in principle by starting in any of the eight components $\{|1010101\rangle + |0101101\rangle + |1100011\rangle + |0011011\rangle + |1001110\rangle + |0110110\rangle + |1111000\rangle + |0000000\rangle\}$ of state $|0\rangle_L$. The advantage of choosing the initial input state $|1010101\rangle$ (instead of e.g. $|0000000\rangle$) is that for this initial state the seven-qubit state is during part of the encoding sequence in a decoherence-free subspace (DFS), in which the system is insensitive to global phase noise, as caused by magnetic field and laser fluctuations of the, which to leading order affect all ions in the same way. This type of noise constitutes one of the dominant noise sources in our setup [38]. Whereas the ideal quantum state after the second state (as given explicitly in Fig. 7.3B) still resides entirely in a DFS, the final state still benefits from partial protection with respect to the described global noise. This partial phase noise protection is described in Sec. 7.7 and essential to achieve the proper initialization of the system in the code space, despite the complexity and overall length of the complete encoding sequence (see Table 7.1).

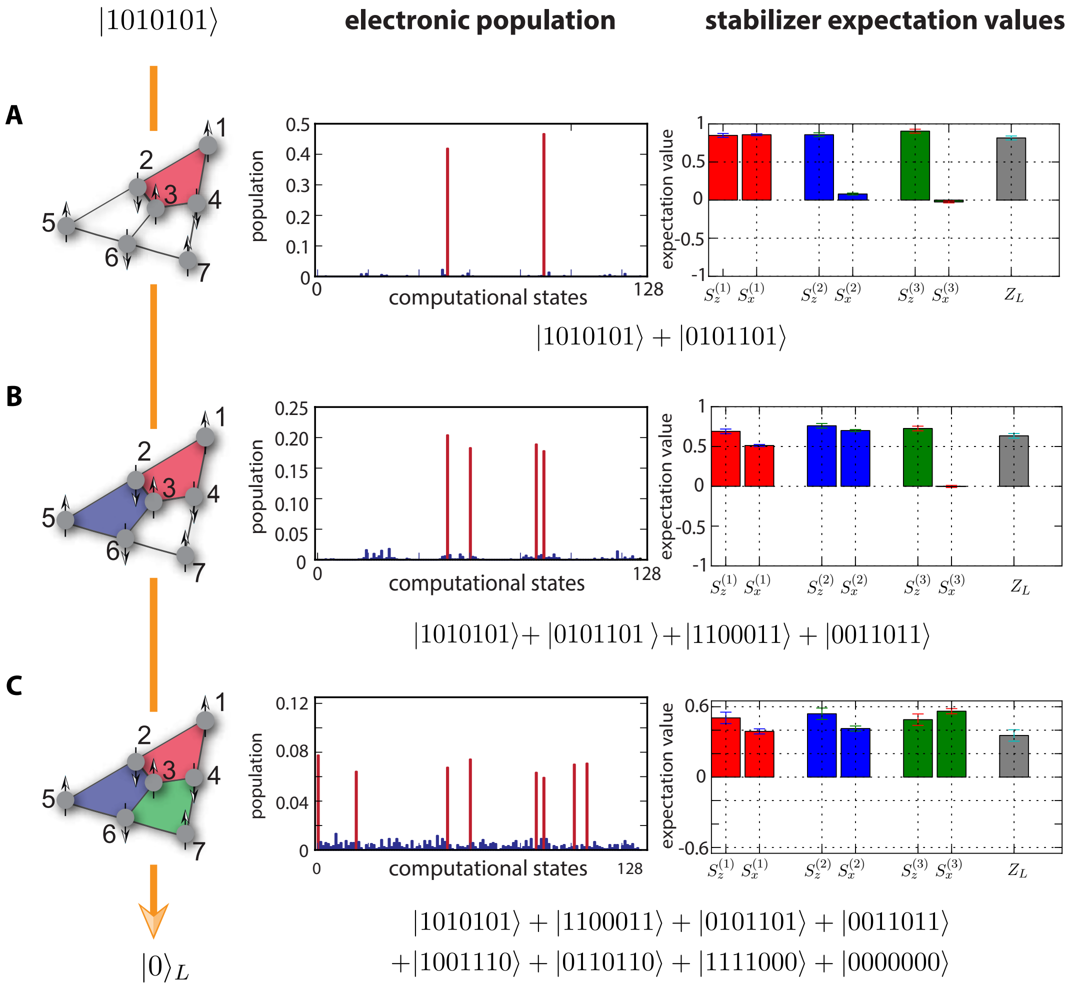

Figure 7.3: Step-wise encoding of a topological qubit: The step-wise encoding of the system in the logical state $|0\rangle_L$ is observed by measurements of the $2^7 = 128$ electronic populations in the computational basis states, as well as by the measured pattern of expectation values of the six stabilizers $\{S_z^{(1)}, S_z^{(2)}, S_z^{(3)}, S_x^{(1)}, S_x^{(2)}, S_x^{(3)}\}$ together with the logical stabilizer Z_L. The initial product state $|1010101\rangle$ is ideally a +1 eigenstate of all three $S_z^{(i)}$ stabilizers and of Z_L. **(A)** In the first step, GHZ-type entanglement is created between the four qubits belonging to the first (red) plaquette, which is signaled by the appearance of a non-vanishing, positive-valued $S_x^{(1)}$ expectation value. In the subsequent entangling steps acting on the second (blue) **(B)** and third (green) **(C)** plaquette, the system populates with high probability the expected computational basis states, and the created coherences show as non-zero expectation values of $S_x^{(2)}$ and $S_x^{(3)}$. (picture also shown in Ref. [124]).

Algorithm	Nr. of MS gates	Nr. of global rotations R	Nr. of ac-Stark shifts S_Z	Nr. of addressed resonant pulses	Total number of operations
Decoupling / Recoupling of population in $\|0\rangle$	0	0	2	4	6
Decoupling / Recoupling of population in $\|1\rangle$	0	0	1	2	3
Complete decoupling / Recoupling of a physical qubit	0	0	3	6	9
Preparation of the logical $\|0\rangle_L$ state	3	0	38	70	111

Table 7.1: Encoding resources: Overview of the required resources $\{$MS gate, global rotations (X,Y), ac-Stark shifts S_Z, addressed resonant pulses$\}$ for the individual parts of the encoding sequence, the preparation of the 6 logical states and the logical Clifford gate operations. For the preparation of the logical $|0\rangle$ state, 3 entangling MS gates, 38 ac-Stark operations and 70 addressed resonant pulses for the de- and recoupling of the individual ions are required, which in total correspond to 111 gate operations (see also [124]).

The number of addressed laser pulses used for decoupling and recoupling of the population within the encoding sequence is much larger than the number of global rotations, as indicated in Table 7.1. Therefore, the addressing errors due to crosstalk between adjacent ions is further reduced by distributing the physicals qubits (Fig. 7.1) along the ion chain in such a way, that the qubits being exposed to many addressed pulses are hosted by ions located further away from the center. Table 7.2 shows the convention, mapping the qubits to the ions and the number of addressing operations applied to ions (qubits) respectively. For example, qubit 5 is exposed to 25 addressed laser pulses and therefore is realized ion 1, which is located at the edge of the ion crystal. The redistribution of the qubits can be done without any change of the principle encoding sequence, but the information of Table 7.2 has to be considered for the evaluation of the measured data.

qubit	1	2	3	4	5	6	7
pulses	19	21	0	21	25	15	7
ion	7	2	4	6	1	3	5

Table 7.2: Mapping of the physical qubits to ions: . The table shows the number of addressed laser pulses each physical qubit is exposed to in the course of the encoding sequence, as shown in Fig. 7.1. In order to minimize the effect of residual errors due to cross-talk with neighboring ions during spectroscopic decoupling and recoupling pulses, the physical qubits are distributed along the chain in such a way that the physical qubits exposed to many (few) addressed laser pulses are hosted by ions at the edge (center) of the chain (see also [124]).

7.2 Phase optimization procedure

In the previous section, the encoding of the logical state $|0\rangle_L$ was described in detail. The preparation of the logical qubit is realized by three plaquette-wise entangling operations, acting in each case on four qubits. The states of the decoupled qubits are affected by off-resonant light-shifts induced by the entangling gates, which manifest themselves in systematic and undesired phase shifts occurring on the decoupled qubits [154].

The fidelity of the encoded state is affected by these systematic phase shifts, which requires the compensation of the systematic errors at the end of the encoding sequence. For simplicity we consider the state after the 1^{st} encoding step, the GHZ state $|\psi_1\rangle = \frac{1}{\sqrt{2}}(|1010\rangle + |0101\rangle) \otimes |101\rangle$, which evolves due to phase shifts to the state $|\psi_1'\rangle = \frac{1}{\sqrt{2}}(|1010\rangle + e^{i\phi}\,|0101\rangle) \otimes |101\rangle$ with an unknown but constant phase $e^{i\phi}$. A measurement of the stabilizer expectation values $\langle S_z^{(1)}\rangle$ and

$\langle S_x^{(1)} \rangle$ of the first plaquette leads to the following results:

$$\begin{aligned} \langle S_z^{(1)} \rangle &= \langle \psi_1 | Z_1 Z_2 Z_3 Z_4 | \psi_1 \rangle = 1 \\ \langle S_x^{(1)} \rangle &= \langle \psi_1 | X_1 X_2 X_3 X_4 | \psi_1 \rangle = \cos(\phi). \end{aligned}$$

The expectation value of the Z-type stabilizer remains unaffected but the X-type stabilizer is alternating between the ideally expected value of +1 and the opposite value -1. Due to the fact that the undesired error corresponds to a constant phase shift, a single qubit rotation $U_{comp} = \exp(i\theta\sigma_z)$ on any of the four qubits enables the compensation of the phase shift error.

This example demonstrates the main idea of the compensation procedure but the situation becomes more complicated after the second encoding step. The ideal target state after the second encoding step is

$$|\psi_2\rangle = \frac{1}{2}(|0000000\rangle + |0110110\rangle + |1111000\rangle + |1001110\rangle).$$

The state up to this stage maximizes the value of the X-type stabilizer generators $S_x^{(1)}, S_x^{(2)}$, as well as the product $S_x^{(1)} S_x^{(2)}$ of the two stabilizers. During the encoding sequence, the state accumulates unknown phases and evolves to the state $|\psi_2'\rangle$

$$\begin{aligned} |\psi_2'\rangle = \frac{1}{2}(&|0000000\rangle + e^{i\phi_1}|0110110\rangle \\ &+ e^{i\phi_2}|1111000\rangle + e^{i\phi_3}|1001110\rangle). \end{aligned} \tag{7.1}$$

The idea is to apply Z-rotations on three of the six qubits taking part of the two encoded plaquettes and iteratively optimizing the expectation values of the three stabilizers $S_x^{(1)}, S_x^{(2)}$ and $S_x^{(1)} S_x^{(2)}$. The optimization procedure after the second step of the encoding sequence is demonstrated in Fig. 7.4. Fig. 7.4(a) shows the measured expectation values of the stabilizer generators of the first (red) and second (blue) plaquette right after the second encoding step. The initial state $|\psi_2'\rangle$ does not correspond to the target state, since the expectation value $\langle S_x^{(1)} \rangle$ of the first plaquette is flipped. As a first iteration, a Z-rotation is applied on qubit 2 resulting in a sinusoidal behaviour of the expectation values $\langle S_x^{(1)} \rangle$ and $\langle S_x^{(2)} \rangle$ (see Fig. 7.4(b)). The expectation value $\langle S_x^{(1)} \rangle$ (red bold line) is maximized with respect to the ac-Stark phase, indicated by the orange circle in Fig. 7.4(b). The expectaion value of $S_x^{(2)}$ is maximized by applying an additional Z-rotation on qubit 5 (Fig. 7.4(c)). At the end of the iteration steps, the stabilizer generators are measured again and show that the Z-type stabilizer did not change, whereas the X-type stabilizers both reveal positive and maximal values (Fig. 7.4(d)). The phase optimization procedure converges already after two iteration steps, independent of the starting position. The required measurement duration for the whole procedure is about 7 minutes. An alternative to this phase optimization procedure would be full state tomography of $|\psi_2'\rangle$ and calculate the Z-rotations required to maximize the fidelity with the ideal target state $|\psi_2\rangle$. A complete six-qubit state tomography requires about 48 minutes without including state reconstruction and calculation of the correction pulses. This makes clear that using tomography for optimizing the relative phases is not feasible.

The same iterative procedure is applied to the final state at the end of the encoding sequence,

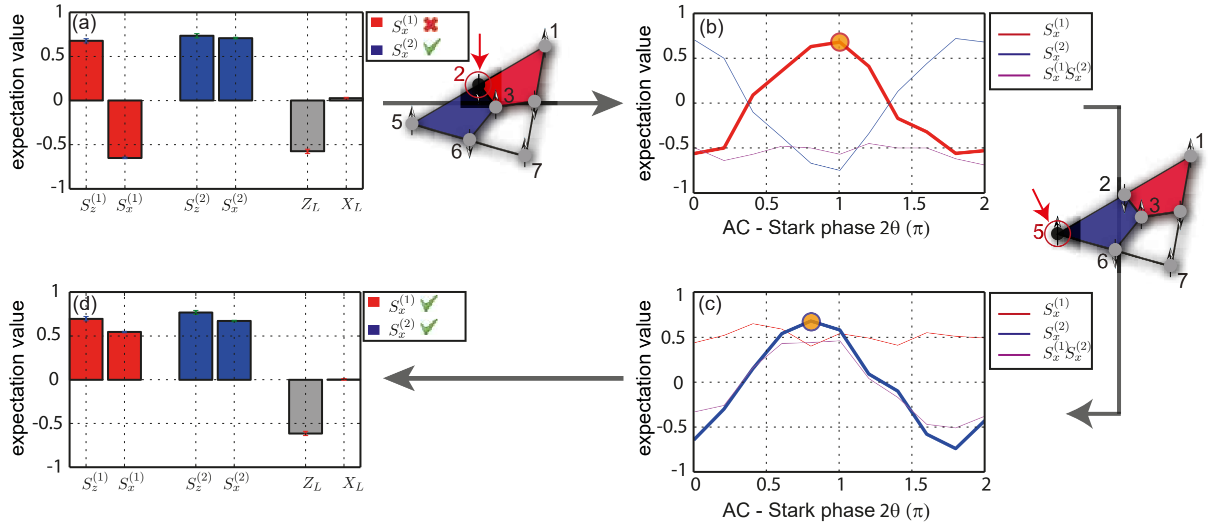

Figure 7.4: Experimental implementation of the phase optimisation protocol. Demonstration of the iterative phase optimization procedure used to compensate the relative phases of the state $|\psi_2'\rangle$ after the second encoding step. (a) Stabilizer generator expectation values of the initial uncorrected state $|\psi_2'\rangle$. (b) Z-rotation applied to qubit 2 and subsequently scanning the ac-Stark phase θ. The expectation value $\langle S_x^{(1)}\rangle$ is optimized, indicated by the bold red line. (c) The Z-rotation on qubit 2 is fixed to the maximum value (orange dot of (b)) and a Z-rotation is applied to qubit 5, optimizing $\langle S_x^{(2)}\rangle$. The Z-rotation on qubit 5 is fixed to the optimum obtained from scan (c) resulting in all stabilizers being positive and maximal. (d) Stabilizer generator expectation values of $|\psi_2'\rangle$ after the optimization procedure. In each scan, different values for the phases characterizing the single-qubit rotations were applied with an elementary step-size of $2\pi/10$. For each phase value, the experiment was repeated 200 times. (picture also shown in Ref. [154]).

shown in Fig. 7.1. The seven-qubit state $|\psi_3'\rangle = |0'\rangle_L$ evolves during the encoding sequence to

$$\begin{aligned} |0'\rangle_L = \frac{1}{2\sqrt{2}}(&|0000000\rangle + e^{i\phi_1}|0110110\rangle + e^{i\phi_2}|1111000\rangle \\ &+ e^{i\phi_3}|1001110\rangle + e^{i\phi_4}|0011011\rangle + e^{i\phi_5}|0101101\rangle \\ &+ e^{i\phi_6}|1100011\rangle + e^{i\phi_7}|1010101\rangle), \end{aligned} \tag{7.2}$$

and is determined by seven relative phases $\{\phi_1, ..., \phi_7\}$. The optimization procedure works similarly to the case of the two plaquettes, but now we have to apply Z-rotations on all seven ions, maximizing the seven expectation values $\langle S_x^{(1)}\rangle$, $\langle S_x^{(2)}\rangle$, $\langle S_x^{(3)}\rangle$, $\langle S_x^{(1)}S_x^{(2)}\rangle$, $\langle S_x^{(2)}S_x^{(3)}\rangle$, $\langle S_x^{(1)}S_x^{(3)}\rangle$ and $\langle S_x^{(1)}S_x^{(2)}S_x^{(3)}\rangle$. Fig. 7.5 shows the iterative optimization procedure of the encoded logical qubit. The stabilizer generators of the initially prepared state $|0'\rangle_L$ are presented in Fig. 7.5(a). The measured X-type stabilizers of the uncorrected state (Fig. 7.5(a)) reveal large deviations from the ideal expectation values - e.g. the expectation value $\langle S_x^{(3)}\rangle$ is almost 0. Starting from the initial state, the phase optimization procedure (see Fig. 7.5(b)-(i)) compensates the phase shift errors after two rounds of optimization and results in the final state shown in Fig. 7.5(j). Fig. 7.5 shows only one of the two optimization cycles. The second cylce is identical to the first. Similar to the case of two plaquettes, the Z-type stabilizer generators are not affected by the optimization procedure. The optimization procedure for the three plaquette case is converging

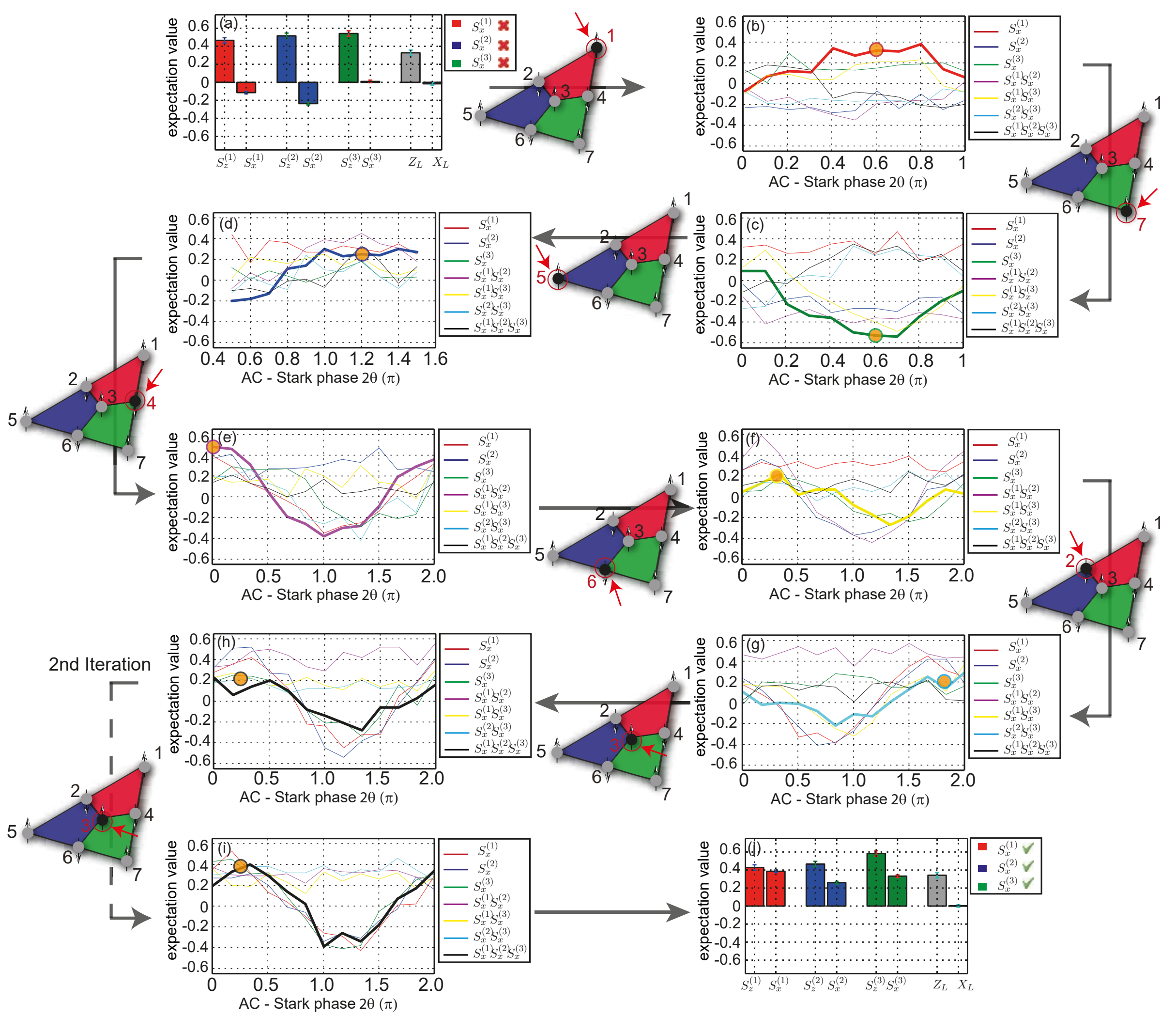

Figure 7.5: Experimental phase optimization of the complete seven-qubit quantum error correcting code. Demonstration of the iterative phase optimization procedure used to compensate the relative phases of the state $|0'\rangle$ after complete encoding sequence. (a) Stabilizer generator expectation values of the initial uncorrected state $|0'\rangle$. (b-i) The seven expectation values $\langle S_x^{(1)}\rangle$, $\langle S_x^{(2)}\rangle$, $\langle S_x^{(3)}\rangle$, $\langle S_x^{(1)}S_x^{(2)}\rangle$, $\langle S_x^{(2)}S_x^{(3)}\rangle$, $\langle S_x^{(1)}S_x^{(3)}\rangle$ and $\langle S_x^{(1)}S_x^{(2)}S_x^{(3)}\rangle$ are optimized iteratively by applying Z-rotations on each of the seven qubits respectively. The maximal expectation value of the corresponding stabilizer operator (indicated by bold lines) is highlighted by the orange circle. (j) Stabilizer generator expectation values of $|0'\rangle$ after two steps of the optimization procedure. In each scan, different values for the phases characterizing the single-qubit rotations were applied with an elementary step-size of $2\pi/10$. For each phase value, the experiment was repeated 200 times. (picture also shown in Ref. [154]).

already after two optimization steps, which is in agreement with numerical simulations presented in Ref. [154]. A more detailed mathematical explanation of the optimization procedure and the convergence for larger systems is presented in Ref. [154].

7.3 Characterization of the encoded qubit

One of the main tasks after encoding the logical qubit is to characterize the prepared logical state. The experimentally generated states can be described by seven-qubit density matrices ρ, which could be reconstructed from seven-qubit quantum state tomographies [21]. This approach is experimentally not practical, since the number of required measurement settings is $3^7 = 2187$. The measurement time for a complete reconstruction of the density matrix ρ would be several hours. Here, we follow a different approach, outlined in [155] enabling the estimation of the logical state fidelity from a subset of Pauli operators. The main assumption of the method described in [155] is that the ideal target state ρ_t is pure, which is the case for the logical state $|0\rangle_L$ and all other states generated by logical operations. Furthermore, if the target state corresponds to a stabilizer state, then the number of required measurements is reduced from d^2 to d with $d = 2^n$ the dimension of the n-qubit Hilbert space [155]. Therefore, the fidelity of the logical states can be revealed from $d = 2^n = 128$ measurement settings.

Besides the overall fidelity of the experimental state ρ with the ideal state ρ_t other interesting figures of merit such as the overlap with the code space, as well as the quantum state fidelities within the code space can be revealed from the reduced set of measurements. For n qubits a general state ρ of the system can be described in the operator basis formed by all possible Pauli operators $W_k, k = 1, \ldots, d^2 = 4^n$, with W_k the n-fold tensor product of the Pauli matrices $\mathbb{1}, X, Y, Z$ for each qubit, with $\mathrm{tr}(W_i W_j/d) = \delta_{ij}$. As an example, a two qubit state $(n = 2)$ can be expanded by $4^2 = 16$ operators $W_k = \{\mathbb{1}, X, Y, Z\} \otimes \{\mathbb{1}, X, Y, Z\} = \{\mathbb{1}\mathbb{1}, \mathbb{1}X, ..., ZZ\}$. A general quantum state can be expressed as $\rho = \frac{1}{d}\sum_k \mathrm{tr}(W_k\rho)\, W_k$, where all 4^n expansion coefficients contribute to the sum. For stabilizer states $\rho_s = |\psi\rangle\langle\psi|$, for which $W_k|\psi\rangle = \pm|\psi\rangle$ if W_k belongs to the stabilizer group of state $|\psi\rangle$, only the 2^n coefficients corresponding to the set of stabilizer elements W_k can be non-zero: $\mathrm{tr}(W_k\rho) = \pm 1$. The quantum state fidelity of the experimental state ρ with the ideal target stabilizer state as ρ_t is given by

$$\mathcal{F}(\rho, \rho_t) = \mathrm{tr}(\rho_t\, \rho) = \frac{1}{d}\sum_k \mathrm{tr}(W_k\rho_t)\mathrm{tr}(W_k\rho). \tag{7.3}$$

Since there are 2^n non-zero coefficients $\mathrm{tr}(W_k\rho_t)$ contributing to this sum, it is sufficient to measure the expectation values of the corresponding 2^n Pauli operators W_k, $\langle W_k\rangle_\rho = \mathrm{tr}(W_k\rho)$, to determine the quantum state fidelity according to Eq. (7.3). For the present case of seven-qubit stabilizer states, this requires the measurement of only 128 expectation values $\langle W_k\rangle_\rho$. In the following we will consider the overlap with the protected code space. Note that the six ideal encoded states $\rho_t = \{\rho_{|1\rangle_L}, \rho_{|0\rangle_L}, \rho_{|\pm_x\rangle_L}, \rho_{|\pm_y\rangle_L}\}$ are determined by the six stabilizer generators $S_x^{(i)}$ and $S_z^{(i)}$, $i = 1, 2, 3$ and the corresponding logical operator $O_L = \{Z_L, X_L, Y_L\}$:

$$\rho_t = \frac{1}{128}\underbrace{(1 \pm O_L)}_{:=P_{\pm O_L}}\underbrace{\prod_{i=1}^{3}(1 + S_x^{(i)})\prod_{j=1}^{3}(1 + S_z^{(j)})}_{:=P_{CS}}. \tag{7.4}$$

Here, P_{CS} denotes the projector onto the code space, defined as the +1 eigenspace of the six stabilizers generators $S_x^{(i)}$ and $S_z^{(i)}$, and $P_{\pm O_L}$ is the projector onto the desired logical state within the code space. Concretely, the encoded states ρ_t can be written as:

$$\rho_{|1\rangle_L} = |1\rangle\langle 1|_L = \frac{1}{128}(1 - Z_L)P_{CS}, \tag{7.5}$$

$$\rho_{|0\rangle_L} = |0\rangle\langle 0|_L = \frac{1}{128}(1 + Z_L)P_{CS}, \tag{7.6}$$

$$\rho_{|\pm_x\rangle_L} = |\pm_x\rangle\langle \pm_x|_L = \frac{1}{128}(1 \pm X_L)P_{CS}, \tag{7.7}$$

$$\rho_{|\pm_y\rangle_L} = |\pm_y\rangle\langle \pm_y|_L = \frac{1}{128}(1 \pm Y_L)P_{CS}. \tag{7.8}$$

Note that the logical operator $Y_L = +iX_LZ_L = -\prod_{i=1}^{7} Y_i$ for the seven-qubit color code.

Quantum state fidelity of the experimentally generated state ρ with the ideal target state, say $\rho_{|1\rangle_L}$, is given by $\mathcal{F}(\rho, \rho_{|1\rangle_L}) = \frac{1}{128}\sum_{k=1}^{128}\langle W_k\rangle$, which is the equal-weighted sum of expectation values of the 128 Pauli operators appearing in the product of the projectors in Eq. (7.5), $\{W_1 = \mathbb{1}, W_2 = -Z_L, \ldots, W_{128} = -Z_L S_x^{(1)} S_x^{(2)} S_x^{(3)} S_z^{(1)} S_z^{(2)} S_z^{(3)} = -X_1Z_2X_3Z_4X_5Z_6X_7\}$. Similarly, there is a set of 128 operators for each logical state, according to the 128 Pauli operators appearing in Eqs. (7.6) - (7.8).

Overlap with or population in the code space is given by $p_{CS} = \mathrm{tr}(P_{CS}\rho) = \frac{1}{64}\sum_{k=1}^{64}\langle W_k\rangle$, where the sum extends over the expectation values of the 64 Pauli operators contained in the expansion of the projector onto the code space P_{CS} (see Eq. (7.4)). The projected (and normalized) density matrix of the experimental state ρ within the code space is given by $\rho_{CS} := P_{CS}\rho P_{CS}/p_{CS}$. Thus, for a given experimental state ρ, the **quantum state fidelity within the code space** with the ideal target state $\rho_t = P_{\pm O_L}P_{CS}$ is given by

$$\begin{aligned}\mathcal{F}(\rho_{CS}, \rho_t) &= \mathrm{tr}(P_{\pm O_L}P_{CS}\,P_{CS}\rho P_{CS})/p_{CS}\\ &= \mathrm{tr}(P_{\pm O_L}P_{CS}\rho)/p_{CS}\\ &= \mathcal{F}(\rho, \rho_t)/p_{CS}.\end{aligned} \tag{7.9}$$

From the latter expression one sees that the fidelity $\mathcal{F}(\rho, \rho_t) = p_{CS}\mathcal{F}(\rho_{CS}, \rho_t)$ is indeed given by the product of the overlap with the code space and the fidelity with the target state *within* the code space.

Measurement of the required set of 128 operators $\{W_k\}$ for a given encoded logical target state $|\psi_L\rangle$, requires the application of a sequence of local unitaries after the preparation sequence for $|\psi_L\rangle$. As in standard quantum state tomography [21], this is needed to transform a given Pauli operator W_k into the measurement basis (Z) of the fluorescence measurements. Pulse sequences for these basis transformations are determined by applying an optimized pulse sequence realizing the required local unitaries. The optimal decomposition into the operations was developed by Esteban Martinez and is described in Ref. [156].

The fidelity of the state $|0\rangle_L$ after the encoding sequence yields 32.7(8)%. Using the current values for the MS gate fidelity of $f_{MS} = 0.89$ and a fidelity of $f_{1ion} = 0.993$ [2] for the single-ion pulses thus yields a rough estimate of $F_{SP} = (f_{MS})(F_{1ion})^{100} \approx 35\%$ for the encoding fidelity, which is in good quantitative agreement with the measured quantum state fidelities of the prepared encoded states. Due to the fact that the encoding of the logical $|0\rangle_L$ state in the present

---

[2] The fidelity of the single-ion operations was obtained from single-qubit randomized benchmark measurements and is mainly limited by intensity fluctuations and beam pointing

experiment requires three 4-out-of-7-ion MS entangling gates and over one hundred addressed single-qubit operations for spectroscopic decoupling, the encoding fidelity is limited by the performance of the single-ion pulses. Besides the fidelity, the population p_{CS} of the logical state $|0\rangle_L$ in the code space is 32(1)%, whereas the fidelity of the experimental state with the target state within the code space is 102(3)%. Due to the fact that the population in the codespace is within the experimental errors equal to the overall fidelity, the fidelity within the code space is nearly perfect within the experimental uncertainty. Therefore, the preparation of the logical color code state is limited by the overlap with the code space 32(1)%.

The error bars of the measured quantum state fidelities and overlap with the code space were determined by a Monte-Carlo method, resampling the measured fluorescence data based on the uncertainty given by the limited number of measurement cycles. Therefore, the measurement data was randomly resampled using a multinomial distribution with a statistical uncertainty of $\sqrt{p(1-p)/N}$ for each measured probability p and number of repetitions N. The fidelity $\mathcal{F}(\rho, \rho_t)$, $\mathcal{F}(\rho_{CS}, \rho_t)$ and the populations in the code space p_{CS} are calculated from the mean value and standard deviation of all Monte-Carlo results.

7.4 Error syndrome detection

As already pointed out before, the topological seven-qubit code has the distance $d = 3$, which implies that it can correct $(d-1)/2 = 1$ physical error appearing on any of the seven qubits. Any single-qubit error pushes the system out of the logical code space and causes a violation of the +1 eigenvalue of certain plaquette operators. The eigenvalues of the six plaquette operators show a unique fingerprint of the induced errors - the error syndrome. The error detection capability of the seven-qubit code is demonstrated by inducing all single-qubit errors coherently and detecting the corresponding error syndrome. Fig. 7.6 shows single-qubit errors applied to the encoded state $|0\rangle_L$, which is prepared (Fig. 7.6A) with all plaquette operators showing a positive eigenvalue. Single-qubit X errors manifest themselves as violation of the Z-type stabilizers (Fig. 7.6B), whereas single-qubit Z errors leads to a flip of the X-type stabilizers only (Fig. 7.6C). This behaviour of independently detecting X-and Z-type errors clearly reveals a characteristic feature of CSS codes. Fig. 7.6D shows the effect of a Y-type error on a single qubit, which is equivalent to a combination of a X and Z error and is signaled by simultaneously flipping of the X and Z stabilizers. The complete error syndrome table including all 21 possible single-qubit errors is shown in Fig. 7.8.

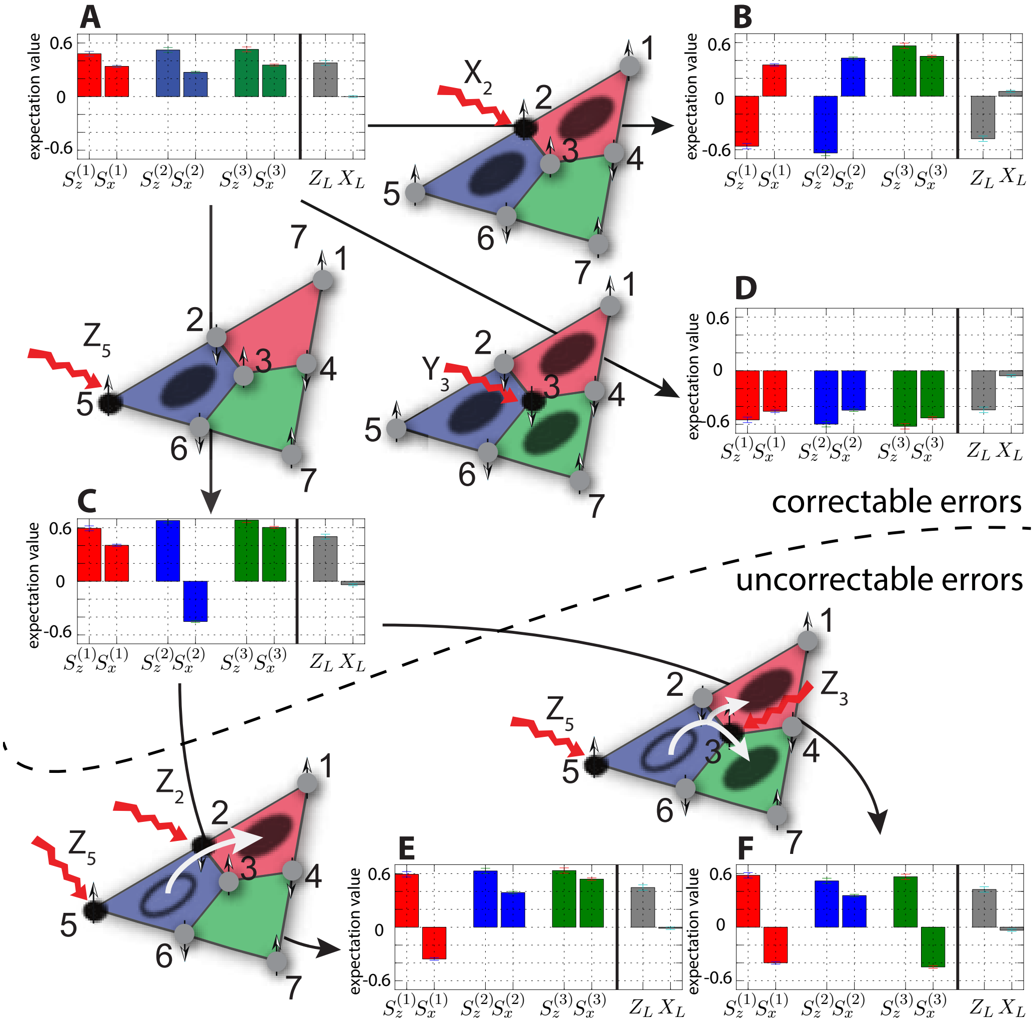

Figure 7.6: Single-qubit error detection: (**A**) The initial logical state $|0\rangle_L$, prior to the occurrence of single-qubit errors, is reflected (i) by the error syndrome, in which all six $S_x^{(i)}$ and $S_z^{(i)}$ stabilizers are positive-valued, and (ii) by a positive expectation value of the logical operator Z_L (X_L). (**B**) A bit flip error (red wiggled arrow) on qubit 2 (marked in black) affects the blue and red plaquettes (visualized by grey-shaded circles) and manifests itself by negative $S_z^{(1)}$ and $S_z^{(2)}$ expectation values and a Z_L sign flip. (**C**) A phase flip error on qubit 5 only affects the blue plaquette and results in a sign flip of $S_x^{(2)}$. (**D**) A Y_3 error – equivalent to a combined X_3 and Z_3 error – affects all three plaquettes and induces a sign change in all six stabilizers and Z_L. Double-error events, such as a Z_5 phase flip (Fig. 2C), followed by a Z_2 (**E**) or a Z_3 error (**F**) result in an incorrect assignment of physical errors, as the detected stabilizer patterns are indistinguishable from single-error syndromes – here, the ones induced by a Z_1 (Fig. 2E) or a Z_4 (Fig. 2F) error. In the correction process, this eventually results in a logical error – here a Z_L phase flip error. Stabilizer violations can under subsequent errors hop (white non-wiggled arrow) to an adjacent plaquette, as in Fig. 2E, where the violation disappears (open grey circle) from the blue and reappears on the red plaquette. Alternatively (Fig. 2F), they can disappear (from the blue plaquette), split up (white branched arrow) and reappear on two neighboring plaquettes (red and green). (picture also shown in Ref. [124]).

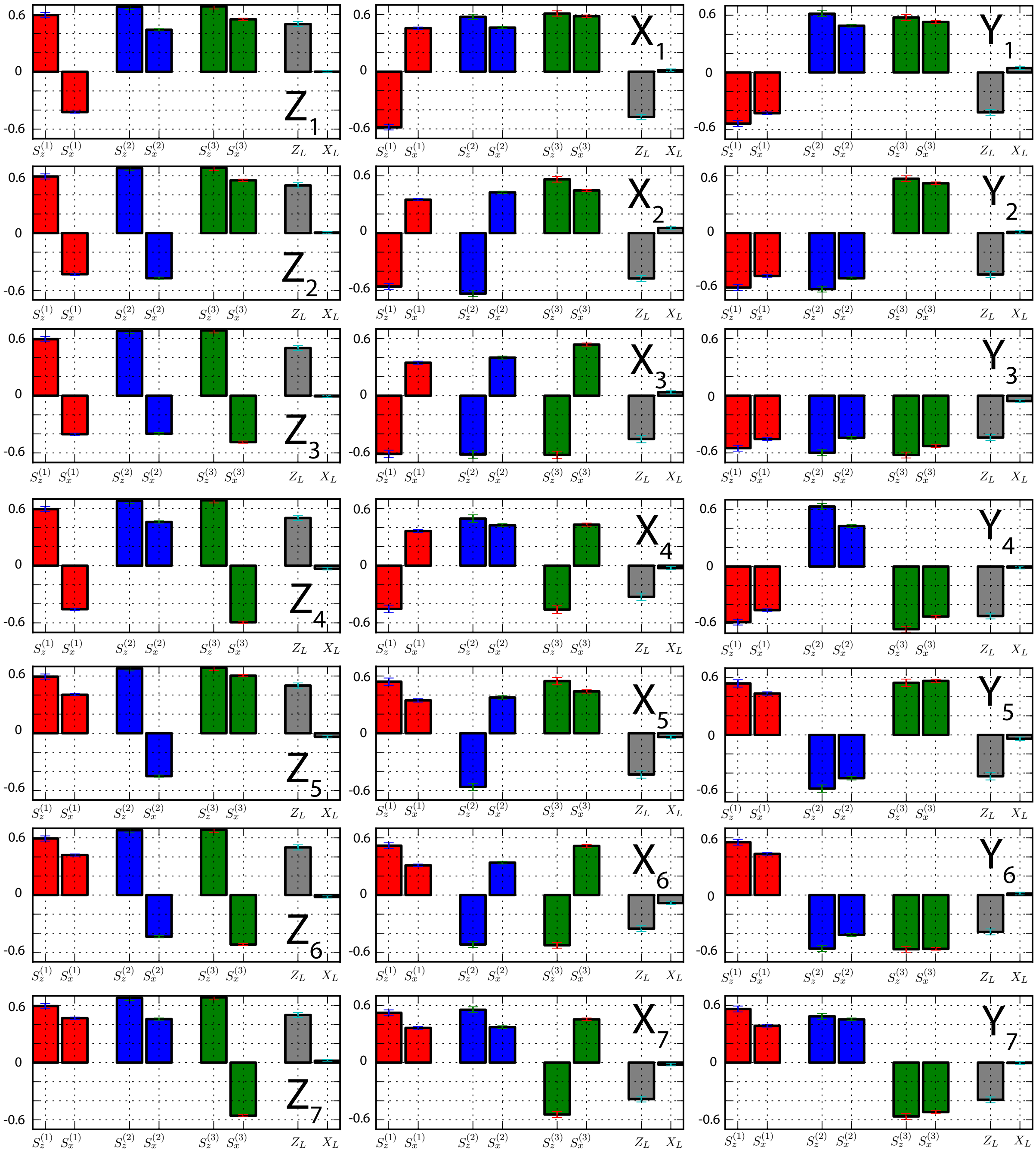

Figure 7.7: Complete error syndrome: Table of the recorded error syndromes for the logical qubit initially prepared in the encoded state $|0\rangle_L$, and subsequently exposed to all 21 single-qubit errors. (picture also shown in Ref. [124]).

Within the experimental uncertainties the measured error syndromes can unambiguously associated with the error syndromes induced by single-qubit errors. To quantify the classification quality of the individual measured syndromes, we perform a Monte-Carlo based simulation of the measured fluorescence data. The idea is to sample the measured data using a multinomial distribution and calculate the stabilizer pattern for each sampled data. For each of the simulated stabilizer patterns, the success of correctly assigning the observed error syndrome to the induced single-qubit error is quantified by calculating the classical trace distance between the sampled stabilizer distributions $S_i^{(sample)}$ and the 21 measured reference stabilizers $S_i^{(ref)}$ of Fig. 7.8. The trace distance D between the two classical distributions of the six stabilizer expectation values is given by

$$D = \sqrt{\sum_{i=1}^{6} \left[S_i^{(ref)} - S_i^{(sample)}\right]^2},$$

and yields $D = 0$ if the distributions are equal. The pattern of stabilizers, as generated by the Monte-Carlo method, is then associated to the reference syndrome for which the trace distance is minimal. Figure 7.8 shows the success rate of assigning the right error syndrome as a function of the number of measurement cycles n_{cycles}. The success rate is defined by the fraction of cases, in which the error syndrome has been correctly assigned to the corresponding single-qubit reference error syndrome, divided by the total number of attempts. It can be seen that the success rate converges rapidly to 100% after about 20 measurement cycles.

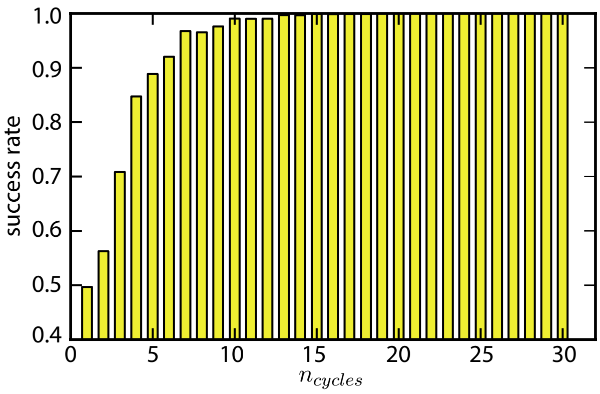

Figure 7.8: Error detection success rate: Simulation of the success rate to identify the right error syndrome for a given number of measurement cycles n_{cycles}. The success rate converges rapidly towards 100% for $n_{cycles} > 20$ measurement cycles, implying that in these cases the error syndromes can be clearly distinguished and perfectly associated to the induced physical single-qubit error. The number of Monte-Carlo samples used to determine each data point is 5000. (picture also shown in Ref. [124]).

Correction of two or more single-qubit errors is beyond the error correction capacity of the seven-qubit code, and requires the encoding of a logical qubit in more physical qubits (such as, e.g., the distance $d = 5$ 2D color code shown in Fig. 6.20). The failure of the seven-qubit code is studied experimentally for two cases: Fig. 7.6E and F of the main text show the recorded error syndromes after inducing two single-qubit phase flip errors Z on qubits 5 and 2 (Fig. 7.6E), and qubits 5 and 3 (Fig. 7.6F), respectively. The comparison with the single-qubit syndrome table in Fig. 7.8 shows that the recorded error syndromes are indistinguishable from the error syndromes induced by a Z_1 error (first column, first error syndrome) and a Z_4 error (first column, fourth error syndrome), respectively. Consequently, the erroneous deduction that a Z_1 (Z_4) error has happened, instead of the physical Z_5 and Z_2 errors (Z_5 and Z_3 errors) effectively result in the application of the operators $Z_1Z_2Z_5$ ($Z_3Z_4Z_5$) to the encoded qubit. These operators are equivalent to the logical operator $Z_L = Z_1Z_2Z_3Z_4Z_5Z_6Z_7$ (since $Z_1Z_2Z_5 = Z_LS_z^{(3)}$ and $Z_3Z_4Z_5 = Z_LS_z^{(1)}S_z^{(3)}$) and thus result in an uncorrectable logical phase flip error Z_L on the encoded state.

For useful QEC, the error syndrome has to be measured in a non-destructive way, as described in Sec. 6.2.2. A quantum non demolition (QND)-measurement of a four-qubit stabilizer operator has been demonstrated in a previous experiment [157]. Such a multi-qubit measurement can be realized in our setup by a quantum circuit involving two MS gates between the four stabilizer qubits and an ancillary qubit, in addition to a few local rotations. The fidelity of the QND readout of a qubit stabilizer can thus be estimated as $\mathcal{F}_{QND} \approx (\mathcal{F}_{MS})^2 \approx 79\%$, which is in agreement with the values found in Ref. [157].

7.5 Global order in the color code state

From our daily experiences, we all know that matter can have different kind of phases or states - *solid, liquid, gas and plasma*. Each of the different phases can be distinguished by the internal structure of the atoms or molecules. This internal structure is also known as *order*. For example the atoms in the gas phase are moving randomly and independent of the other atoms. Therefore, the state of the gas shows no correlations and order. In contrast, at low enough temperatures the atoms can form a crystal, which is manifested by a regular internal structure or order. This order depends on the interaction between the atoms, the temperature and the pressure. A fundamental question in physics is the understanding about the transition from one phase of matter to another - also known as phase transition. A groundbreaking step towards the description of phase transitions was provided by Landau in 1937 [158]. The Landau theory states that the order or internal structure of matter is related to a symmetry and a phase transition corresponds to breaking this symmetry. For example in the case of the transition from the gas phase to the solid state, the symmetry changes from continuous translation symmetry to discrete translation symmetry [159].

In the last century, many other different phases of matter were discovered, as for example (anti)-ferromagnets, superfluids or liquid crystal phases. These phases are described by the ground state of the system Hamiltonian at low temperatures [159]. Analog to the classical phases, the different quantum phases reveal different structures (order) and can be quantified by local order parameters, as for example the correlation of adjacent spins in a magnetic material. The local order parameters correspond to parameters of the system Hamiltonian and changes when the system undergoes a quantum phase transition.

In the 1980s, experiments with a two-dimensional electron gas at low temperatures and strong magnetic fields led to the discovery of the fractional quantum Hall effect (FQH) [160]. The surprising fact was that the orders of different FQH states did not correspond to any symmetry breaking and therefore could not be explained by Landau theory [160]. The different FQH phases could not be distinguished by local order parameters as mentioned before, but rather by correlations extending over the entire system (long-range entanglement). This type of global order is also known as topological order.

Topological quantum codes also reveal the property of global order, which can be detected and manipulated by acting on groups of physical qubits extending over the whole spin system. In the case of the investigated color code states, the expectation value of the logical operator Z_L acting on the whole system corresponds to the global order parameter. Note that the code space is defined as the simultaneous +1 eigenspace of all plaquette stabilizers, thus $S_i \left|\psi_L\right\rangle = +\left|\psi_L\right\rangle$ for any encoded quantum state $\left|\psi_L\right\rangle$. This property allows one to transform the logical operator Z_L into logically equivalent operators $\tilde{Z}_L$ by multiplication with (combinations of) stabilizers: For instance, for the smallest color code, involving seven physical qubits, $Z_L = Z_1Z_2Z_3Z_4Z_5Z_6Z_7$ and $Z_L \left|\psi_L\right\rangle = Z_L S_z^{(2)} \left|\psi_L\right\rangle = Z_L Z_2 Z_3 Z_5 Z_6 \left|\psi_L\right\rangle = Z_1 Z_4 Z_7 \left|\psi_L\right\rangle$. This shows that the string operator $\tilde{Z}_L = Z_1Z_4Z_7$ in the code space is fully equivalent to Z_L. Whereas the logical operator $\tilde{Z}_L$ only acts on three instead of all seven physical qubits, it is still a global operator as it extends over the entire side length of the triangular code. We confirm that topological quantum states cannot be characterized by local order parameters but rather by global properties of the system by measuring two -and three-qubit correlations. Here, local operators refer to one or two-qubit operators, whereas global operators such as $\tilde{Z}_L$ at least involve 3 physical qubits. For the experimental study of the quantum order of the encoded qubit, we first prepare the seven-qubit system in the logical state $\left|1\right\rangle_L$ and $\left|+_x\right\rangle_L$, and subsequently perform a series of quantum state tomography measurements on subsets of two and three qubits. Due to the absence of local order, the two-qubit state tomographies are expected to yield completely mixed states, confirming no correlations between any two-qubit subset. In contrast, the three qubit tomography of the qubits 1, 4 and 7 is supposed to show global order property, manifasting in non-vanishing 3-qubit correlations $\langle Z_1Z_4Z_7\rangle$.

- We perform 2-qubit tomographies on all 21 two-quit subsets, and reconstruct the reduced two-qubit density matrices. We find that these yield an average Uhlmann-fidelity [161] with the two-qubit completely-mixed state of 98.3(2)% (the largest and smallest obtained fidelity values are 99.0(4)% and 97.7(8)%, respectively). Figure 7.9A shows as a representative example the elements of the reconstructed reduced density matrix of qubits 2 and 5.

- From a 3-qubit state tomography on qubits 1, 4 and 7, we determine the expectation value of the global string operator $\tilde{Z}_L = Z_1Z_4Z_7$, which yields 3-qubit correlations $\langle Z_1Z_4Z_7\rangle = -0.46(6)$, signalling the presence of global quantum order. Figure 7.9B shows the reconstructed reduced 3-qubit density matrix.

- Furthermore, we also prepared the logical superposition state $\left|+_x\right\rangle_L = (\left|0\right\rangle_L + \left|1\right\rangle_L)/\sqrt{2}$. Here the global order becomes manifest in non-vanishing three-qubit correlations of the X-type string operator $\tilde{X}_L = X_1X_4X_7$, which is equivalent to the logical $X_L = X_1X_2X_3X_4X_5X_6X_7$ operator ($\tilde{X}_L = X_L S_x^{(2)}$). We find $\langle X_1X_4X_7\rangle$ = 0.40(5). See Figure 7.9C for the reconstructed reduced 3-qubit density matrix.

These measurements confirm the topological character of the encoding of the logical qubit, as they clearly demonstrate the absence of local order in the experimental state, as well as the presence of global quantum order, which for the present size becomes manifest in non-vanishing 3-qubit correlations.

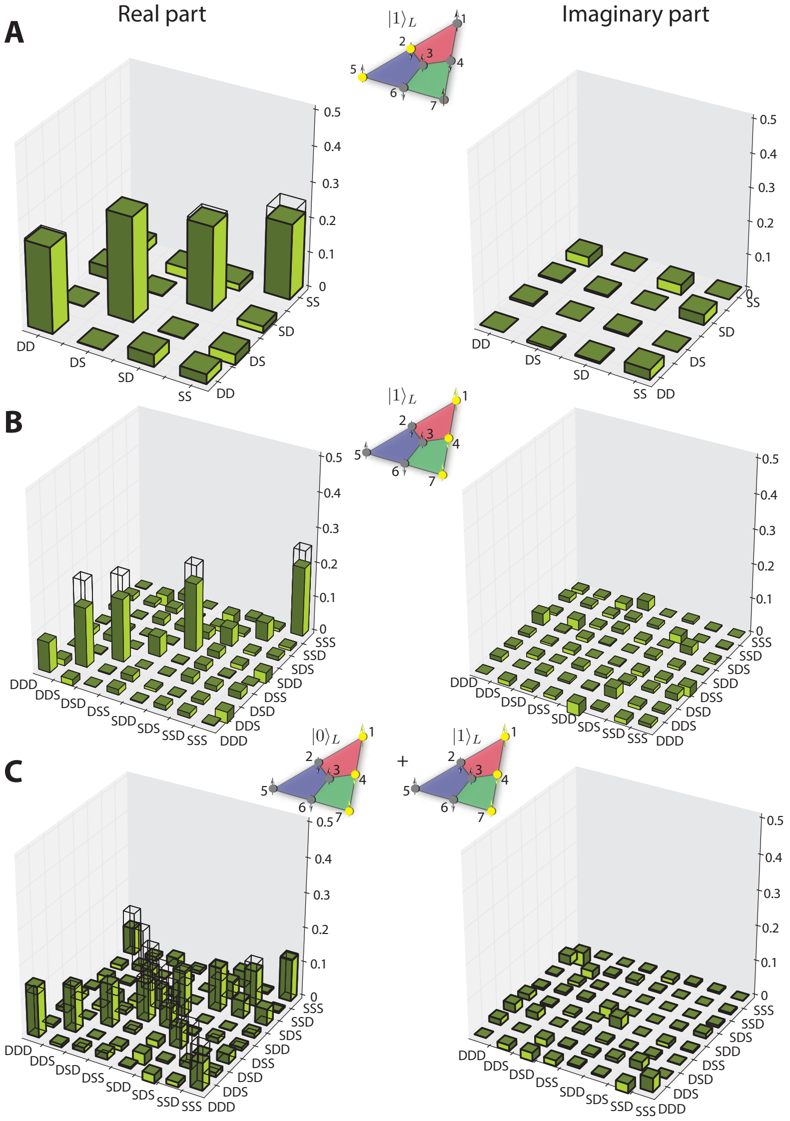

Figure 7.9: Absence of local and presence of global quantum order in the topologically encoded qubit: Real and imaginary elements of reconstructed 2- and 3-qubit density matrices. Matrix elements of the ideal states are indicated as transparent bars. The respective encoded logical state is schematically indicated for each sub-figure, together with the subsets of qubits (marked as yellow filled circles) on which quantum state tomographies have been performed. Electronic populations D (S) corresponds to populations in the computational $|0\rangle$ ($|1\rangle$) state. **(A)** Measured 2-qubit density matrix of qubits 2 and 5, clearly indicating the large overlap (98.3(2)%) with the ideal completely mixed 2-qubit density matrix **(B)** The displayed reduced 3-qubit density matrix (of qubits 1, 4 and 7) has a quantum state fidelity of 85(2)% with the ideal state, which is an incoherent equal-weighted mixture of the four 3-qubit basis states $|111\rangle$, $|001\rangle$, $|010\rangle$ and $|100\rangle$. **(C)** The measured reduced 3-qubit density matrix (of qubits 1, 4 and 7) for the logical qubit initially prepared in $|+_x\rangle_L$, yields a quantum state fidelity of 83(2)% with the ideal state. (picture also shown in Ref. [124]).

7.6 Clifford operations on the logical qubit

The concept of FTQC, introduced in Sec. 6.2, requires computations to be performed directly on the logical qubit level. Errors appearing during the computation are indicated by violation of the plaquette stabilizer operators. The two-dimensional color code enables the bit-wise (transversal) implementation of the group of Clifford operations which are generated by the elementary gate operations Z, X, the Hadamard H and the phase gate K,

$$H = \frac{1}{\sqrt{2}}\begin{pmatrix} 1 & 1 \\ 1 & -1 \end{pmatrix}, \quad K = \begin{pmatrix} 1 & 0 \\ 0 & i \end{pmatrix}, \quad X = \begin{pmatrix} 0 & 1 \\ 1 & 0 \end{pmatrix}, \quad Z = \begin{pmatrix} 1 & 0 \\ 0 & -1 \end{pmatrix}. \tag{7.10}$$

For registers containing several logical qubits the C-NOT gate can also be realized transversally. Note that this concept is different to the surface code, where logical operations are realized by controlled quasi-particle excitations (see Sec. 6.3.2). Here, we implement the generating gate operations Z_L, X_L, H_L and K_L of the single-qubit Clifford group on the topologically encoded qubit and show first experiments demonstrating multiple logical gate operations on the encoded qubit.

7.6.1 Experimental implementation of logical single-qubit Clifford gate operations

We will show that the logical quantum states $|\psi\rangle_L$ remain within the code space under these transversal logical operations. The logical operators $Z_L = Z_1Z_2Z_3Z_4Z_5Z_6Z_7$ and $X_L = X_1X_2X_3X_4X_5X_6X_7$, share an odd number (seven) of physical qubits, and thus fulfill the correct anti-commutation relation $\{X_L, Z_L\} = 0$. Furthermore, they commute with the six stabilizers generators $S_x^{(i)}$ and $S_z^{(i)}$, i=1, 2, 3, of the code, as the logical operators share 4 physical qubits with each stabilizer operators. This means that the logical Z_L-gate can be implemented in our setup by single-ion Z rotations, $Z_L = \prod_{i=1}^{7} U_Z^{(i)}(\pi)$. The logical X_L is realized by a collective local rotation around the X-axis, $X_L = U(\pi, 0)$. The logical Y_L operation is given by the sequential application of both an X_L and a Z_L operation, $Y_L = +iX_LZ_L = -Y_1Y_2Y_3Y_4Y_5Y_6Y_7$..

The logical Hadamard gate $H_L = H_1H_2H_3H_4H_5H_6H_7$ is implemented by a collective local Y rotation, followed by single-ion Z-rotations: $H_L = \prod_{i=1}^{7} U_Z^{(i)}(\pi)U(-\pi/2, \pi/2)$. We furthermore emphasize that – in contrast to other quantum codes, such as the five-qubit code [21], where the logical Hadamard operation requires a five-qubit entangling unitary [162] – here, owing to the transversal character of the logical Hadamard gate operation in the seven-qubit code, the implementation is achieved using exclusively non-entangling local operations.

Finally,the logical phase or K_L gate is realized in a transversal way. As compared to other topological codes, it is a distinguishing feature of 2D color codes to enable a transversal implementation of the K_L gate operation [128], not requiring the technique of magic-state injection via an ancillary qubit [121] nor multi-qubit entangling operations such as, e.g. in the non-transversal five-qubit code [21]. Note that the logical K_L gate operation is required to fulfill $K_LX_LK_L^\dagger = Y_L = iX_LZ_L$. Note that for $K_L = K_1K_2K_3K_4K_5K_6K_7$, however, one obtains $K_LX_LK_L^\dagger = -iX_LZ_L$; thus K_L defined in this way acts as $K_L^\dagger$ within the code space. This can be easily avoided by redefining $K_L := \prod_{i=1}^{7} K_i^\dagger$. We implement the K_L gate operation by bit-wise Z-rotations, $K_L = \prod_{i=1}^{7} U_Z^{(i)}(-\pi/2)$.

7.6.2 Preparation of the encoded cardinal states

Fig. 7.10A and Fig. 7.10B show the required circuits to prepare the six logical states lying on the axes of the logical Bloch sphere, starting with the logical qubit initially in state $|0\rangle_L$. The experimentally generated states, required logical gate operations, average stabilizer expectation values ($\langle S_i \rangle = \frac{1}{6}\sum_{i=1}^{3}(\langle S_x^{(i)}\rangle + \langle S_z^{(i)}\rangle)$), and length L of the logical Bloch vector ($L = \sqrt{\langle X_L\rangle^2 + \langle Y_L\rangle^2 + \langle Z_L\rangle^2}$) for each state are listed in Table 7.3.

Furthermore, the average values of the six stabilizers for each logical state are uncorrelated from the number of logical gate operations applied to prepare them (up to three). Thus, currently imperfections in the initial encoding dominate over errors induced by the relatively short Clifford gate sequences acting on the encoded state. This behavior is confirmed by the measured overlap with the code space of p_{CS} for the states $|0\rangle_L$, $|1\rangle_L$ and $|+_x\rangle_L$ (see Table 7.3). The number of required pulses to generate the six logical states on the Bloch sphere is listed in Table. 7.4.

logical state	$\langle S_i \rangle$	L	required Clifford gates	F (%)	p_{CS} (%)	F_{CS}(%)
$|0\rangle_L$	0.42(1)	0.38(6)	-	32.7(8)	32(1)	102(3)
$|1\rangle_L$	0.54(1)	0.57(6)	X_L	28(1)	27(2)	101(5)
$|+_x\rangle_L$	0.52(1)	0.48(2)	H_L	33(1)	35(2)	95(3)
$|-_x\rangle_L$	0.49(2)	0.58(2)	X_L and H_L	-	-	-
$|+_y\rangle_L$	0.39(1)	0.42(2)	H_L and K_L	-	-	-
$|-_y\rangle_L$	0.42(1)	0.38(2)	H_L, K_L, and X_L	-	-	-

Table 7.3: Logical Clifford operations: Characterization of the experimentally implemented Clifford operations on the encoded qubit. The six logical states, located on the axes of the Bloch sphere (see Fig. 7.10) are generated by a sequence of Clifford gates. The average stabilizer expectation values $\langle S_i \rangle$, the length L of the logical Bloch vector as well as the required Clifford operations are listed for each state. The overall fidelity, the overlap with the code space p_{CS} as well as the fidelity F_{CS} within the code space were only measured for the three states $\{|0\rangle_L, |1\rangle_L$ and $|+_x\rangle_L\}$.

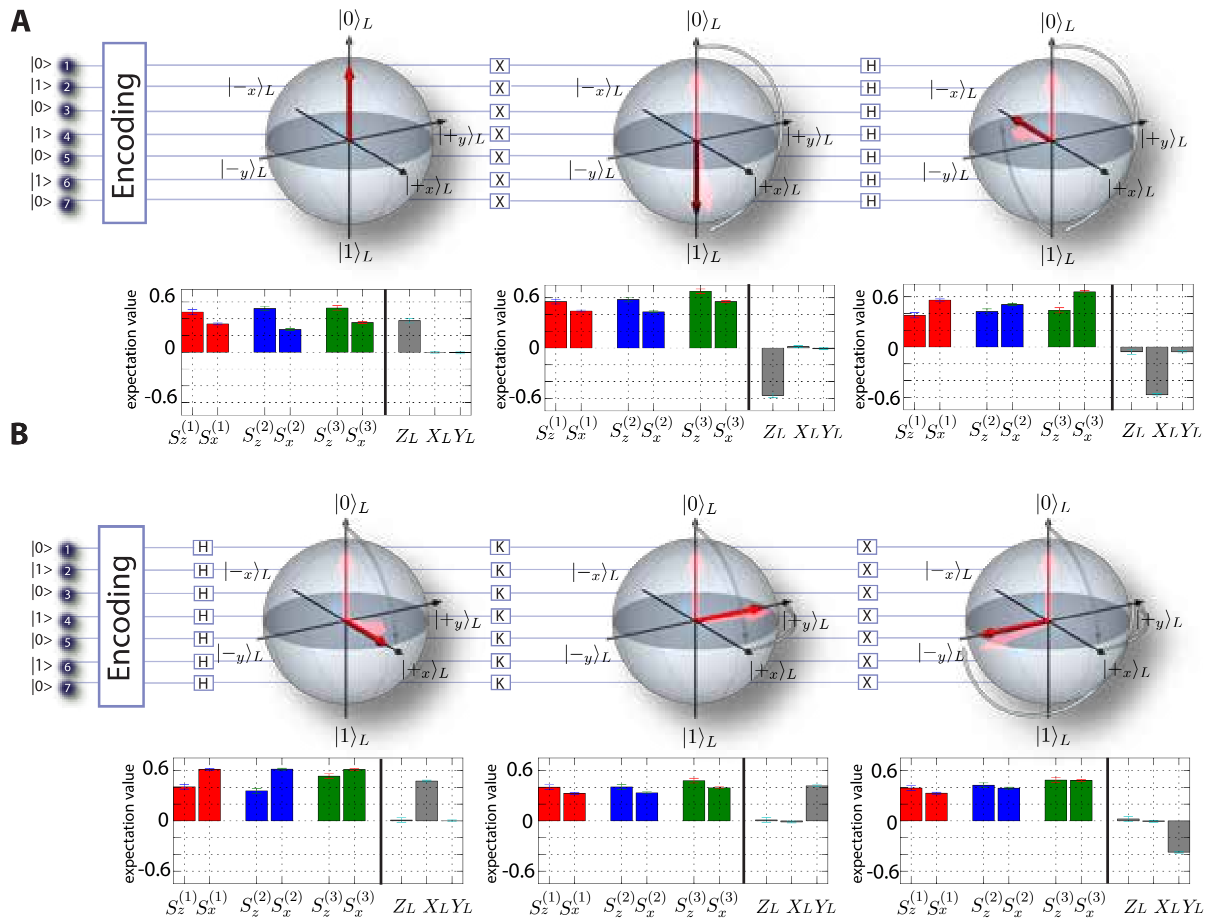

Figure 7.10: Single qubit Clifford gate operations applied on a logical encoded qubit. Starting from the logical $|0\rangle_L$ state, sequences of logical Clifford gate operations $\{X_L, H_L\}$ in **(A)** and $\{H_L, K_L, X_L\}$ in **(B)** are applied consecutively in a transversal way (i.e. bit-wise) to realize all six cardinal states $\{|0\rangle_L, |1\rangle_L, |-_x\rangle_L, |+_x\rangle_L, |+_y\rangle_L, |-_y\rangle_L\}$ of the logical space of the topologically encoded qubit. The dynamics under the applied gate operations is illustrated by rotations of the Bloch-vector (red arrow) on the logical Bloch-sphere as well as by the circuit diagram in the background. Each of the created logical states is characterized by the measured pattern of $S_x^{(i)}$ and $S_z^{(i)}$ stabilizers and the logical Bloch vector, with the three components given by the expectation values of the logical operators X_L, Y_Z and Z_L. The orientation of the logical Bloch vector changes as expected under the logical gate operations. (picture also shown in Ref. [124]).

Algorithm	Nr. of MS gates	Nr. of global rotations R	Nr. of ac-Stark shifts S_Z	Nr. of addressed resonant pulses	Total number of operations
Decoupling / Recoupling of population in $\|0\rangle$	0	0	2	4	6
Decoupling / Recoupling of population in $\|1\rangle$	0	0	1	2	3
Complete decoupling / Recoupling of a physical qubit	0	0	3	6	9
Encoding: preparation of the logical $\|1\rangle_L$ state	3	1	38	70	112
Logical Z gate	0	0	7	0	7
Logical X gate	0	1	0	0	1
Logical Hadamard gate H	0	1	7	0	8
Logical phase gate K	0	0	7	0	7
Preparation of the logical $\|0\rangle_L$ state	3	0	38	70	111
Preparation of the logical $\|+_x\rangle = \|0\rangle_L + \|1\rangle_L$ state	3	1	45	70	118
Preparation of the logical $\|-_x\rangle = \|0\rangle_L - \|1\rangle_L$ state	3	2	45	70	119
Preparation of the logical $\|+_y\rangle = \|0\rangle_L + i\,\|1\rangle_L$ state	3	1	52	70	125
Preparation of the logical $\|-_y\rangle = \|0\rangle_L - i\,\|1\rangle_L$ state	3	2	52	70	126
Encoding and up to 13 Clifford gates	3	14	52	70	136

Table 7.4: Overview of the required resources {MS gate, global rotations (X,Y), ac-Stark shifts S_Z, addressed resonant pulses} for the individual parts of the encoding sequence, the preparation of the 6 logical states and the logical Clifford gate operations. For the preparation of the logical $|0\rangle$ state, 3 entangling MS gates, 38 ac-Stark operations and 70 addressed resonant pulses for the de- and recoupling of the individual ions are required, which in total correspond to 111 gate operations (see also [124]). For the preparation of the logical states $\{|+_x\rangle, |-_x\rangle, |+_y\rangle, |-_y\rangle\}$ in total $\{118, 119, 125, 126\}$ gate operations are used, whereas for the demonstration of multiple Clifford gate operations we apply up to 136 gate operations in total (see also [124]).

7.6.3 Sequences of encoded gate operations

The computational capabilities of the encoded qubit were explored by performing multiple gate operations on the encoded qubit. After preparing the encoded qubit in the logical state $|{-_y}\rangle_L$ by three Clifford gate operations (see Fig. 7.10B), we applied up to 10 additional logical X_L gate operations to evolve the logical qubit between the +1 and -1 eigenstates of Y_L. The experimental result of the logical expectation values $\langle Y_L\rangle$, $\langle X_L\rangle$ and $\langle Z_L\rangle$ as a function of the number of logical gates n_{gate} is shown in Fig. 7.11. A weighted exponential fit of the form $A\exp(-n_{gate}/B)$ into the $\langle Y_L\rangle$ expectation values yields a decay rate of the average expectation value of 3.8(5)% per gate. This decay is consistent with what we expect from the accuracy with which collective resonant π-rotations $U(\pi,0)$ can be implemented on a string of seven ions in our setup. A fidelity as high as about 99.5% of a single collective resonant π-rotation per ion would already lead to a fidelity loss of $\approx 3.5\%$ per gate operation.

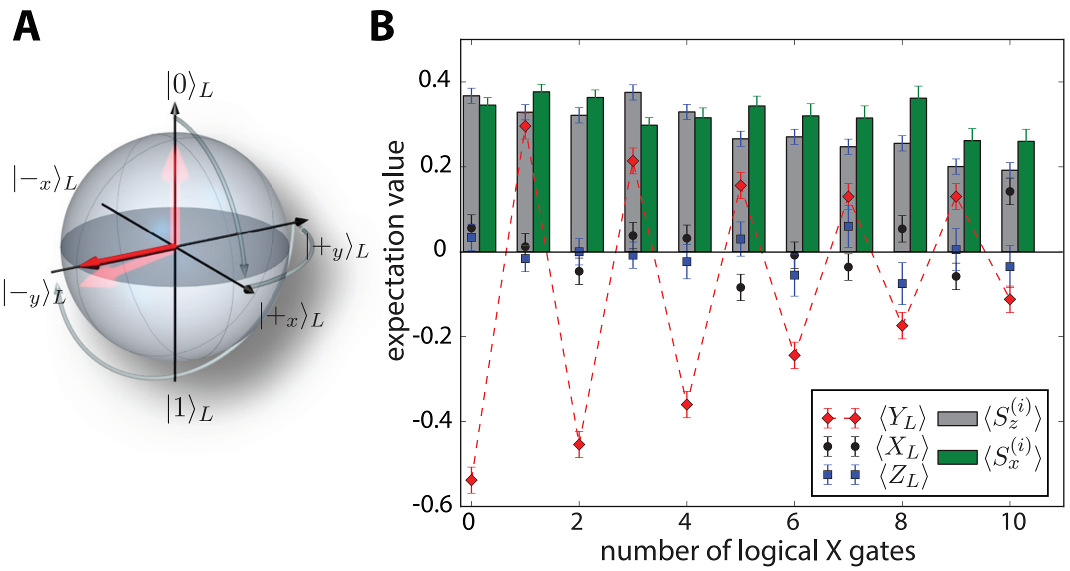

Figure 7.11: Repetitive application of logical quantum gate operations: **(A)** Preparation of the $|{-_y}\rangle_L$ state by applying a H_L, K_L and X_L gate operation on the qubit initially prepared in the $|0\rangle_L$ state. **(B)** Subsequently, flips between the logical $|{+_y}\rangle_L$ and $|{-_y}\rangle_L$ states are induced by consecutively applying logical X_L gate operations up to 10 times. The sign flip of the Y_L expectation value (red diamonds) after each step signals clearly the induced flips of the logical Bloch vector, whereas the expectation values of Z_L (blue squares) and X_L (black circles) are close to zero as expected (the average of $\{\langle Z_L\rangle, \langle X_L\rangle\}$ yields $\{0.01(1), -0.01(1)\}$). Average $S_z^{(i)}$ ($S_x^{(i)}$) stabilizer expectation values after each X_L gate are shown as grey (green) bars. (picture also shown in Ref. [124]).

Here, two error sources dominate the measured fidelity loss per gate: (i) The relative intensity inhomogeneity of the global laser beam across the ion string ($\approx 1\%$) lowering the Rabi-frequencies at the ions located at the edge of the string, and (ii) thermal occupation of motional modes, which lead to decoherence of the global Rabi oscillations (see Sec. 3.5). The latter error could be improved by additionally cooling the higher axial motional modes, as described in Sec. 3.5. The application of the pulses for 10 X_L gate operations requires a time of 200μs. This is a factor of 18 shorter than the $1/e$ time of $3.6(6)$ ms on which logical coherences, as indicated by the expectation value $\langle X_L\rangle$, of the qubit initially prepared in $|+_x\rangle_L$, decay (see Fig. 7.12). A decay of the coherence of the logical superposition state $|+_x\rangle_L$ is indicated by a vanishing expectation value of the logical $\langle X_L\rangle$ stabilizer. This behaviour can be compared to the decay of the $\langle X\rangle$ expectation value of a coherent superposition state $|0\rangle + |1\rangle$ of a physical qubit affected by decoherence. The corresponding decay constant has been obtained by a weighted exponential fit into the $\langle X_L\rangle$ stabilizer expectation values. Thus, for the executed circuit of encoded quantum gates, imperfections in the logical Clifford gate operations dominate over the effect of the bare decoherence of the logical qubit. A more extensive study of the decoherence properties of the logical qubit is presented in Sec. 7.7.

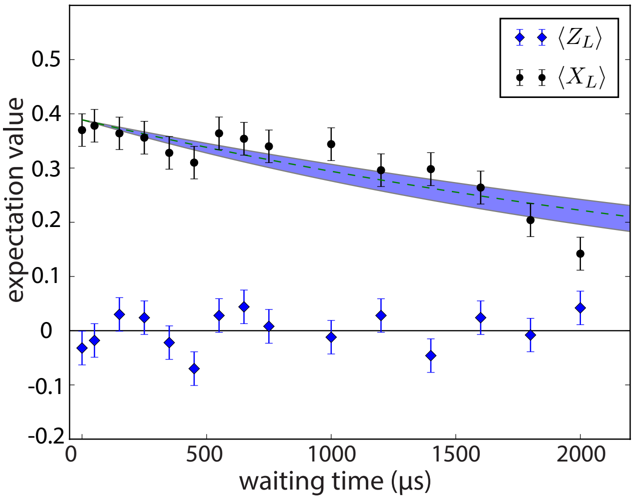

Figure 7.12: Coherence decay of a logical superposition state: Characterization of the coherence of the logical qubit, initially prepared in the X_L eigenstate $|+_x\rangle_L$. A measurement of the decay of the X_L expectation value (black circles) as a function of time yields a $1/e$-time of 3.6(6)ms, while the Z_L expectation value (blue diamonds) remains zero as expected (on average 0.001(8)). (picture also shown in Ref. [124]).

7.7 Coherence during the encoding procedure

As already discussed before, the fidelity of the encoded logical qubit is mainly limited by the single-qubit pulses used for spectroscopic decoupling. During the encoding process, which consists of three different steps preparing the corresponding plaquettes (see Fig. 7.3), the whole system is unavoidably affected by dephasing. In Chapter 5, a model for dephasing in our experimental system was introduced, based on the assumption of collective dephasing. Therefore, it is important to understand the influence of collective dephasing. We analyze the effect of dephasing on the state after each of the three encoding steps, shown in Fig. 7.3.

A more detailed analysis of the dynamics of the entire system during the encoding would be computationally expensive and our analysis allows us to choose a suitable encoding procedure. First, let us consider the effect of noise (e.g. laser and magnetic field fluctuations) acting on a single qubit prepared in the superposition state $|\psi\rangle = \frac{1}{\sqrt{2}}(|0\rangle + |1\rangle)$. The fluctuations can be described by a Hamiltonian $H = 1/2\mu A(t)\sigma_z$, where $\mu A(t)$ corresponds to the instantaneous qubit-laser detuning caused by the imperfections (e.g. magnetic field fluctuations). After the time t, the state $|\psi\rangle$ accumulates a dynamical phase shift and evolves to the state $|\psi(t)\rangle = \exp(-i\int_{t'} H(t')dt')\,|\psi\rangle$ [66]:

$$|\psi(t)\rangle = \frac{1}{\sqrt{2}}(e^{-i\frac{\phi(t)}{2}}\,|0\rangle + e^{+i\frac{\phi(t)}{2}}\,|1\rangle).$$

with the phase $\phi(t) = \mu\int_0^t A(t')dt'$. Therefore, the density matrix of the state $\rho(t)$ is given by

$$\rho(t) = \frac{1}{2}(|0\rangle\langle 0| + e^{-i\phi(t)}\,|0\rangle\langle 1| + e^{+i\phi(t)}\,|1\rangle\langle 0| + |1\rangle\langle 1|).$$

In the experiment we always average over multiple runs and thus we can apply the Gaussian momentum theorem, which states the average of the phase over random noise trajectories $\langle e^{i\pm\phi(t)/2}\rangle = e^{-1/2\langle\phi(t)^2\rangle}$. Therefore the density matrix evolves finally to

$$\rho(t) = \frac{1}{2}(|0\rangle\langle 0| + e^{-1/2\langle\phi(t)^2\rangle}\,|0\rangle\langle 1| + e^{-1/2\langle\phi(t)^2\rangle}\,|1\rangle\langle 0| + |1\rangle\langle 1|). \tag{7.11}$$

A detailed analysis of the function $e^{-1/2\langle\phi(t)^2\rangle}$ and the dependence on the noise correlation for our system is presented in Refs. [66, 42]. Here we do not need to consider the exact temporal behaviour. Equ. (7.11) shows that only the coherences (off-diagonal elements) of ρ are affected by the fluctuations. If we consider a more complex two-qubit Bell state $|\phi^+\rangle = \frac{1}{\sqrt{2}}(|00\rangle + |11\rangle)$, the effect of dephasing is completely identical to the previous state but with a four times stronger decay characteristics [42]. In contrast, the phase evolution of the two states $|10\rangle$ and $|01\rangle$ of the Bell state $|\psi^+\rangle = \frac{1}{\sqrt{2}}(|10\rangle + |01\rangle)$ is identical and therefore the relative phase can be absorbed in a global phase. This Bell state is robust against collective dephasing and is part of so called decoherence free subspace (DFS). An intuitive picture of the robustness of this state against global dephasing is illustrated in Fig. 7.13, showing the level scheme of a two-qubit system.

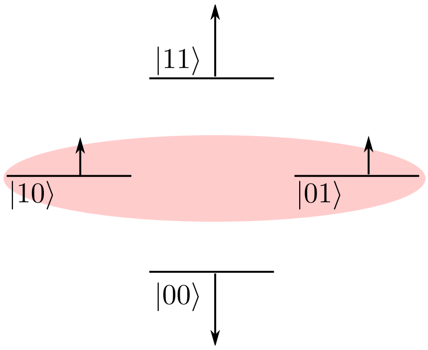

Figure 7.13: Decoherence free subspace: Intuitive picture of the robustness of a decoherence free state $|\psi^+\rangle = \frac{1}{\sqrt{2}}(|10\rangle + |01\rangle)$. Changes in the magnetic field, indicated by the arrows, lead to a frequency shift of the energy levels. The two levels $|10\rangle$ and $|01\rangle$ are shifted by the same amount assuming collective dephasing and therefore the relative phase of the entangles state $|\psi^+\rangle = \frac{1}{\sqrt{2}}(|10\rangle + |01\rangle)$ is canceled out.

The two qubits are prepared in the state the $|\psi^{+}\rangle$ as highlighted in Fig. 7.13 and affected by magnetic field fluctuations of equal strength on both qubits, which are indicated by the arrows. The fluctuations lead to a change of the energy splitting between the $|00\rangle$ state and the $|11\rangle$ state, which causes fluctuations of the relative phase. In contrast, the frequency difference between the two states $|10\rangle$ and $|10\rangle$ remains the same and therefore also the relative phase.

The sate $|\psi\rangle_1 = |1010101\rangle + |0101101\rangle$ after the first step of the encoding sequence can be expressed in the form $|\psi\rangle_1 = (|1010\rangle + |0101\rangle) \otimes |101\rangle$. The first four qubits are in the Bell state $\frac{1}{\sqrt{2}}(|1010\rangle + |0101\rangle)$, being robust against collective dephasing. The state $|101\rangle$ of the remaining qubits (5,6,7) will induce a global phase $e^{i\phi(t)/2}$ during the time evolution, which does not influence the coherence of the state. The coherence of $|\psi\rangle_1$ is probed by measuring the expectation value of the X-type stabilizer $S_x^{(1)}$ of the first plaquette after a waiting time t. An effective loss of coherence due to magnetic field and laser fluctuations would be indicated by a decay of the X-type stabilizer. The Z-type stabilizer of the first plaquette is signaling the population of the state, which is not sensitive to decoherence. Therefore the expectation value $S_z^{(1)}$ is expected to remain constant. The measurement of the $S_x^{(1)}$ (green diamonds) and $S_z^{(1)}$ (blue diamonds) expectation values as a function of the waiting time t is shown in Fig. 7.14.

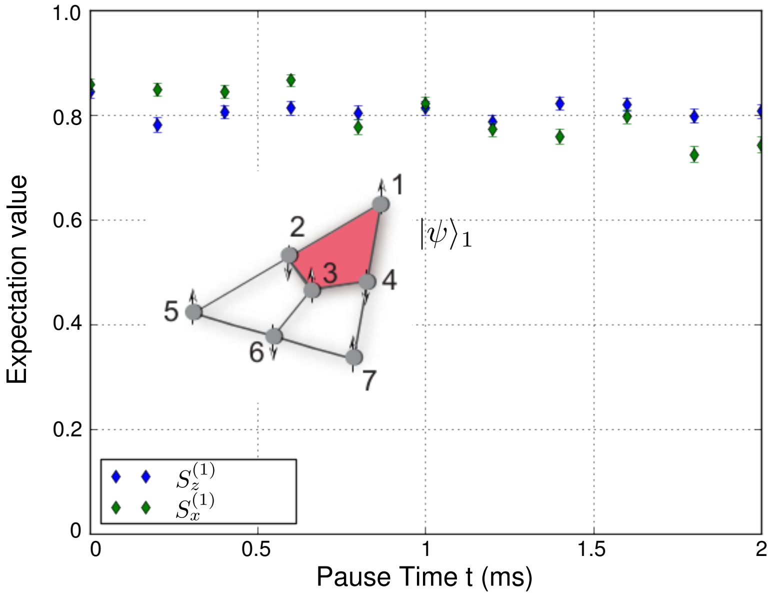

Figure 7.14: Coherence after the first encoding step: Measurement of the coherence after the first preparation step, encoding the first plaquette (red). The coherence is probed by preparing the entangled state $|\psi\rangle_1$ (see text), including a waiting t and measuring by the expectation value of the $S_x^{(1)}$ stabilizer (green diamonds). The results reveal no decay of the coherence, which indicates the robustness of the state against global phase noise. The population remains constant over time, which is confirmed by measuring the expectation value of the $S_z^{(1)}$ stabilizer (blue diamonds).

The results clearly show that the expectation value $\langle S_x^{(1)}\rangle$ remains constant, indicating the robustness of $|\psi\rangle_1$ against global dephasing.

After the second step of the encoding sequence, the resulting state is $|\psi\rangle_2 = (|101010\rangle +$

$|010110\rangle + |110001\rangle + |001101\rangle) \otimes |1\rangle$ (see Fig. 7.3), which features also coherences (entanglement) between the qubits in the second plaquette (blue). The subspace of $|\psi\rangle_2$ including the coherences between qubits 1 to 6 reveals the characteristic of a decoherence free state, since the same number of qubits are in the state $|1\rangle$ leading to a cancellation of the relative phases. The effect of the dephasing was measured similar to the characterization of the first plaquette (see Fig. 7.14). The state $|\psi\rangle_2$ was prepared according to the sequence in Fig. 7.1, followed by a waiting time t and subsequent measurement of the four plaquette stabilizers $S_x^{(1)}, S_x^{(2)}, S_z^{(1)}, S_z^{(2)}$. In Fig 7.15, the mean values of the two X-type stabilizers $(S_x^{(1)} + S_x^{(2)})/2$ and the two Z-type stabilizers $(S_z^{(1)} + S_z^{(2)})/2$ are plotted as a function of the waiting time t. Since each of the X-type stabilizers indicate a decay of the coherence, the average of the two stabilzers is plotted. The average Z-type stabilizer (blue diamonds) remain constant, which indicates that no population loss occurs during the waiting period. The X-type stabilizer (green diamonds) is constant up to a waiting of 1 ms, which indicates the robustness of the state against global phase noise. The measurement reveals a slight decay of the coherence after 1 ms, which is probably caused by drifts of the expectation values $\langle S_x^{(1)}\rangle$ and $\langle S_x^{(2)}\rangle$. Further measurements including longer waiting times would be required to provide meaningful statements about the decay.

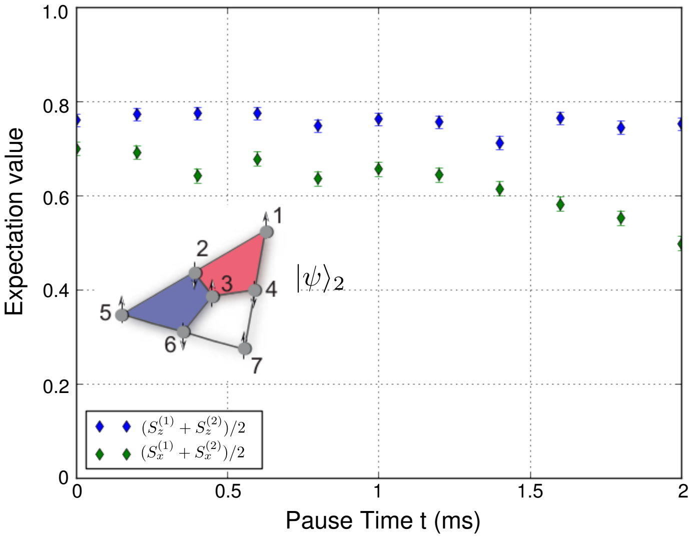

Figure 7.15: Coherence after the second encoding step: Measurement of the coherence after the second preparation step, encoding the first and second plaquette (red, blue). The coherence is probed by preparing the entangled state $|\psi\rangle_2$, including a waiting t and measuring by the mean expectation value of the $S_x^{(1)}, S_x^{(2)}$ stabilizers (green diamonds). The result reveals no decay of the coherence up to 1 ms, which is expected from the DFS characteristic. The populations remain constant over time, which is confirmed by measuring the mean expectation value of the $S_z^{(1)}, S_z^{(2)}$ stabilizers (blue diamonds).

Finally, the coherence of the complete encoded logical qubit $|0\rangle_L$ after the third step of the encoding sequence is investigated. The influence of collective dephasing on the logical state $|0\rangle_L$ is different compared to the first and second encoding steps. The final state $|0\rangle_L = |1010101\rangle + |0101101\rangle + |1100011\rangle + |0011011\rangle + |1001110\rangle + |0110110\rangle + |1111000\rangle + |0000000\rangle$ shows 8 non-zero populations. The first seven states have all three qubits in the state $|0\rangle$ and four qubits in the state $|1\rangle$, which leads to an effective phase accumulation of $e^{+i\phi(t)/2}$ for all 7 states. In contrast, the fully polarized state $|0000000\rangle$ picks up the phase $e^{-7i\phi(t)/2}$ evolving over the time t into

$$\begin{aligned}|0_L(t)\rangle = e^{+i\phi(t)/2}(&|1010101\rangle + |0101101\rangle + |1100011\rangle + |0011011\rangle + \\ &|1001110\rangle + |0110110\rangle + |1111000\rangle) + e^{-7i\phi(t)/2}|0000000\rangle.\end{aligned}$$

The density matrix after decoherence $\rho_0(t) = |0_L(t)\rangle\langle 0_L(t)|$ can be expressed in the basis of physical states forming the 8 components of the logical state $|0\rangle_L$:

$$\left(\begin{array}{cccc} 1 & e^{-8\langle\phi(t)^2\rangle} & \dots & e^{-8\langle\phi(t)^2\rangle} \\ \begin{matrix} e^{-8\langle\phi(t)^2\rangle} \\ \vdots \\ \vdots \\ e^{-8\langle\phi(t)^2\rangle} \end{matrix} & \multicolumn{3}{c}{\underset{\Uparrow}{\boxed{\begin{matrix} 1 & \dots & 1 \\ 1 & \dots & 1 \\ 1 & \dots & 1 \\ 1 & \dots & 1 \end{matrix}}}} \end{array}\right)$$

using the relation $\langle e^{\pm 4i\phi(t)/2}\rangle = e^{-8\langle\phi(t)^2\rangle}$. The density matrix reveals an interesting aspect of the coherence property of the color code state: The 7x7 block, highlighted by the red box, of the 8x8 density matrix corresponds to the identity and implies that a large part of the whole state is not affected by global phase noise. The only non-vanishing decay components appear in the coherences between the $|0000000\rangle$ state and the 7 remaining states. Therefore, the final color code state is not a decoherence free state. The X-type stabilizer expectation values $\langle S_x^{(i)}\rangle (i = 1, 2, 3)$ evolve into

$$\langle S_x^{(i)}(t)\rangle = tr(\rho_0(t) S_x^{(i)}) = \frac{1}{4}(3 + e^{-8\langle\phi(t)^2\rangle}) \rightarrow 0.75 \text{ for } t \rightarrow \infty. \tag{7.12}$$

The mean value of the three X-type (blue diamonds) and three Z-type (red diamonds) stabilizers are measured for different waiting times, as shown in Fig. 7.16. The decay characteristics of the X-type stabilizer in Fig. 7.16 shows a plateau up to 0.5 ms with an average value of 0.3 followed by a decay up to 1.5 ms. The expectation value is leveling out at ≈ 0.2, which is about $\frac{3}{4}$ of the initial value and is in agreement with the theoretical prediction.

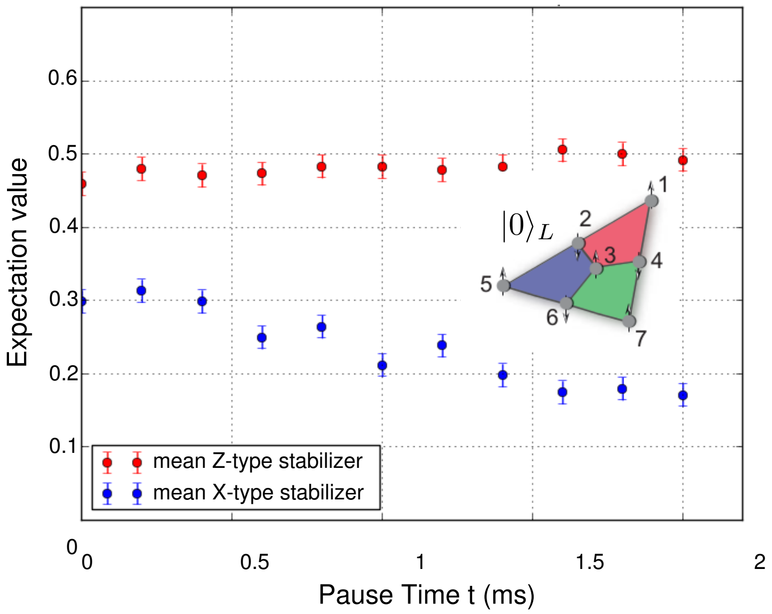

Figure 7.16: Coherence after the third encoding step: Measurement of the coherence after the third preparation step, encoding the logical state $|0\rangle_L$. The coherence is probed by preparing the logical state $|0\rangle_L$ (see text), including a waiting t and measuring the mean expectation value of the X-type stabilizers $S_x^{(1)}, S_x^{(2)}, S_x^{(3)}$ (blue diamonds). The logical color code state is not fully protected against global dephasing (see text) and a decay of the mean X-type stabilizer to $\frac{3}{4}$ of the initial value is expected. This behaviour is confirmed by the experimental result. The populations remain constant over time, which is confirmed by measuring the mean expectation value of the Z-type stabilizers $S_z^{(1)}, S_z^{(2)}, S_z^{(3)}$ stabilizers (red diamonds).

7.8 Perspectives for experimental error correction using the seven-qubit code

In stabilizer quantum error correcting codes - within the framework of topological quantum codes as well as within the approach based on concatenated codes - protection of quantum states against errors is realized by (i) encoding the information in collective, entangled quantum states distributed over many physical qubits, and (ii) subsequent active "supervision" of the system by repetitive "in-situ" measurements of the stabilizer generators in order detect and keep track of dynamically occurring errors, possibly followed by quantum or classical feedback operations to undo the effect of the errors [129, 120]. In this section we estimate the experimental requirements that need to be met in general and in our specific setup, in order to use in the future the seven-qubit code for active error correction.

The simplest model for QEC is perfect initial state encoding, perfect QND measurements of the plaquette stabilizers, and the only errors originate from uncorrelated single-qubit errors occurring at a rate p per error correction round. Under ideal conditions, an encoded logical quantum state $|\psi_L\rangle$ can be recovered if either no error or at most one error occurs on one of the 7 physical qubits. The recovery probability p_{rec}^{ideal} in this case is

$$p_{rec}^{ideal} = (1-p)^7 + 7p(1-p)^6 = 1 - 21p^2 \tag{7.13}$$

where the leading term quadratic in p corresponds to the 21 possible, non-correctable double-error events. Thus, for small single qubit error rates p, protection becomes effective, as under these conditions (p_{rec}^{ideal}) the encoded qubit shows less errors than a single unencoded qubit. We now consider a more realistic scenario that includes the two dominant and generic sources of imperfections, which reduce the recovery probability for an encoded quantum state $|\psi_L\rangle$: (i) First, a logical quantum state $|\psi_L\rangle$ can only be encoded with a finite fidelity $\mathcal{F}_{SP} < 1$, giving rise to a state ρ which we model for the purpose of our estimate by a mixture of the ideal logical state $|\psi_L\rangle\langle\psi_L|$ and the fully mixed density matrix,

$$\rho = \mathcal{F}_{SP}\,|\psi_L\rangle\langle\psi_L| + \frac{1-\mathcal{F}_{SP}}{d}1, \tag{7.14}$$

with $d = 2^7$ for the seven-qubit code and 1 the 7-qubit identity operator. (ii) Furthermore, we take into account that in one round of error correction of bit-flip (phase flip) errors the three Z-(X-)type plaquette stabilizers need to be measured in a non-destructive way in order to deduce the error syndrome. These QND measurements of stabilizer operators can be achieved by a quantum circuit (see Fig. Fig. 7.17(B)) which coherently maps the eigenstates of the stabilizers $S_z^{(i)}$ ($S_x^{(i)}$) onto the computational states $|0\rangle$ and $|1\rangle$ of ancillary qubits, followed by measurements of these ancillary qubits. In practice, the QND stabilizer measurements are faulty as well and can only be realized with a fidelity $\mathcal{F}_{QND}$. Thus, under these conditions the recovery probability is reduced to

$$p_{rec}^{n} \geq \mathcal{F}_{SP}\mathcal{F}_{QND}^{3}p_{rec}^{ideal}. \tag{7.15}$$

It is straightforward to show that for small enough imperfections (fidelities $\mathcal{F}_{SP}, \mathcal{F}_{QND}$) there exist single-qubit error rates p, where $p_{rec}^{n} > 1 - p$ and using an encoded qubit is favourable over using a pure physical qubit:

$$\mathcal{F}_{SP}\mathcal{F}_{QND}^{3} \gtrsim 1 - \frac{1}{4}\frac{1}{21} \simeq 1 - 0.012 = 98.8\%. \tag{7.16}$$

Fig. 7.17(B) displays the discussed lower bounds for the recovery probabilities for an unencoded qubit, as well as for the 7-qubit code under ideal and non-ideal conditions.

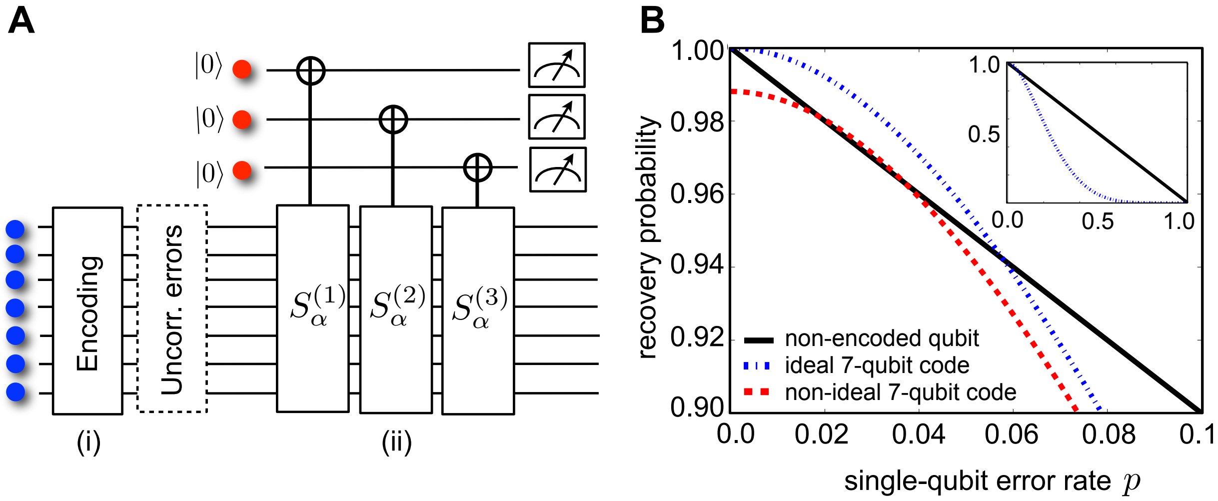

Figure 7.17: Quantum error correction using the seven-qubit code: **(A)** (i) Encoding of a quantum state in 7 physical qubits is followed by (ii) QND measurements of the set of $\alpha = X$ or $\alpha = Z$-type stabilizer operators (generators) via 3 ancillary qubits. The collection of measurement outcomes (the error syndrome) is used to deduce the most probable pattern of physical errors. Note that the set of stabilizers can also be measured sequentially using a single ancillary qubit, which is reset after the measurement of each stabilizer (see also Sec. 6.2.2). **(B)** Logical recovery probability for a quantum state stored in an unprotected, single qubit (black solid line) and using the seven-qubit code under ideal (blue dashed-dotted line) and non-ideal (red dashed line) conditions, as a function of the single-qubit error rate p. The seven-qubit code offers under ideal conditions increased protection – as compared to a non-encoded qubit – provided that the single-qubit error rate p is not too large ($p \lesssim 1/21$). Under more realistic conditions, where errors in the encoding (i) and the QND measurement of stabilizers (ii) are taken into account (see text for details), the seven-qubit code starts to offer improved protection – as compared to single physical qubits – in a finite region of single-qubit error rates p, once the overall fidelity for the encoding and syndrome measurement is larger than about 98.8%. For completeness, the inset shows the recovery probabilities over the full range $0 \leq p \leq 1$ of single-qubit error rates. (picture also shown in Ref. [124]).

Chapter 8

Summary and Outlook

The presented work focuses on the implementation of a topological error correction code in an ion trap based quantum computer. The properties of the color code were investigated for the smallest instance, encoding one logical qubit in seven physical ions. This proof of principle experiment demonstrated important key prerequisites for FTQC: (a) encoding of the logical qubit (b) detection of the complete error syndrome of all 21 single-qubit errors and revealing that the color code belongs to the class of CSS stabilizer codes. (c) applying the set of Clifford operations $\{H_L, X_L, Z_L, K_L\}$ transversally on a logical qubit and generating all 6 cardinal states of the logical Bloch sphere. Additionally, up to 10 logical operations were applied, showing that the fidelity loss per gate is only 3.8%. The fidelities of the generated logical states were estimated by measuring a set of 128 stabilizer operators instead of full state tomography on seven qubits, leading to an enormous reduction of the required measurement settings from 2187 to 128. Protection of the encoded information by successfully correcting occurring errors could not be demonstrated within this work, as the encoding procedure reveals a fidelity of 35% and therefore is not in a regime where the encoded qubit performs better than a single unprotected qubit (see Sec. 7.8).

The performance of the encoding procedure is given by the fidelity of the operations on the physical qubits. In particular, the single-qubit operations are significant for the encoding fidelity due to the large number of pulses (≈120). In the course of this work, the quality of the addressing gates was improved in terms of reducing the addressing errors with the optical setup described in Sec. 3.4.1. Limitations of the single-qubit operations are due to intensity fluctuations of the laser light and beam pointing instabilities. Further efforts including active intensity stabilization and changing the mechanical setup of the objective mount will significantly improve the fidelity.

The fidelity of the coherent global operations was characterized within the master thesis project of Roman Stricker by randomized benchmarking on a single qubit and yielded an infidelity of about 10^{-3} for single-qubit $\pi/2$ rotations. This could be improved by implementing the qubit laser system described in Sec. 3.6.1, yielding an infidelity of about 10^{-5}. This remarkable result pushes the global operations towards the fault tolerant regime.

The effect of the improved coherence of our system on the entangling operations will be investigated with interleaved randomized benchmarking on two qubits in the near future [163]. At the moment, the coherence of our system is limited by fluctuations of the magnetic field, probably caused by current stabilization electronics. Recently, an impressive work by Ruster et al. demonstrated a coherence time of 2 s of a qubit encoded in the two Zeeman levels of the $4^2S_{1/2}$ ground state of ^{40}Ca$^+$using permanent magnets instead of active current drivers [164]. This approach will also be adapted for our future experiments to further improve the coherence of our system and increase the fidelity of the entangling operations.

Improving the physical operations will allow further investigations of the color code. An essential step towards the realization of fault tolerant quantum computation is the correction of occurring errors. This requires the readout of the stabilizer operators in a non-destructive way using the scheme presented in Sec. 7.8. Furthermore, a fundamental proof of concept experiment towards the realization of a *universal* set of operations on the encoded qubit is the achievement of a non-Clifford operation (T-gate) on the logical qubit via magic state injection using one logical qubit and one physical ancilla qubit.

The experimentally implemented color code represents a proof-of-principle experiment in a small-scale ion trap quantum computer. Nevertheless, the fundamental steps required to successfully encode the logical qubit are certainly of particular importance for other physical platforms. The method used to correct unknown but constant phase shifts appearing during the encoding procedure (see Sec. 7.2) can be applied to other AMO systems. In addition, noise models including spatial correlations play a crucial role for the simulation of QEC codes in a realistic setting. The technique introduced in Ref. [36] is readily applicable to any quantum system and was demonstrated in this work to act as a practical tool for the characterization of spatial correlations (see Sec. 5.2).

As a long term goal, the presented color code as well as the achieved concepts are preferably adapted to scalable 2D architectures using trapped ions [165] and various other atomic, optical and solid-state systems [126]. Further technological progress of the scalable quantum architectures will potentially enable fault tolerant QC on a topologically protected qubit and pave the way towards a useful quantum computer. The demonstrated proof of concept experiments in this work and the investigated methods contribute to this progress and to our vision of *keeping a qubit alive*.

Appendix A

Msquared laser locking details

As already described in Sec. 3.6.1, the Msquared laser is locked to the reference cavity by a feedback loop to one external AOM and two Piezos mounted within the laser resonantor. The AOM has the capability to cancel out high frequency noise up to 1 MHz, whereas acoustic fluctuations up to 100 kHz are compensated by the fast Piezo. The slow Piezo is ony used to compensate slow drifts of the laser frequency.

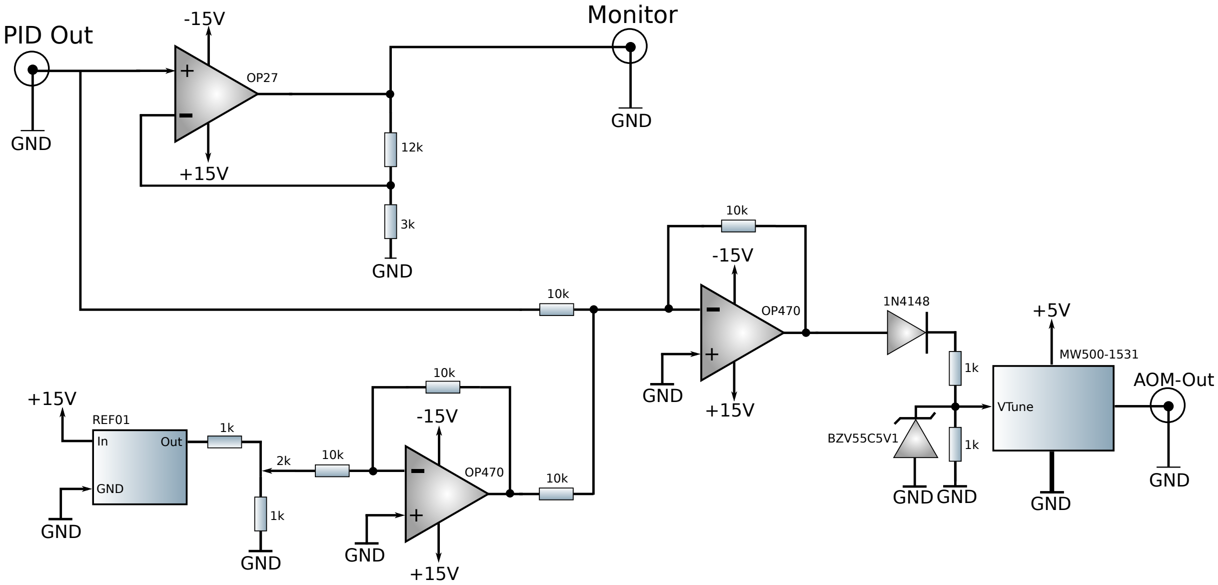

Figure A.1: Noise cancellation AOM electronics: Electronic circuit diagram used to feedback on the noise cancellation AOM. The output signal of the PID regulator (PID Out) is added up with a constant voltage and applied to the voltage controlled oscillator (VCO). The constant offset voltage is adjusted by the potentiometer and sets the VCO center frequency to 80 MHz.

Fig. A.1 shows a schematic representation of the electronic circuit used to actuate on the noise cancellation AOM (see Fig. 3.20). The output signal of the Falc 110 PID controler is added to an internal offset voltage, which is created by the REF01 precision voltage reference in combination with a voltage divider. The signals are added up by a summing amplifier OPA470 with a gain-bandwidth product of 6 MHZ. The final signal is applied to a voltage controlled oscillator (VCO) MW500-1531 with a center frequency of 80 MHz and a tuning voltage of 0.4 V to 4 V and a frequency sensitivity of 1MHz/V. The offset voltage is adjusted to set the radio frequency to 80 MHz. The feedback to the AOM is realized by a limited intergrator and a differntiator branch. Furthermore, the output of the ulimited integrator (± 5V output range) of the Falc 110 is used to compensate for slow drifts.

Actuator	Dip switch settings	lower frequency (gain)	higher frequency (gain)
AOM (limited integrator)	[4,5]	370 Hz (37 dB)	22 kHz (1.6 dB)
AOM (differentiator)	[7,8]	140 kHz (0 dB)	750 kHz (15 dB)
fast Piezo (slow limited integrator)	[5]	240 Hz (37 dB)	14 kHz (1.6 dB)
fast Piezo (fast limited integrator)	[7]	14 kHz (0 dB)	170 kHz (15 dB)
slow Piezo (unlimited integrator)	[1,5]	30 Hz	-

Table A.1: Settings of the Falc 110 PID controller used to feeback on the slow Piezo as well as the noise cancelling AOM.

The AOM feedback has gain of 37 dB up to a frequency of 370 Hz and decreases to 1.6 dB at a frequency of 22 kHz. The higher frequency range is covered by the differentiator, which has a voltage gain of 0 dB up to a frequency of 140 kHz and increases to 15 dBm at 750 kHz. The main gain is required at frequencies in the lower kHz range, which leads to the assumption that the dominant noise is also in the same frequency regime. Nevertheless, we observed that acoustic noise is broadening the laser linewidth up to several hundred kHz and therefore we could not achieve stable locking only by actuating on the fast Piezo. The feedback to the fast Piezo is required to increase the stability in the acoustic frequency domain (≤ 2 kHz). Therefore an additional Falc 110 controller was used to actuate on the fast Piezo with a 37 dB gain level up to 240 Hz. The settings of the Falc 110 regulators are shown in Table A.1. It was observed that the fast Piezo leads to an improvement of the locking stability with respect to perturbations in the acoustic frequency domain. The most dominant resonance peak when stimulating the laser system with external acoustic noise was observed at 1.9 kHz.

Appendix B

From Choi-Jamiolkowski to χ representation

The main task is to find a map from the Choi-Jamiolkowski representation S to the χ matrix. The χ matrix representation of a quantum process is defined by the following equation:

$$\mathcal{E}(\rho) = \sum_{m,n} \chi_{m,n}\, A_m \rho A_n^\dagger. \tag{B.1}$$

The process $\mathcal{E}$ is expanded in the basis A with the expansion factors $\chi_{m,n}$. In general, the basis used for this representation consists of the Pauli matrices $\{\mathbb{1}, \sigma_x, \sigma_y, \sigma_z\}$. Without any kind of restriction, the process $\mathcal{E}$ can also be written in a different basis B. The mapping of the χ matrix caused by the basis transformation will be calculated in detail. Assume that the transformation between the basis A and B can be written in the following way:

$$B_i = \sum_k C_{ki} A_k \tag{B.2}$$

with the transformation matrix C. The process $\mathcal{E}_B$ in the basis B can be defined by:

$$\begin{aligned}
\mathcal{E}_B &= \sum_{m,n} \chi^{(B)}_{m,n} B_m \rho B_m^\dagger = \\
&= \sum_{m,n} \chi^{(B)}_{m,n} \Big(\sum_k C_{k,m} A_k\Big) \rho \Big(\sum_l C^*_{l,n} A_l^\dagger\Big) = \\
&= \sum_{k,l} \underbrace{\sum_m \sum_n C_{k,m} \chi^{(B)}_{m,n} C^\dagger_{n,l}}_{=[C\chi^{(B)}C^\dagger]_{kl}} A_k \rho A_l^\dagger
\end{aligned}$$

As a result, the transformation between the chi matrices $\chi^{(B)}$ and $\chi^{(A)}$ is given by the following expression:

$$\chi^{(B)} = C \chi^{(A)} C^\dagger. \tag{B.3}$$

The basis transformation matrix C can be calculated from the following equation:

$$C = (AA)^{-1}\,AB, \tag{B.4}$$

with the corresponding matrix elements $(AA)_{i,j} = \mathrm{Tr}(A_i A_j)$ and $(AB)_{i,j} = \mathrm{Tr}(A_i B_j)$. The reason for calculating the possible basis transformation is that the S matrix has a particular form when choosing a special basis G of the process. Assume the orthonormal basis G with:

$$G_1 = \begin{pmatrix} 1 & 0 \\ 0 & 0 \end{pmatrix},\ G_2 = \begin{pmatrix} 0 & 1 \\ 0 & 0 \end{pmatrix},\ G_3 = \begin{pmatrix} 0 & 0 \\ 1 & 0 \end{pmatrix},\ G_4 = \begin{pmatrix} 0 & 0 \\ 0 & 1 \end{pmatrix}. \tag{B.5}$$

It can be shown easily that the S matrix using the basis G for the χ matrix representation is identical to χ, therefore $S = \chi$. This means that the S matrix corresponds to the χ matrix in the basis G. Therefore the basis transformation from G to the Pauli basis σ by the transformation map $C_{G\to\sigma}$ applied to the Choi-Jamiolkowski matrix S will result in the χ matrix:

$$\boxed{\chi = C_{G\to\sigma} S C^{\dagger}_{G\to\sigma}} \tag{B.6}$$

Appendix C

Direct characterization of collective longitudinal and transverse relaxation processes

Let us consider a global quantum *homogenization or thermalization* process acting on some qubits for a time t. Thus for each single-qubit density matrix ρ, with $\rho_{00} = a$ and $\rho_{01} = b$ in the computational basis, ρ evolves into the state $\rho(t)$ with $\rho_{00}(t) = (a - a_0)\exp(-t/T_1) + a_0$ and $\rho_{01}(t) = b\exp(-t/T_2)$, where T_1 and T_2 ($T_2 \leqslant 2T_1$) are relaxations and dephasing time-scales of the system, respectively. That is, the system approaches an equilibrium state identified by $a_0 \in [0, 1]$.

In order to measure these time scales using the DCQD approach we need to create quantum correlations between each pair of neighboring qubits, e.g., in the form of a Bell-state $\rho = |\Phi^+\rangle\langle\Phi^+|$ where $|\Phi^+\rangle = (|00\rangle + |11\rangle)/\sqrt{2}$, and then let all of the qubits evolve for a time t leading to state $\mathcal{E}(\rho)$. Thus by performing a Bell-state measurement between the same neighboring qubits we obtain ([95], [1]):

$$Tr[P^{11}\mathcal{E}(\rho)] - Tr[P^{44}\mathcal{E}(\rho)] = e^{-\frac{2t}{T_2}}$$

where $P^{kk'} = |B^k\rangle\langle B^{k'}|$, and $|B^k\rangle$ for $k = 1, 2, 3, 4$ corresponds to the Bell-states $|\Phi^+\rangle$, $|\Psi^+\rangle$, $|\Psi^-\rangle$, and $|\Phi^-\rangle$, respectively, where $|\Phi^\pm\rangle = (|00\rangle \pm |11\rangle)/\sqrt{2}$, $|\Psi^\pm\rangle = (|01\rangle \pm |10\rangle)/\sqrt{2}$. Using the fact that $Tr[P^{11}\mathcal{E}^T(\rho)] = \chi_{1,1}$ and $Tr[P^{44}\mathcal{E}^T(\rho)] = \chi_{4,4}$ we obtain:

$$e^{-\frac{\mathrm{2t}}{\mathrm{T_2}}} = \chi_{1,1} - \chi_{4,4}. \tag{C.1}$$

It is important to mention that this expression is only valid for Markovian noise acting on the entire system. For our system it was observed [18] that the phase decoherence of Greenberger-Horne-Zeilinger (GHZ) states scales with $\exp(-N^2t)$ instead of $\exp(-Nt)$, with N the number of ions. Therefore Eq. (1) has to be modified, which leads to the following result for the phase-decoherence:

$$e^{-\frac{\mathrm{N^2t}}{\mathrm{T_2}}} = \chi_{1,1} - \chi_{4,4}. \tag{C.2}$$

---

[1] M. Mohseni, in preparation, 2012

In the case of T_1, the outcome of a BSM within the DCQD formalism yields:

$$\begin{aligned} &1-2(Tr[P^{22}\mathcal{E}(\rho)]+Tr[P^{33}\mathcal{E}(\rho)])= \\ &=(1-2a_0)^2(1-2e^{-\frac{t}{T_1}})+(2+4a_0(a_0-1))e^{-\frac{2t}{T_1}}. \end{aligned} \tag{C.3}$$

For our system the equilibrium state is described by the ground state and therefore $a_0 = 1$, which leads to:

$$1-2(\chi_{22}+\chi_{33})=(1-2e^{-\frac{t}{T_1}})+2e^{-\frac{2t}{T_1}}.$$

For a unital quantum *homogenization* process ($\mathcal{E}(I) = I$), we have $a_0 = \frac{1}{2}$ (i.e., a completely stochastic equilibrium state). Thus the relation for T_1 becomes:

$$e^{-\frac{2\mathrm{t}}{\mathrm{T}_1}}=1-2(\chi_{2,2}+\chi_{3,3}).$$

It is remarkable that even if we use the relations developed for the ideal DCQD scheme, assuming T_1 and T_2 acting only on the system qubit (considering the other system as a reference signal or a noiseless ancilla), we can still obtain both T_2 and T_1 only to be smaller than the actual value by a factor of 2. Note that, due to orthogonality of the BSM outcomes, it is easy to unambiguously distinguish T_1 from T_2. Traditionally, in order to measure the longitudinal and transverse relaxation times, one needs to measure two non-commutative observables (e.g., Pauli operators σ_z and σ_x) on two sub-ensembles of identical systems.

Appendix D

Controlled amplitude- and phase-damping

The process of **phase damping** is implemented by the following steps (see Fig. D.1(a)): (i) Hiding the population of the $D_{5/2}(m_j = -1/2)$ state of both ions by applying a π-pulse on the $D_{5/2}(m_j = -1/2) \leftrightarrow S_{1/2}(m_j = 1/2)$ transition. (ii) Transfering a certain amount of the population of the $S_{1/2}(m_j = -1/2)$ state to the $D_{5/2}(m_j = -5/2)$ state. The excitation probability is experimentally controlled by the pulse length t and is given by $\gamma = \sin(\frac{\pi t}{T})^2$, with the Rabi-oscillation period time T. (iii) Repumping the transfered population into the $P_{3/2}$ state by a laser pulse at a wavelength of 854 nm whereupon the system qubit decays spontaneously into the ground state. (iv) Finally the second step is repeated to reverse the hiding process. Because of the spontaneous decay after the third step the state loses its phase information. The hiding process described in the first step is necessary to prevent the $D_{5/2}(m_j = -1/2)$ state from not being affected by the repumping process which would have the same effect as amplitude damping.

Amplitude damping is carried out within two steps (see Fig. D.1(b)). First the population is coherently transfered from the $D_{5/2}(m_j = -1/2)$ to the $S_{1/2}(m_j = 1/2)$ state by an addressed laser pulse with length t. Then the population of the $S_{1/2}(m_j = 1/2)$ state is transfered to the $S_{1/2}(m_j = -1/2)$ ground state by an optical pumping process performed by a σ^--polarized laser beam at 397 nm exciting the ion first to the $P_{1/2}(m_j = -1/2)$ state followed by spontaneous decay to the $S_{1/2}(m_j = -1/2)$. The ancilla ion is not affected by the optical pumping process because the σ^--polarized pulse can only excite the $S_{1/2}(m_j = 1/2)$ ground state.

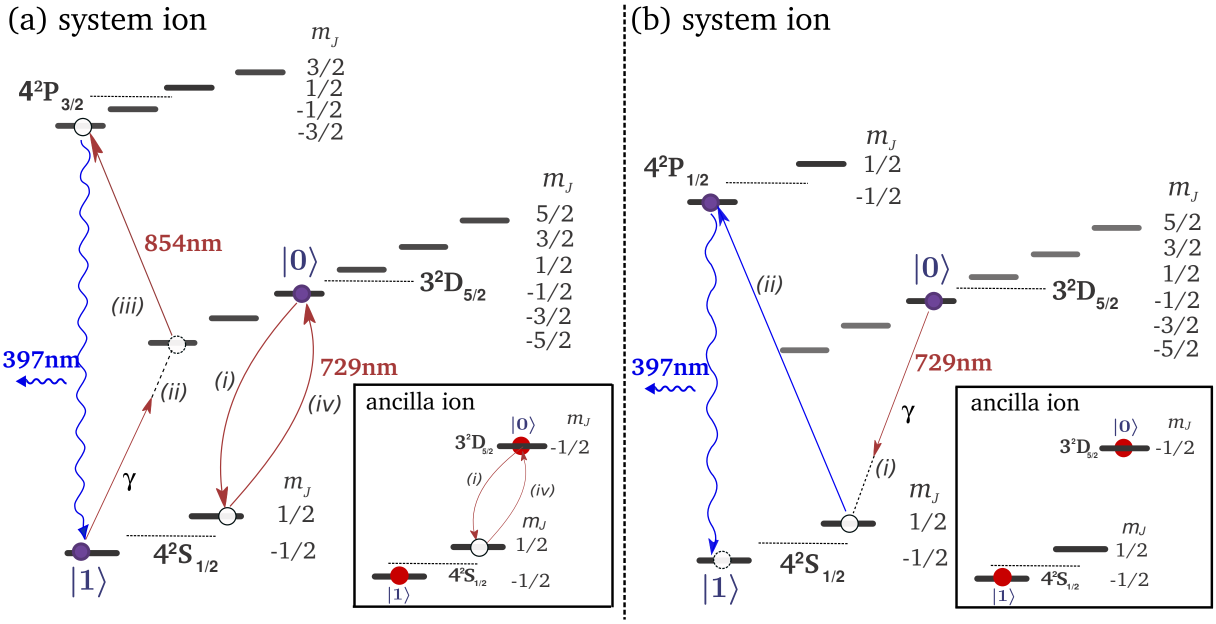

Figure D.1: Amplitude- and phase-damping: Schematic of the phase damping (a) and amplitude damping (b) processes acting on the system ion S: (a) Transfer of the $S_{1/2}(m_j = -1/2)$ population with a probability of γ to the $P_{3/2}$ state followed by optical repumping to the ground state while the population of the $D_{5/2}(m_j = -1/2)$ state is hidden in the $S_{1/2}(m_j = 1/2)$ state. (b) The amplitude damping process is carried out by coherently transfering the population of the $D_{5/2}(m_j = -1/2)$ state to the $S_{1/2}(m_j = 1/2)$ state of the system ion followed by optical pumping to the ground state $S_{1/2}(m_j = -1/2)$. The ancilla ion is not affected during the whole processes, as shown in the inset figures. (picture also shown in Ref. [79]).

Bibliography

[1] M. Planck, Annalen der Physik **4**, 553 (1901).

[2] A. Einstein, Annalen der Physik **332**, 132 (1905).

[3] E. Schrödinger, Phys. Rev. **28**, 1049 (1926).

[4] E. Schrödinger, Brit. J. Phil. Sci. **3**, 233 (1952).

[5] M. H. Holzscheiter, Physica Scripta **1995**, 69 (1995).

[6] T. Sauter, W. Neuhauser, R. Blatt, and P. E. Toschek, Phys. Rev. Lett. **57**, 1696 (1986).

[7] J. C. Bergquist, R. G. Hulet, W. M. Itano, and D. J. Wineland, Phys. Rev. Lett. **57**, 1699 (1986).

[8] W. Nagourney, J. Sandberg, and H. Dehmelt, Phys. Rev. Lett. **56**, 2797 (1986).

[9] W. Neuhauser, M. Hohenstatt, P. Toschek, and H. Dehmelt, Phys. Rev. Lett. **41**, 233 (1978).

[10] D. J. Wineland and W. M. Itano, Phys. Rev. A **20**, 1521 (1979).

[11] R. Feynman, International Journal of Theoretical Physics **21**, 467 (1982), ISSN 0020-7748.

[12] D. Deutsch, Proceedings of the Royal Society of London A **400**, 97 (1985).

[13] P. W. Shor, Foundations of Computer Science, 1994 Proceedings., 35th Annual Symposium. pp. 124–134 (1994).

[14] J. I. Cirac and P. Zoller, Phys. Rev. Lett. **74**, 4091 (1995).

[15] F. Schmidt-Kaler, H. Häffner, M. Riebe, S. Gulde, G. P. T. Lancaster, T. Deuschle, C. Becher, C. F. Roos, J. Eschner, and R. Blatt, Nature **422**, 408 (2003).

[16] M. Riebe, H. Häffner, C. Roos, W. Hänsel, J. Benhelm, G. Lancaster, T. Körber, C. Becher, F. Schmidt-Kaler, D. James, et al., Nature **429**, 734 (2004), ISSN 0028-0836.

[17] M. D. Barrett, J. Chiaverini, T. Schaetz, J. Britton, W. Itano, J. D. Jost, E. Knill, C. Langer, D. Leibfried, R. Ozen, et al., Nature **429**, 737 (2004).

[18] T. Monz et al., Phys. Rev. Lett. **106**, 130506 (2011).

[19] D. Leibfried, E. Knill, S. Seidelin, J. Britton, R. B. Blakestad, J. Chiaverini, D. B. Hume, W. M. Itano, J. D. Jost, C. Langer, et al., Nature **438**, 639 (2005), ISSN 0028-0836.

[20] C. A. Sackett, D. Kielpinski, B. E. King, C. Langer, V. Meyer, C. J. Myatt, M. Rowe, Q. A. Turchette, W. M. Itano, D. J. Wineland, et al., Nature **404**, 256 (2000), ISSN 0028-0836.

[21] M. A. Nielsen and I. L. Chuang, *Quantum Computation and Quantum Information* (Cambridge University Press, Cambridge CB2 8BS, 2010).

[22] D. P. DiVincenzo, Fortschr. Phys. **48**, 771 (2000).

[23] B. Joshi, D. Pradhan, and J. Stiffler, *Fault-Tolerant Computing* (Wiley Encyclopedia of Computer Science and Engineering, 2009), pp. 1191–1202.

[24] W. K. Wootters and W. H. Zurek, Nature **299**, 802 (1982).

[25] A. Steane, Proc. Roy. Soc. Lond. A **452**, 2551 (1996).

[26] P. W. Shor, Phys. Rev. A **52**, 2493 (1995).

[27] D. Aharonov and M. Ben-Or, Proceedings of the Twenty-Ninth Annual ACM Symposium on Theory of Computing **97**, 176 (1997).

[28] D. Gottesman, Phys. Rev. A **57**, 127 (1998).

[29] R. Laflamme, C. Miquel, J. P. Paz, and W. H. Zurek, Phys. Rev. Lett. **77**, 198 (1996).

[30] D. Forney, Technical Report - MIT **440** (1965).

[31] P. Aliferis, D. Gottesman, and J. Preskill, Quant. Inf. Comput. **6**, 97 (2006).

[32] A. Y. Kitaev, Ann. Phys. **303**, 2 (2003).

[33] B. Hector, arXiv:1311.0277v1 (2013).

[34] A. G. Fowler, M. Mariantoni, J. M. Martinis, and A. N. Cleland, Phys. Rev. A **86**, 032324 (2012).

[35] H. G. Katzgraber, H. Bombin, and M. A. Martin-Delgado, Phys. Rev. Lett. **103**, 090501 (2009).

[36] A. Rivas and M. Müeller, New J. Phys. **17**, 062001 (2015).

[37] M. Mohseni, A. T. Rezakhani, and D. A. Lidar, Phys. Rev. A **77**, 032322+ (2008).

[38] P. Schindler, D. Nigg, T. Monz, J. T. Barreiro, E. Martinez, S. X. Wang, S. Quint, M. F. Brandl, V. Nebendahl, C. F. Roos, et al., New J. Phys. **15**, 123012 (2013).

[39] S. Gulde, Ph.D. thesis, University of Innsbruck, Austria (2003).

[40] P. Schindler, Ph.D. thesis, University of Innsbruck, Austria (2013).

[41] W. M. Itano, J. C. Bergquist, J. J. Bollinger, J. M. Gilligan, D. J. Heinzen, F. L. Moore, M. G. Raizen, and D. J. Wineland, Phys. Rev. A **47**, 3554 (1993).

[42] T. Monz, Ph.D. thesis, University of Innsbruck, Austria (2011).

[43] Z. Hradil, J. Rehacek, J. Fiurasek, and M. Jezek, *Quantum State Estimation* (Springer-Verlag Berlin Heidelberg, 2004).

[44] M. Paris and J. Rehacek, *Quantum State Estimation* (Springer-Verlag Berlin Heidelberg, 2004).

[45] M. Ježek, J. Fiurášek, and Z. c. v. Hradil, Phys. Rev. A **68**, 012305 (2003).

[46] P. Schindler, D. Nigg, T. Monz, J. T. Barreiro, E. Martinez, S. X. Wang, S. Quint, M. F. Brandl, V. Nebendahl, C. F. Roos, et al., New J. Phys. **15**, 123012 (2013).

[47] P. A. Barton, C. J. S. Donald, D. M. Lucas, D. A. Stevens, A. M. Steane, and D. N. Stacey, Phys. Rev. A **62**, 032503+ (2000).

[48] R. W. P. Drever, J. L. Hall, F. V. Kowalski, J. Hough, G. M. Ford, A. J. Munley, and H. Ward, Appl. Phys. B **31**, 97 (1983).

[49] M. Chwalla, Ph.D. thesis, University of Innsbruck, Austria (2009).

[50] G. Kirchmair, Master's thesis, University of Innsbruck, Austria (2006).

[51] D. Rotter, Master's thesis, University of Innsbruck, Austria (2003).

[52] J. Eschner, G. Morigi, F. Schmidt-Kaler, and R. Blatt, J. Opt. Soc. **20** (2003).

[53] P. Wolfgang and H. Steinwedel, Zeitschrift für Naturforschung A **8**, 448 (1953).

[54] D. Leibfried, R. Blatt, C. Monroe, and D. Wineland, Rev. Mod. Phys. **75**, 281 (2003).

[55] P. Schindler, Master's thesis, University of Innsbruck, Austria (2008).

[56] C. J. Foot, *Atomic physics* (Oxford University Press, 2005).

[57] H. Häffner, S. Gulde, M. Riebe, G. Lancaster, C. Becher, J. Eschner, F. S. Kaler, and R. Blatt, Phys. Rev. Lett. **90**, 143602+ (2003).

[58] B. E. H. Saleh and M. C. Teich, *Fundamentals of Photonics* (Wiley, 2008).

[59] D. James, Appl. Phys. B **66**, 10 (1998).

[60] D. McGloin, G. Spalding, H. Melville, W. Sibbett, and K. Dholakia, Optics Express **158**, 281 (2003).

[61] S. Schunke, Master's thesis, University of Innsbruck, Austria (2015).

[62] C. Roos, Ph.D. thesis, University of Innsbruck, Austria (2000).

[63] A. Sørensen and K. Mølmer, Phys. Rev. A **62**, 022311 (2000).

[64] G. Kirchmair, J. Benhelm, F. Zähringer, R. Gerritsma, C. F. Roos, and R. Blatt, New J. Phys. **11**, 023002 (2009), ISSN 1367-2630.

[65] H. Häffner, S. Gulde, M. Riebe, G. Lancaster, C. Becher, J. Eschner, F. Schmidt-Kaler, and R. Blatt, Phys. Rev. Lett. **90**, 143602 (2003).

[66] T. Monz, P. Schindler, J. T. Barreiro, M. Chwalla, D. Nigg, W. A. Coish, M. Harlander, W. Hänsel, M. Hennrich, and R. Blatt, Phys. Rev. Lett. **106**, 130506+ (2011).

[67] N. F. Ramsey, Reviews of Modern Physics **62**, 541 (1990).

[68] E. L. Hahn, Phys. Rev. **80**, 580 (1950).

[69] T. Yuge, S. Sasaki, and Y. Hirayama, Phys. Rev. Lett. **107**, 170504 (2011).

[70] L. Postler, Master's thesis, University of Innsbruck, Austria (2015).

[71] L.-S. Ma, P. Jungner, J. Ye, and J. L. Hall, Optics Letters **19**, 1777 (1994).

[72] E. Knill et al., Phys. Rev. A **77**, 012307 (2008).

[73] C. Roos, T. Zeiger, H. Rohde, H. C. Nägerl, J. Eschner, D. Leibfried, F. Schmidt-Kaler, and R. Blatt, Phys. Rev. Lett. **83**, 4713 (1999).

[74] S. Stenholm, Rev. of. mod. Phys. **58** (1986).

[75] T. Monz, D. Nigg, E. A. Martinez, M. Brandl, P. Schindler, R. Rines, S. X. Wang, I. L. Chuang, and R. Blatt, Science **19**, 1777 (2016).

[76] P. Schindler, T. Monz, D. Nigg, J. T. Barreiro, E. A. Martinez, M. F. Brandl, M. Chwalla, M. Hennrich, and R. Blatt, Phys. Rev. Lett. **110**, 070403 (2013).

[77] J. Bateman, A. Xuereb, and T. Freegarde, Phys. Rev. A **81**, 043808 (2010).

[78] M. Lindberg and J. Javanainen, J. Opt. Soc. **3**, 1008 (1986).

[79] D. Nigg, J. T. Barreiro, P. Schindler, M. Mohseni, T. Monz, M. Chwalla, M. Hennrich, and R. Blatt, Phys. Rev. Lett. **110**, 060403 (2013).

[80] A. M. Childs, I. L. Chuang, and D. W. Leung, Phys. Rev. A **64**, 012314 (2001).

[81] J. B. Altepeter et al., Phys. Rev. Lett. **90**, 193601 (2003).

[82] W. Dür and J. I. Cirac, Phys. Rev. A **64**, 012317 (2001).

[83] G. M. D. Ariano and P. L. Presti, Phys. Rev. Lett. **86**, 4195 (2001).

[84] M. Mosheni, A. T. Rezakhani, and D. A. Lidar, Phys. Rev. A **77**, 032322 (2008).

[85] M. Mohseni and D. A. Lidar, Phys. Rev. Lett. **97**, 170501 (2006).

[86] M. Mohseni and A. T. Rezakhani, Phys. Rev. A **80**, 4 (2009).

[87] Z. W. Wang et al., Phys. Rev. A **75**, 044304 (2007).

[88] W. T. Liu et al., Phys. Rev. A **77**, 032328 (2008).

[89] T. Graham et al., arXiv **1205.2587**, 4 (2012).

[90] C. Schmiegelow et al., Phys. Rev. Lett. **104**, 123601 (2010).

[91] A. Bendersky, F. Pastaeski, and J. P. Paz, Phys. Rev. Lett. **100**, 190403 (2008).

[92] A. Shabani et al., Phys. Rev. A **84**, 1 (2011).

[93] A. Shabani et al., Phys. Rev. Lett. **106**, 1 (2011).

[94] D. Gross et al., Phys. Rev. Lett. **105**, 250401 (2010).

[95] M. Mohseni, A. T. Rezakhani, and A. Aspuru-Guzik, Phys. Rev. A **77**, 042320 (2008).

[96] M. Mohseni et al., Phys. Rev. A **81**, 032102 (2010).

[97] M. Mohseni and D. A. Lidar, Phys. Rev. Lett. **97**, 170501+ (2006).

[98] G. Kirchmair et al., New J. Phys. **11**, 023002 (2009).

[99] P. E. M. F. Mendonca et al., Phys. Rev. A **78**, 11 (2008).

[100] M. A. Nielsen, Phys. Lett. A **303**, 249 (2002).

[101] B. Efron and R. Tibshirani, *Statistical Science* (Institute of Mathematical Statistics, 1986), pp. 54–57.

[102] F. Schmidt-Kaler et al., J. Phys. B: At. Mol. Opt. Phys. **36**, 623 (2003).

[103] P. Staanum et al., Phys. Rev. A **69**, 032503 (2004).

[104] B. Lanyon et al., Science **334**, 57 (2011).

[105] X. Hu, R. de Sousa, and S. D. Sarma, *Foundations of Quantum Mechanics in the Light of new Technology* (eProceedings, 2001).

[106] M. Mohseni et al., J. Chem. Phys. **129**, 174106 (2008).

[107] J. Yuen-Zhou et al., PNAS **108**, 17615 (2011).

[108] J. T. Barreiro, Nature Physics **7**, 927 (2011).

[109] D. Aharonov, A. Kitaev, and J. Preskill, Phys. Rev. Lett. **96**, 050504 (2006).

[110] P. W. Shor, Phys. Rev. A **52**, R2493 (1995).

[111] T. Monz, K. Kim, W. Hänsel, M. Riebe, A. S. Villar, P. Schindler, M. Chwalla, M. Hennrich, and R. Blatt, Phys. Rev. Lett. **102**, 040501+ (2009).

[112] P. Schindler, J. T. Barreiro, T. Monz, V. Nebendahl, D. Nigg, M. Chwalla, M. Hennrich, and R. Blatt, Science **332**, 1059 (2011).

[113] J. T. Barreiro, M. Muller, P. Schindler, D. Nigg, T. Monz, M. Chwalla, M. Hennrich, C. F. Roos, P. Zoller, and R. Blatt, Nature **470**, 486 (2011), ISSN 0028-0836.

[114] R. Laflamme, C. Miquel, J. P. Paz, and W. H. Zurek, Phys. Rev. Lett. **77**, 198 (1996).

[115] A. R. Calderbank and P. W. Shor, Phys. Rev. A **54**, 1098 (1996).

[116] A. M. Steane, Phys. Rev. Lett. **77**, 793 (1996).

[117] D. Gottesman, Phys. Rev. A **57**, 127 (1998).

[118] C. H. Bennett, H. J. Bernstein, S. Popescu, and B. Schumacher, Phys. Rev. A **53**, 2046 (1996).

[119] C. H. Bennett, G. Brassard, S. Popescu, B. Schumacher, J. A. Smolin, and W. K. Wootters, Phys. Rev. Lett. **76**, 722 (1996).

[120] J. Preskill, arXiv **quant-ph/9712048**, 58 (1997).

[121] S. Bravyi and A. Kitaev, Phys. Rev. A **71**, 022316 (2005).

[122] E. Knill and R. Laflamme, arXiv:quant-ph/9608012 (1996).

[123] J. Preskill, *“Fault-Tolerant Quantum Computation" in“Introduction to Quantum Computation and Information"* (World Scientific, 1997).

[124] D. Nigg, M. Müller, E. A. Martinez, P. Schindler, H. M., T. Monz, M. A. Martin-Delgado, and R. Blatt, Science **345**, 302 (2014).

[125] C. H. Bennett, D. P. DiVincenzo, J. A. Smolin, and W. K. Wootters, Phys. Rev. A **54**, 3824 (1996).

[126] T. D. Ladd, F. Jelezko, R. Laflamme, Y. Nakamura, C. Monroe, and J. L. O’Brien, Nature **464**, 45 (2010).

[127] S. Bravyi, M. B. Hastings, and S. Michalakis, J. Math. Phys. **51**, 093512 (2010).

[128] H. Bombin and M. A. Martin-Delgado, Phys. Rev. Lett. **97**, 180501 (2006).

[129] E. Dennis, A. Kitaev, A. Landahl, and P. J., J. Math. Phys. **43**, 4452 (2002).

[130] H. G. Katzgraber, H. Bombin, R. S. Andrist, and M. A. Martin-Delgado, Phys. Rev. A **81**, 012319 (2010).

[131] D. S. Wang, A. G. Fowler, C. D. Hill, and L. C. L. Hollenberg, Quant. Inf. Comp. **10**, 780 (2010).

[132] A. J. Landahl, J. T. Anderson, and P. R. Rice, arXiv:1108.5738 (2011).

[133] M. Ohzeki, Phys. Rev. E **80**, 011141 (2009).

[134] R. S. Andrist, H. G. Katzgraber, H. Bombin, and M. A. Martin-Delgado, New J. Phys. **13**, 083006 (2011).

[135] H. Bombin, R. S. Andrist, M. Ohzeki, H. G. Katzgraber, and M. A. Martin-Delgado, Phys. Rev. X **2**, 021004 (2012).

[136] S. S. Jahromi, M. Kargarian, S. F. Masoudi, and K. P. Schmidt, Phys. Rev. B **87**, 094413 (2013).

[137] C. Wang, J. Harrington, and J. Preskill, Ann. Phys. **303**, 31 (2003).

[138] T. Ohno, G. Arakawa, I. Ichinose, and T. Matsui, Nucl. Phys. B **697**, 462 (2004).

[139] K. Takeda, T. Sasamoto, and H. Nishimori, J. Phys. A: Math. and Gen. **38**, 3751 (2005).

[140] R. Raussendorf and J. Harrington, Phys. Rev. Lett. **98**, 190504 (2007).

[141] R. Raussendorf, J. Harrington, and K. Goyal, New J. Phys. **9**, 199 (2007).

[142] A. G. Fowler and S. J. Devitt, arXiv:1209.0510 (2012).

[143] A. Al-Shimary, J. R. Wootton, and J. K. Pachos, New J. Phys. **15**, 025027 (2013).

[144] C. G. Brell, S. Burton, G. Dauphinais, S. T. Flammia, and D. Poulin, arXiv:1311.0019 (2013).

[145] A. Kitaev, Ann. Phys. **303**, 2 (2003).

[146] B. M. Terhal, Rev. Mod. Phys. **87**, 307 (2015).

[147] S. B. Bravyi and A. Y. Kitaev, quant-ph/0601201 (2006).

[148] C. Horsman, A. Fowler, S. Devitt, and R. Van Meter, New J. Phys. **11**, 123011 (2012).

[149] H. Bombin and M. Martin-Delgado, Phys. Rev. Lett. **98**, 160502 (2007).

[150] H. Bombín, Phys. Rev. X **5**, 031043 (2015).

[151] D. Gottesman, Phys. Rev. A **54**, 1862 (1996).

[152] L. M. K. Vandersypen and I. L. Chuang, Rev. Mod. Phys. **76**, 1037 (2005).

[153] M. Müller, K. Hammerer, Y. Zhou, C. F. Roos, and P. Zoller, New J. Phys. **13**, 085007 (2011).

[154] Müller, A. Rivas, M., E. A. Martinez, D. Nigg, P. Schindler, T. Monz, and M. A. Blatt, R. Martin-Delgado, arXiv:1603.00402 (2016).

[155] S. T. Flammia and Y. K. Liu, Phys. Rev. Lett. **106**, 230501 (2011).

[156] E. A. Martinez, T. Monz, D. Nigg, P. Schindler, and R. Blatt, New Journal of Physics **18**, 063029 (2016).

[157] J. Barreiro, M. Müller, P. Schindler, D. Nigg, T. Monz, M. Chwalla, M. Hennrich, C. F. Roos, P. Zoller, and R. Blatt, Nature **470**, 486 (2011).

[158] L. Landau, Zh. Eksp. Teor. Fiz. **7**, 19 (1937).

[159] X.-G. Wen, arXiv:quant-ph/10.1155 (2012).

[160] D. C. Tsui, H. L. Stormer, and A. C. Gossard, Phys. Rev. Lett. **48**, 1559 (1982).

[161] A. Uhlmann, Rep. Math. Phys. **9**, 273 (1976).

[162] J. Zhang, R. Laflamme, and D. Suter, Phys. Rev. Lett. **109**, 100503 (2012).

[163] E. Magesan, J. M. Gambetta, B. R. Johnson, C. A. Ryan, J. M. Chow, S. T. Merkel, M. P. da Silva, G. A. Keefe, M. B. Rothwell, T. A. Ohki, et al., Phys. Rev. Lett. **109**, 080505 (2012).

[164] T. Ruster, C. T. Schmiegelow, H. Kaufmann, C. Warschburger, F. Schmidt-Kaler, and U. G. Poschinger, arXiv:1606.07220 (2016).

[165] M. Kumph, P. Holz, K. Langer, M. Meraner, M. Niedermayr, M. Brownnutt, and R. Blatt, New J. Phys. **18**, 023047 (2016).

Danksagung

Am Ende meiner Arbeit möchte ich gerne all denen danken, die mich während der letzten Jahre unterstützt haben. In erster Linie möchte ich meinem Doktorvater und Betreuer Professor Rainer Blatt danken, der mir die Möglichkeit gab in einem großartigen Team zu arbeiten und mich seit vielen Jahren begleitet.

Die Ergebnisse dieser Arbeit wären ohne die Unterstützung des gesamten Teams und im speziellen der *Linearen* nicht möglich gewesen. In diesem Sinne möchte ich vor allem Philipp Schindler, Monz Thomas, Esteban Martinez, Alexander Erhard und Julio Barreiro danken. Ihr habt mir nicht nur unzählige Nächte im Labor (*Zitat: "Wo findet man noch was für eine Nacht"*) zur Seite gestanden, sondern auch eine lustige und "seriöse" Zeit abseits des Labors ermöglicht. Zusätzlich möchte ich Roman Stricker und Matthias Brandl für weitere Unterstützung danken. Michael Chwalla und all jenen die vor mir an diesem Experiment gearbeitet haben gebührt mein Dank für die großartige Arbeit. Philipp Schindler, Markus Hennrich und Tracy Northup möchte ich für das Korrekturlesen danken.

Die expermentellen Ergebnisse sind unter Zusammenarbeit mit den theoretischen Physikern Markus Müller, M. A. Martin-Delgado, Masoud Mohseni und Angel Rivas entstanden. Vor allem möchte ich Markus Müller danken, der mir die Welt der Fehlerkorrektur zeigte und nicht nur viele Nächte im Labor mit mir verbrachte, sondern der einzige theoretische Physiker ist, der unsere Maschine bedienen kann. M. A. Martin-Delgado und Markus möchte ich für die schönen Aufenthalte in Madrid danken.

Unsere Arbeit wäre nicht möglich ohne die hervorragende Unterstützung des Sekreteriats, sowie der elektronischen und mechanischen Werkstätten. Besonderer Dank gebührt Patricia Moser, die sich immer um unsere Anliegen kümmert.

Ein herzliches Danke gebührt meinen gesamten Freunden die mich stets aufgemuntert haben und denen ich unzählige schöne Zeiten verdanke. Besonders hervorheben möchte ich Daniel, der mit mir gemeinsam das Studium und die Doktorarbeit bestritten hat. Ich bin glücklich so tolle Freunde zu haben.

Meinen Eltern, Elfriede und Egon, möchte ich von ganzem Herzen für die Unterstützung während meines gesamten Studiums danken - ohne euch wäre das alles nicht möglich gewesen. Besonderer Dank gebührt auch meinen Schwestern Isabella, Bernadette und Juliane, denen ich immer wichtig war. Monika, Albert, Simon und Anna möchte ich ebenfalls für die Unterstützung während der gesamten Zeit danken.

Am Ende meiner Doktorarbeit passierte mit Sicherheit das schönste Ereignis — die Geburt meines Sohnes Felix. Ich danke meiner Freundin Catherina für alles was sie für micht getan hat und dass sie mir immer zur Seite gestanden hat -DANKE!